Probing the diffuse interstellar medium with diffuse interstellar bands

Amanda Bailey

Doctor of Philosophy

Environment, Physical Sciences and Applied Mathematics Research Institute,
University of Keele.

June, 2014

Abstract

This work investgates the small scale structure of the Diffuse Interstellar Medium. To do this optical spectroscopy is used to obtain spectra of early type stars which are used as background targets with which the Diffuse Interstellar Medium (ISM) is probed. The spectra obtained contain the highly diagnostic Diffuse Interstellar Bands (DIBs), Na I D and Ca II lines.

The maps I present here are of the Local Bubble, the Small Magellanic Cloud and the Large Magellanic Cloud. These are the first DIB maps of the solar neighbourhood and large portions of external galaxies. The specta were obtained with the New Technology Telecsope (NTT) at La Silla Observatory in Chile (Local Bubble survey) and at the Anglo-Australian Telescope (AAT) at Siding Spring Observatory, NSW, Australia. The NTT spectra are long slit spectra of 239 individual targets, whilst the AAT spectra were obtained with the multi-fibre spectrograph 2dF/AAOmega (about 350 targets in each of the Magellanic Clouds).

I have succesfully used the 5780 and 5797 Å DIBs to map the ISM in the Local Bubble and the Magellanic Clouds. The 5797 Å DIB traced neutral structures whereas the 5780 Å DIB traced warmer and/or more highly irradiated gas, possibly residing in the skins of those neutral clouds It showed a more highly structured Local Bubble than revealed by the sodium maps, on sub parsec scales; tracing the walls of the Bubble and clearly showing the Bubble opening out into the Halo. In the Magellanic Clouds the DIBs trace molecular clouds surrounding regions of active star formation; they are weak or absent in quiescent molecular cloud complexes and hot gas bubbles.

Acknowledgements

"*It is never too late to be what you might have been*"
– George Eliot

I dedicate this thesis to my late parents, Chris and Len Brown.

Dad did not know that I had returned to study; he never knew that our discussions about the Moon landings and my subsequent fascination with the stars would one day see me make a journey from observing high up in the mountain tops of Chile across to the other side of the world to China to attend a conference. I owe my insatiable curiosity and determination to our in-depth and often argumentative discussions. Mum did know that I had obtained a degree and had started my PhD, she knew I had travelled to observe and loved to hear about it all. She too was fascinated with astronomy and found a renewed interest as a result of my work. Although one of my observing trips to Australia was tinged with sadness at her passing while I was away, I do have a wonderful memory of her waving me off on that trip, a memory that got me through the most difficult parts of the PhD. I promised her I would complete it and I have. There are many other thanks to give for the support I have received while doing this PhD: the rest of my family, my son Josh, Sue and Rod in particular, for their support and encouragement; my supervisor, Jacco, for giving me the opportunity (and putting up with me!); Emily, for warning me what a nightmare it would be but also for just being there for me throughout; the "12:30 at Foyles" gang - Jon, Colin, Rob and Adam, with whom many a boozy lunchtime was spent discussing my work, life the Universe and everything; Donovan, Tony and the lads at the garage for achieving the impossible on more than one occasion and keeping my car on the road so I could get to Keele; the many friends and colleagues too numerous to mention from the Society for Popular Astronomy, the Open University, the Royal Astronomical Society and last but not least the Shropshire Astronomical Society. My final thanks go to Vic Tyne, as one of my Open University tutors and then a colleague at Keele, Vic bridged the two types of my study. Indeed, I really could not have done this without his encouragement.

Contents

List of Figures

List of Tables

1 Introduction and literature review

"Astronomy compels the soul to look upwards and leads us from this world to another"

- Plato

1.1 Motivation

The Interstellar Medium (ISM) is both the birthplace of stars and their final resting place; the alpha and the omega. As such it is an incredibly complex and diverse environment the study of which is paramount to our understanding the evolution not only of stars, planets and galaxies but ultimately of life itself. In fact, the study of galaxy evolution would not be complete without accounting for the Interstellar Medium. Galaxies are ecosystems in which stars form, evolve and die; constantly interacting with the ISM.

Surprisingly, small, neutral ISM structures are encountered in both the cold ISM and in the much warmer (weakly-)ionized diffuse ISM. This poses many questions one of which is "Are the materials that make up these small structures the same or different in each type of environment?" By using Diffuse Interstellar Bands (DIBs), some of which are known to form in hot, UV-irradiated environments while others form in cooler environments, we can probe the distribution of material and conditions within extreme environments such as the Local Bubble (LB) and the Disc-halo interface. Thus, we can learn about the nature of the diffuse Interstellar Medium in such regions.

1.2 The Interstellar Medium

The Interstellar Medium consists of a tenuous gas of hydrogen and helium enriched with a scattering of heavier elements. Whether the gas of the ISM occurs as ions, molecules

or atoms depends upon the presence of radiation fields as well as the temperature and density of the gas.

The ISM is a turbulent and dynamic place where the majority of its volume contains diffuse ($n \sim 0.1\,cm^{-3}$) hot ionised gas ($T \sim 10^5\,K$) in which most of the gas mass is either in HI clouds ($10^2\,K < T < 10^4\,K$) or in cold, dense, star forming molecular clouds ($T < 10^2\,K$), (Avila-Reese 2007; Cox 2005). In small scale interactions stars return chemically enriched gas to the ISM by ionising radiation and stellar winds. Large scale interactions such as supernovae return the enriched gas to the Galactic Halo or inter-galactic space where it cools and rains down onto the Galaxy or is accreted by another galaxy close by (Bland-Hawthorn et al. 2007). The molecular clouds in which star formation occurs appear to form during the large scale compression of the ISM by supernova explosions (Avila-Reese 2007), colliding gas flows or spiral wave gravitational modulations. The intense star formation also produces massive gas outflows in the form of galactic fountains and winds returning material into galactic and intergalactic space. The ISM on small scales often displays filamentary structure resulting from hydrodynamic and thermal dynamic instabilities in environments ranging from supernova remnants to the diffuse interstellar cirrus.

1.3 The Local Bubble

The Local Bubble is a desolate place, it is a cavity in the interstellar medium that contains so little matter it can be considered a near-perfect vacuum. Nevertheless our solar system is embedded within this desolate region. This gives us the unique opportunity to study the interstellar gas in such extreme environments via accurate absorption line measurements along lines-of-sight which are essentially free from intervening contaminating features. The LB is a region of unusually low gas density in the interstellar medium (ISM); it extends for $\sim 100\,pc$ in the plane of the Galaxy and for hundreds of parsecs vertically, presumably as far as the galactic halo (Welsh et al. 1999; Welsh et al. 2010).

Conditions in the ISM can be probed in many ways; for example: O VI absorption, absorption lines arising from neutral or singly-ionized atoms or molecules, X-ray and synchrotron emission. However, there is a problem with understanding the nature of the gas within the LB using the absorption line method as such atoms and molecules are not expected to survive at the high temperatures inferred for the LB. To overcome this problem it is necessary to probe the LB using species which may survive under these conditions. To achieve this we use absorption in the Diffuse Interstellar Bands. The carriers of DIBs are thought to be large molecules such as polycyclic aromatic hydrocarbons and such molecules are resistant to UV radiation.

The DIBs are a set of over 400 broad optical absorption features which are omnipresent in the ISM; for reviews see Herbig (1995), Sarre (2006). They are absorption bands in the visual and near-infrared spectral region. Their carriers are, as yet, unknown but are likely to be molecular. I will describe them in more detail in section 1.6. The nature of their carriers has been much debated since Mary Lea Heger first observed them in 1922 (Heger 1922); however, the current consensus of opinion is that they are large molecules such as polycyclic aromatic hydrocarbons (PAHs). Such molecules are thought to be resistant to UV radiation. Observations of DIBs have shown that they are sensitive to their environment; for instance, the ratio of $\lambda\,5780/\lambda\,5797$ equivalent widths is indicative of the transition between diffuse atomic and diffuse molecular gas and at least some well-known DIBs are known to exist in hot, UV-irradiated environments. Although the signal-to-noise required is high, Cordiner et al. (2006) have shown there are DIB absorption towards stars within the Local Bubble with very unusual band ratios (e.g., $\lambda\,5780/\lambda\,5797$) that identify a difference in band strength on a scale of a few hundred AU. The low reddening towards our stellar probes will result in rather weak DIB features, but as shown by van Loon et al. (2009) DIBs are also seen in the relatively harsh environments such as the Disc-Halo interface and the high $\lambda\,5780/\lambda\,5797$ ratio indicates the existence of interfaces between cool/warm and hot gas. This opens the possibility of probing the distribution and conditions within the LB via DIB absorption, whilst the differences in distributions of the various DIB carriers can provide constraints on the nature of the carriers. Another correlation that

is important is the near perfect correlation between the 6196 and 6614 Å DIBs. The correlation coefficient for this DIB pair has been determined to be $r = 0.986$ with a goodness of fit measurement taken as $r^2 = 0.971$, indicating that 97.1% of the variance in one DIB can be explained by corresponding changes in the other DIB (McCall et al. 2010). Such a tight correlation is believed to be indicative of a common carrier but this has not yet been proved.

Here we use the DIBs to probe the interaction region (the wall of the LB) between the hot gas in the bubble and its cooler neutral surroundings as well as looking for neutral structures located within the bubble itself. The neutral structures within the LB are indicative of thermal instabilities leading to cold compact structures immersed within the hot gas. The wall/bubble interface shows dynamic instabilities due to pressure gradients, leading to small scale structure. Although several optically-varying lines-of-sight are known [see Crawford (2003) and references therein], a systematic inventory is lacking. My sample of high signal-to-noise observations of interstellar absorption towards nearby stars offers a first point of reference suitable for a systematic investigation of time-varying interstellar absorption. By re-observing those targets which are found to exhibit substantial interstellar absorption a few years later, it will be possible to search for time variations in the interstellar absorption which, are caused by the changing line-of-sight due to the stellar proper motion. This will probe the ISM on scales of a dozen AU, which is a much smaller scale than the tens of pc probed by the maps we create here.

1.3.1 The origin of the Local Bubble

The origin of the Local Bubble has been a bit of a mystery. Its presence was initially indicated by the very low values of interstellar extinction measurements of stars within 100 pc of the Sun when compared with more distant regions of the Galaxy (Fitzgerald 1968; Lucke 1978). The observation of a diffuse soft-X-ray background by the ROSAT satellite provided the first evidence for the LB and was interpreted as indicating that the Sun was surrounded by a region of hot ($\sim 10^6$ K) gas (Snowden et al. 1998).

However, such a volume of hot gas should emit copious energy in EUV emission lines, which were searched for with the CHIPS satellite but not detected (Sasseen, Hurwitz & Team 2004). Hot gas should also strongly absorb in the O VI 1032 Å line, which is far weaker towards nearby sources than expected (Cox 2005; Barstow et al. 2010).

Stellar winds and supernovae (SN) events that are associated with clusters of massive early-type stars, OB associations, are known to create large cavities, or 'interstellar bubbles', which are ubiquitous in the Milky Way galaxy as well as the Magellanic Clouds (e.g. N44 and N19) (Welsh & Shelton 2009). Therefore, it was reasonable to assume that such stellar winds and multiple SN explosions created the hot plasma filled, low-density cavity with surrounding dense shell of material that we find ourselves residing in.

The age of the LB has been inferred as being ~ 14 Myr and its formation is probably the result of multiple supernovae (Breitschwerdt & deAvillez 2006; Breitschwerdt, deAvillez & Baumgartner 2009).

The origin of the LB was thought to be the result of multiple nearby SN (Cox & Anderson 1982) or possibly a single explosive event in the Sco-Cen OB association (Frisch 1981). Under this scenario the LB can be interpreted as being a region which is an old, cooling SN remnant or superbubble. However, there was no firm evidence for this as no OB association was found within boundaries of the LB (Fuchs et al. 2006).

1.3.2 The location and trajectory of the Sun

Figure 1.1 is an artist impression of the Local Bubble showing our location as the orange dot with the arrow showing the direction we are moving in, with respect to the Local Standard of Rest velocity frame. Regions of recent star formation are shown by nearly spherical bubbles. Near the Sun, the purple filaments represent gas shells left over from star formation that occurred 4 million years ago in the Scorpius-Centaurus Association just to the lower left of the Sun.

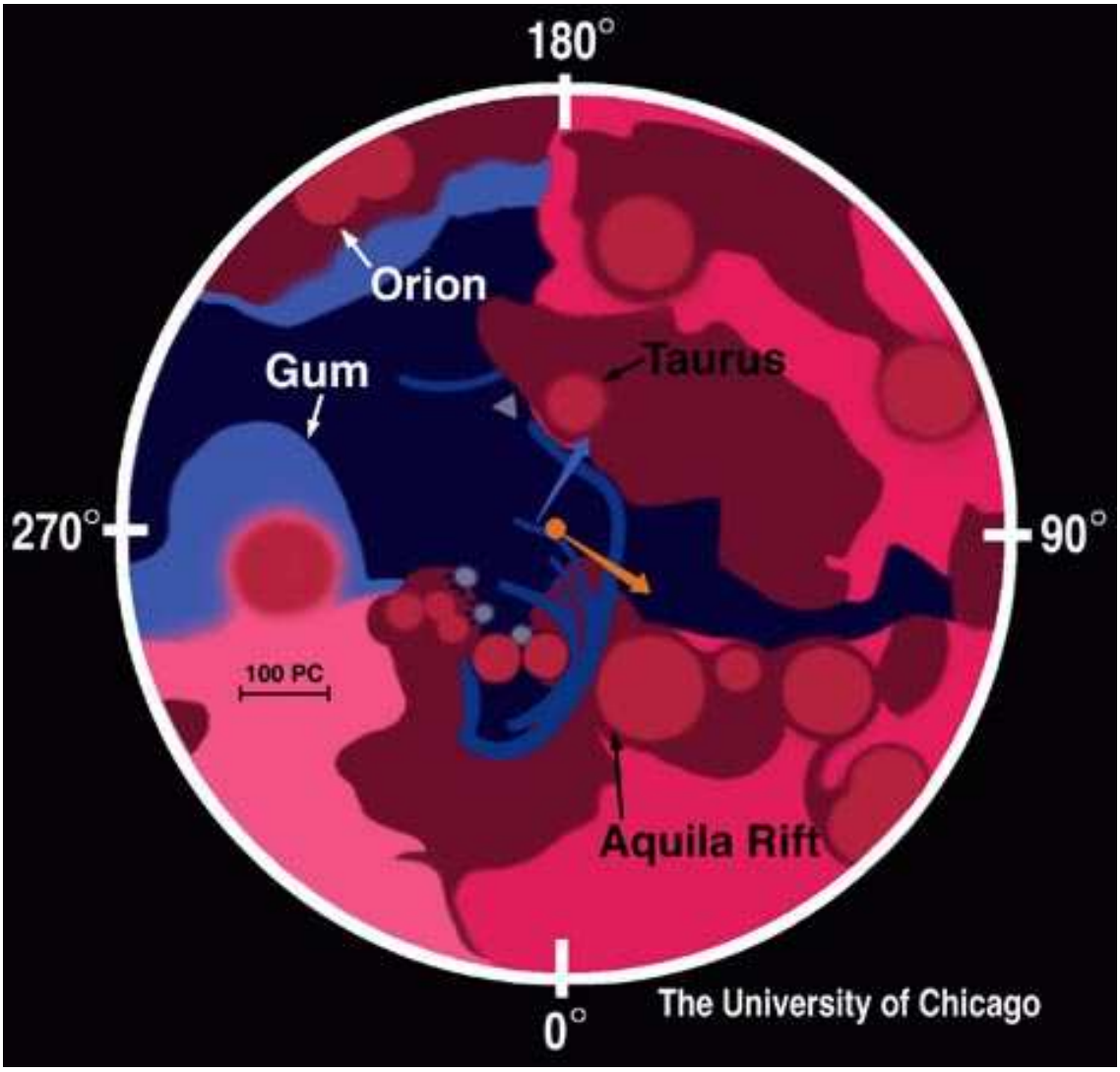

Figure 1.1: Impression of the Local Bubble by C. Wellmann showing the location of the Sun, (Frisch 1998).

1.4 The Small and Large Magellanic Clouds (SMC and LMC)

The Small and Large Magellanic Clouds (SMC, LMC) are our nearest extragalactic neighbours; they have low-metallicity environments (the LMC has a metallicity of about 40% of the Milky Way Galaxy and the SMC has a metallicity of about 20% of the Milky Way Galaxy). The distance of the Magellanic Clouds is well known (about 50 kpc for the LMC and 60 kpc for the SMC, (Cioni et al. 2008)). They are receding from us at a rate of about 200-400 km s^{-1} for the LMC and 100-200 km s^{-1} for the SMC. Gas only records its most recent dynamical history as its kinematics are affected by non-gravitational processes and its chemistry reflects the most recent enrichment and mixing. Stars with age ranges from a few to approximately 100 Myr allow the evolution of a galaxy to be followed since the ISM processes will have dominated its evolution. With their low-metallicity environments and their proximity, which allows individual stars in the Clouds to be resolved, the Magellanic Clouds offer a unique and ideal opportunity to study the details of star formation and feedback under a range of conditions considered typical of the conditions which occurred at the height of cosmic star and galaxy formation at around redshifts 1–3.

1.4.1 Differences between the SMC, LMC, Milky Way (the role of metallicity)

The Tarantula Nebula (30 Doradus (30 Dor), or NGC2070) in the LMC is the nearest example of a mini starburst region. It is a spectacular region of ionized hydrogen and irradiated dust clouds, which outshines all other HII regions in the Local Group. 30 Dor contains hundreds of powerful O- and B-type stars whose evolution is dominated by the effects of mass-loss from their strong stellar winds. The stellar winds themselves are accelerated by momentum transfer from photons in the radiation field to metal ions in the outer regions of the star. Thus it is expected that the mass lost by a star is dependent on the metallicity of the region. The proximity, metallicity and the

interaction with the ISM of 30 Dor make it an ideal case study with which to investigate the connection between the ISM and the dynamical evolution of this cluster and it provides an ideal template to investigate the dense regions of star formation in distant galaxies.

1.5 Diffuse interstellar bands (DIB)

One of the most powerful tools for detecting differences in the physical conditions of the gas in the ISM are observations of Diffuse Interstellar Bands (DIBs). Although excellent tracers of molecular material DIBs are under-used as a diagnostic. The carriers of DIBs, (PAHs), are thought to be resistant to UV radiation, and at least some well-known DIBs are known to exist in hot, UV-irradiated environments. This opens up the possibility of using DIBs to probe the distribution of material and conditions within the extreme environments of regions such as the Local Bubble and the Disc-halo interface, which are home to the diffuse interstellar medium.

Diffuse Interstellar Bands are weak absorption features seen in the spectra of hot stars. They are caused by the absorption of photons by the ISM and have been detected in the near UV, visual and near IR parts of the electromagnetic spectrum. Their name reflects the fact that the absorption features are much broader than the normal absorption lines seen in stellar spectra. The first observational record of DIBs was made by Mary Lea Heger in 1922 during her PhD research at the Lick Observatory (Heger 1922; Sarre 2006; Wszołek 2007; Xiang, Liang & Li 2009). Heger's work was based on that of Hartmann (1904) who discovered that in the spectrum of Nova Persei the H (3969 Å) and K (3934 Å) absorption lines of calcium and the sodium D lines (5890 and 5896 Å) remained in a fixed position while hydrogen lines and lines of other elements were broadened, displaced and changed form. This led Hartmann to conclude that the H, K and D lines had their origins not in Nova Persei itself but in a nebulous mass lying in the line-of-sight (Hartmann 1904). Heger undertook a more complete investigation of the sodium lines in class B stars and concluded they had the same

anomalous behaviour as the calcium lines as observed by Hartmann. During her work Heger noticed two broad features that appeared to be interstellar in origin; these were at 5780 and 5797 Å and she simply made a note of their existence (Heger 1922). Over a decade later observations at Mount Wilson by Merrill (1936) disclosed four detached interstellar lines, which included the two lines observed by Mary Heger and, which had the approximate wavelengths of 5780.4, 5796.9, 6283.9 and 6613.9 Å; these behaved like interstellar lines but were wider than expected and had diffuse edges, (Merrill (1936), Sarre (2006) and references therein). Further observations and investigations followed: notably by Merrill (1934); Merrill & Humason (1938); Merrill & Wilson (1938); Beals & Blanchet (1938); Baker (1949); Duke (1951); Herbig (1975); and Jenniskens & Desert (1994). Their work led to more DIBs being discovered and surveys of the observed diffuse features being published. Their results proved that the intensity of DIBs was correlated with distance and degree of interstellar reddening of the star that provided the background continuum. Their results also showed that the DIBs were of interstellar origin; they did not exhibit the velocity variations of the spectroscopic binaries they were observed against and they shared the same Doppler shift of the sodium lines that were formed in the intervening clouds, (Krełowski (1988),Herbig (1995),Xiang, Liang & Li (2009) and references therein). Evidence that DIBs arise in the interstellar medium is given by further work on the stationary lines observed in spectra that led to their initial discovery. For instance: Krełowski & Sneden (1993) observed the ISM in the direction of the binary HD23180 on two successive nights; their results showed that the diffuse bands together with interstellar sodium do not share the Doppler shift of stellar features.

In the top panel of Figure 1.2 it can be seen that the D lines remain stationary as the stellar 5876 Å He I line oscillates in response to the orbital period of the binary system; the bottom panel shows that the well known strong DIBs (at 5780, 5797, 5850 Å) and weaker features, which Krełowski & Sneden (1993) claim as DIB detections, also remain fixed in the sodium velocity space whereas the Si III line at 5739.73 Å and the Fe III at 5833.94 Å shift from night to night in the same manner as the He I line. A major survey was conducted by Jenniskens & Desert (1994) to

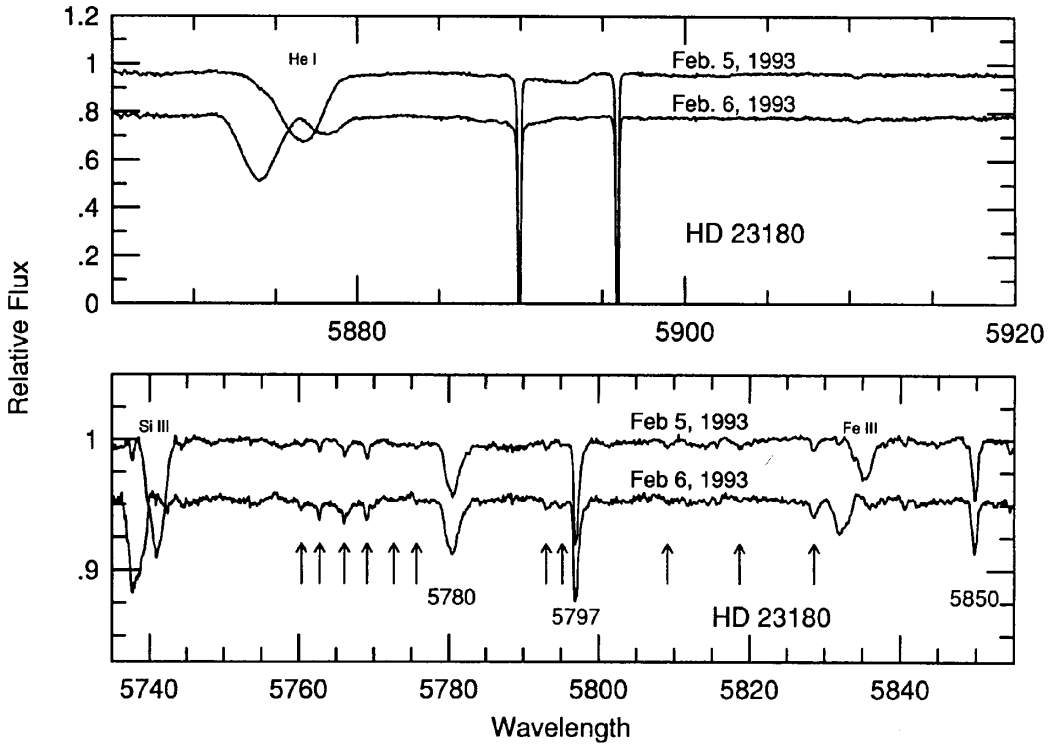

Figure 1.2: Two spectra of the binary HD 23180 showing the Doppler shifts of the stellar lines and stationary nature of the interstellar features: Na, Si III, known DIBs and claimed DIB detections marked with arrows, (Krełowski & Sneden 1993).

meet the need for a comprehensive survey that could be compared with laboratory results. The main characteristics of their survey was high spectral resolution ($\Delta\lambda = 0.3\,\text{Å}$) over a wide spectral range (3800–8680 Å); however, it involved only four reddened stars chosen to cover a range in reddening, spectral type and relative radial velocity between the star and the interstellar dust. This catalogue is published on-line at http://leonid.arc.nasa.gov/DIBcatalog.html and has been updated with new discoveries by Krełowski, Sneden & Hiltgen (1995) and Jenniskens et al. (1996). Figure 1.3 shows a composite spectrum of the certain and probable DIBs listed in the Jenniskens & Desert (1994) catalogue. It gives a reasonably complete picture of the strongest of the DIBs and their distribution in the electromagnetic spectrum.

1.5.1 The carriers of the DIBs

To date 414 DIBs have been documented. Their most remarkable characteristic is the varying widths of the bands; they range from $\sim 10^{-10}$ Å to $\sim 2 \times 10^{-10}$ Å. The spectra are found between the range ~ 4000 Å and ~ 13000 Å, which is equivalent to photon energies in the 1–3 eV range. The breadth of the bands is considered to be a defining characteristic and should play a major role in defining their origin (Sarre 2006). Some important spectroscopic characteristics are the lack of regularity in the wavenumbers of the bands (used as a unit of energy in spectroscopy) and a lack of common band widths (Sarre 2006). Some of the DIBs are strong contrary to others which are extremely weak. There are narrow DIBS (e.g., 5797 Å) and very broad bands (e.g., 4430 Å). Such diversity is sufficient to indicate there must be many carriers of DIBs and possibly DIBs could be divided into families where one carrier is responsible for producing the bands that belong to each family (Wszołek 2007).

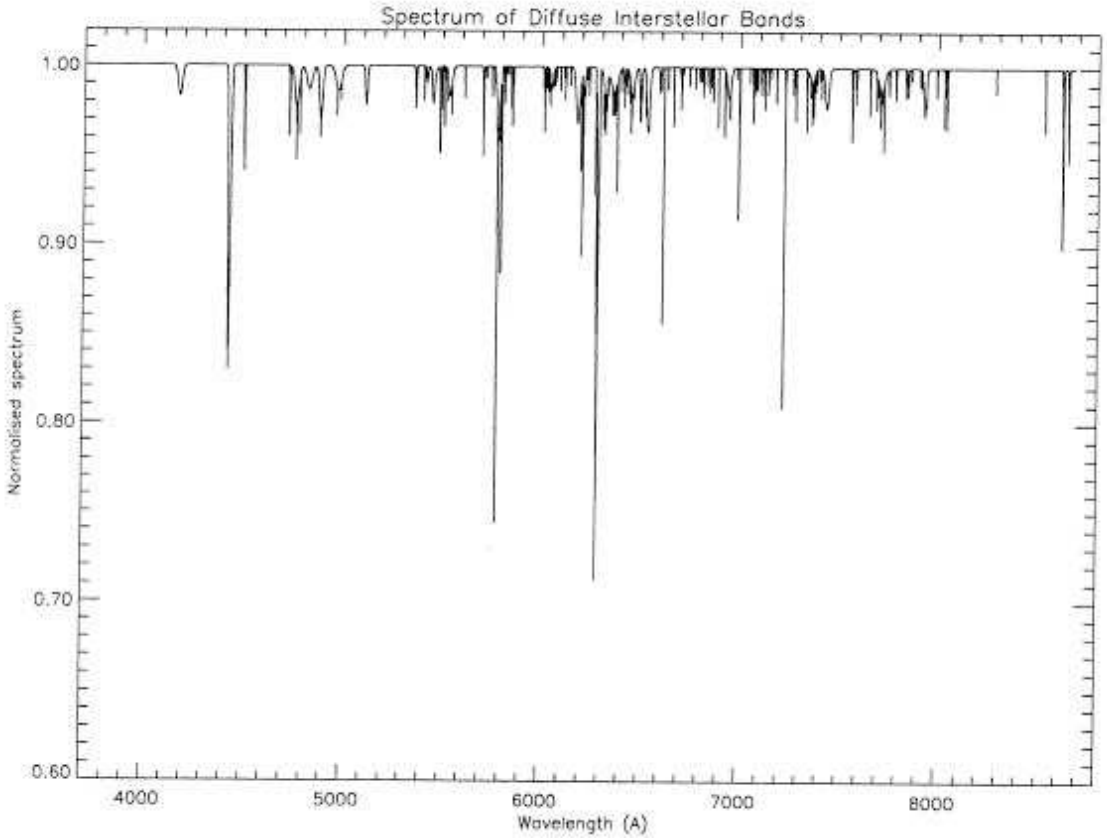

Figure 1.3: Composite DIB spectrum of DIBs listed in the 1994 DIB catalogue, (Jenniskens & Desert 1994).

In 1987 Krełowski & Walker (1987) summarised the following groupings as families:

1. The broad shallow bands 4428, 6177 and perhaps 4882 Å
2. The relatively symmetric DIBs 4763, 4780, 5362, 5449, 5487, 5780, 6195, 6203, 6269, 6283 and perhaps 5535 Å
3. The relatively sharp but usually asymmetric bands 4726, 5545, 5797, 5849, 6376, 6613 and possibly 5494, 5508 and 6379 Å

The identity of the DIB carriers is a long standing problem. The large numbers of known DIBs and their wide distribution across the spectrum (see Figure 1.3 above) suggested that more than one carrier is involved, (Wszołek 2007). The carriers are omnipresent; they are found in numerous reddened Galactic lines of sight and in external galaxies including the Magellanic Clouds (Sarre 2006). Krełowski et al. (1999) observed ~ 70 stars representing various degrees of interstellar reddening; their results showed there was a good correlation between the band strengths and the reddening index $E(B-V)$ indicating some association between the DIBs and the dust particles that cause optical extinction (see Figure 1.4). However, the dust grains are unlikely to be directly responsible for the diffuse band absorptions. Wszołek (2007) notes that solid-state transitions in large-grains should produce features that exhibit changes in profile shape and central wavelength that correlate with grain size and that emission wings would be expected for grain sizes of radii $> 0.1\,\mu$m; these have not been observed. Also there is a lack of polarisation in the features that would link them to larger aligned grains, (Wszołek 2007). Therefore, if solid particles are carriers of DIBs they must be very small in comparison with the wavelength. Figure 1.4 shows the correlation of the equivalent width, W_λ of the 5780 Å diffuse band vs. $E(B-V)$ (Krełowski et al. 1999) on which Sarre (2006) noted that it also highlights the scatter that exists the reasoning for which is not understood.

A key point to consider for the possible carriers of DIBs is the understanding that large molecules can undergo photon absorption without being destroyed and that this results in broad spectra due to fast internal relaxation processes. The list of possible

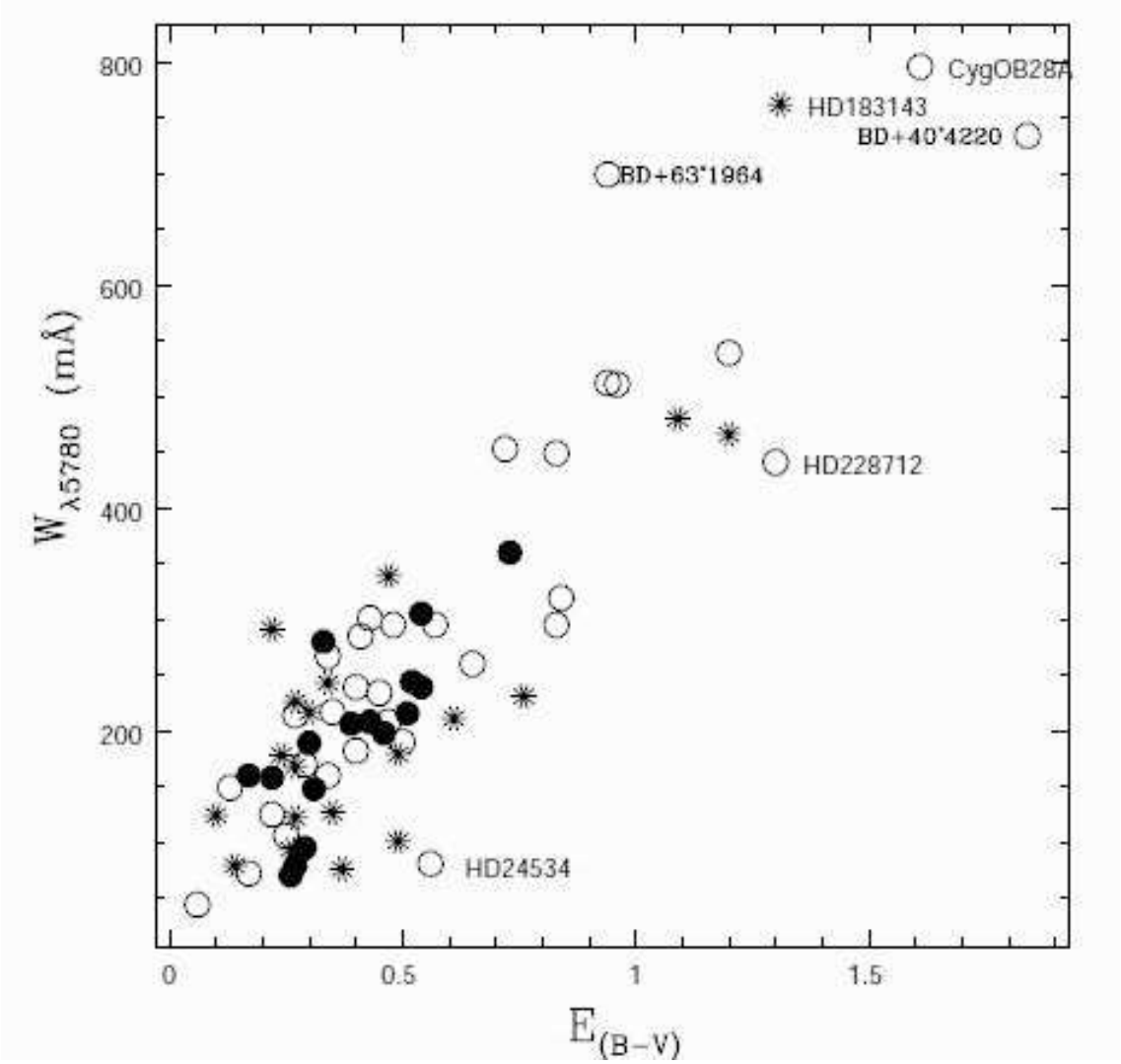

Figure 1.4: Showing the relationship between the strong 5780 Å DIB and $E(B-V)$, Krełowski et al. (1999).

carriers now include: lattice defects; the hydrogen anion; porphyrins; carbon chains; molecular hydrogen; polycyclic aromatic hydrocarbons (PAHs); fullerenes and carbon nanotubes, (Sarre (2006) and references therein). DIB carrier abundances depend on various environmental factors particularly the UV radiation field. Cox et al. (2006) undertook a study of DIBs in the LMC including 30 Dor, in which the dense cluster of OB stars produce a strong UV field, to gain an insight to the chemical properties of the DIB carriers. They examined the relationship between the DIBs and atomic lines of several key interstellar species, which were observed simultaneously in several LMC lines-of-sight. Two of the strongest DIBs are 5780 and 5797 Å; their $W_{DIB5797}/W_{DIB5780}$ ratio indicates the degree of ionisation conditions as inferred from the atomic to total $(H + H_2)$ hydrogen ratio (Cami et al. 1997). Certain correlations between DIBs are well known so these DIBs and ratios of DIBs can be used to detect differences in physical conditions in the gas. Thus DIBs are a very powerful tool despite the fact we do not know what their carriers are!

1.5.2 The use of DIBs in mapping the ISM

The first systematic survey of DIBs was published by Herbig (1975); this covered a total of 39 diffuse absorption features between 4400 and 6850 Å which were regarded as probably originating in the ISM and another seven features considered possible DIB candidates. Herbig (1975) investigated the 17 bands with the most data available and noted an excellent correlation between the equivalent width, which provides a quantitative measure of the strength of a spectral feature, and colour excess E, which is a measure of the amount of interstellar reddening caused by light being scattered and absorbed by dust in the intervening ISM. This correlation showed that the entire diffuse line spectrum strengthened together with, and in direct proportion to, increasing stellar extinction; supporting the hypothesis that diffuse lines can be considered as fine structure in the ISM. As new data appear and better observations are made it may be possible to re examine the situation and create a more reliable set of family groupings, (Herbig (1995) and references therein). Snow & Destree (2011) list, as follows, the important properties of DIBs:

1. Limited wavelength region: Most are in the red range; almost none are in the blue.

2. Generally weak strengths: DIBs have very small depths; there are none below 20 percent down from the continuum. Most are less than 5 percent below continuum and less than 30mÅ in equivalent width.

3. Specific widths: The broad DIBs are up to 20 Å wide; the narrow ones are less than 1 or 2 Å wide.

4. Cloud type dependent: Slightly different sets of DIBs are seen in different environments; they are not constant everywhere. One factor seems to be cloud density, from diffuse to translucent.

5. Lack of saturation: All DIBs, whether strong or weak, grow linearly with increasing extinction.

6. Not circumstellar: Several studies of various types of stars with circumstellar material do not show DIBs, despite many searches.

7. Well-correlated with extinction: All correlations with extinction are good (meaning correlation coefficients are generally above 0.7), but they are far from perfect. This includes UV extinction.

8. Well-correlated with atomic hydrogen: DIBs are significantly better correlated with atomic hydrogen than with molecular hydrogen.

9. Poor correlations between DIBs: Different authors have defined different sets or families of the DIBs that seem to be well correlated. Only one pair of DIBs comes close to being perfectly correlated, 6196.0 and 6613.3 Å.

10. Invariant central wavelengths: DIB central wavelengths show little to no shift between sightlines, except for Doppler shifts with cloud motion.

11. Distinct profiles: Many DIBs are asymmetric, though some of the broad ones are symmetric. The profiles are invariant in most lines of sight.

12. Intrinsic structure: Some narrow DIBs show structure possibly consistent with rotational bands. This is not caused by Doppler shifts, as they are the same everywhere. Broad DIBs generally do not show structure.

13. Rarely found in emission: DIBs in emission have only been observed in the Red Rectangle and toward one other star.

14. Lack of emission wings: No DIB has shown emission wings in any environment.

15. Lack of polarization: Several DIBs have been studied in searches for polarization, with no positive results.

16. Reasonable elemental composition: Expectations about ISM gas composition should be consistent with the cosmic abundances of common elements.

17. Lack of UV DIBs: Recent searches have shown that any UV DIBs are weak and do not resemble strong DIBs such as 4428 Å.

There is increasing interest in searching for correlations between bands by observing through many lines of sight through different types of clouds. Sarre (2006) has conducted an observation program to record spectra at high signal-to-noise ratio towards binary stars that are only separated by $\sim 100 - -10,000$ AU. This will mean that two lines-of-sight should have chemical and physical similarities in the cloud conditions unlike two widely separated unrelated lines-of-sight. This will complement other work to determine the small scale structure of the interstellar medium (Sarre 2006). Herbig (1975) calculated the mean wavelengths of the diffuse lines assuming that they shared the Doppler shift of interstellar Na I. To try and directly determine whether the diffuse lines showed the fine structure of atomic lines produced in multiple clouds Herbig (1975) conducted a rough test to overcome the problem of the wide diffuse lines preventing this determination. The reasoning was that in a spectrum with widely spaced

double Na I lines of equal strength the unresolved diffuse lines would have an intermediate displacement; assuming other factors were equal. This hypothesis was tested using 6 Cas (HD 223385), which can be seen through both the Orion and Perseus arms and where the double Na I lines have a separation of 39 km s^{-1}. The results show that the mean displacement of the diffuse lines is in 6 Cas is -17 km s^{-1} and so clearly corresponds to the Na I component at -16 km s^{-1} and not an intermediate value. The only conclusion that could be reached is that the diffuse lines share the displacement of the Orion arm interstellar lines and there is little or no contribution from the Perseus arm (Herbig 1975).

The spatial distribution and physical state of the ISM is an important current question; the discoveries of unexpectedly high abundances of H_3^+ along optical transmitting sightlines and radio detections of molecules in absorption in translucent clouds have raised new challenges. One possibility is that diffuse clouds have fine structure; for example: sheets; filaments or cloudlets. If this is so it could alter the understanding of the chemical constituents of the diffuse ISM and have significant implications for the early stages of star formation. Cordiner et al. (2006) searched for small changes in the absorption-line strength in the diffuse bands between lines of sight. From their observations they modelled C_2 and CN abundances in several lines-of-sight using their results to commence a study to link this data with the chemistry of known atoms and molecules along these lines-of-sight, (Cordiner et al. (2006), and references therein).

It is possible the diffuse bands could trace a relatively diffuse component of the interstellar gas. Work by Herbig (1993) has found that the carrier of the 5780 Å diffuse band is dependent on the amount of atomic hydrogen and independent of molecular hydrogen, which controls the abundance of neutral carbon diatomic molecules like CH in diffuse clouds. The variations in diffuse band strengths could be explained by species-dependant reaction rates for the diffuse band carriers in the different lines-of-sight and therefore, could explain the small scale structure observed for atomic species (Cordiner et al. (2006), and references therein).

The investigations of Welty et al. (2006) suggest that the general correlations of DIB strength with the column densities of other components of the ISM, coupled

with the different DIB behaviour noted in different regions of the ISM, make DIBs a powerful tool as quantitative tracers of diffuse interstellar material and as diagnostic of the physical conditions in the regions they probe. Since their discovery in 1922 a large number of DIB data has been accumulated. The emphasis has been on determining the nature of their carriers and this has lead to a veritable cornucopia of information which can now be used to determine the nature of hitherto un-mapped regions of the ISM such as hot, UV-irradiated environments where at least some well-known DIBs are known to exist. This overcomes the problem of understanding the nature of the gas within such extreme environments as, typically, conditions in the ISM are probed via lines arising from neutral or singly-ionized atoms or molecules, which are not expected to survive at such high temperatures and are therefore not useful as tracers in these extreme environments. With new, large telescopes and advancements in image detectors and processing systems high signal-to-noise spectra are being obtained; this is an essential way forward to gain insight into the intrinsic profiles of DIBs.

1.6 Direction of thesis research

1.6.1 Pertinent scientific questions to be addressed

Mapping the the small scale structure of the ISM in order to determine the small scale structure of the ISM has the potential to answer some important questions. It can give a global picture, an overview of small scale structure. Creating the maps using different tracers can reveal detail and then standing back to look at the whole picture can suddenly make things obvious that before had gone unnoticed because study has been too concentrated in one small area. The global picture that mapping can give also highlights areas of interest to study in detail.

Knowing what type of environment is where and how that changes on small scales is key to understanding how some molecules may be able to survive the harsh interstellar space. By mapping the abundances of the Diffuse Interstellar Bands, sodium

and calcium we can put constraints on conditions that are needed for DIBs to survive, for the environment the need to form or in what type of environment they may be destroyed. It is the the question that has been asked since their discovery and to date we still do not know the answer.
Specific questions that are still to be answered include the following:

1. What is the structure of the Interstellar Medium, in particular of the Local Interstellar Medium (LISM)?

2. What is the Earth going to run into next?

3. What is or are the carriers of the Diffuse Interstellar Bands (DIBs)?

To try to answer these questions I have used absorption-line spectroscopy of back-ground stars to obtain spectra that include DIBs, I have observed different regions, the low metallicity of the Magellanic Clouds and the higher metallicity of the local Bubble. Does metallicity make a difference? I have observed nearby stars for the Local Bubble to see the detail and get the local picture. I have observed the distant LMC and SMC that would also trace the environment though the Local Bubble and the Galactic Halo. With the SMC and LMC I am the distant observer and I observe the global picture. Are there areas where there are similarities between the LB and MC - are there differences?

1.6.2 Methodology (absorption-line spectroscopy of back-ground stars)

Spectroscopy is the study of the interaction between matter and radiation as a function of wavelength or frequency and is used in astronomy mainly to determine the chemical composition and physical properties of astronomical objects or to measure the velocity of objects from the Doppler shift of their spectral lines. Spectral lines are observed either in absorption or emission and are the result of a photon carrying a specific

amount of energy that allows a change in the energy state of the atomic or molecular system it encounters. Absorption lines occur when the detector is in a direct line with the photon source and the gas; a decrease in the intensity of light at the frequency of the incident photon is seen as the re-emitted photons from the gas are generally in random directions different to the original direction. Emission lines occur when the detector is not in line with the photon source; in this case the detector sees the photons that are randomly emitted from the gas, see Figure 1.5 which was obtained from http://www.atnf.csiro.au/outreach/education/senior/astrophysics/spectra_astro_types.html on 03 May 2010.

As spectral lines are specific to a type of atom they are used to identify the chemical compositions of the medium the photons encounter and are re-emitted from (emission); the stars that emit the original photon (absorption); and the interstellar medium (absorption). As interstellar absorption lines are produced by atoms in the interstellar medium and seen in absorption against the spectrum of a background star, they are observed in stellar spectra but have no connection with the star. There are two major advantages of absorption-line studies over emission-line studies when studying the ISM. Firstly, the angular resolution of a telescope and the Earth's atmospheric seeing limit the spatial scales that are probed by emission-line studies; whereas those two problems do not affect absorption-line studies and the spatial scales probed are as narrow as the angular size of the background source. As stars subtend very small angles on the sky the scales probed by absorption-lines studies are three or more orders of magnitude finer than the scales probed by emission-line studies. This means that even if a star only moves a milliarcsecond per year across the sky a different portion of the ISM will be encountered when a star is re-observed the following year. Secondly, emitted photons are spread isotropically and so line emission is much weaker than the corresponding absorption of background light. Therefore, absorption-line studies are vastly more sensitive to small amounts of interstellar matter than emission-line studies are.

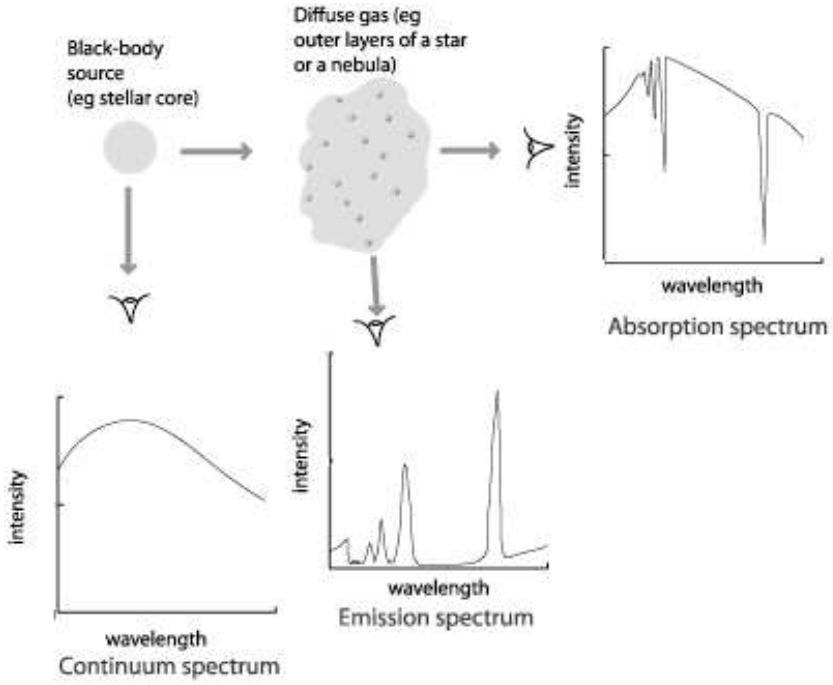

Figure 1.5: Adapted from a diagram by Kaler (1989) by Australia Telescope National Facility.

1.6.3 Overview of this work

The remainder of this work describes the contributions I have made to the study on the Interstellar Medium during my Ph.D studies. Chapter two describes in detail the code I had to write in order to be able to reduce the set of data from the New Technology Telescope in Chile and how I fitted the profiles to the data to take the measurements I wanted from the data. Chapter 3 presents the maps I created of the Local Bubble and discusses the findings. Chapter 4 presents the maps I created of the Small Magellanic Cloud and the Large Magellanic Cloud together with Galactic foreground maps that I could create using the same observation as the Galactic component of the DIBs and sodium lines were well separated from the Magellanic Clouds because of the Doppler shifts of the Clouds. Chapter 5 discuses the two projects together, what are the similarities and differences between the local ISM, the SMC and the LMC as well as considering the implications for the nature of the carriers of the Diffuse Interstellar Bands.

2 Data collection and processing

"I don't see the logic of rejecting data just because they seem incredible"
– Fred Hoyle

2.1 Observations

This chapter details the telescopes and instrumentation used to obtain the data for all the projects considered in this thesis. It describes the targets chosen, the methodology of data acquisition, the data reduction process, the problems encountered with data reduction where this occurred and the code written to overcome these problems.

2.1.1 Spectroscopy of the Local Bubble sample using the New Technology Telescope

The observations were taken in visitor mode, at the 3.5m New Technology Telescope (NTT) at the European Southern Observatory (ESO), La Silla, Chile (Latitude $29^\circ 15'$ south, Longitude $70^\circ 44'$ west, altitude 2400m), on the nights of 21st–23rd March 2011, 15th–17th August 2011 and 19th–21st August 2012. The author wrote the successful proposal for the observing time, was principal investigator of the project and was present at all observations. The author was accompanied in March 2011 and August 2012 by J.Th. van Loon and was the solo observer in August 2011.

2.1.1.1 Instrument setup

Charge-coupled device

The data are collected using a semiconductor chip called a charge-coupled device (CCD), which is a highly sensitive solid-state detector consisting of a two-dimensional array of light-sensitive elements. These light-sensitive elements generate images consisting of an array of picture elements (pixels) where each pixel corresponds to one

light-sensitive element. Each photon of light that falls on a pixel generates one electron-hole pair in the semiconductor, so the number of pairs generated depends upon the intensity of the radiation. As the electron is produced by a photon it is called a photo-electron. Once the exposure is completed the accumulated charge is converted into a digital signal. To do this the accumulated charge is read out as a tiny electric current that is amplified and converted into a number and expressed in analogue data units (ADU). This value does not represent the number of electrons detected in the pixel but it is proportional to it. An analogue-to-digital conversion (ADC) factor is applied to the ADU number to quantify the number of photons that were incident on the pixel during exposure. The ADC factor represents the number of photoelectrons per ADU. Table 2.1 lists the characteristics of the CCD used at the NTT.

Grisms, offset slits and filters

The Faint Object Spectrograph and Camera (EFOSC2) is used with Volume-phased Holographic (VPH) grisms. A grism is a combination of a prism and a grating arranged in such a way that light at a chosen wavelength can pass straight through so that light is dispersed but not deviated. Unlike classical gratings, which have a surface structure, VPH grisms disperse light by Bragg diffraction from the refractive index modulations within a thin layer of processed dichromated gelatin sandwiched between two glass substrates. Light is diffracted at angles corresponding to the classical grating equation but the diffraction must also obey the Bragg condition. Maximum efficiency is achieved when the incident angle and wavelength match the Bragg condition and is much higher than the efficiencies achieved with surface gratings. Any given VPH grism will diffract different wavelengths as it is tilted with respect to the incident beam. If a camera can be tilted with twice the tilt of the grism the spectrograph can be tuned to a range of wavelengths and resolutions with the same grism, thus making it a very efficient and versatile piece of equipment (Hill et al. 2003). For these observations EFOSC2 was used with grism #20 and the $0.3''$ blue offset slit. The offset slit has a fixed offset of 15mm and it is used to extend the wavelength covered by the VPH grisms. The

Table 2.1: Characteristics of the CCD used at the NTT

General characteristics		
Type	–	Loral/Lesser, Thinned, AR coated, UV flooded, MPP chip
CCD size	–	2060×2060
Image Size	–	2048×2048
Pixel Size	–	15 microns $\times$ 15 microns; 0.157arcsec $\times$ 0.157arcsec
Field Size	–	5.2arcmin $\times$ 5.2arcmin
Full well capacity	–	104,000 electrons/pixel
Dark Current	–	7 electrons/pixel/hour
Digital saturation	–	65535 ADU
In fast readout mode		
Bias	–	201–210 (ADU)
Readout Noise	–	12.6 (electrons)
Gain	–	1.31–1.38 (electron/ADU)
CCD readout time (1x1 binning)	–	24 s

wavelength shift resulting from using this offset slit is found using the equation:

$$\mathrm{d}\lambda = 45.5\mathrm{D} \times \mathrm{dY}$$

where $\mathrm{d}\lambda$ is the wavelength shift in Angström, D is the dispersion of the grism in Angström per pixel (0.55 for grism #20) and dY is the displacement of the slit in mm (15mm for the 0.3″ blue offset slit). Hence, the wavelength shift we achieved was 375.375 Å which altered the wavelength range to 5672–6772 Å. This combination of grism and slit gave a spectral resolution of $\Delta\lambda = 1.2$ Å with a resolving power (per 2.2-pixel resolution element) of $R \sim 5500$, where $R = \lambda/\Delta\lambda$. This combination of grism and offset slit covers the wavelength range of 5672–6772 Å, which includes the major λ5780, 5797, 5850, 6196, 6203, 6269, 6283 & 6614 Å DIBs. Following the recommendations in the EFOCS2 user manual, because a 0.3″ slit was used a fast readout with 1×1 binning was selected to ensure sufficient sampling in the dispersion direction and to reduce the overhead time per target. To maximise the signal-to-noise ratio (S/N) we achieved and the number of targets that could be observed during the night we aimed to expose the target until just below saturation level. This was optimal because our targets were bright and had short exposure time, thus, the overhead times including readout for each exposure was a major contribution to the total observation time spent per target.

The slit was originally positioned at column 1100 on the CCD to avoid known bad pixels on CCD#40. However, grism #20 introduces a lateral shift of the beam, therefore, the slit was later re-positioned at column 1680 to ensure the photons arrived approximately at column 1107 which corresponds to the area on CCD#40 that is free from bad pixels. The V-band magnitudes of the target stars ranged from 2.9 to 8.4 with exposure times ranging from 3.4 seconds to 847 seconds respectively. The V Bessel #641 and Hbe Cont #743 filters were chosen for the acquisition images with the latter being a narrowband pass filter to use with the brightest stars ($\leq$ 3rd magnitude) to avoid saturation in the shortest exposures. The V Bessel #641 filter has a central wavelength of 5470 Å with a Full Width Half Maximum (FWHM) of 1134 Å, The Hbe Cont #743 filter has a central wavelength of 4770 Å with a FWHM of 72 Å, The

observation blocks for each target were prepared with the Phase 2 Proposal Preparation Tool (P2PP); version 2.13 was used in 2011 and version 3 was used in 2012.

Exposure times

Exposure times were calculated using the EFOSC2 Exposure Time Calculator on the ESO website and amended to take account of the limitations in slit width and grism that were available to choose from. This was necessary because the VHP grisms and offset slits were new additions and the online calculator had not been updated to include them. In the Instrumental Setup part of this calculator the smallest slit width that could be chosen was 0.5″ and grism #20 was only available from 2012. For the 2011 exposure times the Grism information table on page 11 of the EFOSC2 manual (Monaco & Snodgrass 2008) was used as a guide to estimate the exposure times for our set up. As the seeing would likely alter during the night and the targets were bright it was expected that real time changes to the exposure time would be needed. The information in the table stated that for grism#18 the dispersion was 1.0 Å per pixel and the resolution at FWHM was 8.19 Å per arcsecond. For grism #20 the dispersion was 0.55 Å per pixel and the resolution at FWHM was 8.19 Å per 0.5 arcsecond. The online exposure calculator was used for grism #18 and a 0.5″ slit, the required S/N was set to be 2000. As the targets were bright, uncertainties due to the Poisson distribution were insignificant. Therefore, to make the exposure time amendments, the maximum intensity value returned by the online calculator was first divided by the square root of the resolution given for grism #18 (rounded up to the nearest integer), this value was then divided by approximately two thirds of the saturation level as given by the online calculator to give the number of exposures per target required to gain the S/N level required. To scale the exposure time that was given by the online calculator it was first multiplied by 0.55 to take account of the difference in the dispersion for grism #20 (as given in the manual) and then multiplied by five thirds to adjust for the slit used being 0.3″ instead of 0.5″. So for the 2011 observing runs the exposure time were estimated as above and repeated 3 times for each target.

For the 2012 observing run the online calculator has been upgraded to include

grism #20. Therefore, the only adjustment needed was to account for the 0.3″ slit being used. To estimate the exposure times for this run the maximum intensity returned by the online calculator using grism #20 and a 0.5″ was divided by the saturation level and rounded up to the nearest integer to give the number of exposures needed. The exposure times were adjusted by multiplying by five thirds as before. This lead to the estimate of needing 6 exposures of the target at the estimated exposure time.

As mentioned, the seeing conditions at the time lead to many live time amendments to these estimated exposure times. In poor seeing the photons were spread out more so further exposures or an increase in exposure time was needed. In exceptionally good seeing the image of the target star was very sharp and so often difficult to accurately place onto the slit to achieve optimum number of photons, in which case the observations sometimes needed the target to be reacquired on the slit and further exposures taken, whilst in such good conditions when the target was accurately placed the exposure times needed reducing to avoid saturation. The quality of the spectra were inspected as they were acquired; for targets where the maximum counts per pixel were $< 20,000$ a further three exposures were made to achieve the required S/N. This was needed in the 2011 observing runs more than the 2012 observing run which justified the increase in the number or repeat exposures calculated for 2012.

In March 2011 the skies were clear with seeing varying between 0.4″ and 2.0″. In August 2011 one and a half nights were lost due to bad weather conditions. For the remainder of the August 2011 run fast moving clouds were present and observations were made though cirrus and thicker cloud. Individual exposure times were altered to accommodate the fast changing conditions with seeing varying between 0.4″ and 2.4″. In August 2012 cirrus and thicker cloud were present during most of the observing sessions with seeing varying between 1.0″ and 1.8″. On the last night (August 21st) the wind was strong and northerly restricting the direction on which observations could be made with the dome closing due to strong wind at 05:20, loosing an hour and a half of observing time. In the afternoon before the start of each night a set each of bias frames, dome flat field ($4 \times 1,000$W quartz-halogen lamps) and arc frames for wavelength calibration (HeAr) were taken, this is described later.

2.1.1.2 Targets

The targets were chosen from the Na I D Local Bubble survey of Lallement et al. (2003) and are listed in Table B1 in Appendix B on the accompanying CD. The criteria used to choose the targets were that they should be bright stars with B magnitudes < 8.7, be of spectral type earlier than A5 (to provide a clean continuum), have well-known distances from the satellite survey *Hipparcos* satellite survey (to ensure targets probed the interior and walls of the LB) and accurately known, high proper motions. As this is intended to be an initial survey to determine which areas of the LB may be more interesting to observe further and to provide a first epoch against which later observations can be compared, the high proper motions of the stars will ensure that future observations will probe a slightly different sightline so any differences observed between the sets of observations will reveal the tiny scale structure of the ISM. The target list for the 2011 and 2012 observations contains 303 stars chosen to populate the volume of the Local Bubble sufficiently densely to allow derivation of the three-dimensional distribution. In all, 239 targets were observed during the three observing periods (see Chapter 3).

2.1.1.3 Data reduction of New Technology Telescope spectra

To reduce the data, removing any effects that are due to the nature of the instruments used during the data collection, the following general procedure is followed. A master bias frame and master flat frame (which has been subtracted with the master bias frame) for each night of the observation run are created. The science frames are prepared by subtracting the master bias frame from them and dividing them by the master flat frame. The wavelength calibration is obtained using Helium and Argon lamps and finally the spectra are extracted from the science frames.

The purpose of bias and flat fields

During the analogue-to-digital conversion process in which the charge on the CCD pixel is converted to a digital image, a bias signal (an electronic offset) is intentionally introduced during the signal amplification stage. This is to prevent the signal from being negative at any point on the CCD, which may occur due to random fluctuations or noise in the electronic signal. The value of the bias signal may depend on the position on the CCD or the temperature and it can vary over the read-out time. This bias signal must be corrected in the final image. To make this correction bias frames are obtained at the beginning of the observing run each night and they may also be obtained during the night. To produce bias frames an image is created by reading out the CCD after a zero second exposure with a closed shutter. This ensures there are no photoelectrons stored in the pixels and the resulting image is a result of the introduced bias signal. The average noise across the CCD can then be measured and accounted for. This is done by creating a master bias frame by stacking many individual bias frames and taking the median value of each pixel. The master bias frame is then subtracted from every other image obtained during the night to correct for the bias signal leaving the data values of the image directly related to the number of photons detected in each CCD pixel.

Flatfielding is the process that corrects for the variation in light sensitivity of the CCD pixels resulting from the manufacturing process. Flatfielding will also correct for any effects caused by dust on the filters and the CCD itself as well as correcting for vignetting (the dimming of objects near the edges of the field-of-view of the telescope). Flat fields are obtained by taking images of a uniformly illuminated light source such as the inside of an observatory dome. This produces a featureless image that reveals the variation in sensitivity of the CCD pixels and other effects. A master flat field is created by median stacking individual bias-subtracted flat frames. The master flat field can be used as a sensitivity map to correct the science images to the values they would have had if all the pixels had the same sensitivity to light. The bias-subtracted science frames are divided by the master flat field to make these corrections.

Reduction pipelines

The data can be reduced using existing pipelines that have been written to deal with the most common data reduction requirements that occur using specific instruments or the user can develop a bespoke pipeline to overcome any problematic data issues or for an unusual instrument configuration that is not covered by the standard pipelines provided.

The EFOSC2 Pipeline is a subsystem of the *Very Large Telescope Data Flow System* (DFS) and is used by the *La Silla Site Operations* (LSO) to assess data, generate master calibration data, reduce scientific exposures and for data quality control. The EFOSC2 pipeline recipes are also available to the user community. Using pipeline-generated master calibration products the user produces science products that are bias-corrected and flat-fielded images, from which spectra are optimally extracted and wavelength-calibrated. However, the ESO manual notes that the automatic reduction strategies may not be suitable for all scientific goals and lists some known data reduction problems together with possible solutions. To launch the pipeline recipes ESO provide two front-end applications: *Gasgano*, which provides a complete graphical interface for directly executing the pipeline recipes on a set of selected data and *Esorex*, which is a command line utility for running the pipeline recipes (ESO. 2011).

Initial attempts at reducing data using *Gasgano* were unsuccessful. Despite all entries being correct in the header *Gasgano* did not read the header information and labelled the files as unclassified. Hence, the efosc_bias recipe would not complete when it was executed and returned the error: Execution failed with code 1. This error code states that required files are missing. Initially further progress was made by using *Esorex* and a master bias was created. However, this method failed at the next stage because *Esorex* could not find the line catalogue or grism table for grism #20. As grism #20 is relatively new, being introduced in Period 82, it appeared as though the GRISM_TABLE (a calibration table supplied in the calibration directories and delivered with the pipeline recipes) had not been updated. The ESO User Support Group (usg-help@eso.org) was contacted for help but the issues could not be resolved. The problems were due to the non-standard configuration where grism #20 was used and

the fact pipelines have been written to accommodate the most common user requirements. While waiting for a response from ESO an alternative method of reducing the data using MIDAS (Munich Image Data Analysis System) was investigated.

MIDAS is command driven and provides a basic image processing environment for the reduction and analysis of astronomical data. It is possible to programme reduction sequences in procedures using the MIDAS Control Language (MCL), which provides the tools to construct such procedures from existing commands. The procedures are written as normal text files and constructed by stringing commands together where each command can use results from a previous command. The MCL provides the basic features of a programming language including definition of parameters, looping, conditional statements, procedure calls and built-in functions. The individual commands in MIDAS fall into three categories: intrinsic monitor commands, basic commands and application specific commands. The intrinsic monitor commands are simple commands for manipulating keywords and debugging and include image display. The basic commands are general commands for data manipulation such as arithmetic, statistics and rebinning; the display commands allow cursor interaction and of image data. The application commands are specific procedures including spectral reduction of long slit data (Grosbøl 1989). Given the simplicity and flexibility of MIDAS it was considered to be a suitable alternative to create a pipeline to reduce the NTT data once it became clear the issues encountered with *Gasgano* and *Esorex* could not be easily or quickly overcome.

Initial reduction issues

The data obtained with EFOSC2 are long slit spectra. To reduce long slit spectra with MIDAS the command 'SET/CONTEXT long' is needed to initialise keywords and to be able to use all the commands needed to manipulate the data. The full step by step procedure listing the MIDAS commands and programmes used to reduce the data is reproduced in Appendix F on the accompanying CD and described by the following text.

As rows and columns are added to the image during the readout process and because grism #20 introduces a lateral shift of the beam, reducing the effective field-of-view to 2.8′, the usable part of the image that contains data needs to be extracted from the image read out from the CCD. To determine what area of the image is usable the flat frames were inspected by displaying the images with MIDAS and using a cursor to check pixel values. The range of pixels that consistently showed values > 2000 on all flat frames was considered to be the usable area of the image. This was determined to be the range (17,6:1393,2032) where the first pair of numbers defines the "lower left" corner and the second pair of numbers defines the "upper right" corner of the required region. Outside of this range the pixel values fell to the order of a few hundred, indicating either that these were the additional rows and columns introduced during readout or that the pixels had not been fully illuminated. This range was used to extract a sub image of all the bias, flat, HeAr and science frames. The spectral images were orientated so that the dispersion direction was along the rows of the images so that the wavelength increased from left to right. In order to reduce the spectra with the calibration images all bias, flat and HeAr frames were orientated in the same way. This was achieved using the MIDAS command ROTATE/CLOCK, which rotates an image by $90\,^{\circ}$ without interpolating the pixel values. The extracted and rotated bias frames for each night were combined, taking the median average of the frames, to create a single master bias frame for each night.

In a similar way the extracted and rotated flat-field frames for each night were combined, taking the median average of the frames to create a single flat frame for each night. The combined flat frames were normalised using the MIDAS command NORMALIZE/FLAT. This command performs a bias correction on the flat frame by subtracting the specified bias frame and then normalises the flat frame by interpolating the flat-field continuum by a polynomial of a specified degree to produce a master flat frame. When checking that the flat-field fit was optimal an anomaly was noticed; the polynomial fit was not appropriate at all. Figure 2.1 shows the flat-field fit obtained for 21st March 2011 which showed the extremely poor polynomial fit.

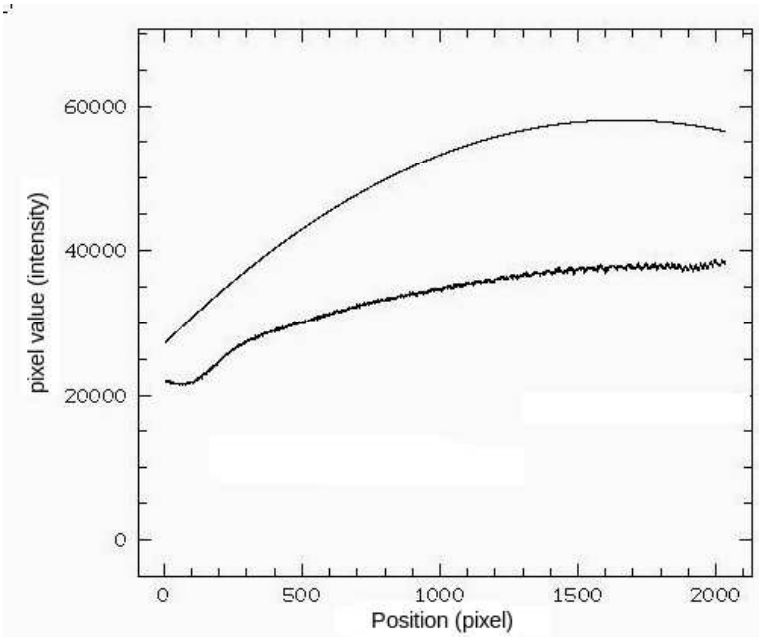

Figure 2.1: The polynomial fit (top trace) used to normalise the flat frame (bottom trace) is not appropriate. This is shown for one row of the frame.

Altering the degree of the polynomial used in the MIDAS command NORMALIZE/FLAT did not improve the fit. Closer inspection of the raw individual flat frames and bias frames, by randomly checking intensity values across the images with a cursor to sample specific areas of the frames and by loading the images into the MIDAS viewer to determine the maximum intensity values, showed the maximum intensity values varied widely over each night from values of ~ 200 to ~ 4000 and that occasionally there was a negative value. The negative values and large variation of values indicated that the bias levels throughout each night were unstable. I will come back to the flat field construction but first describe how I dealt with the bias issue.

The lateral shift introduced by using grism #20 means that part of the right hand side of each frame is unilluminated. The values in this part of the flat and science frames should, in theory, reflect the true bias levels. However, it was decided against using the unilluminated part of the flat to create a dark frame to use as a bias as is likely to be some light seepage and being a non zero integration time it is not really that useful as a bias. Also it was considered that if the bias frames are time varying then it may not be worth trying to create a bias out of the unilluminated part of those frames as the problem would persist. Another issue to consider was the fact that the bias frames show two different bias levels as a result of using the fast readout mode which makes use of two amplifiers, one for the left and one for the right.

Investigation of reduction problems

To fully investigate the nature of the bias instability, statistical analysis was performed on all the raw bias frames. The report created using the MIDAS command STATISTICS/IMAGE created a very large and unreadable table. However, IRAF (Image Reduction and Analysis Facility), which is a general purpose software system for the reduction and analysis of astronomical data, produced easier to access information. With the IRAF command IMSTAT a rectangular region can be specified to obtain statistical information, which can then be exported as a table. Although the unilluminated parts of the flat and science frames did not reflect the true bias levels, as mentioned above, this area was the closest approximation available. Two areas for the

statistical analysis were chosen, an area covering the region of the unilluminated part of the CCD and a narrow strip at the very far right hand side of the unilluminated part of the CCD. The very far right hand side being chosen as it was considered this region would be least likely to be affected by any light seepage. Statistics on these two areas for the bias, flat and science frames were calculated as well as statistics for the left hand side of the bias frame so that the difference between the two levels of the bias could also be investigated. From these figures bar charts were created to give a visual overview of the median values for each frame, see Figure 2.2.

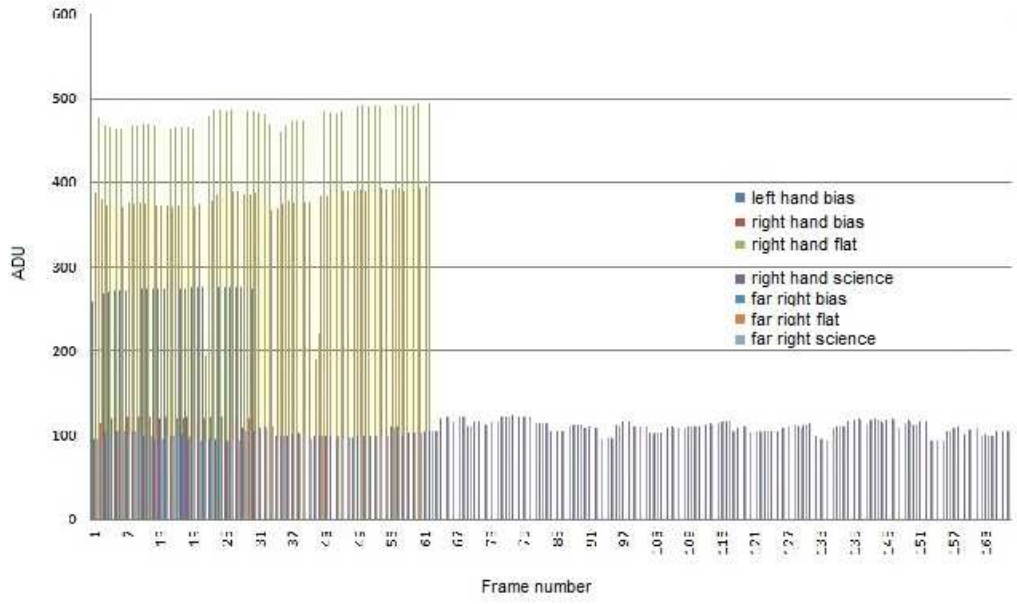

Figure 2.2: Bar chart showing the median values of the bias, flat and science frames from the 22nd March 2011.

Figure 2.2 shows the median intensity values of all the frames taken on the night of 22nd March 2011. At the start of the observing nights in all three observing runs, 30 bias frames were exposed and as many flat frames as could be exposed in the

time available before the onset of astronomical twilight were taken. The left hand side of the 30 bias frames are represented by the blue columns that have an approximate intensity of 280 ADU but it was noticeable that the first three frames were of a slightly lower intensity than this and gradually increased to that level. The same pattern of the first three frames gradually increasing to a steady level was also noticeable in the right hand side of the bias frames (red columns) and far right hand columns (turquoise columns). This was the first indication that a problem with the bias frames could be responsible for the reduction problems because the first three normalised flat frames showed a different response to the polynomial fitting than the subsequent flat frames. The right hand side of the flat frames (green columns) and far right hand side of the flat frames (orange columns) mainly have intensity values of $\sim 570 - 595$ and $\sim 470 - 495$ respectively. In comparison to the bias frames these intensities are large and as these regions are taken from the unilluminated part of the flat frame it seemed clear this region recorded some light seepage. The fact that the intensity reduced at the far right hand side of the flat frames supported this idea of light seeping through from the illuminated part of the CCD. The flat frames were exposed in batches of 20. At the end of each batch of exposures the lamps would automatically be turned off and then back on again for the next batch of exposures. This practice is reflected in the two areas which show the intensity levels only reached a value of ~ 200. This confirmed the flat frames were not suitable for use to create a bias frame substitute. The right hand side of the science frames (purple columns) and far right hand side of the science frames (light blue columns) mainly have intensity values similar to one another and ranged in value from ~ 90 to ~ 125. The larger intensity values of the science frames were similar to the values of the far right bias frames. Moreover it was clearly seen that the intensity values of the science frames varied throughout the night supporting the idea that the bias signal was indeed unstable throughout the night. As the far right parts of the science frames should not have been affected by light seepage; the values recorded should reflect the actual bias signal.

Comparing the statistics of the bias frames in the three days of the first observing run in March 2011 showed that the variation in intensity not only changed during the

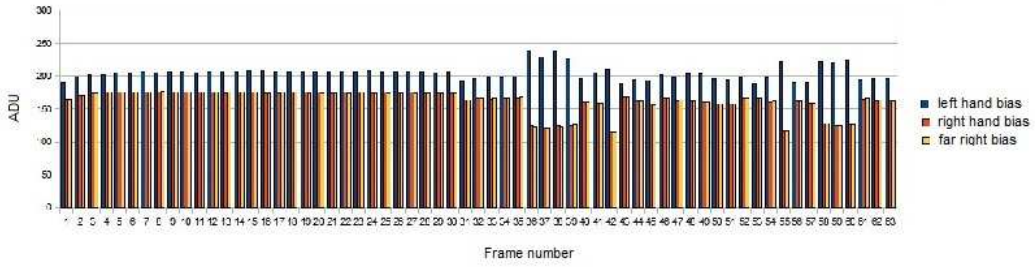

Figure 2.3: Bar chart showing the median values of the bias frames from the 20th August 2012.

night but that there was a big difference in behaviour between the individual nights. Most noticeably each night showed a different ratio between the left and right hand sides of the individual bias frames from another night. This is probably due to a slightly different bias signal level being produced in the left and right hand sides of the amplifiers on each night.

As a result of the investigations of the 2011 data it was decided to take a bias after each science observation in subsequent observing runs so that the behaviour of the bias throughout the night could be monitored more accurately. Figure 2.3 shows the bar chart created from the statistical analysis of the bias frames from 20th August 2012.

From Figure 2.3 it can be seen that the first 30 frames, which were taken at the beginning of the night were fairly stable. The increase in intensity for the first few frames as noted in the March 2011 data was not as great this time but it was still evident. However, the bias frames taken after each set of science frames for an individual target had been exposed do show a marked variation in intensity. This further supports the assumption that the bias signal was unstable and that this was not an uncommon occurrence.

Bias frames

In order to create a bias frame which could be used successfully in the data reduction it was decided to scale the bias frames to a common intensity level and create a master bias frame out of the individually scaled bias frames. This was done as follows and the procedure repeated for each night. The intensity level required was determined as follows: the median values for the left and right hand side of each bias frame were recorded; the mean values of all left hand frames and all right hand frames were calculated; the difference between each frame half and the mean value relating to that same half was calculated for use as an addition factor, see table Table B.4 in Appendix B on the accompanying CD for an example of the calculations for 20th August 2012.

These addition factors were used to scale the individual bias frames to the median intensity level for each night. By scaling the bias frames in this way any pixel to pixel variation in the frames was preserved. Where there were frames that had a markedly different behaviour to the majority of frames (i.e. extremely low intensity values in comparison to the majority of frames) these were omitted from calculating the mean value to which each of the frames would be scaled. A copy of the bias frames was made and a MIDAS programme, bias_ext.prg (see attached CD for code), to extract the left and right hand sides of each original frame was run. Each extracted half was scaled by adding the addition factor previously calculated for that frame. Two MIDAS programmes, bias_insL.prg and bias_insR.prg (see attached CD for code), were used to insert the scaled frames into the copy of the original bias frames which overwrote the original data with the new scaled values. These new frames were median averaged to produce one combined bias frame for each night. A subimage was extracted and rotated as described earlier so that they matched the size and orientation of the rest of the data. The descriptor values of the images were checked and the start and step values set to 1,1 in all cases so that the bias, flat, and science frames could be used together during the reduction process.

To make a master bias frame suitable for use with the flat frames for each day the lowest intensity levels on the far right hand side of the bias frames where looked at. Any anomalously low values were ignored and the lowest value of the remainder of

the frames was used as the value to scale the combined bias frame to. This was done by subtracting the difference between the median value of the combined bias and the lowest value determined from the bias frames for each night from the combined frame. As before this preserved any pixel to pixel variation in the bias frames.

As noted above, the statistics for the flat frames indicated that light seepage to the unilluminated part of the flat frames had occurred with values much higher than the values determined for the bias frames. This was why the values for the flat frames were not considered a reliable indication of the true bias level and not used to determine a suitable value to scale the combined bias frame to. For the March 2011 observations bias frames were only taken at the start of each night's observing. In the subsequent August 2011 and August 2012 observations bias frames were taken after every science frame. The statistics on these bias frames also showed the erratic behaviour of the bias levels throughout the night and confirmed that the above approach for creating two separate bias frames for use with the flat and science frames was sensible.

The bias instability issue was noticed on all three observing runs, March 2011, August 2011 and August 2012 although it did not show the same pattern each time. This indicates the problem is erratic and probably long standing. This was brought to the attention of the observatory staff at La Silla and also the technical staff at ESO in Munich; its cause was not identified. Possible contributing factors to this issue are:

1. Temperature variations throughout the night.

2. The movement of telescope causing disruption to the electronics. As the camera is located at the Nasmyth focus of the NTT and the observation programme is an all sky survey there was occasionally large movements from one target to another especially during runs when fast moving cloud needed to be avoided.

3. The use of fast read out mode which uses two amplifiers.

Temperature fluctuations being something that is beyond an observer's control means there is little that can be done on the first two points above to minimise any possible

affect on the bias. However, on any future observing run of a similar nature a normal read mode, which only uses one amplifier can be tried to see if the situation is improved.

Flat frames

The flat field polynomial fit was still not satisfactory. To correct this instead of running the MIDAS command to normalise the flats a new MIDAS programme was written, flat3.prg, (see Appendix D on the accompanying CD). Before running this programme the master bias prepared for use with the flat frames was subtracted from each flat and a first approximation for normalisation was made by dividing each flat by its median value. The programme, flat3.prg, fine tuned this normalisation. For each flat, flat3.prg median-averaged the rows to produce a one-dimensional image, which was expanded to become a two-dimensional image. The two-dimensional image was then smoothed using the parameter $2x+1$ as the bin size over which the median-averaged-rows profile is median-averaged. Each flat is then divided through by its smoothed profile to produce a normalised flat. All the flats for each night where then combined taking the median average of all the frames to produce a master flat for each night.

Wavelength calibration

The wavelength calibration was achieved using the Graphical User interface (GUI) XLong as described in Izzo (1998). An image of a HeAr frame was loaded, pixel numbers that relate to emission lines were noted and used to help estimate and identify the wavelengths of the emission lines. The line catalogue hear.tbl was chosen with the wavelength range covering the DIBs of interest being restricted to 5700 - 6800 Å. Taking each HeAr frame in turn a plot of the frame was displayed and the cursor used to interactively select an emission line on the plot and match it to a wavelength from the hear.tbl as shown in the GUI displays, the image of the HeAr frame previously loaded being used to help identify the pattern of emission lines on the plot. Once the lines had been identified wavelength calibration was performed by using the 'calibrate all' button on the GUI, which estimated the dispersion relation for the complete spectrum. The results were checked by plotting the dispersion relation (see Figure 2.4) and written as

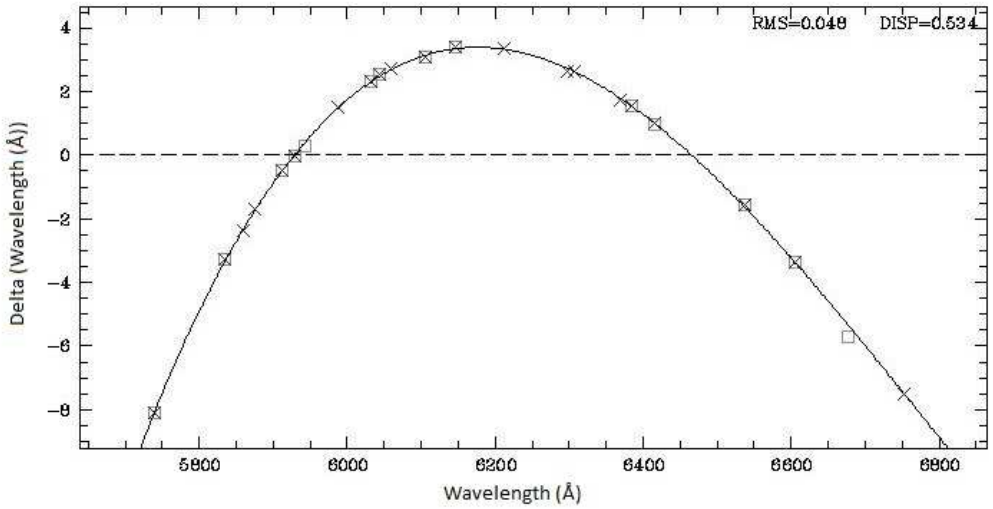

Figure 2.4: Dispersion relation for 19th August 2012.

tables for use when rebinning the spectra to wavelength. The results from the frame with the best fit of dispersion plot for each day were the results used to rebin the spectra for that day.

EFOSC2 was originally designed to be mounted in Cassegrain focus where the aperture wheel moved in a horizontal plane inclining only with the telescope. Now that EFOSC2 is located at the Nasmyth focus at NTT, flexure problems are experienced. This is due to the fact that the instrument is now turned on the side and gravity can influence the position of the slits depending on the rotator position of the instrument. The effect of the flexure is a variation of the central Y-position of the slits, which results in shifts of the wavelength scale that can be as big as several Angström as stated in the EFOSC2 manual (Monaco & Snodgrass 2008). This shift was noticed in the NTT data, moreover the shift varied from observation run to observation run. As the data from all three runs were being combined this was corrected in the IDL code during the profile fitting stage. This was achieved by recalibrating using the

telluric absorption line that was present. A wavelength range around the telluric line was specified (6272 – 6280 Å). The minimum value between this wavelength range was found for each spectrum. From Figure 2.5 it can be seen that the two telluric lines at 6278.07 and 6278.13 Å are blended but that the line at 6278.13 Å is stronger and so will dominate the blend. Therefore, 6278 Å was taken as the expected wavelength for the telluric line in the NTT data. A correction figure for each spectrum was determined by subtracting the wavelength at the position of the minimum value found, as above, from the expected wavelength for the telluric line. The wavelength axis was redefined by adding this correction figure to the original calibrated wavelength. Thus all spectra showed the telluric absorption at 6278 Å with all other absorption lines being close to their expected rest wavelength position.

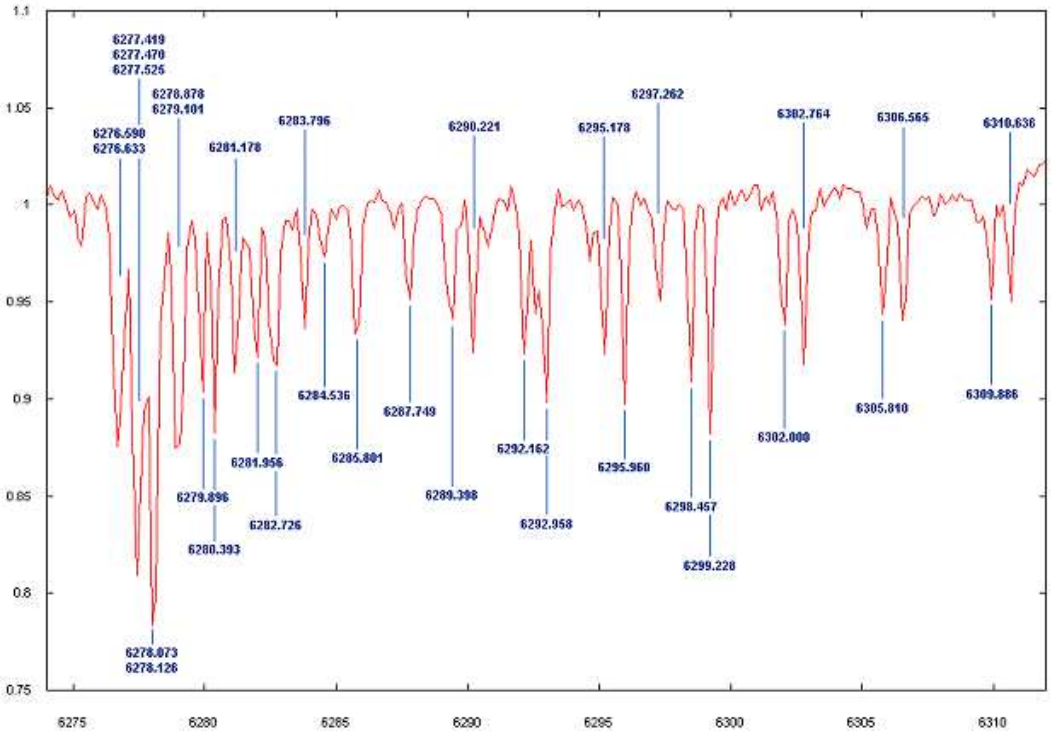

Figure 2.5: Identification of telluric lines in the 6290 Å region. The x-axis shows the wavelength in angstroems and the y-axis shows the normalised intensity. (Credit www.astrosurf.com /buil/us/spectro11/specalib.htm on 25 April 2013).

Extracting the spectra

A MIDAS programme, science_prep[date].pro (See Appendix D on the accompanying CD) was written to extract the usable area of the science frames, rotate them to match the orientation of the bias and flat frames, subtract the master bias frame specific to each day from the science frames, divide the science frames by the master flat frame specific to each day and rebin the spectra to wavelength using the tables created each day by the calibration process. Thus preparing the science frames so that the spectra could be extracted.

There are two common methods of extracting a spectrum. Linear (row averaging) and optimal extraction (Horne 1986). With linear extraction all the pixels are integrated with equal weighting and a corresponding signal in the background channel is subtracted. With this method there is no allowance for the fact that the pixels at the edges of the profile contain a smaller part of the signal than those in the middle of the profile. Therefore, these pixels will have a smaller signal-to-noise ratio and should carry reduced weighting for the best possible extraction. This method is useful for a 'quick look' at data. Optimal extraction is designed to give the best possible signal-to-noise ratio with CCD spectral data. The optimal extraction method weights the contributions to the signal by using the Poisson statistics of photons, information about the CCD signal processing electronics transfer function, and the modelled profile for the object. Therefore, to use this method the readout noise (RON) and gain for the CCD camera used to obtain the data is needed.

Spectrum extraction can be done using a MIDAS GUI. However, this method produced a spectrum that contained a lot of noise. Experimenting with a manual spectrum extraction using the MIDAS command EXTRACT/LONG indicated that the process was rejecting a lot of good signal as if it were cosmic rays. Since a very high signal-to-noise ratio was required it was decided to optimally extract the spectra manually so that each spectrum could be investigated individually, determining values for sky subtraction and range of the spectra specific to each. To do this each spectrum was viewed, checked for saturation and rejected if this was the case, a constant value to use for sky subtraction was determined by sampling the sky values with an interactive

cursor and the lower and upper boundaries of the object spectrum also determined with the cursor. The default values for order for the polynomial fitted to the spatial profile (3) and the number of iterations (3) were used. The previous experimenting, which included investigation of the header information, showed that the default values for the RON (read-out-noise [ADU]), gain (inverse gain factor [e^-/ADU]) and sigma (the number of noise levels, outside of which data are rejected), respectively 7, 2, 3, were not appropriate for these data and the values of 0, 0.1, 100 were determined as more appropriate. The values for RON and gain were determined from inspection of the header and the sigma value were determined by experiment. The sigma value was set this high to ensure all the useful signal of the spectra was included. The cosmic ray event rate for CCD#40 measured with EFOSC2 mounted at the telescope, is about 940 ± 30 events hour^{-1} for the whole array. As the exposures for the majority of the targets were short the number of cosmic ray hits was considered to be negligible and therefore raising the value of sigma to 100 was appropriate in this case. Once the spectra had been extracted, spectra relating to the same target were combined to produce a final spectrum for each target observed.

This method of image reduction, wavelength calibration and spectrum extraction produced spectra which in the majority of cases showed the sodium doublet, in many cases the 5780 Å DIB was evident while in a significant number of spectra there was also absorption features evident at the positions of the remaining DIBs of interest. In a few cases spectra showed evidence of all the DIBs of interest, whereas the majority of spectra showed evidence of just a few of the DIBs of interest. An IDL code was written to fit profiles to the absorption feature and this is described in Section 2.2.1.

2.1.2 Spectroscopy of the Magellanic Clouds sample using the Anglo-Australian Telescope

The observations were taken in visitor mode, at the 3.9m Anglo-Australian Telescope (AAT) at the Australian Astronomical Observatory situated at Siding Spring Observatory near Coonabarabran, NSW, Australia (Latitude $31^\circ 16'$ south, Longitude $149^\circ 4'$

east, altitude $\sim$ 1100m), on the nights of 3rd–6th November 2011: a previous observing run on the 27th–30th November 2010, where the author and author's supervisor J.Th. van Loon were present, had been completely lost to fog and rain. The proposal was written by the author's supervisor J.Th. van Loon who was also the principal investigator of the project although all data reduction and analyses have been completed by the author. For the successful observing run in 2011 the author was accompanied by J.Th. van Loon and a second year PhD student, B Tatton, on his first observing run. For these observations the AAOmega spectrograph was used with the 2dF multi-object system.

The Anglo-Australian Observatory's 2dF (Two-degree Field) facility was designed mainly to carry out galaxy redshift surveys. A key feature of 2dF is the ability to observe 392 stars at once and after an hour observe another set of 392 stars (Lewis et al. 2002). This facility provides multiple object spectroscopy over a 2° field of view at the prime focus of the Anglo-Australian Telescope (AAT) with order of magnitude improvements on previous systems regarding the field area and the number of objects it is possible to observe simultaneously. It consists of a wide-field corrector, an atmospheric dispersion compensator and a robot gantry. The gantry positions optical fibres to an accuracy of $0.3''$ on the sky, this process takes about an hour to complete. There are two field plates and a tumbling mechanism which allows the next field to be configured while the current field is being observed.

AAOmega has a bench-mounted, double-beamed design. It is not attached to the telescope but is located in the Coudé west laboratory, which provides a thermally and vibrationally stable environment. It comprises: an f/3.15 Schmidt collimator, dichroic beam-splitter, interchangeable VPH gratings and articulating red and blue f/1.3 Schmidt cameras each with a focal length of 247mm. The 38m length multi-object spectroscopy (MOS) fibres are permanently attached to 2dF and deliver the fibre units from the prime focus to the AAOmega spectrograph. The collimator houses a mirror, the dichroic beam-splitter and two Schmidt corrector plates. The beam-splitter is angled at 35° to the incident beam. The cross over wavelength for the beam-splitter is at 5700 Å which gives a wavelength coverage from $\sim$ 3700 Å to $\sim$ 8800 Å. The

VPH gratings are an assembly of two 10mm glass plates that sandwich a thin layer of dichromated gelatin containing the actual grating. The VPH gratings are cheaper, have less scattered light and are more efficient than traditional reflection gratings. They can be designed to a desired specification and be made in large formats. They are also versatile as the wavelength coverage for a particular grating angle is determined by the camera angle, hence the need for articulating cameras. The peak efficiency wavelength can be altered by adjusting the grating angle, which has a secondary effect on the wavelength coverage resolution. For any given set up, the resolution is more strongly dependant upon the wavelength than is the case for reflection gratings. The red and blue Schmidt cameras only differ in the coatings used on the correctors, mirrors and the curvature of the field flatteners and wavelength responses of the detectors. The detectors are E2V CCD44-82 detectors and are orientated so that there are 4,000 pixels in the spatial direction and 2,000 pixels in the spectral direction. The cameras are enclosed in stainless steel shelled vacuum vessels, they are cooled with liquid nitrogen and can maintain a detector temperature of 160 K for sixteen hours (Sharp et al. 2006; Smith et al. 2004).

2.1.2.1 Instrument setup

The gratings 3200B and 2000R were used with 570nm dichroic beam-splitter, with the central wavelengths set as 3935 Å for the blue arm and 5840 Å for the red arm. These were the central wavelengths of the critical wavelength ranges we required for our observations, which were 3933–3397 Å for the blue arm and 5775–5790, 5792–5805 and 5889–5897 Å for the red arm. For our chosen gratings and central wavelengths the online grating calculator was used to determine the grating and camera angles and the wavelength coverage, dispersion and resolution of the central and end fibres as the slit curvature causes a variation between the central and outer fibres. For the 3200B grating the values calculated were: grating angle = 39.79 °; camera angle = 78.05 °; wavelength coverage = 3779–4084 Å; dispersion = 0.156–0.141 Å /pix; resolution = 0.519–0.471 Å /pix for the central fibre and wavelength coverage = 3751–4054 Å;

dispersion = 0.156–0.141 Å /pix; resolution = 0.519–0.471 Å /pix for the end fibres. For the 2000R grating the values calculated were: grating angle = 40.54 °; camera angle = 71.74 °; wavelength coverage = 5569–6101 Å; dispersion = 0.269–0.249 Å /pix; resolution = 0.813–0.754 Å /pix for the central fibre and wavelength coverage = 5528–6056 Å dispersion = 0.267–0.248 Å /pix; resolution = 0.807–0.748 Å /pix for the end fibres. To observe the DIBs, which have a depth below the continuum of about a percent, we required a $S/N \approx 400$ per Å. We chose the highest resolution gratings available for the wavelengths we were interested in so that each DIB is resolved into a few resolution elements. A high resolution was also needed to obtain accurate measurements of the Ca II K and Na D. The online exposure calculator together with the previous experience of J.Th. van Loon who had experience of observing with AAOmega using near-identical settings, similar targets and the same science objectives (van Loon et al. 2009) indicated that to reach the required S/N on a 15 mag star with bright conditions and where the seeing was 1.5″, an exposure time of 12 hours was needed split into 24 half hour exposures.

The weather conditions deteriorated throughout the observing run. For the 3rd November conditions were clear with seeing varying between 1.3″ and 1.5″. The 4th November was initially clear but clouds appeared about 23:00 with seeing deteriorating from 1.8″ to 3.0″. The 5th November was very cloudy with seeing going from 2.0″ to 4.0″ for the second half of the night The 6th November had a mixture of clouds and rain with seeing of 2.0″ before the dome closed due to rain, reopening a few hours later with seeing of 1.7″. At the start and end of each night a set of biases, darks, sky flats, arcs and dome flats (20W lamps for the red and 75W lamps for the blue) were taken. The SMC field was observed in the first half of the night with the aim of making 7×30 minute exposures for each of the SMC and LMC during the night. This was achieved for the first 3 nights but the loss of time on the last night meant we obtained 4 exposures for the SMC and 5 exposures for the LMC on that last night.

2.1.2.2 Targets

The targets were selected from the Magellanic Clouds Photometric Survey (Zaritsky et al. 2002) using optical colour and magnitude cuts, rejecting stars with close or bright neighbours, optimising their spatial distribution to maximise the number of stars that can be allocated to fibres. An order of 10^3 potential targets for each 2° field was selected and an input file created (see Figure 2.6 and compare with the maps of the targets actually observed in Figure 4.2 in Chapter 4). The input file was created using a FORTRAN code that had been written by J.Th. van Loon for use in previous observing runs using 2dF for a similar observation and amended to accommodate the needs of the current project. The FORTRAN code detailed the central position of the target field, the date of intended observation, the targets with name, position, magnitude, target type and a priority flag allocated to them, the locations of some reference stars and some sky positions. This code was run a number of times choosing various central positions and plotting the results to ascertain which variation of the code produced the most useful target field with enough potential targets to allow *configure* to optimise the spatial distribution of the targets.

2dF configure

The *configure* software uses the input file containing the list of target objects and generates a configuration in which as many fibres as possible are allocated to targets, taking into consideration instrumental constraints and any specified target priorities. A file containing a list of fibre allocations is produced which needs to be supplied to the instrument software so that it can configure the instrument to this predetermined configuration. The minimum spacing (in arc seconds on the sky) of the 2dF fibres is 30 arcseconds corresponding to a 2mm separation on the plate. However, the typical separation is 30–40 arcseconds and depends upon location in the field and the target distribution.

Once *configure* has been started up the target file is read in using the 'open file' button on the GUI, an allocation statistics panel shows the distribution of the

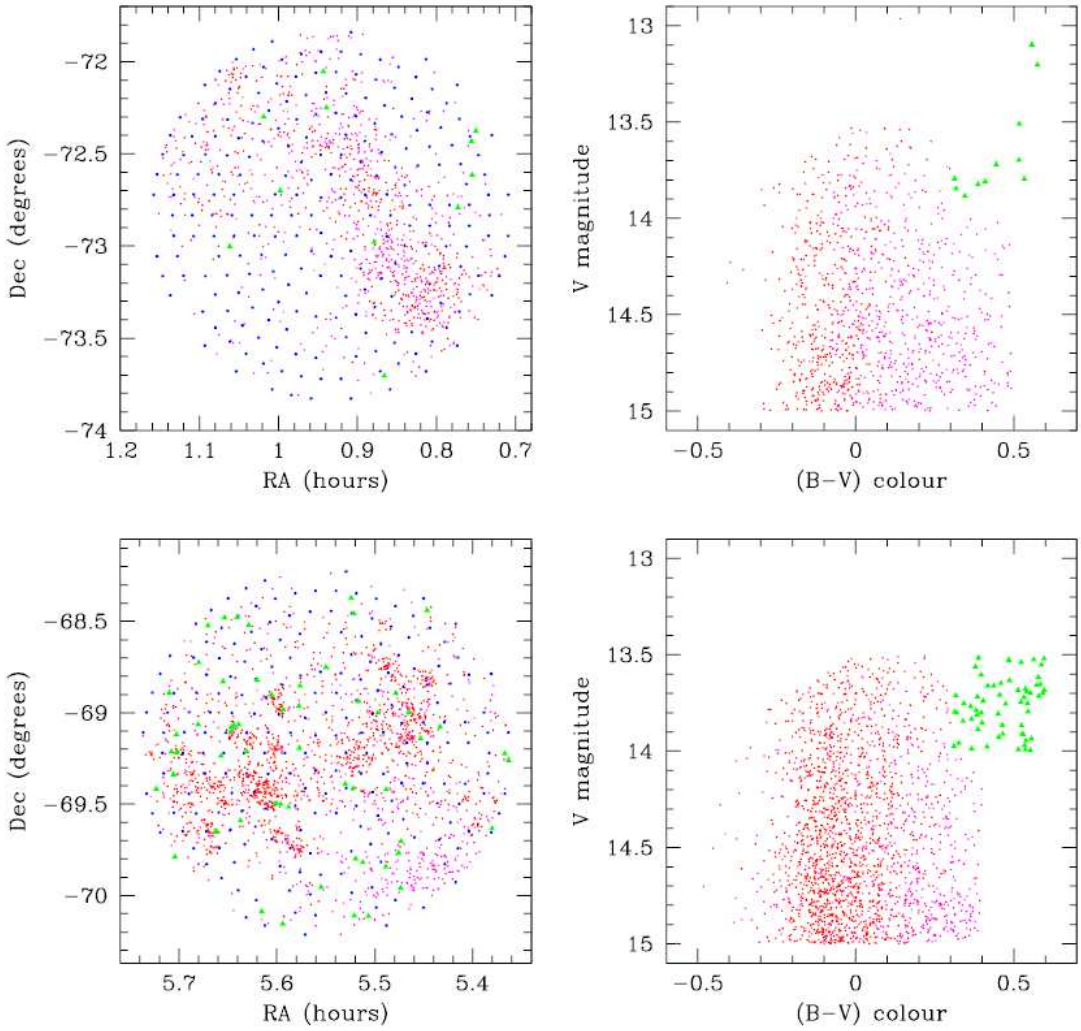

Figure 2.6: Potential targets chosen for (Top:) the SMC and (Bottom:) the LMC. The left hand panels show the location of the potential targets in the 2 ° field of view. The right hand panels show the V magnitude versus (B-V) colour. The symbols denote: high-priority (red), low priority (magenta), fiducial stars (green triangles) and empty sky positions (blue).

allocated fibres by priority and the targets are displayed in a mimic window. The 'Allocate' button in the basic sequence window opens a dialogue box in which the details of the allocation algorithm can be controlled. The default options are for a standard annealing process where the fibres are never straightened and 25 fibres to be assigned to sky. Other options are for quick or thorough annealing, moderate or heavy fibre straightening and the number of sky allocations can be manually input. Once the options have been selected clicking OK starts the allocation process which draws the fibres in their new positions on the mimic window (see Figure 2.7). This allocation is then saved as an SDS file to be supplied to the instrument software so that it can configure the instrument ready for observing.

Using the 2dF configure software it was ascertained that $\approx$ 350 stars per field could be allocated with the remaining, unbroken fibres used to sample the sky. However, the fibres do often break (and get repaired) so although this preparation should be done in advance of arriving at the observatory because of the time involved to ensure an optimised target field has been selected, configure should be run again in the afternoon of the observations to ensure all working fibres are allocated.

2.1.2.3 Data reduction of Anglo-Australian Telescope data

As 2dF is capable of generating enormous amounts of data during a single night (up to 3000 spectra) a new data reduction package was developed called 2dfdr. This programme uses as much of the known instrumental parameters as possible; it can be run automatically via a GUI and it is able to reduce an entire night's data in about an hour (Lewis et al. 2002). The system does the bias and dark subtraction, flat fielding tramline mapping to the fibre locations on the CCD, fibre extraction, arc identification, wavelength calibration, fibre throughput calibration and sky subtraction. To reduce the data using 2dfdr at least one fibre flat field exposure, at least one arc exposure and one or more exposures on the target field are needed. As we had two target fields and a red and blue set of data for each target field four sets of data were created each night. Although some spectra were not as good quality as other data it was decided

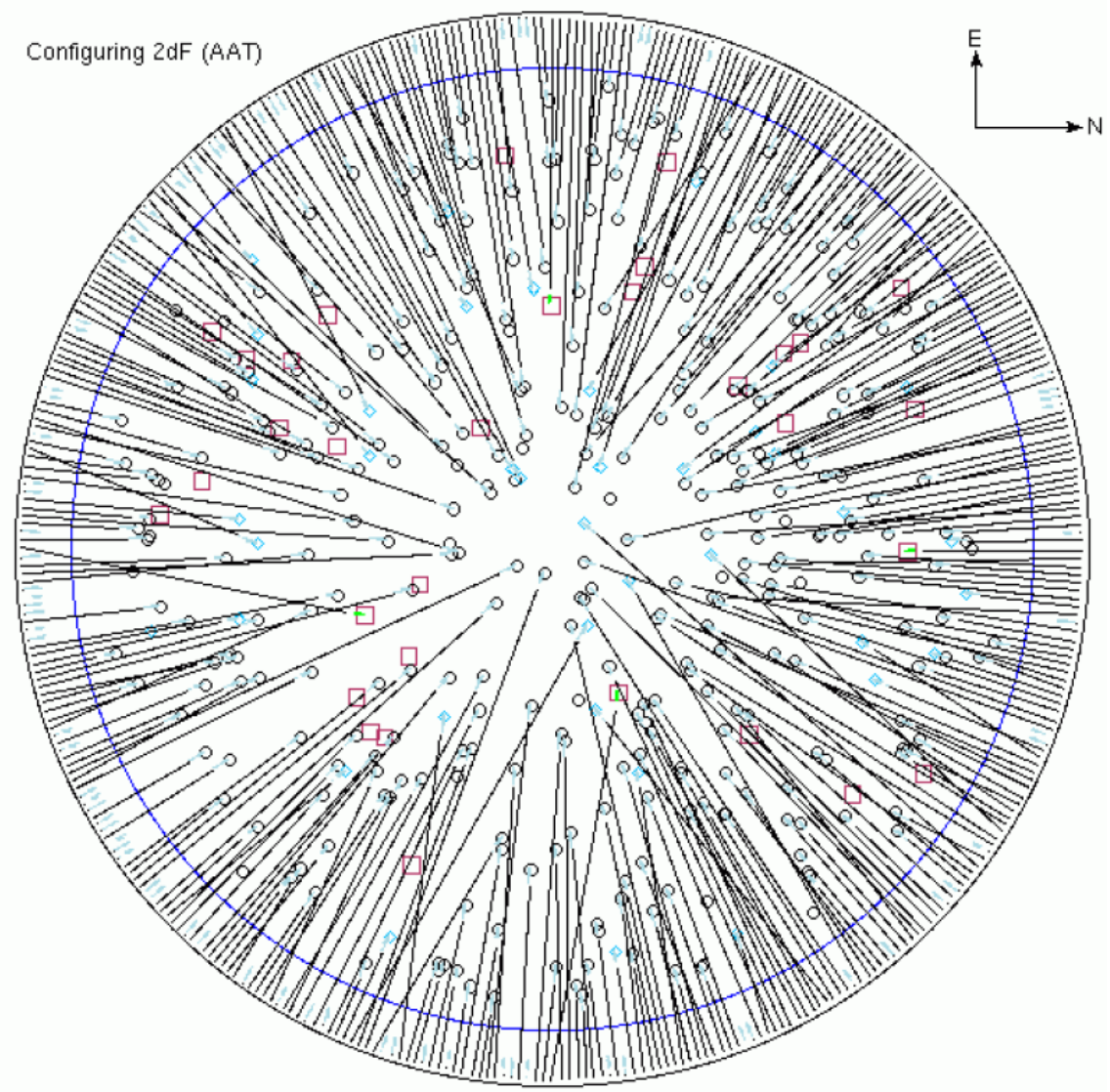

Figure 2.7: The configure mimic window once the allocation process has been completed and the fibre positions drawn (taken from the AAO 2dF/6dF/AAOmega CONFIGURE User Manual). The black circles represent all possible star targets; The magenta squares represent the possible fiducial (guide) targets; the cyan diamonds represent the possible sky targets; the black lines to symbols show which targets the fibres have been allocated to and the blue dashes around the edge show the unallocated fibres.

to combine the four sets of data for all four days to produce a single combined frame for the LMC red data, a single combined frame for the LMC blue data and to do the same for the SMC data resulting in four combined data frames for the whole observing run. It was possible to combine all the data without the not so good data adversely affecting the quality of the good data as weighting was applied to give less importance to the low quality data. By combining the data in this manner the overall S/N was improved giving the best opportunity for detecting which absorption features actually related to the DIBs.

The standard way of reducing data with 2dfdr is as follows. When 2dfdr is started a dialogue box is displayed with tabbed pages: Data, General, Extract, Calibration, Sky, Combine and Plots. The setup button shows a dialogue which lists the directory and root names of the data files to check all the required files are present. The system locates and checks the class of all the raw data files. The parameters are checked in the remaining tabbed pages and either defaults selected or altered as required. The start button then commences the reduction process to reduce all the files in sequence, ensuring that calibration files are reduced before the runs they calibrate and producing a combined frame of the reduced data. Once a set of data has been reduced the Tram Map can be plotted from the command menu. The 2dF spectrographs have a large curvature and 2dfdr uses a complex algorithm to determine the curvature for the 2dF tramline map incorporating the full optical model for 2dF and ray traces from the slit to CCD to make predictions on the positions on the CCD. The 'Plot Tram Map' item over plots the tramline map onto the data from which it was generated to check it is a good match to the data. The tramline lines should run down the centre of the data for each fibre (see Figure 2.8).

To check the arc reduction is satisfactory the reduced arc file can be plotted from the Data tabbed page and the plot should show lines running straight up the image because all the fibres have been scrunched on to the same wavelength scale (see Figure 2.9).

Initial attempts at using 2dfdr with the default parameters did not work, the reduced skyflats did not combine. Advice from the AAT technical support suggested

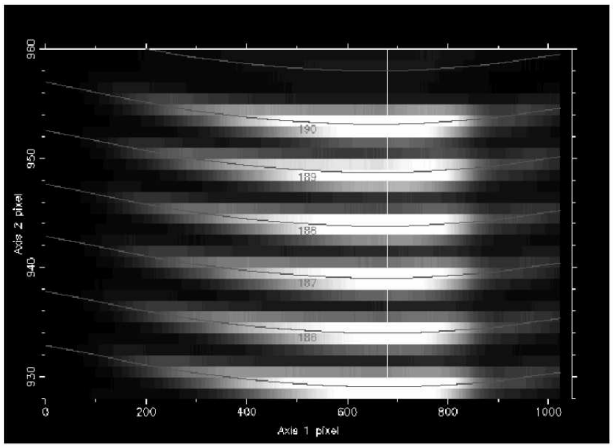

Figure 2.8: Typical result from the Plot Tram Map option after zooming in. The tramlines run through the centre of the data on which they are overlaid. Figure taken from the Anglo-Australian Observatory 2dfdr Data Reduction System Users Manual, 2005 version.

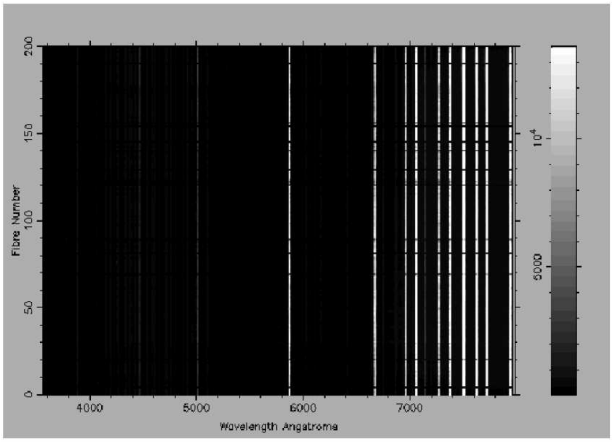

Figure 2.9: Correct appearance of a reduced arc exposure. Figure taken from the Anglo-Australian Observatory 2dfdr Data Reduction System Users Manual, 2005 version.

reducing the Bias frames and the Flat frames separately so that 2dfdr only worked on one frame of each. However, no throughput map was generated by following this procedure. Changing the throughput method to SKYFLUX(MED) caused the reduction procedure to crash when trying to reduce an object frame giving the message 'no skylines found'. Changing the flux weight to OBJECT instead of FRAMES produced an unreadable file where the flux weights had the value NaN. Various changes to the parameters were tried and a successful method was found.

To successfully reduce the data the following procedure was followed for each of the four sets of data on all four days. The bias frames were combined separately using 2dfdr with OBJECT chosen for the flux weight. The resulting *BIAScombined* frame was copied to a directory with all the other raw data for each set, that is: skyflats; the relevant arc frame (blue or red); the relevant flatlamp (blue or red) and all object frames for the night. The parameters on each tabbed page were set as listed in Table 2.2.

With these parameters in place 2dfdr is run. When the process is complete, manually combine the reduced frames for each set of data for each night by using the 'Commands menu' and selecting the frames to combine in the dialogue box choosing the flux weight as 'OBJECTS'. This produced one red frame and one blue frame for the LMC data and another red and blue frame for the SMC data for each night.

To combine the data for all four days to have just one red and one blue set of data for the LMC and one red and one blue set of data for the SMC an IDL code 'combine' was written and modified to suit each data set. The code will be described for the Red SMC data with any variations for the blue SMC data and for the LMC data noted.

SMC red data

Each combined frame was renamed to denote which data set it referred to, e.g., 'combined_frames 03smcr.fits' denoted that this was the SMC red data for the 3rd November. The arrays were set to be Double Precision to sample the data with greater precision with the length of the arrays being taken from the header information. The four data frames for each of the observing nights was read in with the number of pix-

Table 2.2: Parameters used on 2dfdr to reduce the data.

Data	–	Choose the root directory with raw data and BIAScombined frame
General	–	select 'Verbose'
	–	select 'FIT' as fit for overscan (default)
	–	enter '9' for order of overscan (default)
	–	select 'Subtract Bias Frame'
	–	select 'divide spectra by Fibre Flat Field'
	–	select 'No' for use Laplacian edge detection cosmic ray rejection (default)
	–	enter '10' for smoothing parameter (default)
Extract	–	Keep all defaults
	–	select 'Subtract Scattered light from offset frames'
Calibration	–	Keep all defaults
Sky	–	select 'Throughput calibrate'
	–	select 'OFFSKY' for throughput calibration method
	–	select 'MEDIAN' for sky fibre
	–	select 'Use optimal Sky subtraction'
Combine	–	select 'Use optimal Sky subtraction'
	–	make sure 'combine reduced data' is NOT selected
	–	select 'adjust continuum levels'
	–	select 'FRAMES' for the flux weight
	–	Keep values at default values
	–	make sure 'combine A/B spectra' is NOT selected
	–	make sure 'Arm rescrunch' is NOT selected again
Plots	–	Keep all defaults

els, the starting wavelength, starting pixel number and the wavelength step being read from each header with the wavelength axis for each frame being defined from these values. Two 'FOR' loops were set up to read each of the 400 spectra in each of the combined rows, a spline was applied to the spectrum, a small region of the continuum of the spectra was chosen that appeared to be a true representative of the continuum in all the spectra to be used for normalisation and the mean of the spectrum in that region was calculated using the IDL function 'MEAN'. The spectrum with the spline applied was then divided by the mean of the spectrum to give a first approximation to normalisation. The root mean square (rms) was calculated using the IDL function STDEV and used to divide the approximated normalised spectra. Using the IDL function CREATE_STRUCT a fits header was written for the resulting combined spectrum with values for the reference pixel, reference coordinate value and increment value being taken from the original spectra headers.

Each spectrum that related to a target file was then printed to a file showing its fibre number so that the data reduction and final combining of all four days data could be checked for quality. This method produced data files for the SMC and LMC red and blue data that was of sufficient quality for the absorption features of interest; the 5780 and 5797 Å DIBS, the Na D lines and the Ca II K and H lines to be identified and fitted (see Section 2.2.2).

SMC blue data and LMC data

Exactly the same procedure was repeated for the remaining three sets of data, with the only differences being in the number of pixels in the blue spectra (10,000 instead of 19,630 in the red data) and in how each data file was labelled. The final files being called 'combined_specsmcr.fits' for the SMC red data, 'combined_specsmcb.fits' for the SMC blue data, 'combined_speclmcr.fits' for the LMC red data and 'combined_speclmcb.fits' for the LMC blue data.

2.2 Data analysis

2.2.1 NTT data

An IDL code, lb_dibs_2012.pro (see Appendix E on the accompanying CD), was written to plot the spectra obtained at the NTT in La Silla. The purpose of the code, described more fully below, is to plot each spectrum with the absorption lines of He, Na and the main DIBs. The equivalent width of the absorption lines was measured along with the error in that measurement. Each spectrum has eight plots associated with it that show the region around each of the absorption lines of interest. The first plot of each spectrum has the name of the target star included (see Appendix C on the accompanying CD).

Basic code requirements

The IDL code was constructed as follows. The initial floating and string arrays were defined with the length of the arrays being set to the maximum number of pixels in the image (which ranged from 2016 to 2022) and the maximum number of measurements made for each profile or set of profiles. Sometimes two profiles were fitted simultaneously because they were close in wavelength, in the following discussion the words profile and absorption line can be read to also mean the set of simultaneously fitted profiles unless otherwise stated. In order to fit a profile to each absorption line an IDL structure containing the information needed to constrain the fit was defined using the IDL function, REPLICATE. This defined a structure for the code whereby (using boolean values as defined in the function REPLICATE) parameters could be fixed, could be given a set value, could be assigned upper and lower limits of set values or values linked to a parameter. The final figure in the REPLICATE structure referring to the number of parameters needed to fit that particular profile; e.g. 'const5780 = REPLICATE({FIXED:0, VALUE:0.D, LIMITED:[0,0], LIMITS:[0.D, 0.D]},4) . A replicate structure was also defined where it was needed to determine the continuum. The number of spectra to be fitted was defined (239) along with empty strings as nec-

essary for the code to execute. A colour table was set so that fitting lines could be over plotted in a contrasting colour. A catalogue of all the spectra was read in and the information stored in the temporary memory 'stari' which had been previously defined as an empty string. The information about each target; RA; Dec; proper motions; parallax; visual magnitude and spectral type was read in and held in memory. Using this information the RA and Dec were defined as decimal coordinates; spectral type was defined to be the spectral type value held in the memory and the distance was defined to be the parallax value. These four arrays being defined as floating or string arrays at the beginning. Two data files were opened; 'measures.dat' for storing all the measurements calculated (with their associated errors) for each profile and 'plots.dat' for storing the information to be plotted which included the RA, Dec and distance information. As the Local Bubble project is an all sky survey of the local Galactic region it will be useful and give a more intuitive view to plot the information created with this code for the LB data in Galactic coordinates. This would not be so useful for plotting data from the Magellanic Clouds, which lie outside our Galaxy and each have a line of sight subtended over a few degrees rather than being observed in all directions. Therefore a section of code was written to convert the decimal values of the RA and Dec into Galactic coordinates. This was done using the IDL function GLACTC and the resulting Galactic longitude (gl) and Galactic latitude (gb) were also stored in the 'plot.dat' data file. Each page has 8 plots side by side representing the plots that show all the absorption features relating to each individual spectrum and there are 8 rows, therefore 8 targets per page (see Appendix C on the accompanying CD).

Code to loop over all spectra

At the start of the loop to be run over all spectra, "spectrum" was defined as being the string array listing the files from the catalogue so that the header information for each spectrum could be read using the IDL function MRDFITS. To use the header information the name of each target was defined as the header item 'OBJECT', the number of pixels (npixels) in the spectrum (which varied between 2016 and 2022) was defined as the header item NAXIS1, the wavestart, pixelstart and wavestep were defined

as the header items, CRVAL1, CRPIX1 and CDELT1 respectively. The wavelength axis was initially defined for each spectrum using the wavestart, pixelstart and wavestep values. The correction to the wavelength calibration using the telluric line was made here by selecting as 'valid' a wavelength range in which the telluric line fell for all spectra; defining 'wavecorrect' to be an array the same size as the wavelength array in each spectrum, where the wavelength correction was determined by finding the minimum value in the 'valid' wavelength range and subtracting it from where the telluric line should be found as determined by using Figure 2.5. The wavelength axis for each spectrum was redefined by adding the correction values as determined by 'wavecorrect' to the original wavelength. Thus aligning the wavelengths of all spectra to the position expected in relation to the position of the O_2 telluric line.

Normalising the spectra and fitting a profile to the absorption features

Each absorption line is fitted by a block of code which has a general form that is repeated for subsequent absorption lines and altered to accommodate any variations specific to the absorption line in question. A full description of the method is described for the 5780 Å and 5797 Å DIBs below with brief descriptions for other absorption features which use the same coding pattern and a fuller description where there is any variation in the coding.

The 5780 and 5797 Å DIBs

Although the 5780 and 5797 Å DIBs were plotted on the same graph the code to fit each profile was written in a separate block of coding. The 5780 Å DIB is described first.

At the start of this coding section a floating array was defined to store the measured values of each parameter for every spectrum (measures5780 = FLTARR(4, 238)). This shows that for the 5780 Å DIB there are 4 parameters to be measured for each of the 238 spectra. In a similar way the floating array "pcerror" was defined to store the error associated with each parameter for every spectrum. Three more arrays were defined to store the equivalent width measured for the 5780 Å DIB (ew1), the error in

that measurement (ew1err) and the ratio between the two (ew1select) which is used as a guideline to select the profiles that are considered to relate to the 5780 Å DIB. A wavelength range was set to span the DIB and include enough of the continuum either side to use for normalisation of the spectra. For the 5780 Å DIB the range was set from w1 = 5750 to w2 = 5830. This wavelength range was broken up into five smaller ranges, two to the left side of the 5780 Å DIB and two to the right side of the 5797 Å DIB and chosen to be clear of the wings of the absorption lines and one in between the DIBs. These were the ranges used to normalise the spectrum with the exact starting and finishing values for each improved by trial and error.

Baseline fitting

Following initial attempts at fitting profiles and inspection of the spectra and the the average spectra it was noticed that in a lot of spectra there were stellar features contaminating the 5780 Å DIB profile. These showed up as a shallow broadening of the DIB near the continuum and in many cases an absorption line very close to 5780 Å was evident. This needed to be corrected for. Given that the range of the wavelength under consideration was a very small part of the whole spectrum a first order polynomial should have been sufficient to normalise that part of the spectrum. However, this was not the case in practice. It turned out that a second order polynomial corrected for the shallow broadening and a Gaussian profile fitted the stellar absorption line. Correcting for these features to get a reasonable normalisation and measurements as accurate as possible for the 5780 Å DIB was achieved using two equations. Polgauss was defined as the equation:

$$a + bx + cx^2 + d \cdot exp\left(\frac{-(x-e)^2}{(2f^2)}\right)$$

where x is the wavelength.

Its purpose was to fit a Gaussian profile added to a second order polynomial which corrected for the stellar absorption line and shallow overlying feature. Polgauss2 was

defined as the equation:

$$a + bx + cx^2 + d \cdot exp\left(\frac{-(x-e)^2}{(2f^2)}\right) + g \cdot exp\left(\frac{-(x-h)^2}{(2k^2)}\right)$$

Its purpose was to fit two Gaussians added to a polynomial to give a better fit to the 5780 Å DIB and the stellar absorption line. In both cases a, b etc., are parameters to which initial guesses are assigned such as a = 1. Constraints on some of the parameters were set using upper and lower limits. The initial values used for the central wavelengths of the DIBs were taken from the Diffuse Interstellar Band Catalogue (Jenniskens & Desert 1994) as accessed from http://leonid.arc.nasa.gov/DIBcatalog.html. This was also used to provide an estimate of the width of the DIBs from the FWHM value stated. The National Institute of Standards and Technology (NIST) Handbook of Basic Atomic Spectroscopic Data as accessed from http://physics.nist.gov/PhysRefData/Handbook/Tables/findinglist.htm was used for the helium and sodium wavelengths and to check if unexpected absorption lines were of stellar origin. For the parameter relating to the depth of the absorption line the upper limit was set at 0 ensuring that emission lines were not included. The central wavelength of the 5780 Å DIB was allowed to vary by ±2 Å as was the central wavelength of the stellar absorption line (5785 Å) that was to be removed. The width of the 5780 Å DIB was allowed to vary between half and twice its initial estimate, the width of the 5785 Å stellar feature was allowed to vary by ±0.2 Å. See Table 2.3 for a list of the constraints used for all absorption features.

The median of the spectrum between the specified wavelength range was taken and used as the baseline to divide the spectrum by to make a first approximation to normalise the spectrum around the 5780 Å DIB (spect1). Note, a first approximation to normalise the spectrum for subsequent absorption lines in the spectrum were called, spect2, spect3 etc., so that each region was normalised from the original spectrum and considered separately from the rest of the spectrum. Next the four smaller regions defined above were selected and used for the wavelength range and the range of spect1 with the IDL function MPFITEXPR, which fitted the polynomial equation 'polgauss2' to the spectrum. The result of this was used in the calculation of the baseline

Table 2.3: Constraints for fitting absorption lines

absorption line	**depth**	**λ Å**	**range**	**σ width Å**	**range**
5780 DIB	-0.1	5780.6	± 2.0	1.25	$0.625 - 2.5$
5797 DIB	-0.5	5780 + 16.5	± 0.5	1.0	$0.5 - 2.0$
5850 DIB	-0.01	5780 + 69.6	± 0.5	1.0	$0.5 - 2.0$
He	-1.0	5875.6	± 2.6	1.3	$0.65 - 2.6$
Na D_2	-1.0	5889.95	± 2.0	1	$0.5 - 2.0$
Na D_1	-0.2	Na D_2 + 5.97		λ Na D_2	
6196 DIB	-0.5	5780 + 415.6	± 0.5	0.7	$0.35 - 1.4$
6203 DIB	-0.1	5780 + 422.6	± 0.75	1.0	0.5.2.0
6270 DIB	-0.1	5780 + 489.5	± 0.5	1.0	0.5.2.0
6283 DIB	-0.1	5780 + 503.7	± 0.5	1.0	0.5.2.0
6614 DIB	-0.5	5780 + 833.1	± 0.8	1.0	0.5.2.0

around the 5780 Å DIB in order to 'fine tune' the normalisation using the IDL function MPEVALEXPR and the polynomial equation 'polgauss'. Finally the spectrum was normalised by dividing the first approximation of the normalised spectra by the baseline calculated with the polynomial expressions. This result was given the label spect5780, subsequent absorption lines were labelled in a similar way making it clear to which absorption line they related to.

DIB fitting

To fit the 5780 Å DIB a Gaussian profile was chosen. During early attempts at profile fitting it seemed that a Lorentzian profile might fit this DIB more closely. However, all references in the literature suggested a Gaussian profile was more appropriate; for example (Herbig 1975; Hobbs et al. 2008; Jenniskens & Desert 1994; Krełowski 1988; Westerlund & Krełowski 1998). A close inspection of the plots to see if using a Lorentzian profile against common practice was justified led to the discovery of the shallow broadening of the DIB near the continuum. A plot of the average profile of

all 5780 Å DIB profiles confirmed that a Gaussian profile was the most appropriate fit (see Chapter 3) and the equation Gauss was defined as:

$$a \cdot exp\left(\frac{-(x-b)^2}{(2c^2)}\right)$$

Where a is the calculated depth of the absorption line, b is the central wavelength and c is the calculated width of the absorption line. Parameters to be used with this equation and the constraints on those parameters were set using the same considerations as for fitting the baseline. Two wavelength ranges either side of the 5780 Å DIB were chosen to work out the standard deviation of the continuum using the IDL function STDEV. The standard deviation was used to calculate the weights to apply to the data in the region under consideration. The fit to be applied to the 5780 Å DIB was restricted to lie between wavelengths 5773 and 5788 Å (labelled as w5780); this choice of region was improved by trial and error from an initial guess. The Gaussian profile was then fitted using the IDL function MPFITEXPR using the initial parameters and the constraints on those parameters, in the restricted region w5780, using the weights as calculated above. The results of this function; the calculated values of the parameters; the chi squared value and the associated error in the calculation of the value of each of the parameters was written into the holding place 'result'. These results were then used in the IDL function MPEVALEXPR to compute the spectrum of the Gaussian function using the best fit values of the parameters as held in 'result'.

The errors were scaled over the wavelength range w5780 by calculating the degrees of freedom (the number of elements in the wavelength range less the number of elements in 'result'), dividing the chi squared value by the degrees of freedom, taking the square root of this and multiplying it by the errors as calculated in MPFITEXPR.

In this thesis the maps and the interpretation of the data have been based on the comparison of the equivalent widths (EW) of the absorption features observed in the data. The shapes of observed absorption spectral lines can differ from sight-line to sight-line; their width and shape is determined by the absorbing material that causes them and the physical environment in which that material lies, as well as the resolution of the spectrograph used to record the data. This diversity means the depth

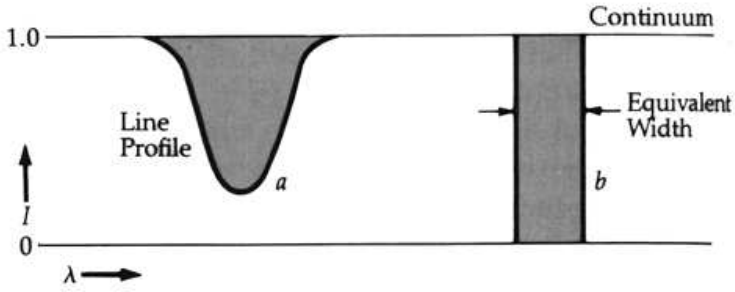

Figure 2.10: Illustrating the relationship between equivalent width and the area of an absorption line. (credit: Arizona.edu, Lecture 15: Stellar Atmospheres, Variable Stars).

of absorption lines are not necessarily a good measure of the overall strength of the line. As equivalent widths measure the amount of energy removed by the line they are a convenient measure to use for quantitative comparisons of the strengths of spectral features.

The profile of an absorption line can be plotted on a graph of intensity versus wavelength. The EW of the absorption line is defined by forming a rectangle, centred on the absorption line, with a height equal to that of continuum emission and a width such that the area of the rectangle is equal to the area in the absorption line, see Figure 2.10

During the line profile fitting procedure both Lorentzian and Gaussian profiles were tried and inspected by eye in order to determine the best fit. Only data that showed a good fit was included in the analysis. Although the DIBs do not have an intrinsic Gaussian profile it was noted that the Gaussian profile, generally, provided the most accurate fit to the observed data. The average EWs of the 5780 and 5797 Å DIBs are 0.579 and 0.132 Å respectively (Jenniskens & Desert 1994) but the instrumental set up on the NTT and the AAT gave a resolution of 1.3 and 0.9 Å respectively. Hence, the DIB absorption lines in both the NTT and AAT data are unresolved. Thus it is appropriate to use a Gaussain profile to calculate the EWs of the DIBs.

As a Gaussian profile was used to fit the absorption lines the EW can calculated from the integral of the Gaussian function as:

$$\mathrm{EW} = \int_{-\infty}^{\infty} ae^{\frac{-(x-b)^2}{2\sigma^2}} dx = ac \cdot \sqrt{2\pi}$$

Where a is the calculated depth of the absorption line, b is the central wavelength and c is the calculated width of the absorption line.

The error in the equivalent width was calculated as:

$$\mathrm{EW(error)} = \sqrt{(2\pi) \cdot ((a(\mathrm{error}) \cdot \sigma)^2 + (a \cdot \sigma(\mathrm{error}))^2)}$$

where 'a' and 'σ' are as for EW and 'a(error)' is the error in the calculated depth of the absorption line and 'σ(error)' is the error in the calculated width of the absorption line. A value that could be used as a filter to check for a reliable measurement was defined as: EW(select) = EW/EW(error).

As the 5780 Å DIB is the strongest of all the DIBs being considered here and it was expected to be the most common DIB detected, the measured central wavelength for this DIB for each spectrum was used as a reference point to which other DIBs in the same spectrum could be tied to. The difference in wavelength between the 5780 Å DIB and the other DIBs being taken from the Diffuse Interstellar Band Catalogue (Jenniskens & Desert 1994). This was to minimise the risk of any noise being identified as a DIB absorption particularly in the case of a very shallow DIB which may have a depth similar to that of nearby noise features.

The 5797 Å DIB was to be plotted on the same graph as the 5780 Å DIB therefore the same criteria for selecting the wavelength range to fit a baseline to normalise the spectra for the 5780 Å DIB was used. This time, however, the stellar absorption feature did not need to be removed from the spectrum as it was far enough away not to contaminate the 5797 Å DIB. Hence, when using the IDL function MPEVALEXPR to calculate the baseline a second order polynomial was used and not a Gaussian added to the second order polynomial as had been done for the 5780 Å DIB. Initial parameters

with their constraints were set in a similar way as for the 5780 Å DIB with the exception that the parameter for the central wavelength was fixed to the 5780 Å DIB by adding on the wavelength difference of 16.5 Å as given by the Diffuse Interstellar Band Catalogue (Jenniskens & Desert 1994) to the calculated central wavelength of the 5780 Å DIB. The central wavelength for the 5797 Å DIB was only allowed to deviate from this fixed value by ± 0.5 Å.

The standard deviation and weights were calculated in the same way as for the 5780 Å DIB and applied to the spectrum normalised for the 5797 Å DIB. The Gaussian profile to be applied to the 5797 Å DIB was restricted to lie between wavelengths 5791 and 5803 Å (labelled as w5797). This wavelength range was used when using the IDL functions MPFITEXPR and MPEVALEXPR to fit and evaluate the Gaussian profile to the 5797 Å DIB using the equation Gauss as defined above. This range was also used for scaling the errors. The equivalent width and associated error for the 5797 Å DIB were calculated as for the 5780 Å DIB.

The normalised spectrum for the 5780 Å DIB was plotted defining the wavelength range to be between 5765 and 5810 Å. The normalised spectrum for the 5797 Å DIB was over plotted in blue, to highlight the spectral feature that had been removed when fitting the 5780 Å DIB, the profile of the 5780 Å DIB was over plotted in red and the profile of the 5797 Å DIB was over plotted in green. For this first plot for each spectrum the name of the target star was inserted in the bottom right hand corner of the plot.

The 5850 Å DIB

Floating arrays were redefined for the 5850 Å DIB to store the measured values of each parameter, equivalent width and associated errors relating to this DIB. The wavelength range to span this DIB was set from w1 = 5840 to w2 = 5870. This wavelength range was broken up into four smaller ranges, two either side of the DIB and chosen to be clear of the wings of the absorption line. To normalise this baseline a first order polynomial, pol $= a + bx$ was used. A first approximation to normalise the spectrum around the 5780 Å DIB was made using the median of the spectrum between the specified wavelengths. The normalisation was 'fine tuned' using the IDL functions MPFITEXPR and MPEVALEXPR in the same manner as for the 5780 Å DIB.

Initial parameters with their constraints were set in a similar way as for the 5797 Å DIB with the wavelength difference 69.6 Å being added to the calculated central wavelength of the 5780 Å DIB and allowed to deviate from this fixed value by ±0.5 Å.

The standard deviation and weights were calculated in the same way as for the 5780 Å DIB and applied to the spectra normalised for the 5850 Å DIB. The Gaussian profile to be applied to the 5850 Å DIB was restricted to lie between wavelengths 5845 and 5856 Å(labelled as w5850). This wavelength range was used when using the IDL functions MPFITEXPR and MPEVALEXPR to fit and evaluate the Gaussian profile to the 5850 Å DIB using the equation Gauss as defined above. This range was also used for scaling the errors. The equivalent width and associated error for the 5850 Å DIB were calculated as for the 5780 Å DIB.

The normalised spectrum for the 5850 Å DIB was plotted defining the wavelength range to be between 5835 and 5865 Å. The profile of the 5850 Å DIB was over plotted in red.

The helium line

As for the DIB profiles the helium line (He) (rest wavelength of 5876 Å) of the target stars were fitted and measured. Floating arrays were redefined for the He line to store the measured values of each parameter, equivalent width and associated errors. The wavelength range to span the He line was set from w1 = 5865 to w2 = 5885. This wavelength range was broken up into four smaller ranges, two either side of the line and chosen to be clear of the wings of the absorption line. To normalise this baseline a first order polynomial was used as for the 5850 Å DIB. The normalisation was carried out using the same procedure as for the DIBs as described previously.

Initial parameters with their constraints were set in a similar way as for the DIBs. However, the central wavelength of the He line was allowed to vary by ±2 times its width.

The standard deviation and weights were calculated in the same way as for the DIBs and applied to the normalised spectra. The Gaussian profile to be applied was restricted to lie between wavelengths 5870 and 5882 Å. This wavelength range was

used with the IDL functions MPFITEXPR and MPEVALEXPR to fit and evaluate the Gaussian profile using the equation Gauss as defined above. This range was also used for scaling the errors. The equivalent width and associated error were calculated as for the DIBs.

The normalised spectrum for the He line was plotted with the profile being over plotted in red.

The sodium doublet

Initial attempts at fitting the sodium doublet (Na D_1 and Na D_2) revealed a broad dip in the spectra that sometimes spanned both Na absorption lines. As for the 5780 Å DIB a second order polynomial corrected for this. Floating arrays were redefined to store the measured values of each parameter, equivalent width and associated errors. This time the two absorption lines of the Na doublet were fitted simultaneously. Therefore, extra floating arrays were defined for the second of the absorption lines, associated error and selection value (ew2, ew2err and ew2select). The wavelength range to span the Na lines was set from w1 = 5875 to w2 = 5910. This wavelength range was broken up into five smaller ranges, two either side of the Na lines and one in between the two Na lines. To normalise this baseline and remove the broad dip a second order polynomial was used and the normalisation was carried out using the same procedure as for the previous DIBs and He line.

Initial parameters with their constraints were set in a similar way as for the He line. However, the central wavelength of the Na D_2 line was allowed to vary by ± 2 times its width. The standard deviation and weights were calculated and used as previously. The double Gaussian profile to be applied was restricted to lie between wavelengths 5884 and 5901 Å. This wavelength range was used with the IDL functions MPFITEXPR and MPEVALEXPR to fit and evaluate the double Gaussian profile using the equation gauss2nd defined as:

$$a \cdot exp\left(\frac{-(x-b)^2}{(2c^2)}\right) + d \cdot exp\left(\frac{-(x-b-5.97)^2}{(2c^2)}\right) + e$$

where the Na D_1 line was fixed to be 5.97 Å away from the stronger Na D_2 line and fixed to have the same calculated width as the Na D_2 line.

Another baseline was fitted to the same region but this time using a first order polynomial for the normalisation which was carried out using the same procedure as for the previous absorption lines. This normalisation result was divided by the previous absorption line fitting result to remove the Na lines and reveal the profile of the broad shallow dip that sometimes spanned both sodium lines (see Chapter 3 for an example).

The double Gaussian profile was fitted again using the same initial parameters, constraints and double Gaussian equation as previously but this time it was the spectrum normalised by the first order polynomial that was used with the IDL functions MPFITEXPR and MPEVALEXPR to calculate the measurements between the wavelengths 5884 and 5901 Å.

The first order normalised spectrum for the Na lines was plotted with the double profile being over plotted in red and the broad shallow dip over plotted on blue, see Figure 3.13 in Chapter 3.

The 6196 and 6203 Å DIBs

As the 6196 and 6203 Å DIBs are so close together these were fitted by a double Gaussian profile. Floating arrays were redefined to account for the two profiles. The wavelength range to span these DIBs was set from w1 = 6180 to w2 = 6220. This wavelength range was broken up into five smaller ranges as had been done for the Na lines. To normalise this baseline a second order polynomial was used. Although the wavelength range is small and so a first order polynomial should be sufficient there is a lot of noise in the region and the DIBs are very shallow. The second order polynomial seemed to provide a reasonable correction for the noise and slope and was a visually better fit than a first order polynomial.

Initial parameters with their constraints were set in a similar way as previously with the wavelength difference of 415.6 Å and 422.6 Å being added to the calculated

central wavelength of the 5780 Å DIB for the 6196 and 6203 Å DIBs respectively. The 6196 Å DIB was allowed to deviate from this fixed value by ±0.5 Å, while the 6203 Å DIB was allowed to deviate by ±0.75 Å.

A different approach to normalising the spectrum was taken for this region because of the increased noise. As before the median of the spectrum over the specified wavelength range was taken and used as the baseline to divide the spectrum by to make a first approximation to normalise the spectrum around the DIBs. However, instead of using the whole of the smaller wavelength ranges just the central wavelengths within these smaller ranges along with the median values of each range were used with the IDL function MPFITEXPR. The median value of these wavelengths being calculated in an IDL 'FOR'loop structure. As previously, the result of MPFITEXPR was used with the second order polynomial in the IDL function MPEVALEXPR. The result of MPEVALEXPR being used to divide the first approximation to 'fine tune' the normalisation of the spectra as before.

The standard deviation and weights were calculated in the same way as previously. The double Gaussian profile to be applied was restricted to lie between wavelengths 6190 and 6212 Å. This wavelength range was used with the IDL functions MPFITEXPR and MPEVALEXPR to fit and evaluate the double Gaussian profile using the equation gauss defined as:

$$a \cdot exp\left(\frac{-(x-b)^2}{(2c^2)}\right) + d \cdot exp\left(\frac{-(x-e)^2}{(2f^2)}\right) + g$$

This wavelength range was also used for scaling the errors. The equivalent width and associated error for the two DIBs were calculated as for the 5780 Å DIB. The normalised spectrum for the 6196 and 6203 Å DIBs was plotted. The profile of both DIBs being over plotted in red.

The 6270 Å DIB

The 6270 Å DIB was fitted by a Gaussian profile. For the similar reason as the previous two DIBs a second order polynomial was used to normalise this baseline. Floating

arrays were redefined and the wavelength range to span this DIB was set from w1 = 6249 to w2 = 6273. This wavelength range was broken up into four smaller ranges, two at either side of the DIB. Initial parameters with their constraints were set in a similar way as previously with the wavelength difference of 489.5 Å being added to the calculated central wavelength of the 5780 Å DIB and allowed to deviate from this fixed value by ±0.5 Å.

The 'FOR' loop method to normalise this part of the spectrum was used following the same procedure as for the 6196 and 6203 Å DIBs. The standard deviation and weights were calculated in the same way as previously. The Gaussian profile to be applied was restricted to lie between wavelengths 6261 and 6275 Å. This wavelength range was used with the IDL functions MPFITEXPR and MPEVALEXPR to fit and evaluate the Gaussian profile using the equation gauss defined as:

$$a \cdot exp\left(\frac{-(x-b)^2}{(2c^2)}\right) + d$$

This wavelength range was also used for scaling the errors. The equivalent width and associated error for the 6270 Å DIB were calculated as previously. The normalised spectrum for the 6270 Å DIB was plotted. The profile of the DIB being over plotted in red.

The 6283 Å DIB and telluric line

The 6283 Å DIB falls on the O_2 telluric line, in many cases just the faintest trace of the absorption line could be detected. To get the most accurate measurements possible from these data this DIB was fitted by a Gaussian profile added to a first order polynomial so that the DIB was fitted along the side of the telluric line. To normalise the spectrum a second order polynomial was used to account for the contamination by the telluric line. As previously, floating arrays were redefined and the wavelength range to span this DIB was set from w1 = 6250 to w2 = 6310. This wavelength range was broken up into five smaller ranges. Initial parameters with their constraints were set in a similar way as previously with the wavelength difference of 503.7 Å being added to

the calculated central wavelength of the 5780 Å DIB and allowed to deviate from this fixed value by ±0.5 Å.

The 'FOR' loop method to normalise this part of the spectrum was used following the same procedure as for the 6196 and 6203 Å DIBs. The standard deviation and weights were calculated in the same way as previously. The Gaussian profile to be applied was restricted to lie between wavelengths 6280 and 6288 Å. This wavelength range was used with the IDL functions MPFITEXPR and MPEVALEXPR to fit and evaluate the Gaussian plus first order polynomial profile using the equation GaussLin defined as:

$$a \cdot exp\left(\frac{-(x-b)^2}{(2c^2)}\right) + d + ex$$

This wavelength range was also used for scaling the errors. The equivalent width and associated error for the 6283 Å DIB were calculated as previously. The normalised spectrum for the 6283 Å DIB was plotted. The profile of the DIB being over plotted in red.

The 6614 Å DIB

Some of the grisms introduce fringing towards the red end of the spectrum as a result of multiple internal reflections, which cannot always be adequately removed by flat fielding. Internal flats taken at the position of the science object can be used to remove fringing, the dome flats during the day are not suitable due to the flexure of the telescope. However, fringing only becomes a major issue redwards of about 7000 Å. Fringing in these data starts at about the location of the 6614 Å DIB although its effect is not major. Using a second order polynomial to normalise this region of the spectrum dealt with the effect sufficiently and enabled the 6614 Å DIB to be measured using a Gaussian profile.

Again floating arrays were redefined and the wavelength range to span this DIB was set from w1 = 6598 to w2 = 6620. This wavelength range was broken up into four smaller ranges. Initial parameters with their constraints were set in a similar way

as previously with the wavelength difference of 833.1 Å being added to the calculated central wavelength of the 5780 Å DIB and allowed to deviate from this fixed value by ±0.8 Å.

The 'FOR' method to normalise this part of the spectrum was used following the same procedure as for the 6196 and 6203 Å DIBs. The standard deviation and weights were calculated in the same way as previously. The Gaussian profile to be applied was restricted to lie between wavelengths 6610 and 6618 Å. This wavelength range was used with the IDL functions MPFITEXPR and MPEVALEXPR to fit and evaluate the Gaussian profile using the equation gauss as defined for the 5850 Å DIB. This wavelength range was also used for scaling the errors. The equivalent width and associated error for the 6614 Å DIB were calculated as previously. The normalised spectrum for the 6614 Å DIB was plotted. The profile of the DIB being over plotted in red.

Code to produce average spectra

As well as plotting the absorption lines of individual spectra it was decided to plot the average absorption line of all spectra to see if any overall trend was noticeable. To do this the wavelength axis for the averaged spectra was defined for a region around each absorption line (e.g. wave5780ave=5760. + FINDGEN(200)*0.25) and the average spectrum was set to zero (e.g. spect5780ave =0.*wave5780ave) at the start of the code. Then in each block of code after the absorption line had been fitted, the spectra were resampled to the average wavelength axis defined at the beginning (e.g. spect5780res=RESAMPLE(wavelength, spect5780, wave5780ave)) and each spectrum added to the previous spectrum (e.g. spect5780ave=spect5780ave + spect 5780res). At the end of the entire code after all the spectra had been resampled and stacked the average of the spectra was taken by dividing the accumulated spectra by the number of targets (238) (e.g. spect5780ave=spect5780ave/238). This average spectrum was plotted at the end of all the individual plots of the spectra and gave a good indication of the general profile shape and provided a check on the central wavelength of the absorption lines. This was used to check the right form (Gaussian or Lorentzian profile)

of fit had been applied and to confirm whether or not some very weak features were actually caused by a DIB and were not, in fact, noise.

The plots were written to a postscript file, lb_dibs_2012.ps, and arranged so that plots of all the absorption lines relating to an individual spectrum were in the same row. This spectral atlas is in Appendix C on the accompanying CD.

2.2.2 AAT data

For the AAT data both the LMC and the SMC were observed and for both sets of data there were a blue set of data and a red set of data making four separate data sets in all. An IDL code to plot the spectra was written for each data set, although each code closely resembles the other three with the main differences being between the codes for the blue and red data. The code is also very similar to the code written to plot the spectra obtained from the NTT and fully explained in Section 2.2.1. Therefore, in this section the code will be fully described for the SMC with reference to the code written for the LB as appropriate and just the minor adjustments needed to apply the code to the LMC will be explained. The full codes can be found in Appendix E on the accompanying CD. The purpose of the codes described here, is to plot each spectrum with the absorption lines of Ca II, Na D_1 and D_2, 5780 Å DIB and 5797 Å DIB for the SMC and LMC and also the Galactic components of these absorptions along the lines of sight to the SMC and LMC. The blue spectra have two absorption lines, the Ca II K and H lines, which are superimposed onto the hydrogen Balmer H_ε. The red data has three plots associated with it for the Na and DIB absorption. In each case the first plot for each data set has the name of the target star included and all plots are labelled to show the approximate location of the Galactic, SMC or LMC components.

Basic code requirements for the SMC red spectra

The IDL code for the red spectra for the SMC was constructed as follows. As the spectra had been combined using Double Precision this was also chosen here. The initial double and string arrays were defined with the length of the arrays being set to the maximum

number of pixels in the image (19630) and, as the spectra were a two-dimensional array due to the simultaneous collection of data with 2dF, the maximum number of fibres (400) as well as the maximum number of measurements for each profile to be fitted. To fit each profile the IDL structure REPLICATE was used in the same way as it was for the Local Bubble data. The number of spectra to be read into the code was defined as 400 even though not all of the 400 fibres were target stars and the necessary empty strings to allow the code to execute were defined. Using the information in the header for the start wavelength, pixel number, wavestep values, number of pixels in the spectra, the wavelength axis was defined to start at 5770 Å. As for the LB data, the average absorption line of all the spectra was to be plotted. Therefore, the wavelength axis for the averaged spectra was defined for a region around each absorption line so that after each block of code for each absorption line the spectra could be resampled to the average wavelength axis and added to the previous spectrum. The average of these data was taken and plotted at the end of all the individual plots in the same way as it was done for the LB data. The colour table was set to allow over plotting of fitting lines in a contrasting colour. As for the LB code, a catalogue of all the spectra was read in and information stored, the RA and Dec were defined as decimal coordinates and also converted to Galactic coordinates (for use with the Galactic components of the data if required), a file called 'measures_smcr.dat' was opened for storing all the measurements calculated and a postscript file was set to plot all the data.

Code to loop over all spectra enlargethispage

At the start of the loop to be run over all spectra, an 'IF' statement was set so that if the item named 'target' in the input catalogue had the value 'P' then the information for that target would be read in and the code would proceed in the loop. The 'P' denoted all the spectra in the set of 400 spectra in each frame that related to a target star as opposed to a sky, fiducial or parked/broken fibre. The frame 'combined_specsmcr.fits was read in using the IDL function MRDFITS to access all the header information in the frame.

Normalising the spectra and fitting a profile to the absorption features

As for the LB code each absorption line was fitted by a block of code with a general form that was repeated and altered to accommodate variations for other absorption features. The block of code for the 5780 Å DIB is described here with reference to similarities to the LB code and is followed by descriptions of the code variations in other features.

The 5780 Å DIB

Following very closely the method used in the LB code, double arrays were defined to store measured values and calculated errors, The wavelength range that spanned the 5780 Å DIB and included enough of the continuum to use for normalisation was set from w1 = 5750 to w2 = 5815, This range was broken into five smaller ranges chosen to sample the continuum and avoiding the DIB, any wings of the DIB that occurred in some spectra and any anomalies that were present in the continuum of some data. These were the ranges used to normalise the spectrum.

Baseline fitting

As the wavelength range under consideration was a small part of the whole spectrum a first order polynomial was used and initial guesses for the values to be used in the polynomial were set. The median of the spectrum between the specified wavelength range was taken and used as a baseline to divide the spectrum by as a first approximation to normalise the spectra.

As for the LB code the smaller regions were selected for use with the IDL function MPFITEXPR to fit the first order polynomial expression. The result of this was used to 'fine tune' the normalisation of the spectra using MPEVALEXPR with the result of that operation being used to divide the first approximation to the normalised spectra to complete the normalisation process.

Table 2.4: Constraints for fitting absorption lines.

SMC direction	**depth**	**λ Å**	**range**	**σ width Å**	**range**
Ca II K gal	−0.1	3933.6	±2.0	0.3	0.15 − 0.60
Ca II K smc 1	−0.2	3936.6	±2.0	0.2	0.10 − 0.40
Ca II K smc 2	−0.1	3937.5	±1.0	0.2	0.10 − 0.40
5780 gal	−0.1	5780.1	±1.0	0.6	0.036 − 0.90
5797 gal	−0.1	5780 gal + 16.5	±0.75	0.5	0.25 − 1.00
Na D_2 gal	−0.1	5890.0	±2.0	0.5	0.25 − 1.00
Na D_1 gal	−0.1	Na D_2 gal + 5.97		λ Na D_2 gal	
5780 smc	−0.1	5783.6	±1.0	0.6	0.036 − 0.90
5797 smc	−0.1	5780 smc + 16.5	±0.75	0.5	0.25 − 1.00
Na D_2 smc	−0.2	5893.0	±2.0	0.5	0.25 − 1.00
Na D_1 smc	−0.2	Na D_2 smc + 5.97		λ Na D_2 smc	
LMC direction	**depth**	**λ Å**	**range**	**width Å**	**range**
Ca II K gal 1	−0.1	3933.6	±1.0	0.2	0.12 − 0.30
Ca II K gal 2	−0.2	3935.0	±0.5	0.2	0.12 − 0.30
Ca II K smc 1	−0.1	3937.0	±1.0	0.2	0.12 − 0.30
Ca II K smc 2	−0.1	3937.5	±0.5	0.2	0.12 − 0.30
5780 gal	−0.1	5780.8	±1.0	0.6	0.036 − 0.90
5797 gal	−0.1	5780 gal + 16.5	±0.75	0.5	0.25 − 1.00
Na D_2 gal	−0.1	5890.0	±2.0	0.5	0.25 − 1.00
Na D_1 gal	−0.1	Na D_2 gal + 5.97		λ Na D_2 gal	
5780 smc	−0.1	5786.0	±1.0	0.6	0.036 − 0.90
5797 smc	−0.1	5780 smc + 16.5	±0.75	0.5	0.25 − 1.00
Na D_2 smc	−0.2	Na D_1 smc - 5.97		λ Na D_1	
Na D_1 smc	−0.2	5901.0	±2.0	0.5	0.25 − 1.00

DIB fitting

To fit the 5780 Å DIB a Gaussian profile was chosen which had the same mathematical form as described in the LB code with the parameters, initial guesses and constraints set in a similar way as for the LB code; Table 2.4 lists the values chosen for all four data sets. As the spectra show both the Galactic and SMC components of the DIB

the two profiles were fitted with a double Gaussian profile. Two wavelength ranges either side of the 5780 Å DIB were chosen to work out the standard deviation using the function STDEV. This was used to calculate the weights to apply to the data. The fit to be applied to the 5780 Å DIB was restricted to lie between the wavelength ranges 5778 and 5788 Å. The Gaussian profile was fitted to the restricted region with MPFITEXPR using the initial guesses for the parameter, the constraints on those parameters and the weights as calculated previously. This calculated the values of the parameters and associated errors. These results were then used in the function MPEVALEXPR to compute the spectrum of the Gaussian function. The errors were scaled and the equivalent widths and their associated errors were calculated in the same way as for the LB data. The plot of the spectrum around the 5780 Å DIB was set with the fitted Gaussian profile over plotted and all the measurements were written in to the file 'measures_smcr.dat'.

The 5797 Å DIB

Floating arrays were redefined for the 5797 Å DIB to store the measured values of each parameter, equivalent width and associated errors relating to this DIB. The wavelength range to span this DIB was set from w1 = 5750 to w2 = 5815. As for the 5780 Å DIB this wavelength range was broken up into five smaller ranges to normalise the baseline with a first order polynomial. A first approximation to normalise the spectrum was made using the median of the spectrum between the specified wavelength and the normalisation 'fine tuned' using the IDL functions MPFITEXPR and MPEVALEXPR in the same manner as for the 5780 Å DIB.

A double Gaussian profile was used. Initial parameters with their constraints were set in a similar way as for the 5780 Å DIB with the exception of fixing the parameter for the central wavelength to the 5780 Å DIB by adding 16.5 Å to the calculated central wavelength of the 5780 Å DIB; again following the procedure detailed for the LB code. This parameter was fixed for both the Galactic and SMC components of the DIB.

The standard deviation and weights were calculated as previously. The Gaussian profile to be applied to the 5797 Å DIB was restricted to lie between wavelengths 5794

and 5805 Å. This wavelength range was also used for scaling the errors. The equivalent width and associated error for the 5797 Å DIB were calculated as for the 5780 Å DIB. The normalised spectrum for the 5797 Å DIB was plotted defining the wavelength range to be between 5792 and 5808 Å. The profiles of the 5797 Å DIB were over plotted in red.

The sodium doublet

As the Galactic and SMC components of the Na D lines are well separated each D_1 and D_2 line for both components could be fitted. In many spectra the Galactic component also showed a Na telluric emission line. To improve the fit of the Na lines themselves Gaussian profiles were added to fit the telluric lines. With all profiles being fitted simultaneously. Floating arrays were redefined to store the measured values of each parameter, equivalent width and associated errors for just the Na absorption lines. The wavelength range to span the Na lines was set from w1 = 5850 to w2 = 5915. This wavelength range was broken up into four smaller ranges to use for normalisation using a first order polynomial as before.

Initial parameters with their constraints were set in a similar way as previously. However, the Na D_1 line was fixed to be 5.97 Å away from the stronger Na D_2 line and fixed to have the same calculated width as the Na D_2 line, for both the Galactic and SMC components. Also the telluric Na D_1 emission line was fixed to its Na D_2 companion in the same way. The standard deviation and weights were calculated and used as previously.

The multiple Gaussian profile to be applied was restricted to lie between wavelengths 5850 and 5914 Å. This wavelength range was used with the IDL functions MPFITEXPR and MPEVALEXPR to fit and evaluate the multiple Gaussian profile using the equation defined as:

$$a \cdot exp\left(\frac{-(x-b)^2}{(2c^2)}\right) + d \cdot exp\left(\frac{-(x-e)^2}{(2f^2)}\right) +$$
$$g \cdot exp\left(\frac{-(x-b-5.97)^2}{(2c^2)}\right) + h \cdot exp\left(\frac{-(x-e-5.97)^2}{(2f^2)}\right) +$$
$$k \cdot exp\left(\frac{-(x-l)^2}{(2m^2)}\right) + n \cdot exp\left(\frac{-(x-l-5.97)^2}{(2m^2)}\right) + p$$

where components g, h, k and l refer to the telluric components whose amplitudes were forced to be positive). The standard deviation, weights, equivalent widths and associated errors were calculated as previously. The normalised spectrum for the Na lines was plotted defining the wavelength range to be between 5885 and 5910 Å. The profile of the Na lines were over plotted in red.

Basic code requirements for the SMC blue spectra

The IDL code for the blue spectra for the SMC was constructed as follows in a similar way to the red data. A double array was chosen with the length of the array being set to the maximum number of pixels in the image (10000). This differed in length to the red spectra due to the instrumental set up, which was designed to maximise the range of wavelengths observed critical to our project. The wavelength was calibrated to start at 3780 Å. A file called 'measures_smcb.dat' was opened for storing all the measurements calculated. The rest of the basic code requirements were the same as for the red data.

The Ca II K Line

As for the red spectra, an 'IF' statement was set to select the target stars. The wavelength range that spanned the Ca II K Line was set from w1 = 3910 to w2 = 3990. This range was broken into five smaller ranges chosen to sample the continuum and used to normalise the spectrum. As for the absorption features in the red spectra a first order polynomial was used to fit the baseline, first taking the median of the

spectrum over the specified wavelength range to make a first approximation and then 'fine tuning' the normalisation using MPEVALEXPR.

Profile fitting

It was noted that the SMC component of the Ca II K line often showed a second component. Therefore, the Galactic and SMC component of this line were fitted with a triple Gaussian expression. The wavelength range to span the Ca II K line was set from w1 = 3910 to w2 = 3990. This wavelength range was broken up into five smaller ranges to normalise the baseline with a first order polynomial. A first approximation to normalise the spectrum was made using the median of the spectrum between the specified wavelength and the normalisation 'fine tuned' using the IDL functions MPFITEXPR and MPEVALEXPR in the same manner as for the 5780 Å DIB.

Initial parameters with their constraints were set in a similar way as for the 5780 Å DIB. The standard deviation and weights were calculated as previously. A check was run to determine whether or not the second component truly was a second kinematic component of the feature. To do this, once all the constraints had been set and the measurement made, we calculated the difference in the central wavelength between the two components of the SMC Ca II K line, we set a threshold equal to 0.5 and ran an 'IF' statement so that if the difference between the two central wavelengths was less than the threshold value then the depth of that second component would be fixed at a zero value and the measurements recalculated. The Gaussian profile to be applied was restricted to lie between wavelengths 3910 and 3990 Å. This wavelength range was also used for scaling the errors. The equivalent widths and associated errors for the three components were calculated as previously. The normalised spectrum for the Ca II K line was plotted defining the wavelength range to be between 3930 and 3943 Å. The profiles of the Ca II K lines were over plotted in red. It was not possible to fit a profile to the Ca II H line because of contamination by a Balmer H_ε at 5876 Å. However, the spectra were normalised in that region using the same setting as used to normalise the spectra for the Ca II K line. The expected central wavelength of the Ca II H lines for all three components were fixed to the measured values of the Ca II K

lines by adding 34.8 Å to the measured values. The resulting measurements for the Ca II H lines were then plotted as tick marks on a plot of the normalised spectra between the wavelengths 3930 and 3943 Å.

The average spectrum of both the Ca II K line and Ca II H line were calculated and plotted in the same way as the average spectra for the 5780 Å DIB, 5797 Å DIB and Na had been done in the red data.

The LMC red spectra

The code to normalise the spectra and fit 5780 Å DIB, 5797 Å DIB and Na profiles was constructed in the same way as for the SMC data. The only differences being in some of the wavelength ranges chosen to normalise the spectra avoiding any anomalies present in the LMC data, the initial guesses for the parameters and the constraint values (see Table 2.4). The differences in the initial parameters arise because there is a greater Doppler shift between the Milky Way and the LMC (~ 5.5 Å) than there is between the Milky Way and the SMC (~ 3.5 Å) resulting in a larger separation between the Galactic and LMC components of the absorption features than there are between the Galactic and SMC components.

The sodium doublet The separation between Galactic and LMC components of the Na D lines in the LMC meant that on most occasions the Galactic D_1 line was superimposed by the LMC D_2 line and was visually difficult to separate. However the two components must be distinct, therefore it was decided to fit the profiles separately in the same way as it was done for the SMC data by tying the D_1 lines to their respective D_2 lines by adding 5.97 Å to the measured values of the D_2 lines and using the same measured width of the D_2 lines for the D_1 lines. This then allowed a separate fitting of the lines on the occasions where the Galactic D_1 line was separate to the LMC D_2. As for the SMC data the Galactic Na telluric lines were also fitted. As will be seen by the maps created in Chapter 4 this proved to be a reasonable decision to make. The measurements for these data were stored in a file called 'measures_lmcr.dat'

The LMC blue spectra

The code to normalise the spectra and fit Ca II K line profiles and mark the positions of the Ca II H lines was constructed in the same way as for the SMC data taking into account the Doppler shift difference. The main difference between the LMC data and the SMC data being that a second component of the Ca II K line was noted in the Galactic component as well as the LMC component. A check was run to determine whether or not the second components of both Galactic and LMC components were truly a second kinematic component of the feature in the same way as the check had been made in the SMC data, setting the depth of the second component to zero in both cases if the difference between the two central wavelengths for the Galactic or LMC component was less than the threshold value of 0.5 Å. The measurements for these data were stored in a file called 'measures_lmcb.dat'

3 The Local Bubble

"If you are keeping yourself in the bubble and only looking at your own data or only watching the TV that fits your agenda then it gets boring."

– Nate Silver

3.1 Introduction

It has been known for over 40 years that our Sun sits in a region of unusually low gas density, which we call the Local Bubble (LB). The LB extends for $\sim$ 100 pc in the plane of the Galaxy and for hundreds of parsecs vertically, presumably as far as the Galactic Halo (Welsh et al. 2010). The presence of the LB was initially indicated by the very low values of interstellar extinction measurements of stars within 100 pc of the Sun (Welsh & Shelton 2009).

The origin is probably the result of one or more supernovae and the first evidence for the LB was provided by the observation of a diffuse soft-X-ray background by the ROSAT satellite (Lallement 2004). Initially this was interpreted as a scenario in which the Sun was surrounded by a region of hot ($\sim 10^6$ K) gas. However, such a volume of hot gas should emit copious energy in EUV emission lines, which were searched for with the CHIPS satellite but not detected (Sasseen, Hurwitz & Team 2004). Hot gas should also strongly absorb in the O VI 1032Å line, which is far weaker towards nearby sources than expected (Barstow et al. 2010; Cox 2005). To date this conundrum has not been solved. It is clear there is a hot ($\sim 10^6$ K) gas in the region of the Sun, it seems likely there will be a hot gas at the edges of the LB where the walls of the LB have formed creating an interface between the hot gas and the warm/cool neutral gas of the LB walls. How the temperature of the ISM varies between the Sun and the walls of the LB is simply not known (private discussion with Rosine Lallement at the IAU Symposium IAUS 297: The diffuse interstellar bands, Leiden, May 2013).

Conditions in the ISM are typically probed via lines arising from neutral or singly-

ionized atoms or molecules. This poses a problem with understanding the nature of the gas within the LB. The temperature is high in the region of the Sun and it may be as hot throughout the whole of the cavity of the LB. If that is the case, then the neutral or singly-ionized atoms or molecules are simply not expected to survive. To overcome this problem it is necessary to probe the LB using species which may survive under these conditions. It was shown by van Loon et al. (2009) that Diffuse Interstellar Bands (DIBs) are seen in the relatively harsh environments such as the Disc-Halo interface, the high $\lambda5780/\lambda5797$ ratio indicating the existence of interfaces between cool/warm and hot gas.

Welsh et al. (2010) created 3-D gas density maps of Na I and Ca II interstellar absorption with in 300 pc of the sun. With the Na I maps Welsh et al. (2010) revealed a central region of very low neutral gas absorption out to a distance of about 80 pc in most Galactic directions, thereby tracing the well known Local cavity region with the wall of neutral Na I gas beyond the cavity. However, their Ca II maps did not show any sharp increase in absorption at a distance of 80 pc. Instead there was a slowly increasing value of Ca II equivalent width with increasing sight-line distance. Figure 3.1 shows the Na I maps created by Welsh et al. (2010).

In Figure 3.1 the white to dark shading represents low to high values of the Na I volume density. The triangles represent the sight-line positions of stars used to produce the map with the size of the triangle being proportional to the derived Na I column density. Stars plotted with vertex upwards are located above the Galactic Plane and stars plotted with vertex downwards are located below the Galactic Plane. The regions of these maps with a matrix of dots represent areas of uncertain neutral gas density measurements.

I used targets from the Na I D Local Bubble survey of Lallement et al. (2003), as the catalogue of Welsh et al. (2010) was not publicly available at the time, to make an all-sky survey and use DIBs to probe the LB to try to reveal some structure that was not traced by the Na I and Ca II interstellar absorption maps created by Welsh et al. (2010). As well as probing many different sight-lines, some targets, which where in a similar direction but varying distances from the Sun were observed to try and reveal

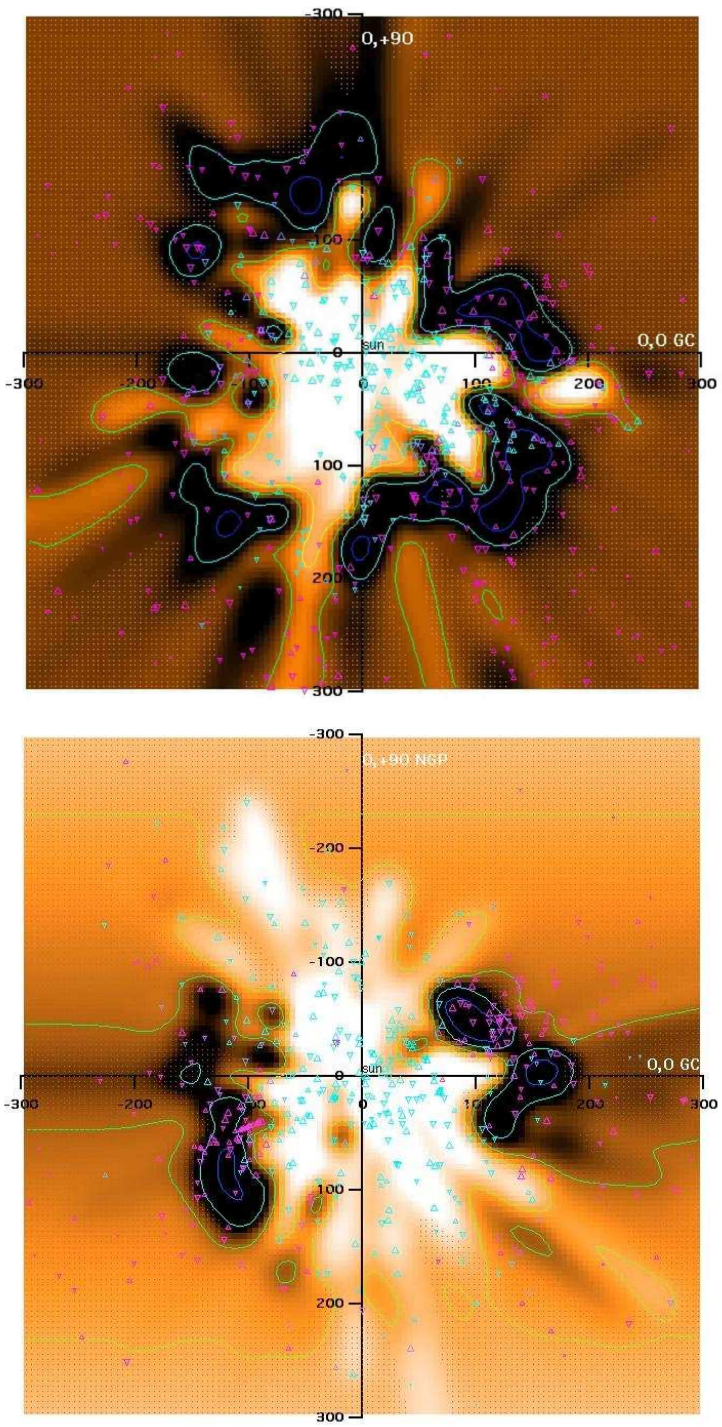

Figure 3.1: Plot of 3-D spatial distribution of interstellar Na I absorption in the (Top:) Galactic Plane projection and (Bottom:) the Meridian Plane projection. Distances are in parsecs and the symbols are described in the text. Credit Welsh et al. (2010).

a change in the environment along a particular sight-line and so reveal the small scale structure of the ISM.

Observations at the NTT

For this project I used the EFOSC2 instrument at the NTT as it is an efficient low-/medium-resolution spectrograph, which when used with Grism 20 and a 0.3″ slit width was well suited to my required spectral resolution. The location of the NTT at La Silla allowed me to observe stars in both the Northern and Southern hemispheres which is essential for mapping the Local Bubble. I observed early type stars which are bright at optical wavelengths and so provide a relatively clean continuum against which interstellar features stand out. The aim was to take a large sample of high signal-to-noise measurements of the equivalent widths of strong, highly-diagnostic DIBs (5780, 5797, 6196 and 6614 Å) towards nearby stars in and surrounding the Local Bubble. The DIBs are used to probe the interaction region (the wall of the LB) between the hot gas in the bubble with its cooler surroundings as well as looking for neutral structures located within the bubble itself. Our target stars have well known high proper motions so this survey also offers a first point of reference suitable for a systematic investigation of time-varying interstellar absorption. This will probe the ISM on scales of a dozen au. The observed stars are listed in Table B.1 in Appendix B on the accompanying CD. The distribution of the targets is shown in Figure 3.2.

There are four sizes of symbol on the map. The largest symbol represents targets that are within 50 parsecs of the Sun; the next size down represents targets that are between 50 and 100 parsecs away; the third size represents targets that are between 100 and 200 parsecs away while the smallest symbol represents targets that are over 200 parsecs away from the Sun. The targets are plotted using their right ascension (RA) and declination (Dec) coordinates. Two large regions of the map and two smaller regions are sparsely populated with targets. The larger regions have an RA of 0–8 hours with Dec below −25° and an RA of 18–24 hours with Dec below −45°. The smaller regions have an RA of 7–13 hours with Dec above −25° and an RA of 8–11 hours with Dec between −26° and −40°. This is a result of losing observing time due

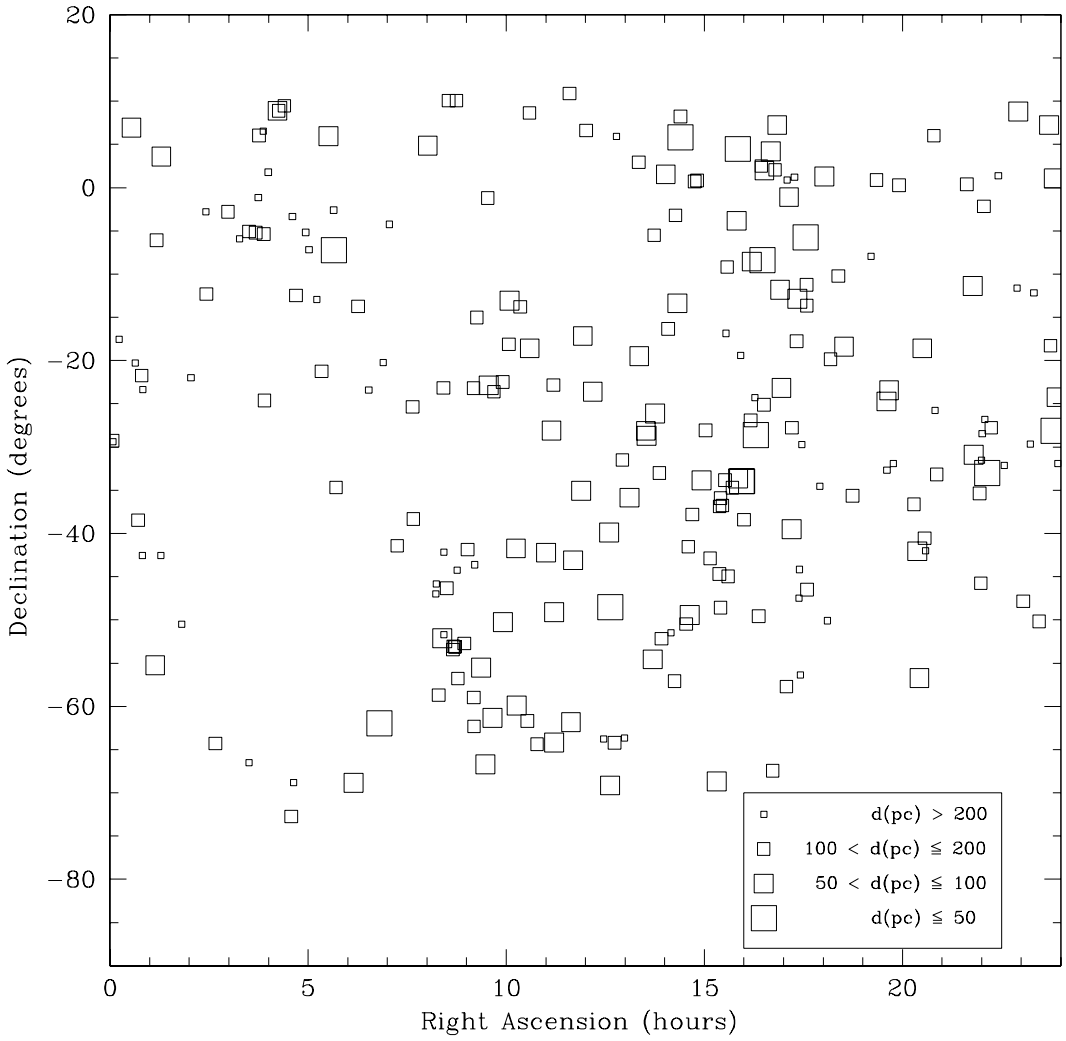

Figure 3.2: Locations of the observed target stars in RA and Dec. Distance is represented by the size of the symbol as given in the legend.

to fog in August 2011 and the restrictions due to cloud coverage and high wind in August 2011 and 2012. The restrictions meant that either part of the sky could not be observed or longer exposure times were needed so fewer targets could be observed during the night. The targets had been chosen to cover the whole sky for the survey and also to overlap with targets at different distances but in similar sight-lines to probe the change along the line-of-sight with distance. Some targets of similar distances were chosen to probe the small scale structure of the ISM in those regions. With the loss of observing time priority was given to choosing targets to populate the sky for the all sky survey over those that might show small scale structure, either with depth or in the same neighbourhood. This was to ensure some view of the whole sky could be obtained and areas of interest, as identified by strong DIB absorption lines, could be marked out for priority observations in the future. A Northern extension to the survey is being carried out at the Isaac Newton Telescope (INT) on La Palma, Canary Islands in a collaboration with the Institute for Research in Fundamental Sciences (IPM) in Tehran, Iran.

3.2 Analysis

In this section correlation plots and maps are presented. The correlations in Section 3.2.1 look at the 5780, 5797, 6196 and 6614 Å DIB strength ratio. The correlations in Section 3.2.2 look at the relationship between the 5780 and 5797 Å DIBs and the Na I D_2 line with some data points of interest being discussed in both sections. The maps presented in Section 3.2.4 show the EW strengths of the DIBs and the sodium line with the distance of the target star in various projections in order to give an overview of the 3 dimensional spatial variations. The maps show the targets plotted in Galactic coordinates, the Galactic plane and meridian plane projections. The maps are described and interesting features highlighted and discussed.

Average profiles of spectral features

Throughout this section reference is made to some of the absorption profiles to illustrate features that help to interpret the data; for example, when comparing spectra along similar sight-lines. When fitting the profile to the spectra the average profile of each absorption line was determined and plotted. Although this is an all sky survey so the spectra are not all in the same direction, averaging the profiles in this way did enhance common features. In particular the average profile of the 5780 Å DIB (see Figure 3.3) showed the successful removal of the stellar feature that sometimes blended with the 5780 Å DIB, justifying the method employed in the profile fitting to account for this source of contamination. This figure also shows the average profile of the 5797 Å DIB. Figure 3.4 shows the average profiles for each of the remaining absorption features: 5850 Å, He, Na I D_2, Na I D_1, 6196 Å, 6203 Å, 6270 Å, 6283 Å and 6614 Å. This shows that the 5850, 6270 and 6283 Å DIBs were not strong enough or detected frequently enough to allow serious consideration of them for this project at the present time and they are not considered further in this work. The average profile of the Na I D lines reveals the overlying shallow dip that was apparent in a large number of cases and again justifies our method of profile fitting to account for this. The profiles of all the spectra are shown in the Spectral Atlas in Appendix C on the accompanying CD.

3.2.1 DIB strengths and band ratios (5780, 5797, 6196, 6614 Å)

The correlation plots shown in this section only plot the data points for which I could be reasonably certain a good detection of the absorption feature has been made. In each case there are sufficient data points for an overall trend to be determined. When comparing these plots note must be taken of the scale of each plot as the weaker DIBs appear at first glance to have much larger error bars than their stronger DIB companions. Although their errors may be larger due to the uncertainly in detecting them because they are so weak they are not so large as to make the detection unreliable. The maps of the Galactic and Meridian Plane projections shown in Section 3.2.4 can be used in conjunction with the descriptions of targets in this Section to give the reader a sense of the location of the targets discussed.

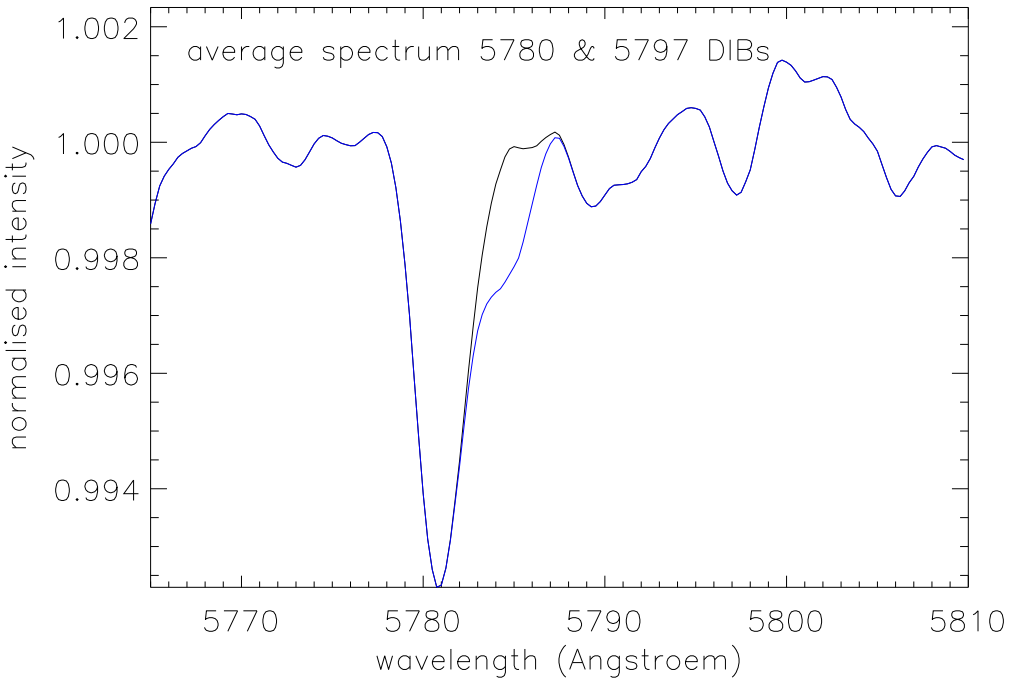

Figure 3.3: The average profile of the 5780 Å DIB showing the blended stellar feature at 5785 Å successfully removed from the DIB profile and also showing the much weaker 5797 Å DIB.

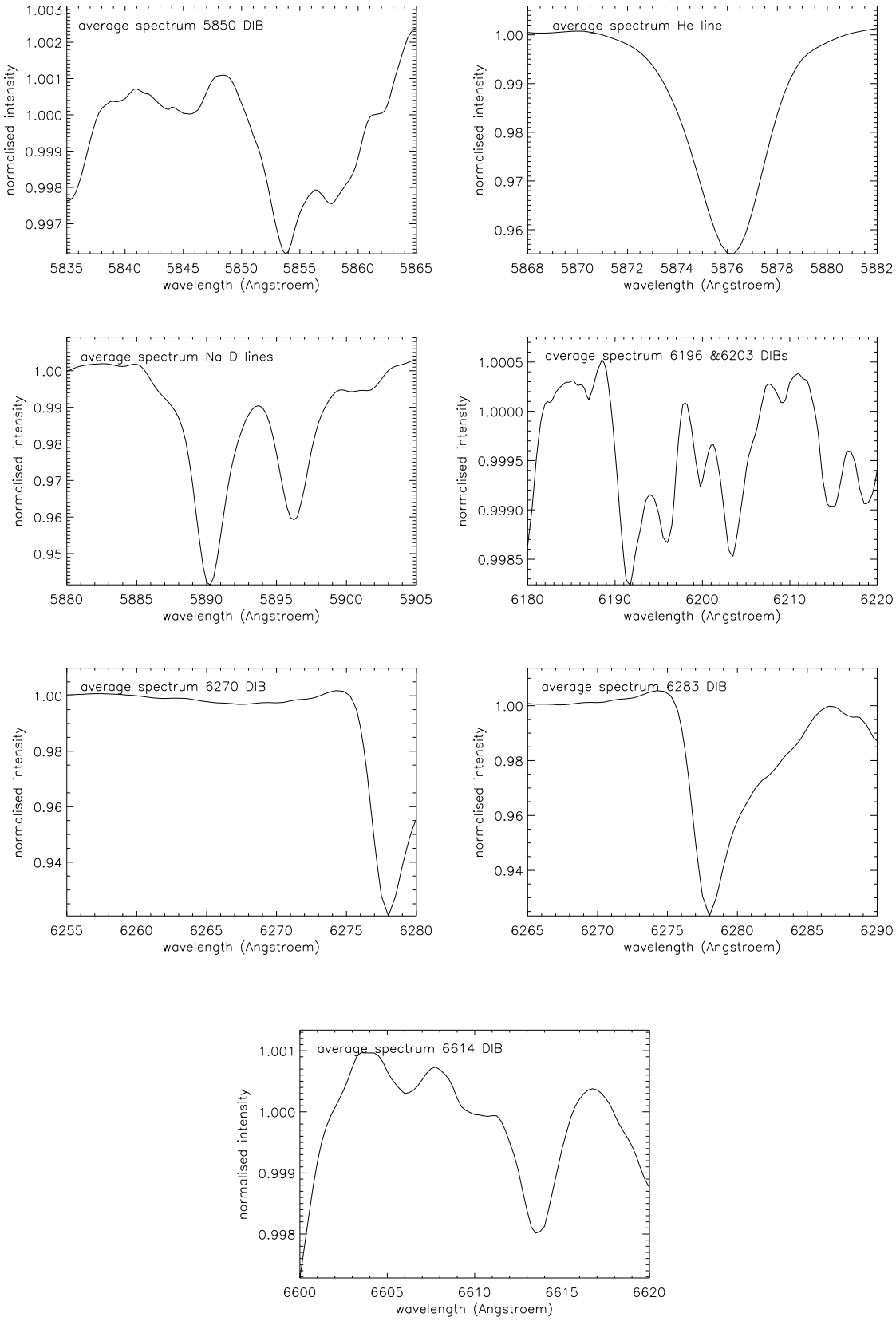

Figure 3.4: The average profiles of the 5850, 6196, 6203, 6270, 6283 and 6614 Å DIBs and the average profiles of the He and Na D lines.

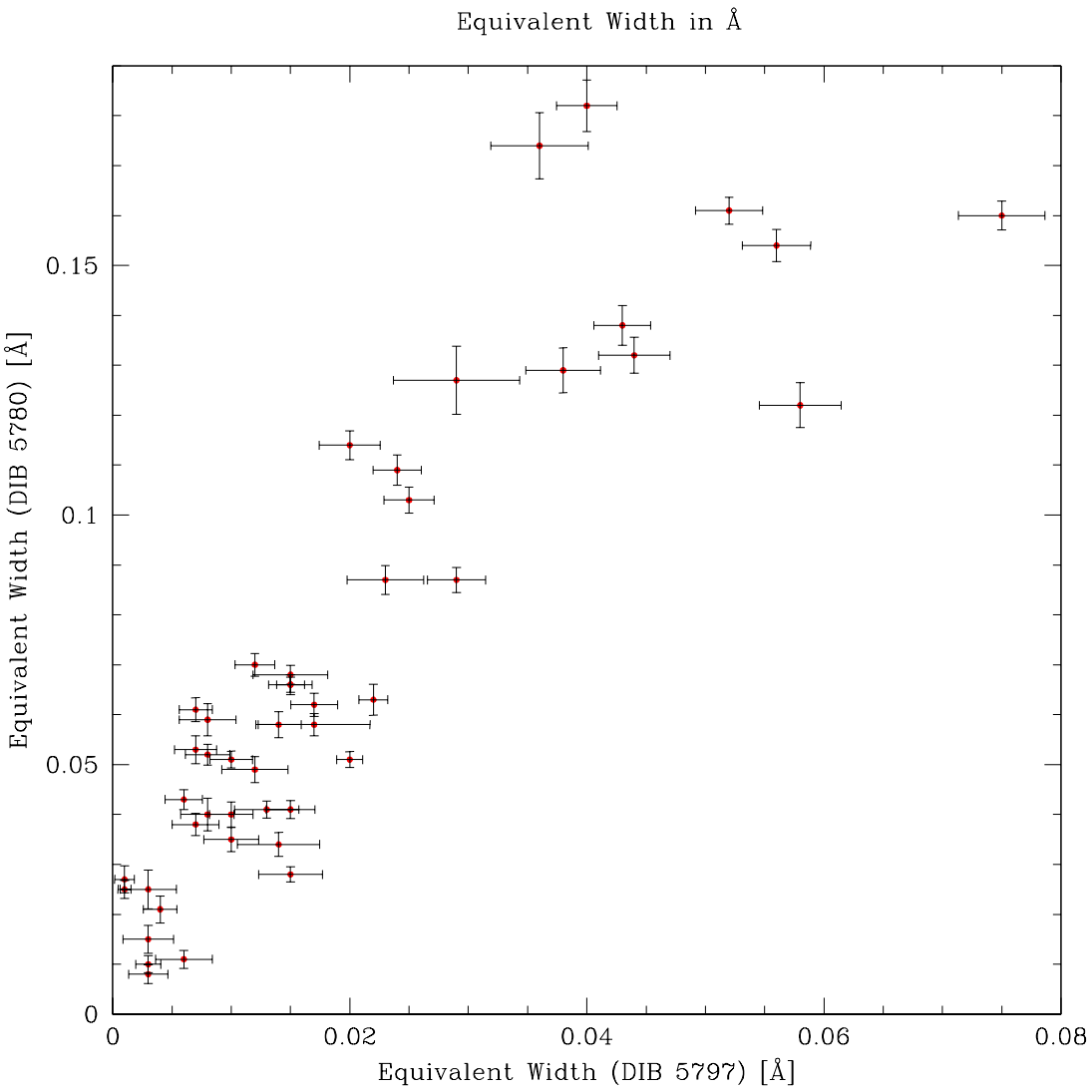

Figure 3.5: Correlation between the equivalent widths of the 5780 and 5797 Å DIBs.

The 5780/5797 Å DIB correlation

Figure 3.5 shows an excellent correlation between the equivalent widths of the 5780 and 5797 Å DIBs. The correlation appears to be tighter at weaker EW values (up to

$\sim$ 0.06 Å for the 5780 Å DIB and up to $\sim$ 0.022 Å for the 5797 Å DIB). At greater strengths there is more scatter but the correlation still appears to hold. However, there does seem to be a threshold above which increasing strength of the 5797 Å DIB is not accompanied by a noticeable increase in the strength of the 5780 Å DIB. This occurs for values above a 5797 Å EW of 0.04 Å. With this data set it cannot be said for certain that this relationship would hold for increasing 5797 Å DIB EW strength but it would not be surprising if this were the case. The 5797 Å DIB does favour a neutral molecular environment, whereas the 5780 Å DIB favours an ionized environment so strong detections of one should not necessarily be accompanied by a strong detection of the other. To investigate this two targets were looked at in more detail (HD146284 and HD169009), both having a similar 5780 Å EW strength but HD169009 having a stronger 5797 Å EW strength (0.058 Å) than HD146284 (0.028 Å). Both are quite near the Galactic Plane, relative to other targets: HD146284 has Galactic coordinates (351°52, 18°72), HD169009 has Galactic coordinates (20°58, 1°62). Target HD146284 is further away from the Sun (at 315 pc) than target HD169009 is (at 102 pc) so it might be expected that HD146284 is outside the LB and therefore should show a stronger 5797 Å EW value than the much nearer target HD169009 which could lie inside the LB. However, HD146284 is also further away from the Galactic Plane, at a distance of 102 pc above the Galactic Plane, than HD169009 is, at a distance of 2.9 pc above the Galactic Plane, where the density of the gas will be less and the environment harsher than it is closer to the Galactic Plane (van Loon et al. 2009), resulting in a weaker EW for the 5797 Å DIB. Figure 3.6 shows the profiles of the 5780 and 5797 Å DIB for these two targets which clearly shows that although these are weak features, they are easily identifiable and clearly show the difference in the strength of the 5797 Å DIB in the two different regions. For comparison Figure 3.6 also shows the profile of HD15004, the spectrum of this target star shows that both the 5780 and 5797 Å DIBs are extremely weak, indicating that there is not much gas in the line of sight to this star. This target has Galactic coordinates (169°61, $-$56°90) and it is at a distance from the Sun of 273 pc, placing it well away from the Galactic Plane. Therefore, although HD15004 is closer to the Sun than HD146284 it is so much further away from the Galactic Plane

(228 pc below the Galactic Plane) that little gas is expected in the region so the weak DIB absorption is not unexpected. Although the 5797 Å DIB is extremely weak in this spectrum I can be confident that this is a DIB detection because of the method of fixing the separation of the 5797 Å DIB from the 5780 Å DIB as described in Section 2.2.1.

The 6196/6614 Å DIB correlation

Figure 3.7 shows the correlation between the EW of the 6196 and 6614 Å DIBs. This particular pair of DIBs is known to have a near perfect correlation (McCall et al. 2010). It is not clear from my data that this is the case but this will be looked at in more detail in Section 3.2.3. Figure 3.7 certainly shows there is a very good correlation but there appears to be a break in the EW values for the 6614 Å DIB with no detection of that DIB with EW between 0.02 and 0.04 Å. Below an EW of 0.02 Å the correlation appears tighter while above 0.04 Å there is more scatter. Are these correlations identifying different environments in the diffuse ISM? Target HD108355 has Galactic coordinates (300°30, −1°04), is 203 pc from the Sun and is 3.65 pc below the Galactic Plane. At that distance from the Sun it could lie within the walls of the bubble and being just 3.65 pc below the Galactic Plane the walls of the bubble there should be relatively thick and so the high EW value of 0.068 Å for the 6614 Å DIB is not unexpected. Target HD159358 has Galactic coordinates (13°86, 11°40), is 123 pc from the Sun and is 24 pc above the Galactic Plane. This places the target in the first quadrant of the Galactic Plane projection map and comparison with the maps in Welsh et al. (2010) shows this target could lie in the interface between the bubble and the walls where the gas density is lower than in the wall of the bubble itself. So the lower EW value for HD159358 is not surprising.

In different sight-lines the 6196/6614 Å ratio is not necessarily the same. Figure 3.8 shows there are sight-lines with different ratios. For HD108355 the EW for the 6196 Å DIB is 0.15 and for the 6614 DIB it is 0.68 giving a ratio of $\sim 1:5$. For HD159358 the EW for the 6196 Å DIB is 0.04 and for the 6614 DIB it is 0.12 giving a ratio of 1:3.

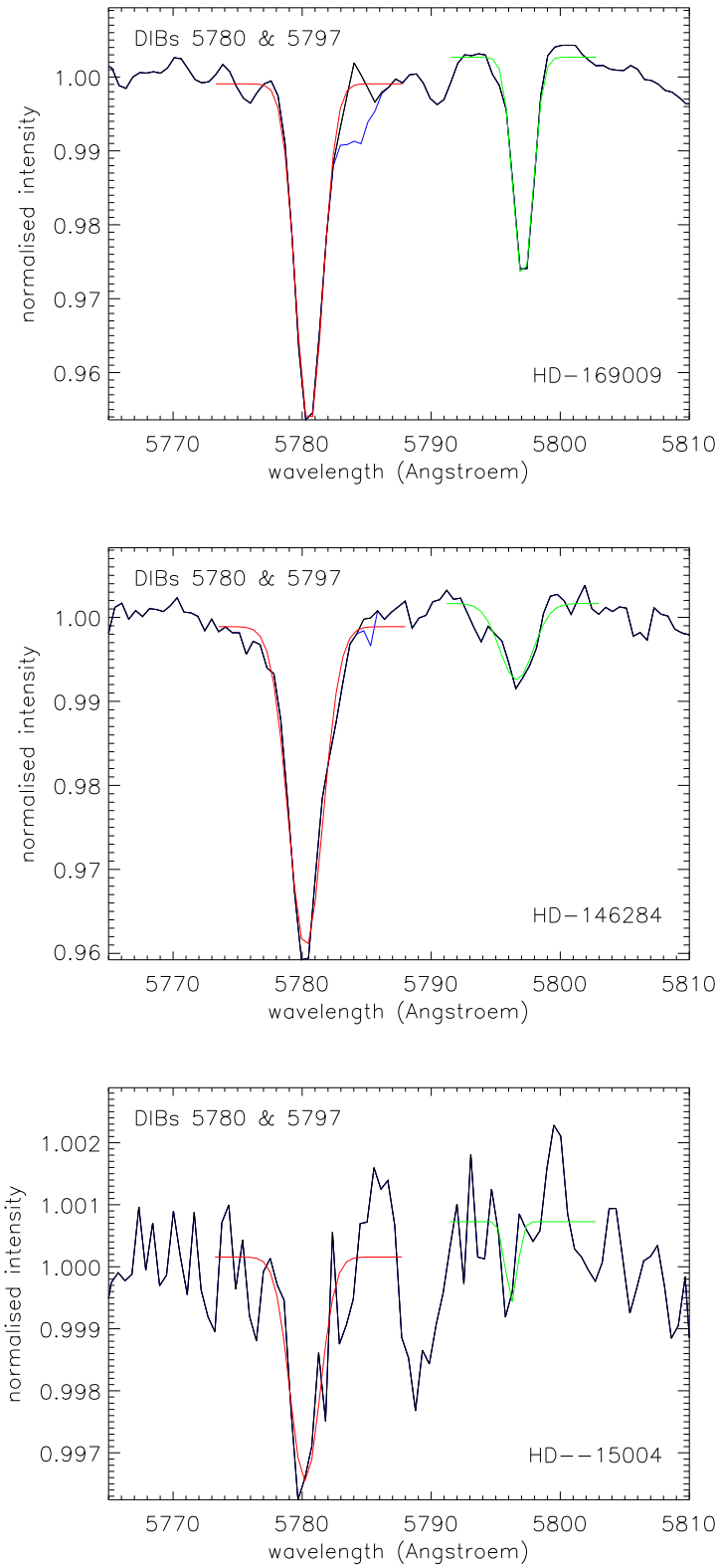

Figure 3.6: Profiles of the 5780 and 5797 Å DIBs, showing that there are progressively larger 5780/5797 ratios as we move away from the Galactic Plane for (Top:) HD169009; located 2.9 pc above the Galactic Plane, (Middle:) HD146284; located 102 pc above the Galactic Plane and (Bottom:) HD15004; located 228 pc below the Galactic Plane.

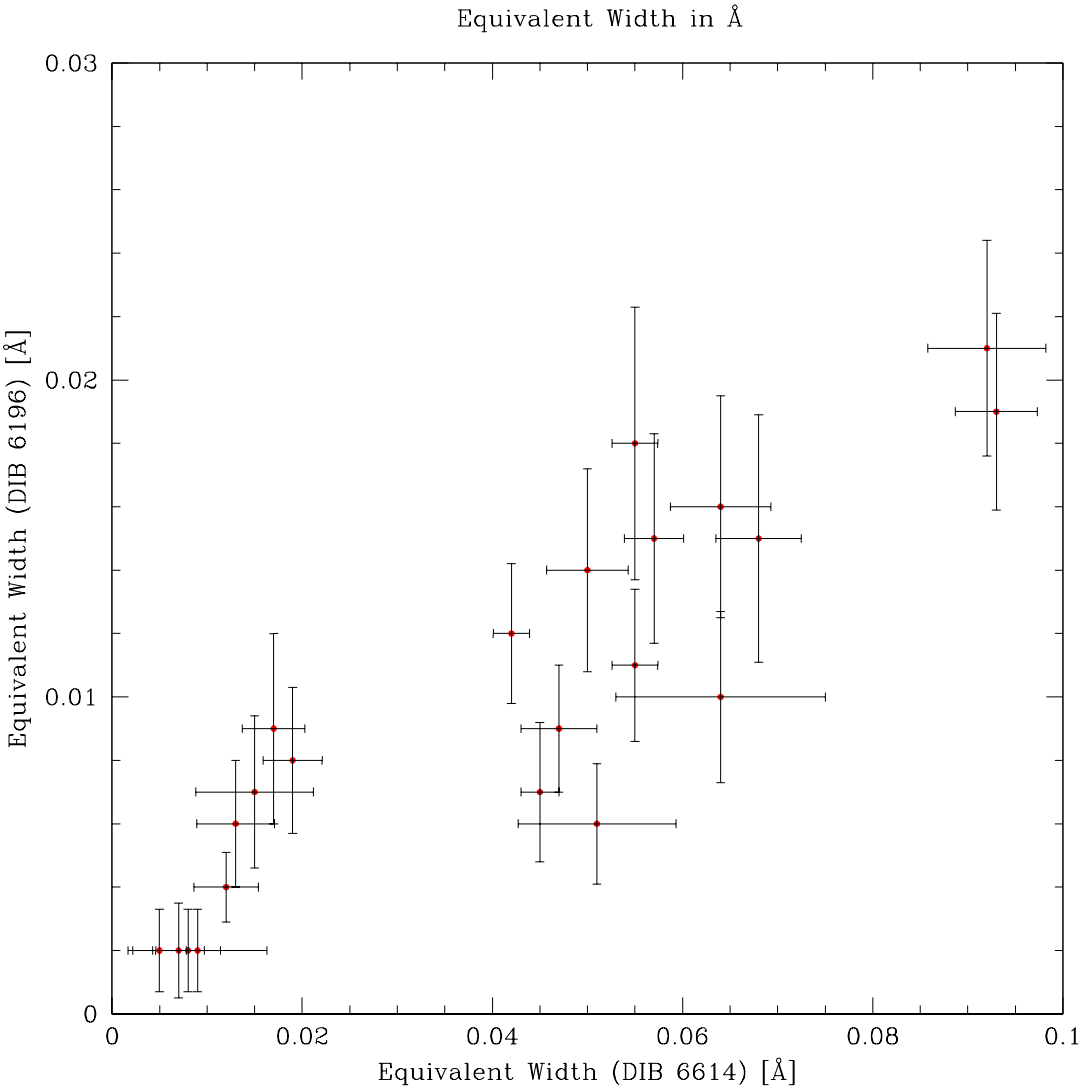

Figure 3.7: Correlation between the equivalent widths of the 6196 and 6614 Å DIBs.

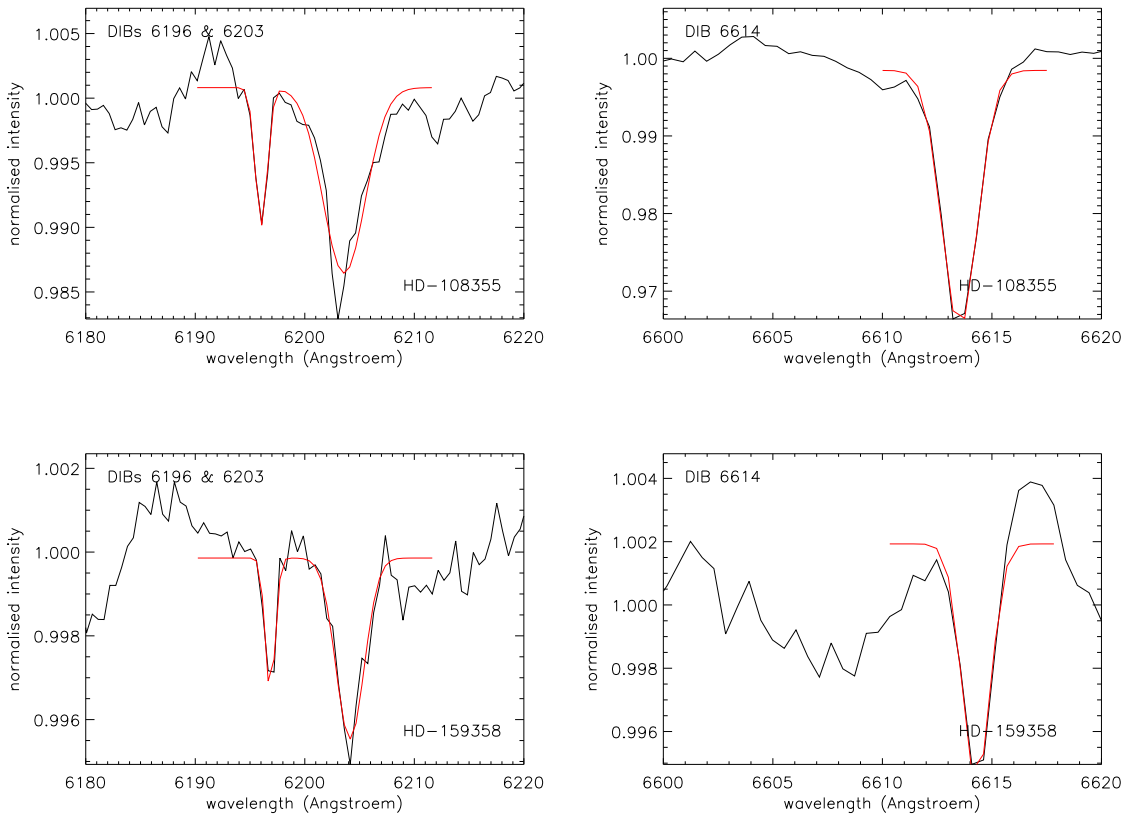

Figure 3.8: Profiles of the 6196 and 6614 Å DIBs for (Top:) HD108355 (distance from the Sun, 203 pc, distance from the Galactic Plane 4 pc), and (Bottom:) HD159358 (distance from the Sun, 123 pc, distance from the Galactic Plane 24 pc) showing the reduction in DIB strength with target star location. The 6196/6614 Å EW ratio for HD108355 is $\sim 1:5$ and for HD159358 it is $\sim 1:3$

It seems that within the LB cavity the closer to the Sun and the further away from the Galactic Plane the target is, the lower the DIB strength is. Figure 3.8 shows the profiles of the 6916 and 6614 Å DIB for these two targets. The 6203 Å DIB is also shown in the plot for the 6916 Å DIB profile although this DIB is not being discussed in this thesis it does help with identifying the weakest 6196 Å DIBs; as explained in Section 2.2.1 the central wavelengths of the DIBs were fixed to the stronger 5797 DIB in order to help with DIB identification. It also seems to correlate quite well with the 6196 Å DIB based on these examples.

The 5797 and 5780 Å DIB correlations with the 6614 Å DIB

During early inspection of the data it was noted that the 6614 Å DIB may correlate well with the 5797 Å DIB. Figure 3.9 shows two sight-lines where the spectra have been superimposed for the regions around the 5780, 5797 and 6614 Å DIBs. These targets are in different directions so the observation is not dependent on targets being in the same or very similar sight-lines. HD18650 has Galactic coordinates (8°26, −24°82), and HD179406 has Galactic coordinates (28°22, −8°29). On Figure 3.9 it can be seen that 5780/5797 Å DIB ratio differs slightly and so implies a difference in the environment in which the two targets lie. Comparing the relative strengths of each DIB in the two targets and it appears the 6614 Å DIB shows a similar change in intensity to the 5797 Å DIB. In order to see if there was a correlation evident the EW of the 5797 Å DIB was plotted against the EW of the 6614 Å DIB (see the top panel in Figure 3.10) and, indeed, this correlation appears to hold. To check the relationship with the 5780 Å DIB, the EW of that DIB was also plotted against the EW of the 6614 Å DIB (see the bottom panel in Figure 3.10). Although there is also a correlation evident the correlation between the 5797 and 6614 Å DIBs appears better.

As the correlation between the 6196 and 6614 Å DIBs is known to be so good and there is also a good correlation between the 5870 and 5797 Å DIBs the correlation plots for the 5780 and 5797 Å DIBs with the 6196 Å DIB were also plotted (see Figure 3.11). Unsurprisingly, because of the relationships between the 5780 and 5797 Å DIBs and the 6196 and 6614 Å DIBs, these plots also show good correlations with the 5797 Å DIB having the better correlation with the 6196 Å DIB.

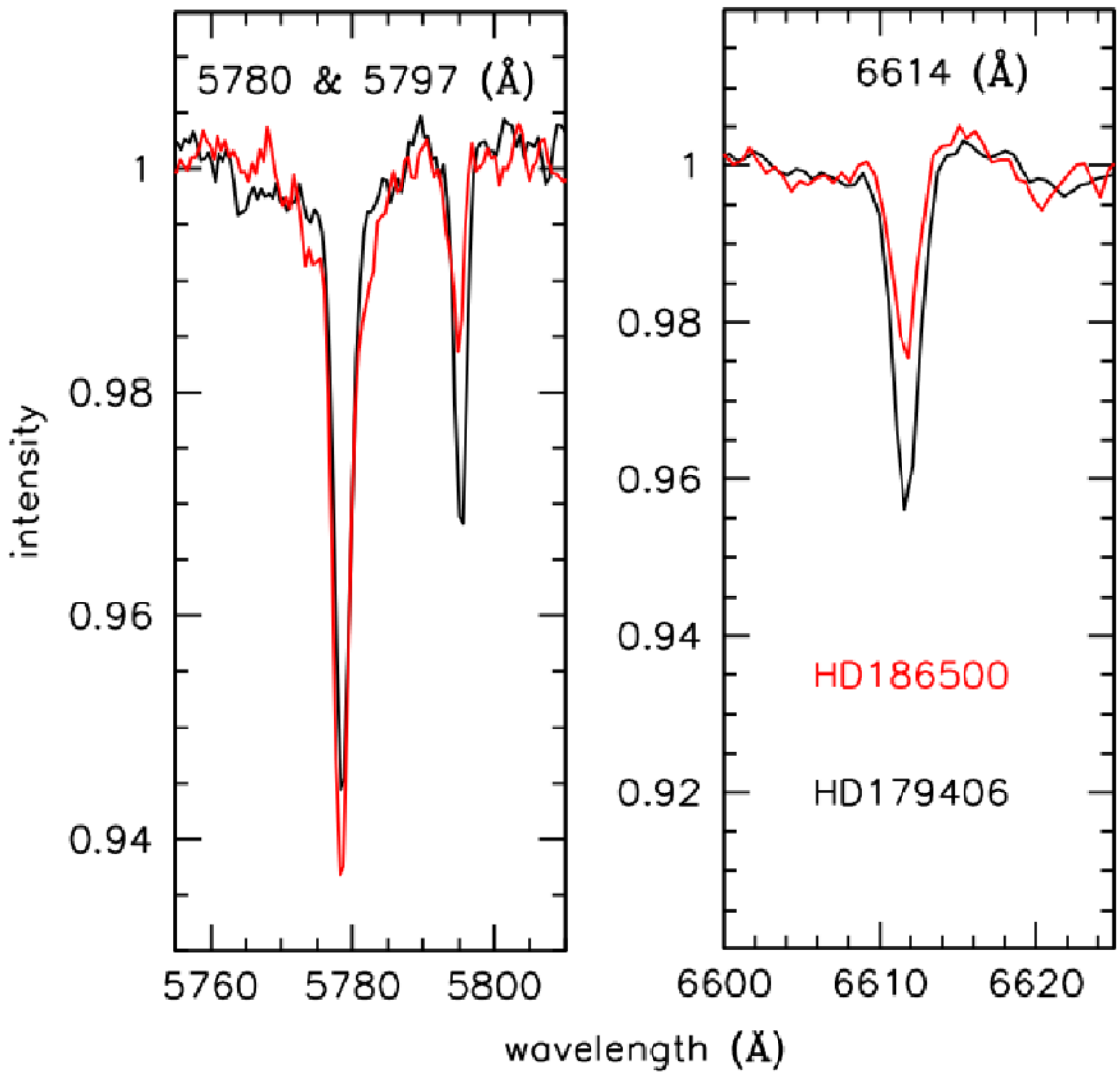

Figure 3.9: Spectra of HD186500 and HD179406 showing that the 6614 Å DIB may correlate well with the 5797 Å DIB.

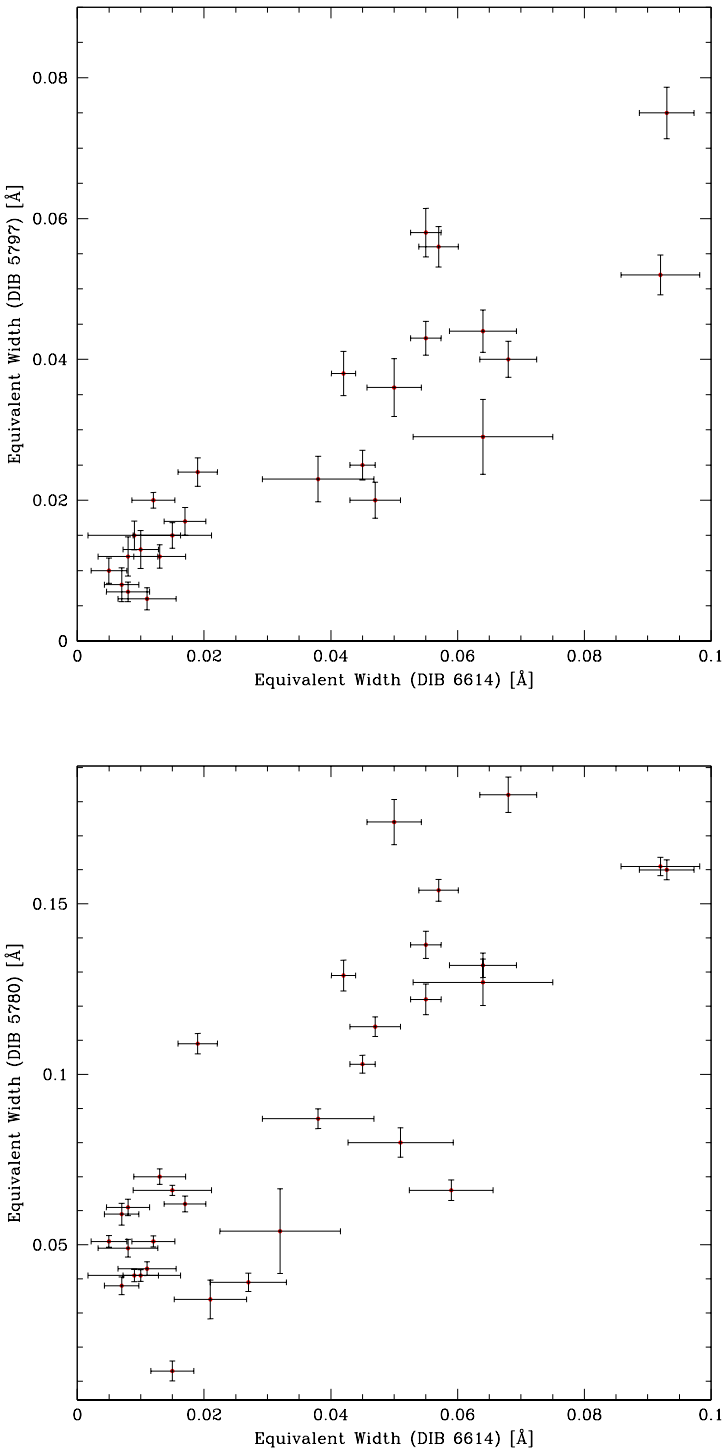

Figure 3.10: Correlation between the equivalent widths of the (Top:) 5797 and 6614 Å DIBs and (Bottom:) 5780 and 6614 Å DIBs.

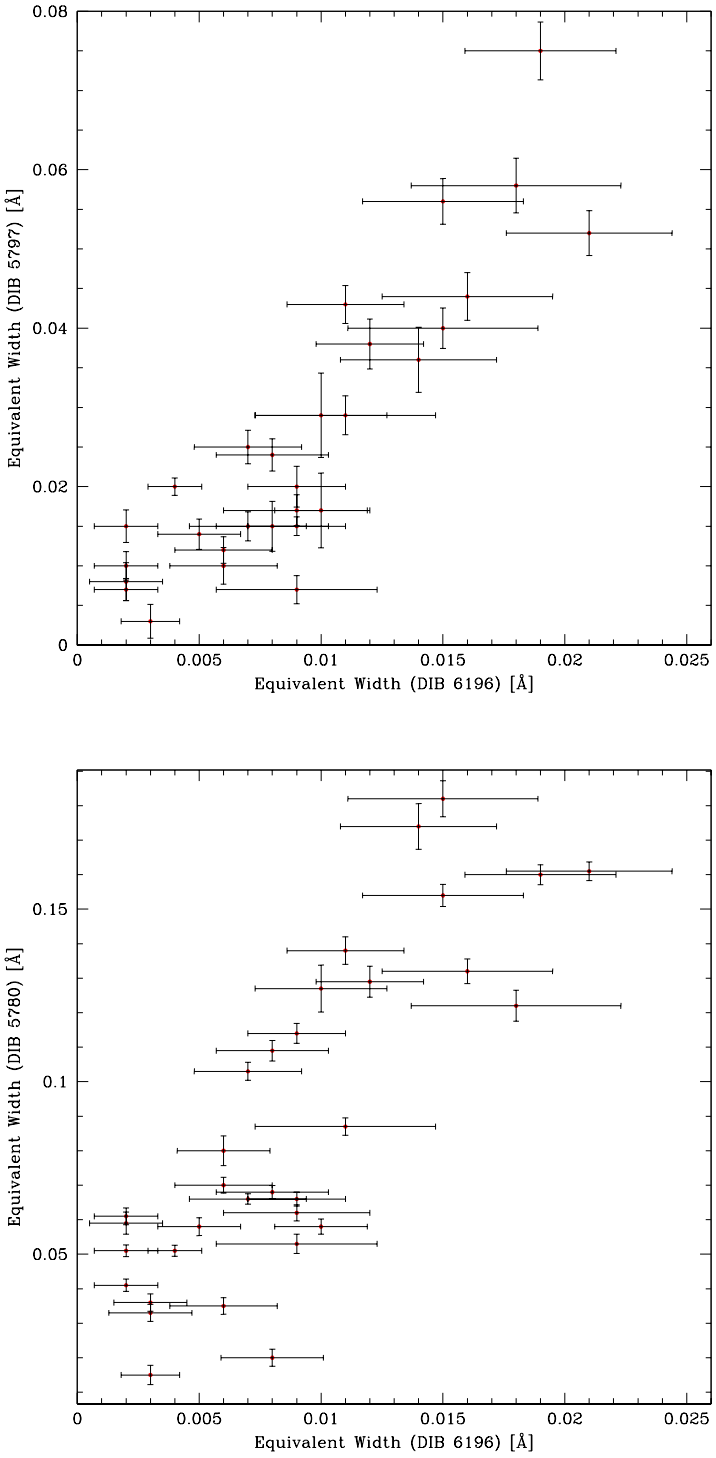

Figure 3.11: Correlation between the equivalent widths of the (Top:) 5797 and 6196 Å DIBs and (Bottom:) 5780 and 6196 Å DIBs.

3.2.2 The neutral sodium D line

The correlation plots shown in this Section are similar to those in the preceding Section and only plot the data points for which I can be reasonably certain a good detection of the absorption feature has been made.

Figure 3.12 shows the correlation of the 5780 Å DIB with the Na D_2 line and the 5797 Å DIB with the Na D_2 line. One difference to note is that the 5780 Å DIB is detected at Na D_2 EW levels of just 0.04 Å whereas Na D_2 EW levels of ~ 0.11 Å are needed for the 5797 Å DIB to be detected. This is a clear indication that the carrier of the 5797 Å DIB needs a greater density of the neutral molecular material as traced by the Na D_2 line to survive than the 5780 Å DIB does. Although, the 5780 Å DIB is not detected below Na D_2 EW levels of 0.04 Å it appears that the 5780 Å DIB carrier may need some of the molecular material present to survive. Both plots show that at Na D_2 EW levels of greater than 0.2 Å there is a rapid increase of DIB EW strength with respect to an increase in the Na D_2 EW strength. That is, as far as my data is concerned. I am looking at a harsh and diffuse region of the local ISM and at greater densities of molecular material the behaviour of the two DIBs is likely to become more diverse as the 5780 Å DIB is known to favour an ionized environment whereas the 5797 Å DIB favours a molecular environment. What is interesting about these plots is that there appears to be a common point of Na D_2 EW strength in the diffuse Local Interstellar Medium (LISM) which favours an increase in EW strength of both DIBs.

Another striking feature of the correlation plots in Figure 3.12 is the huge scatter that is seen. This means that sodium is not a very good indicator of DIB carrier abundance. This is also seen in the maps described in Section 3.2.4 and discussed there. The reason for this is partly due to the ionization potential of Na D; neutral sodium will trace weakly ionized gas as well as neutral gas. Therefore, it is not a very good discriminator between the two types of environment. DIBs, on the other hand, do discriminate between the two environments with 5780 Å DIB favouring the weakly ionized gas and the 5797 Å DIB favouring the neutral gas. Hence, DIBs are a more discerning probe of the environment and give a more detailed picture of harsh environments than Na D can.

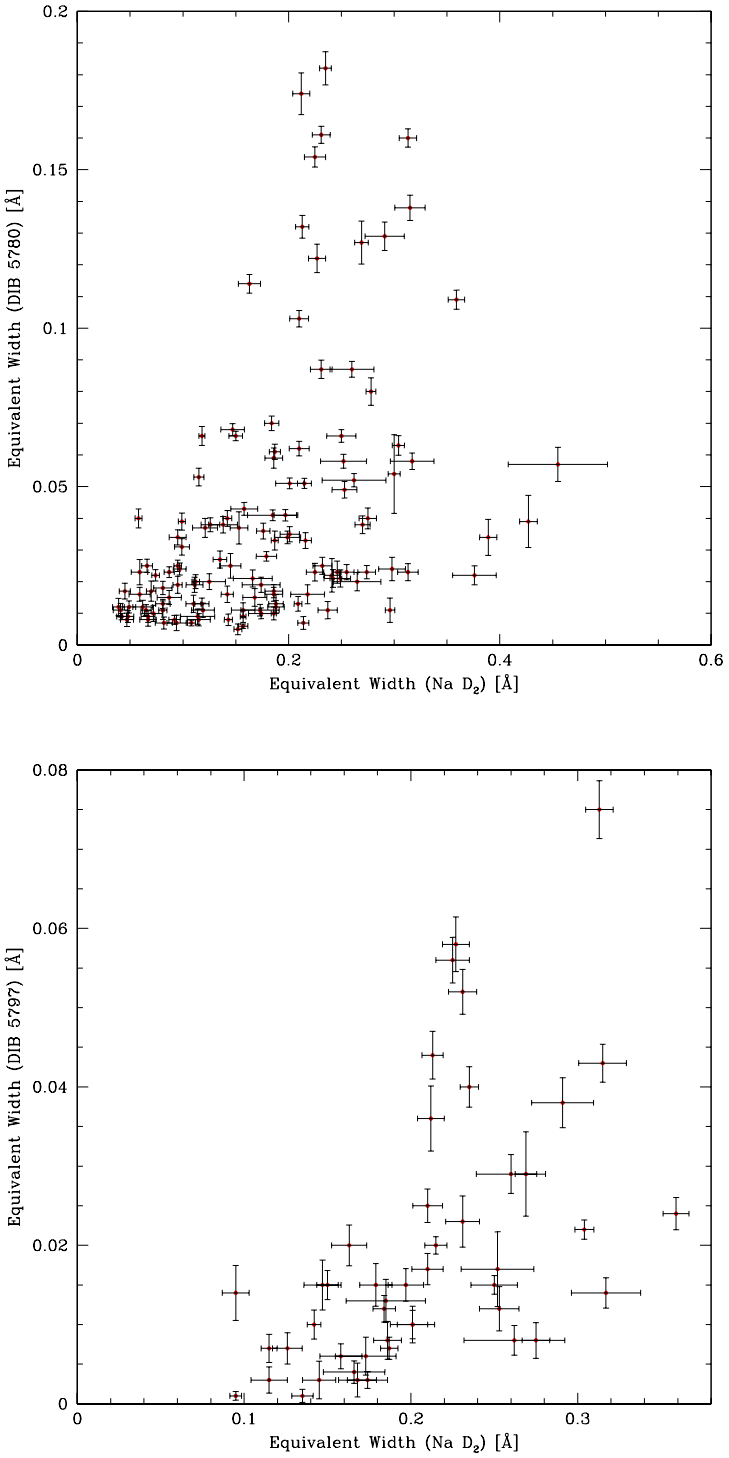

Figure 3.12: Correlation between the equivalent widths of the (Top:) 5780 Å DIB and the Na D_2 line and (Bottom:) 5797 Å DIBs and the Na D_2 line.

The majority of the Na D doublet profiles are well detected in the spectra. However they nearly all show a shallow broad absorption feature overlying the Na doublet. This was subtracted from the sodium absorption line so that the EW measurements of the Na D lines were as accurate as possible. The procedure followed to do this is described in Section 2.2.1. Some of the spectra which have a deeper overlying broad features also show that the Na D lines themselves are broadened. In the extreme cases the broadening is so great and the overlying feature so deep that the two Na lines are indistinguishable (see Figure 3.13 for typical profiles. This feature is more than likely due to well-known telluric contamination caused by terrestrial water-vapour absorption. Figure 3.14 shows the telluric lines due to water-vapour in the 5930 Å region, the red line shows the spectrum when the full width half maximum (FWHM) of the absorption feature is 1.5 Å, the blue line shows the spectrum when the FWHM of the absorption feature is 3.5 Å. The variation in strength of this feature will be due to the variation in atmospheric conditions during the observing runs and the varying distances from the zenith of the target stars. Target stars nearer the zenith will have been observed through less atmosphere than those further from the zenith and so will be subject to less telluric contamination.

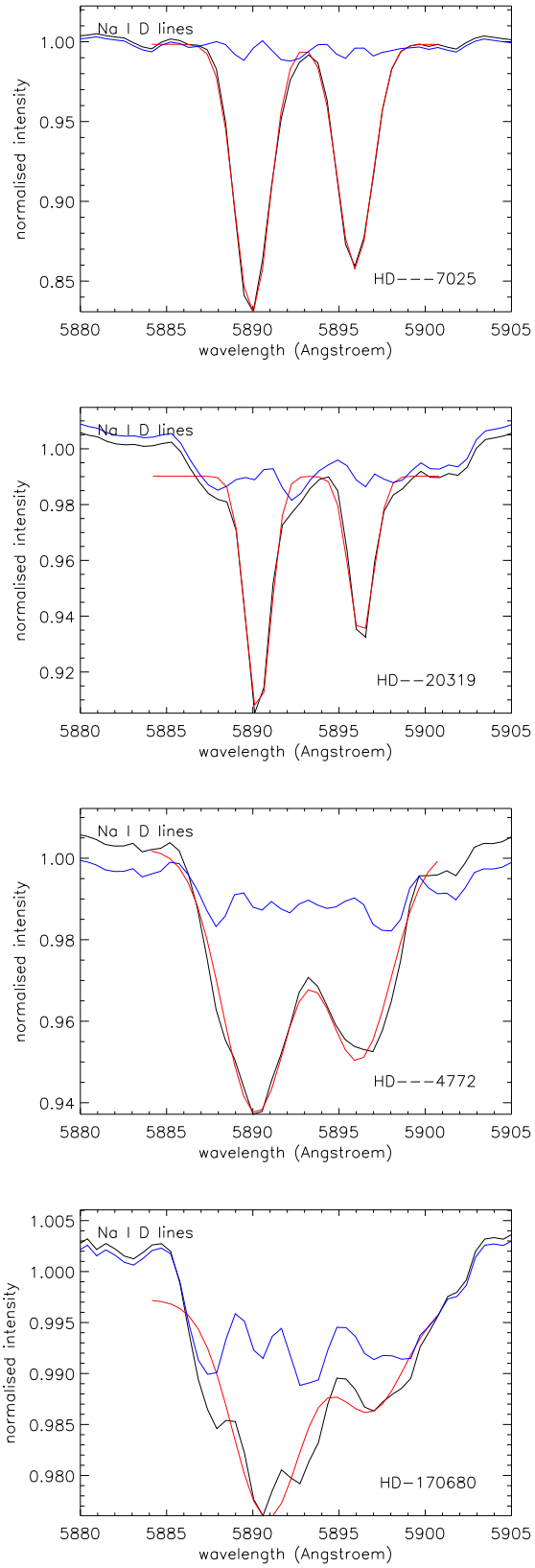

Figure 3.13: Profiles of the Na D lines showing the typical different profiles of the overlying broad absorption feature (blue) and the fitted Na D line profiles (red).

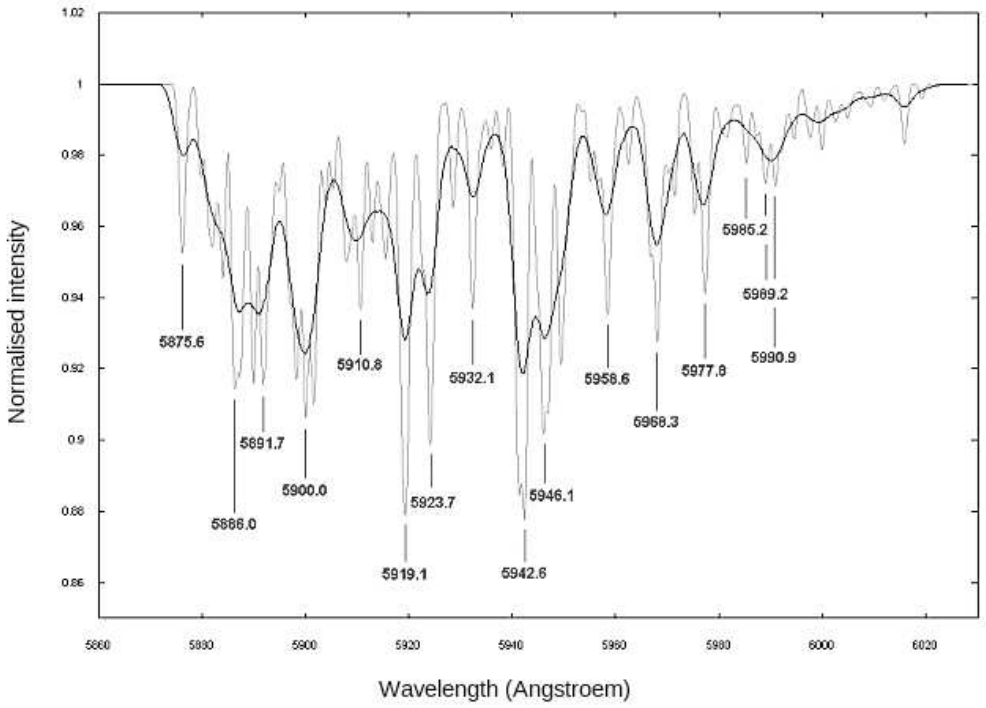

Figure 3.14: Identification of telluric lines in the 5930 Å region (taken from http://www.astrosurf.com/buil/us/spectro11/specalib.htm on 11 April 2014).

3.2.3 Correlations; probing the Local Bubble - surrounding ISM interface

Linear regression is a statistical technique that is used for analysing the relationship between two variables. Such a relationship is best described by a straight line giving the best estimate of the observed trend shown in a scatter plot such as those shown in Section 3.2.1. The correlation coefficient is a measure of how well the data fit the line, with a value of 1 representing a perfect fit and values approaching zero representing progressively worse fits. Other values used in this statistical analysis are the slope, which is the value of the fitting line to the data and the constant, which is where the fitting line (slope) intercepts the y-axis. To calculate these values the IDL function REGRESS was used.

Table 3.1 lists the calculated correlation values between 5780 and 5797 Å and also 6196 and 6614 Å DIBs, the statistical *t*-test values are also given. For both pairs of DIBs the correlation coefficient was calculated for all data for which I was certain I had a DIB detection and also for different areas of the plots that may show different correlation coefficients, again only for data for which I was certain of DIB detections as noted in Section 3.2.1. It is interesting to note that for the 5780/5797 Å DIB correlation it is actually worse for strong 5797 Å DIBs that have EW values ≥ 0.04 Å. The correlation coefficient is actually half the value of the coefficient when all data points are considered, yet the constant value is much greater at 0.111 $\pm$0.041 as opposed to 0.023 $\pm$0.005when all data are considered. This indicates the 5780 Å DIB must be present when some strong 5797 Å DIBs are absent. Yet at EW values for weak 5797 Å DIBs (<0.04 Å) the constant is much nearer zero at 0.008 $\pm$0.005 , indicating that the weak DIBs could co-exist. For the 6196/6614 Å DIBs the constant for all three calculations are close to one another and very close to zero, indicating that these DIBs could co-exist. Although for increasing values of the 6614 Å DIB Table 3.1 shows the coefficient is worse than for all data points at 0.733 as opposed to 0.866. The best correlation figure, 0.949, occurs for EW values for the 6614 Å DIB (≤ 0.02 Å). To test the significance of these

correlations figures, Student's t-test was used (Barlow 1989):

$$t = r\sqrt{\frac{\mathrm{N}-2}{1-r^2}}$$

where r is the coefficient and N the number in the sample. The critical values of t where taken from table 7.2 on p 137 of Barlow (1989) and correspond to a 99% confidence level for a two tailed test. Where t values are greater than the critical value the correlations can be taken as significant. From Table 3.1, it can be seen that for weak 5797 Å DIBs (<0.04 Å) the error on the slope is the same order of magnitude as the value for the slope itself and that its t value is less that the critical value, therefore no conclusions can be drawn from this subset of data. However, this is a very small subset of the data. The t values for the other 5780/5797 Å DIB correlations are greater than their corresponding critical values, therefore the weak 5780 and 5797 Å DIBs could co-exist as suggested. A greater number of observations would be needed in order to confirm the relationship of these DIBs when the 5797,Å DIB has an EW $\geq$ 0.04 Å. For the 6196/6614 Å DIBs the t values are greater than the critical values in all cases so although the errors are generally reasonable for this correlation, the results can not be considered significant and no conclusions should be drawn from the results. Again these results are from a small subset of the data and a greater number of observations are needed to check if there is a significant correlation between the 6196 and 6614 Å DIBs.

Tight correlations between DIBs have been looked for to try and find DIBs which may share a common molecular carrier. To date just one pair of DIBs have exhibited a near perfect correlation, that is, between the 6196 and 6614 Å DIBs (McCall et al. 2010). In the scatter plots in Figures 3.5 and 3.7 it was noted that different areas of the plots may show different correlation coefficients.

McCall et al. (2010) sampled 114 diffuse cloud sight-lines across a wide range of interstellar environments including sight-lines dominated by atomic hydrogen and determined a 6196/6614 Å DIB correlation coefficient of 0.986, although they did not confirm the two DIBs were due to transitions of the same molecular carrier. As seen in Figure 3.7 in Section 3.2.1 and Table 3.1 here, there does not appear to be such a

Table 3.1: Values of the correlation calculations between the 5780 and 5797 Å, and the 6196 and 6614 Å DIBs; also showing the *t*-test values and the corresponding critical values of *t*.

5780/5797 Å	All points	5797 Å <0.04 Å	5797 Å ≥ 0.04 Å
Slope	2.479 ±0.195	3.650 ±0.811	0.612 ±0.620
Constant Å	0.023 ±0.005	0.008 ±0.005	0.111 ±0.041
Coefficient (r)	0.884	0.901	0.442
t-test	12.54	12.46	1.10
critical value of t	2.58	2.58	4.03
6196/6614 Å	All points	6614 Å ≤ 0.02 Å	6614 Å ≥ 0.04 Å
Slope	0.189 ±0.022	0.571 ±0.072	0.209 ±0.058
Constant Å	0.002 ±0.000	-0.002 ±0.002	0 .001±0.001
Coefficient (r)	0.886	0.949	0.733
t-test	2.70	3.01	1.08
Critical value of t	9.93	9.93	9.93

strong correlation, in my data. The correlation coefficient I determined from my data for this DIB pairing is 0.886. I noted an apparent break between EW values of 0.2 and 0.4 Å for the 6614 Å DIB in which there appeared to be no absorption. Therefore, I looked at the correlation coefficients for EW values of the 6614 Å DIB below 0.02 Å and above 0.4 Å. The results are listed in Table 3.1

Table 3.2 lists the calculated correlation values between 5797 and 6614 Å, 5780 and 6614 Å, 5797 and 6196 Å and also 5780 and 6196 Å DIBs. This table shows that the 5797 Å DIB does correlate a lot better with the 6196 and 6614 Å DIBS than the 5780 Å DIB does. On the basis of the figures in this table it would seem the 5797/6196 Å DIB pair behaves in a similar way to the 6196/6614 Å DIB pair when all data points are considered. Both have a constant value very close to zero indicating that the DIBs in each pair are co-existent.

Table 3.2: Values of the correlation calculations between the 5797 and 6614 Å, 5780 and 6614 Å, 5797 and 6196 Å and also 5780 and 6196 Å DIBs; also showing the *t*-test values and the corresponding critical values of *t*.

	Slope	Constant Å	Coefficient (r)	*t*-test	Critical value of t
5797/6614 Å	0.602 ±0.064	0.006 ±0.002	0.892	9.46	2.80
5780/6614 Å	1.537 ±0.188	0.034 ±0.008	0.831	8.18	2.58
5797/6196 Å	3.033 ±0.304	-0.002 ±0.001	0.887	9.98	2.58
5780/6196 Å	7.466 ±0.924	0.022 ±0.009	0.823	8.07	2.58

Figure 5 in the McCall et al. (2010) paper plots the EW for the 6614 Å DIB against the EW for the 6196 Å DIB, whereas, I plot my data the other way around. When comparing both plots I find that where 6614 Å DIB goes to zero, their intercept is about 2 mÅ. My plots are consistent with this if I draw a line through all my data points and that intercept value. However, looking closely at the lowest EW values in my data they do suggest that perhaps both DIBs are zero to start with, or if anything the 6614 Å DIB might appear first and not the other way around as in the McCall et al. (2010) data. Comparing the two data sets, it was seen that in the McCall et al. (2010) paper when the EW for the 6196 Å DIB was about 100 mÅ the EW for the 6614 Å DIB is 400 mÅ. For my data to be consistent with this when the EW for the 6614 Å DIB is 100 mÅ the EW for the 6196 Å DIB would have to be around 25 mÅ. This is very close to what I see but possibly either the 6196 Å DIB is a little weaker or the 6614 Å DIB is a little stronger in my data. I do not have enough data points check this possibility, it is certainly not a large discrepancy but it is an interesting detail.

I also noted in Section 3.2.1 that the 5797 Å DIB appeared to correlate well with the 6614 Å DIB. The correlation coefficients I determined confirmed this. For the 5797/6614 Å correlation I determined the coefficient to be 0.892 and for the 5797/6196 Å correlation the coefficient was 0.887. They are both significant correlations and on a

par with the 5780/5797 Å correlation. For the 5780/6614 Å correlation I determined the coefficient to be 0.831 and for the 5780/6196 Å correlation the coefficient was 0.823. Again both significant correlations but these figures do confirm the conclusion drawn from the plot that the 5797 Å DIB correlates better with the 6196 and 6614 Å DIBs than the 5780 Å DIB does. This conclusion is supported by the reasonable value of the associated errors and the fact that the calculated t values are greater than the critical values of t in all cases. This extremely good correlation has not been remarked upon in the literature before and given the unusual behaviour we see with the 6196/6614 Å correlation in our data the question again arises about the nature of the environment in the LB walls and wall/bubble interface.

Figure 3.15 shows three plots of the Galactic latitude versus the EW of the 5780 Å DIB, the 5797 Å DIB and the Na D_2 line. The top plot shows the Galactic latitude versus EW for the 5780 Å DIB. The distance from the Sun for each target is represented by colour according to the legend in the plot. Surprisingly the plot shows there is no correlation with distance. It does not matter how far away from the Sun the target is, it can be found in any part of the plot. What is very noticeable, however, is the trend for targets with higher EW values to tend towards zero, the Galactic Plane. At low levels of EW the targets are distributed at all Galactic latitudes, it is only at higher EW values that the DIBs appear to be restricted to the Galactic Plane. Thus, it seems the stronger DIBs need a molecular environment in which to survive it is only the weakest DIBs that can survive in the harsh environment of the LB cavity. Noticeably, this plot shows that the weak DIBs can survive well away form the Galactic Plane and reaching towards the Halo. The middle plot in Figure 3.15 shows the same situation for the 5797 Å DIB. As a stand alone plot this would not immediately reveal any pattern in the data. However, having seen the pattern of behaviour for the 5780 Å DIB and it is just possible to pick out a similar trend towards the Galactic Plane at the higher values of the DIB EWs and the same spread throughout the whole range of Galactic Latitude for the weakest of the DIBs.

Contrasting to the DIB plots, the plot for the Galactic latitude versus the EW Na D_2 line shows no pattern whatsoever, it is a completely random set of data points.

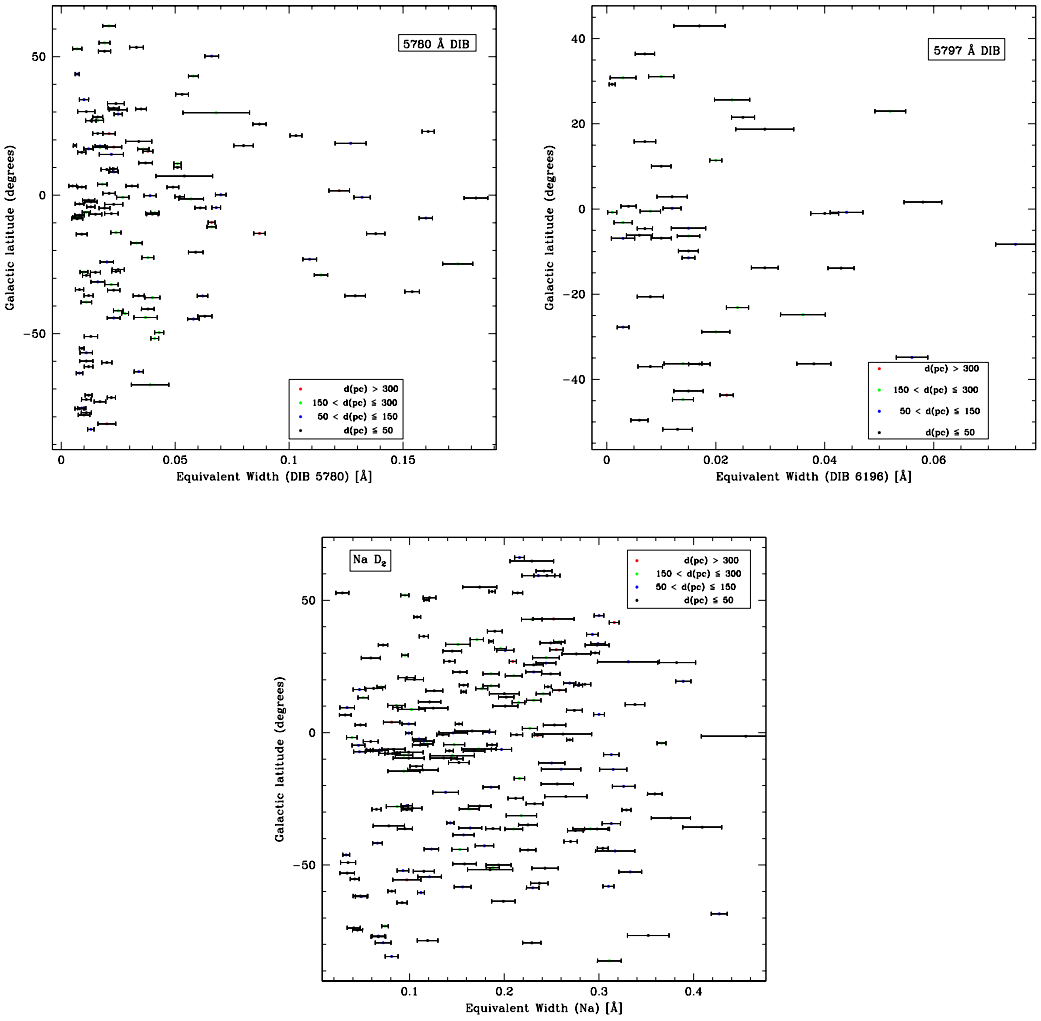

Figure 3.15: Plots of the Galactic latitude v EW for (Top:) the 5780 Å DIB, (Middle:) the 5797 Å DIB and (Bottom:) the Na D_2 line.

Therefore, there must be at least some neutral sodium present throughout most of the regions probed by this survey and because of its ionization potential the neutral sodium will trace weakly ionized gas as well as neutral gas and this is what is evident in this plot. The DIBs however, seem to be more particular as they clearly discriminate between the different environments. The plots in Figure 3.15 show that the 5780 and 5797 Å DIBs do, indeed, trace the LISM in more detail that the neutral sodium can.

3.2.4 All-sky maps of the neutral ISM in and around the Local Bubble

The maps presented in this section give an impression of the intensity of the EW absorption and the location of the target stars. The general colour code is the same for all maps; the darker the colour the more absorption there is. The legend in each map states the absorption levels represented by colour for that map. The size of the symbol (defined in the legend) represents distance, either from the Sun, the Galactic Plane or the Meridian Plane depending on the projection of the map. For the Galactic and Meridian Plane projections the sight-lines for which no reliable absorption measurements could be determined are also plotted in blue with the size of symbol representing distance. For the maps in the Galactic and Meridian Plane projection the shape of the symbol also denotes whether the target is above or below the Plane in question.

In this way these maps give a four dimensional picture of the LB: two dimensions representing position, one dimension representing distance into or out of the plane and the last dimension representing the absorption strength of the DIBs or sodium lines being plotted.

The locations of the target stars in Galactic coordinates

The maps in Figure 3.16 show the EW strength of the the 5780 Å DIB, the 5797 Å DIB and the Na I D_2 absorption. These maps are presented in Galactic coordinates with the Galactic latitude of zero marking the Galactic Plane. For the 5780 Å and 5797 Å DIB maps the strength of the absorption is shown by the same colour scale as

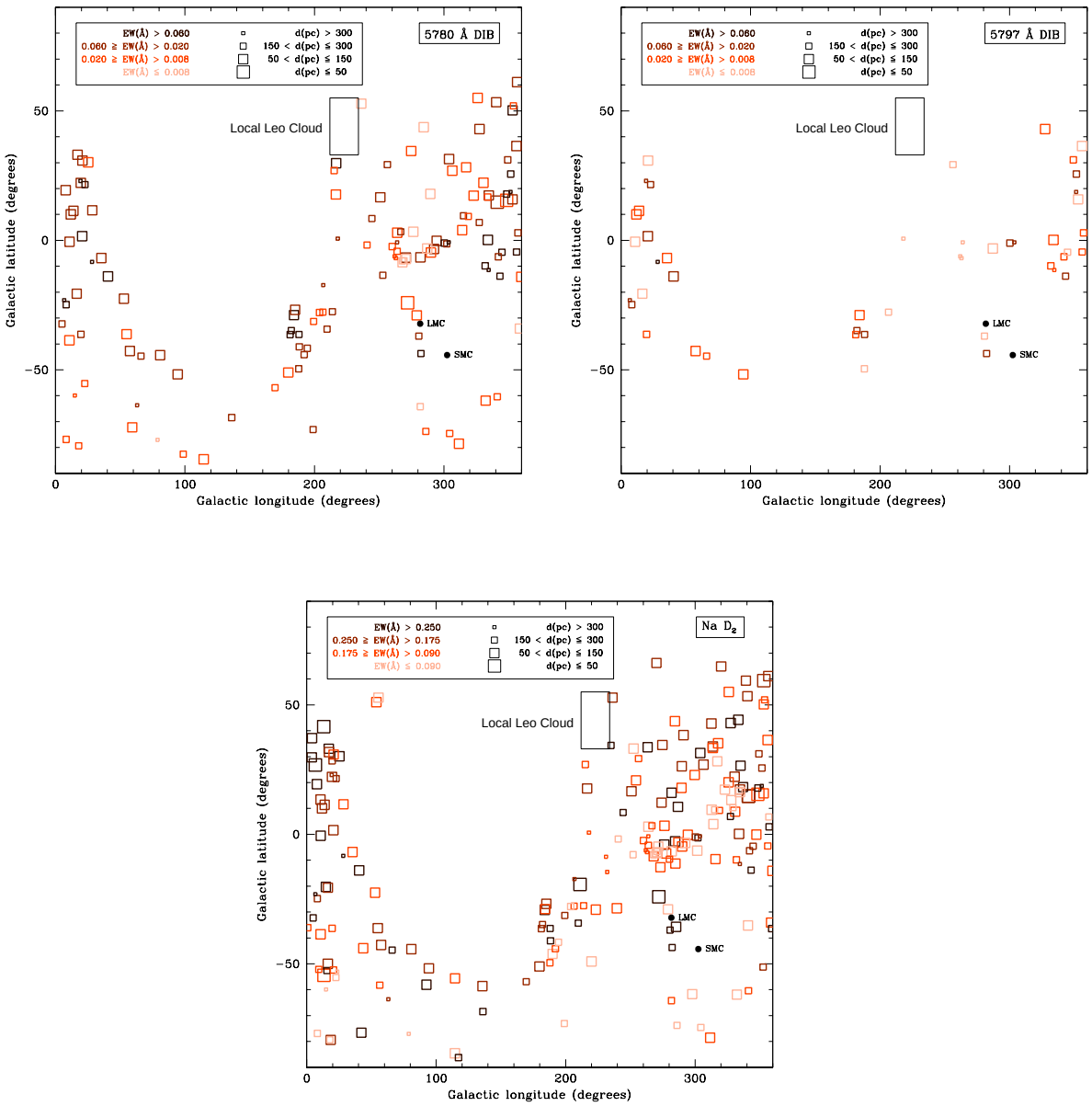

Figure 3.16: EW maps in Galactic coordinates of (Top Left:) the 5780 Å DIB absorption, (Top right:) the 5797 Å DIB absorption and (Bottom:) the Na I D_2 absorption.

given in the legends, for the Na I D_2 map the colours represent a different range of absorption values, this is in order to bring out the variation of the Na I D_2 absorption which is much stronger than either of the DIBs. There is a large area where no points are plotted, this is most clearly seen in the Na I D_2 map. The reason for this is, it is an all-sky survey but I was observing from the Southern Hemisphere and not all of the Galactic Plane is visible from the La Silla Observatory. My colleagues in Tehran are complementing these results with observations of the Northern Hemisphere from La Palma with the Isaac Newton Telescope (INT). On these maps the locations of the LMC and SMC are marked. The observations towards both of the Magellanic Clouds described in Chapter 4 complement the observations described here. None of the targets for this Project actually coincided with the location of either galaxy. Also marked on the map is the approximate location of the Local Leo Cold Cloud (LLCC). The LLCC is a nearby very cold cloud (T $\sim$ 20 K) between 11.3 pc and 24.3 pc away. Hence, it is well within the the cavity of the LB and it is the closest known cold neutral gas cloud (Peek et al. 2011; Meyer et al. 2012). Unfortunately few targets in this survey were successfully observed in that region. However, my colleagues in Tehran have obtained data in this region.

These maps indicate that the highest absorption levels are concentrated near the Galactic Plane; the 5780 Å map showing this for targets within $\pm 25^\circ$ of the Galactic Plane but there are some interesting exceptions to this. There is a cluster of targets with a strong 5780 Å DIB absorption at a Galactic longitude of $\sim 190^\circ$ and a Galactic latitude of between -25° and -40°. Similar strong absorption is seen in the same region in the 5797 Å DIB and the Na I D_2 maps. This must be tracing a neutral cloud, or part of the Bubble Wall that is away from the Galactic Plane.

The area around the LLCC is tantalising; in the 5780 Å DIB map there are two targets with strong DIB absorption to the South of the cloud and one with much lower absorption to the North of the cloud. There is no absorption shown near the LLCC in the 5797 Å DIB map which means the gas there must be diffuse and probably ionised. The Na I D_2 map shows two of those targets; the Northern target and one of the Southern targets. There are too few targets here to say anything for certain but it

could be that these absorption maps are picking out the edges of the LLCC and it could be that the Southern most part of the cloud is more dense than the Northern part. The strong 5780 Å DIBs absorption could be tracing a non-neutral gas cloud; this is supported by the lack of 5797 Å DIB and Na I D_2 detection. The Northern target of the LLCC region shows Na I D_2 absorption and some low value of 5780 Å DIB absorption, this could be tracing the interface between the LLCC and the warm ISM surrounding it. It is hoped that the results from the Northern survey will give more insight to what is going on in this region.

There is one place near the Galactic plane where the absorption levels are low in all maps, this is at a Galactic longitude of $\sim 270°$. The 5797 Å DIB maps shows there is a region of stronger absorption at a Galactic longitude of $\sim 300°$ which is matched by strong absorption in the 5780 Å DIB so this may be indicating an interface between a cavity and a more neutral surrounding. These are interesting regions which are worthy of further investigations.

Maps in the Galactic Plane Projection

The 5780 Å DIB absorption maps

The maps in Figure 3.17 show the EW strength of the the 5780 Å DIB as viewed in the Galactic Plane projection. The strength of the EW absorption is given by the legend with darker colours representing stronger absorption values. The Sun is marked at the coordinates (0°,0°) so the distance from the Sun in the Galactic Plane projection is as plotted. The size of the symbols represent the distance from the Galactic Plane and is given by the legend, with circles representing targets that are North of the Galactic Plane and squares representing targets South of the Galactic Plane. The top map in Figure 3.17 can be compared with the top map shown in Figure 3.1, created by Welsh et al. (2010). Areas of high DIB absorption in Figure 3.17 closely match areas of high Na I volume density in Figure 3.1. However the DIB maps shows more variation of absorption strength than the Welsh et al. (2010) maps. This is particularly noticeable in the fourth quadrant of Figure 3.17 within 100 pc of the Sun. As was seen by the

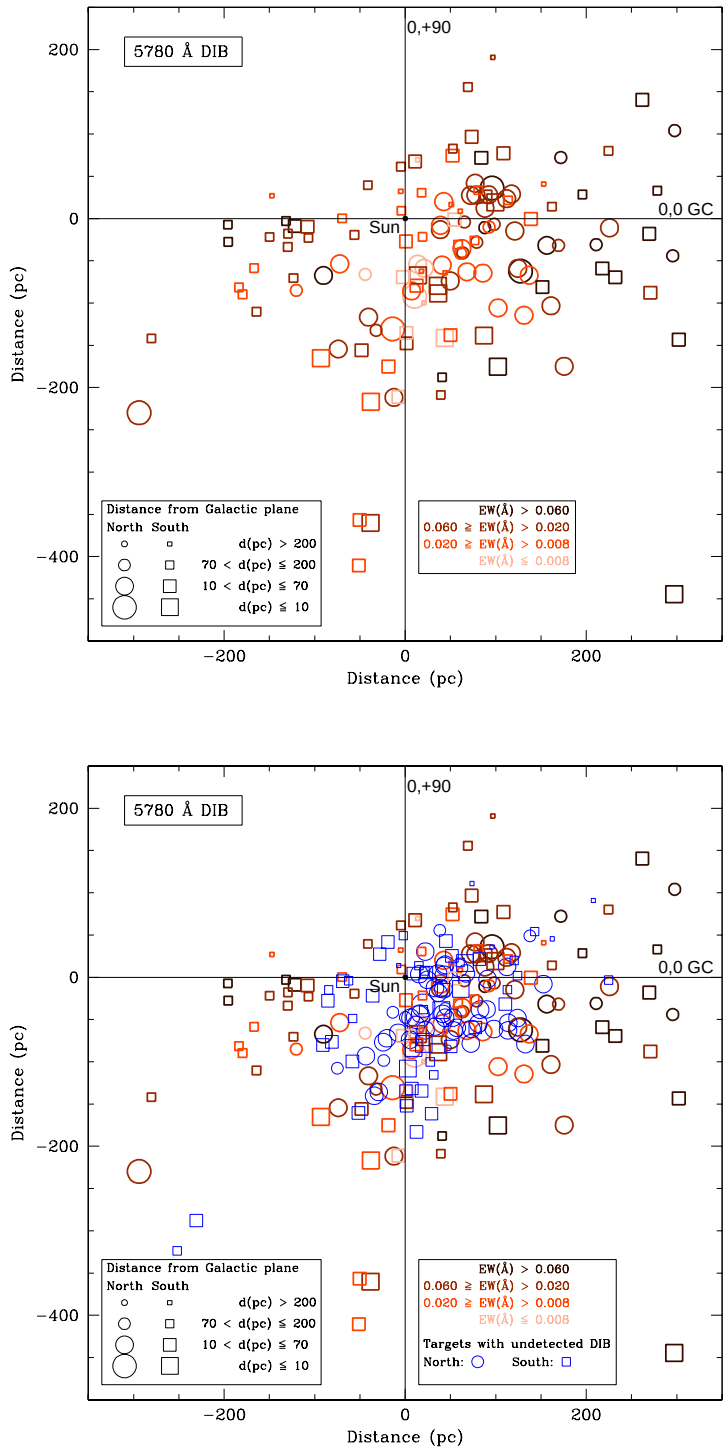

Figure 3.17: EW maps in the Galactic Plane projection of (Top:) the 5780 Å DIB absorption and (Bottom:) the same map including all the sight lines for which there was no 5780 Å DIB absorption detected (marked in blue).

huge scatter in the correlation plots of 5780 and 5797 Å versus the Na I in Figure 3.12, Section 3.2.1 sodium is not a very good indicator of DIB abundance so the DIB maps are revealing more structure in the LISM.

The bottom map in Figure 3.17 shows the sight-lines where no DIB detection could be certain (marked in blue) as well as the DIB information presented in the top map. From this we can see that even in areas where there is a concentration of targets that show strong DIB detection there are some sight-lines in which no DIBs are discernible. The fourth quadrant in particular shows many sight-lines North of the galactic plane where targets are within 60 pc of each other where no DIBs were detected but there are also sight-lines in the same region where reasonably strong detections have been made. So it is not necessarily the case that sight-lines in the regions showing strong DIB detections in the top map are typical and always show DIB absorption. Here we are probing the LISM on scales of less than 70 pc and seeing structure in the environment. On the other hand there appears to be some sight-lines that are 'empty' in the top map of Figure 3.17 and also 'empty' in the bottom map and these may well be areas truly devoid of a gas where DIBs can survive.

These non-detections are as important as the detections themselves because they trace the cavity of the LB very well as will be seen in the following maps. The structure these maps reveal by including the non-detections show where the LISM is porous and where it is perhaps a bit clumpy. The DIB maps show more variation than the sodium maps both those of Welsh et al. (2010) and the sodium maps presented later on in this Section. This is probably because the sodium is less discriminating of exact environmental conditions.

These maps (and those following in this Section) can be used in conjunction with the descriptions of specific targets in Section 3.2.1 to give the reader a sense of the location of the sight-lines discussed.

The 5797 Å DIB absorption maps

The maps in Figure 3.18 can be read in the same way as the preceding maps for the 5780 Å DIB absorption and again it is useful to use this map to locate the targets discussed in Section 3.2.1. The 5797 Å DIB is weaker than the 5780 Å DIB and was not as well detected, hence the sparse map. Comparing the top map in Figure 3.18 with the top map in Figure 3.17 it can be seen that the 5797 Å DIB is only detected when 5780 Å DIB is detected. However it is not the case that whenever there is a strong 5780 Å DIB detection there is a strong 5797 Å DIB detection. For example; at the coordinates of $\sim$(225°,220°) two targets in the Southern hemisphere at a distance from the Galactic Plane of between 10 and 70 pc and visually adjacent to one another can be seen in both maps. In Figure 3.17 the symbols show these the EW strength of the 5780 Å DIB is greater than 0.06 Å for both targets, yet in Figure 3.18 one target has an EW strength of less than 0.008 Å while the other has an EW strength of between 0.02 and 0.06 Å. These targets may not be exactly the same distance away from the Galactic Plane but they are relatively close. The target closer to the Sun has the weaker 5797 Å DIB EW strength. Hence this must be tracing a region of lower neutral gas density than the target which is slightly further away from the Sun. Comparing these maps with maps of Welsh et al. (2010) and it is clear these targets are probing the bubble wall interface. It is interesting to see targets closer to the Sun than these and at varying distance to the Galactic Plane that show EW strengths for the 5797 Å DIB which are between 0.02 and 0.06 Å. These targets do not appear to correspond to any significant levels of Na I volume density as shown by Figure 3.1. The 5797 Å DIB does need a neutral gas environment to survive so here we must be tracing small cool neutral cloudlets within the cavity of the LB.

The bottom map in Figure 3.18 shows the sight-lines where no DIB detection could be certain and it is included here for completeness. With so many sight-lines with no certain 5797 Å DIB detection it is not as informative as the similar map for the 5780 Å DIB.

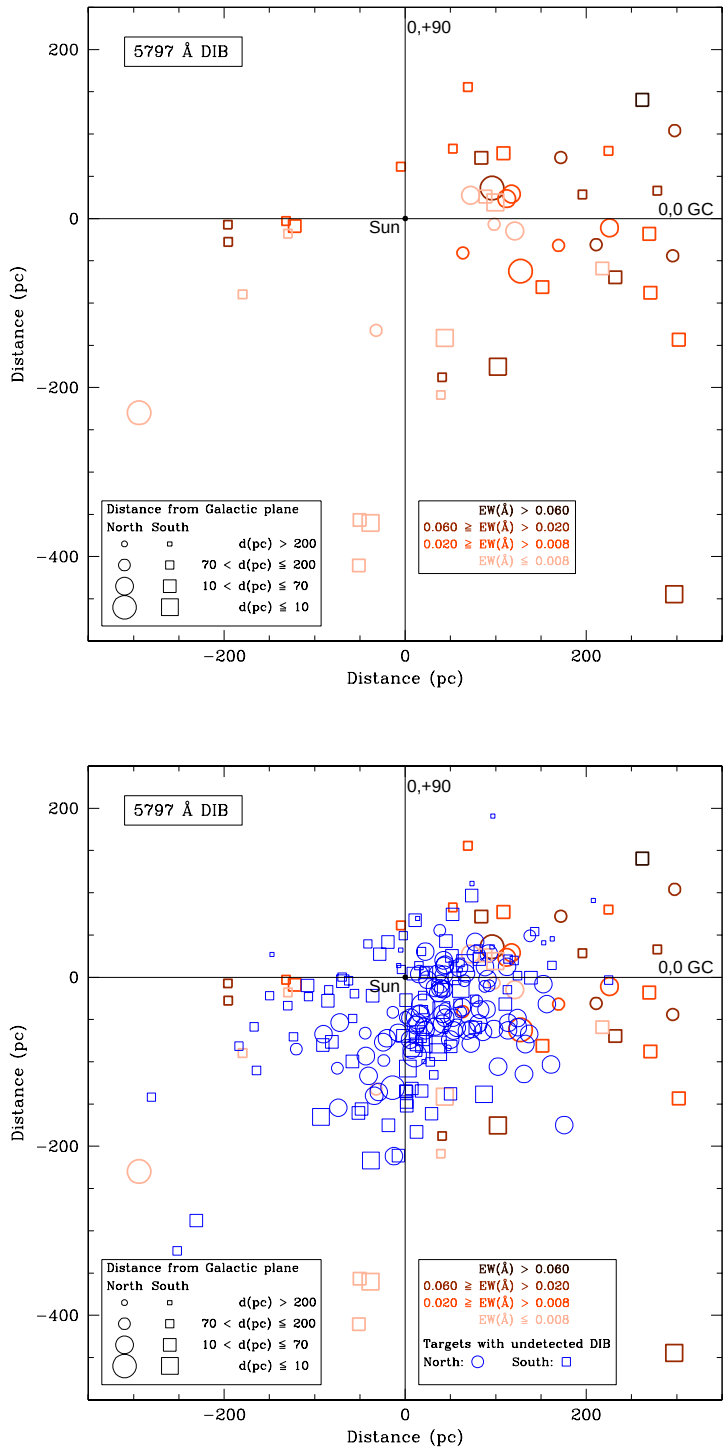

Figure 3.18: EW maps in the Galactic Plane projection of (Top:) the 5797 Å DIB absorption and (Bottom:) the same map including all the sight lines for which there was no 5797 Å DIB absorption detected (marked in blue).

The Na I D_2 absorption maps

With so many sight-lines showing good Na I D_2 detection the maps in Figure 3.19 are 'busy'. The overall pattern of EW strength distribution can be likened to the distribution Na I volume density as shown in Figure 3.1. Yet there are significant differences in the regions close to the Sun. In some cases targets that trace strong Na I D_2 do not trace either of the two DIBs, see the target at coordinates of $\sim (-40°,-20°)$ in Figure 3.19 and compare with the same coordinates in Figures 3.18 and 3.17. The two targets highlighted in Figure 3.18 are again interesting in this map. Once more the target nearer the Sun shows a lower Na I D_2 EW strength than its visual neighbour. This really confirms these targets are probing the wall/Bubble interface. For the EW strength of the Na I D_2 to reduce while the EW strength of the 5780 Å DIB does not, coupled with the greater reduction of the presence of the 5797 Å DIB shows this is a region where the density of the gas will be less and the environment harsher than it is in environments of greater Na I D_2 EW strength (van Loon et al. 2009).

The bottom map in Figure 3.19 shows the sight-lines where no DIB detection could be certain as in the previous two figures but there are few of these sight-lines. Interestingly there are sight-lines in quadrant three of all three maps which show no absorption of the DIB or the sodium. This is reflected in the Welsh et al. (2010) map in the top of Figure 3.1.

Maps in the Meridian Plane Projection

The 5780 Å DIB absorption maps

The maps in Figure 3.20 show the EW strength of the 5780 Å DIB as viewed in the Meridian Plane projection. As for the previous maps the colour, size and shape represent EW strength, distance from the Meridian Plane and location of the target starts being in front or behind the Meridian Plane. The Sun is marked at the coordinates (0°,0°) so the distance from the Sun in the Galactic Plane projection is as plotted. The top map in Figure 3.20 can be compared with the bottom map shown in Figure 3.1, created by Welsh et al. (2010). As for the Galactic Plane maps, areas of high DIB

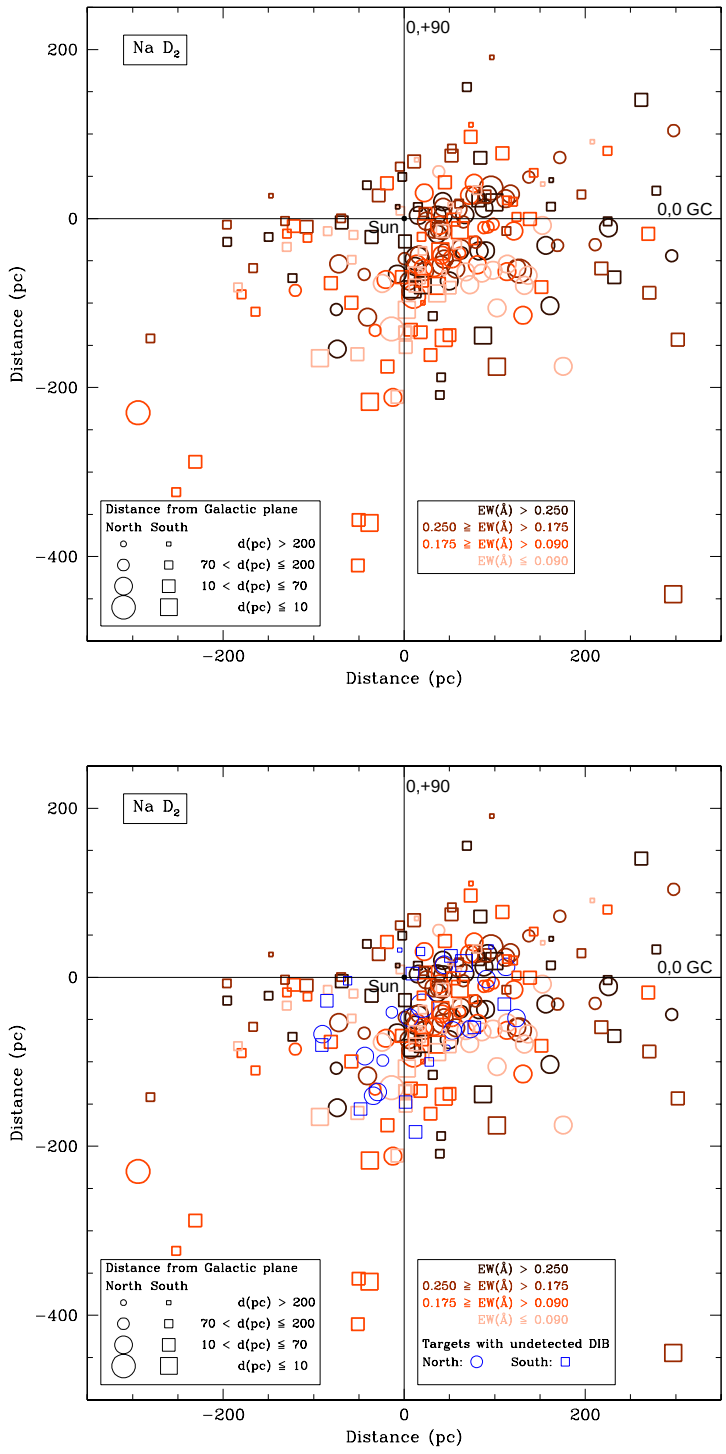

Figure 3.19: EW maps in the Galactic Plane projection of (Top:) the Na I D_2 absorption and (Bottom:) the same map including all the sight lines for which there was no Na I D_2 absorption detected (marked in blue).

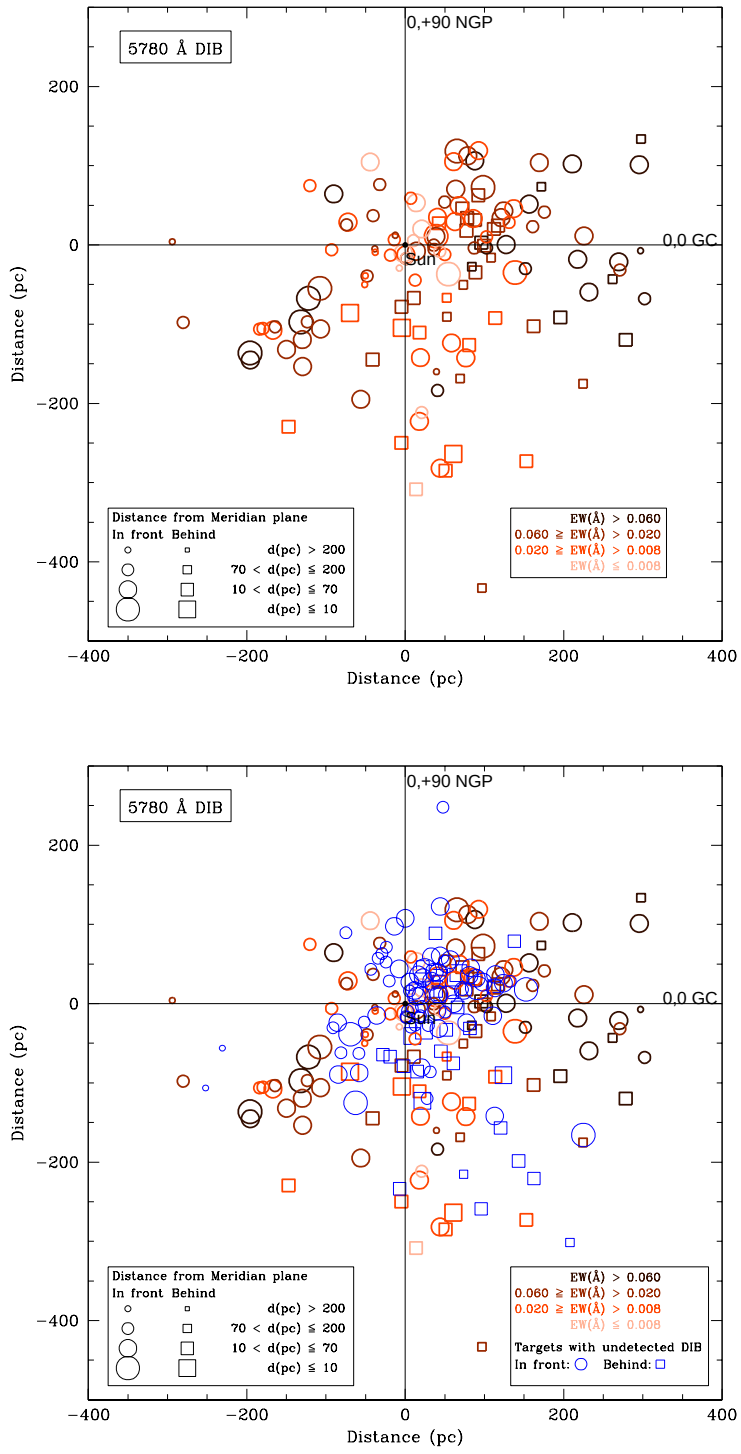

Figure 3.20: EW maps in the Meridian Plane projection of (Top:) the 5780 Å DIB absorption and (Bottom:) the same map including all the sight lines for which there was no 5780 Å DIB absorption detected (marked in blue).

absorption in Figure 3.20 closely match areas of high Na I volume density in Figure 3.1 with one exception at coordinates of ∼(90°,180°). Again the DIB maps shows more variation of absorption strength than the Welsh et al. (2010) maps.

The bottom map in Figure 3.20 shows the sight-lines where no DIB detection could be certain (marked in blue) as well as the DIB information presented in the top map. The pattern seen in Figure 3.17 of areas where there is a concentration of targets that show strong DIB detection intermingled with some sight-lines in which no DIBs are discernible is also evident here.

The 5797 Å DIB absorption maps

As for the Galactic Plane maps, the top map in Figure 3.21 can be compared with the top map in Figure 3.20 and the same can be seen that the 5797 Å DIB is only detected when 5780 Å DIB is detected. The target marked as an exception in the preceding section at coordinates of ∼(90°,180°), is detected in this map as well and also shows a strong EW absorption (between 0.02 and 0.06 Å) which is at odds with the Welsh et al. (2010) map. Similar to the targets highlighted in the Galactic Plane projection which probe environments of neutral gas, this target must also be tracing a neutral gas cloud within the cavity of the Bubble. The bottom map in Figure 3.18 shows the sight-lines where no DIB detection could be certain and it is much more enlightening than other maps which show all sight-lines. In the bottom map of Figure 3.20 the blue symbols are intermingled with symbols showing 5797 Å DIB EW detections and highlight areas of the ISM which may be porous and largely devoid of matter. In the bottom map of Figure 3.21, however, the lack of neutral material which can host the 5797 Å DIB actually highlights regions which could be 'clumpy'. This is where there are a few sight-lines that do show weak EW measurements for the 5797 Å DIB. These sight-lines showing weak absorption are surrounded, and in one case at coordinates of ∼(50°,10°) almost obliterated, by sight-lines which do not detect any DIBs. More significantly this map clearly shows that there are no 5797 Å DIB detections to the North or the South, there is no neutral gas in which the 5797 Å DIB can survive. The Bubble is opening out to the Halo in both directions.

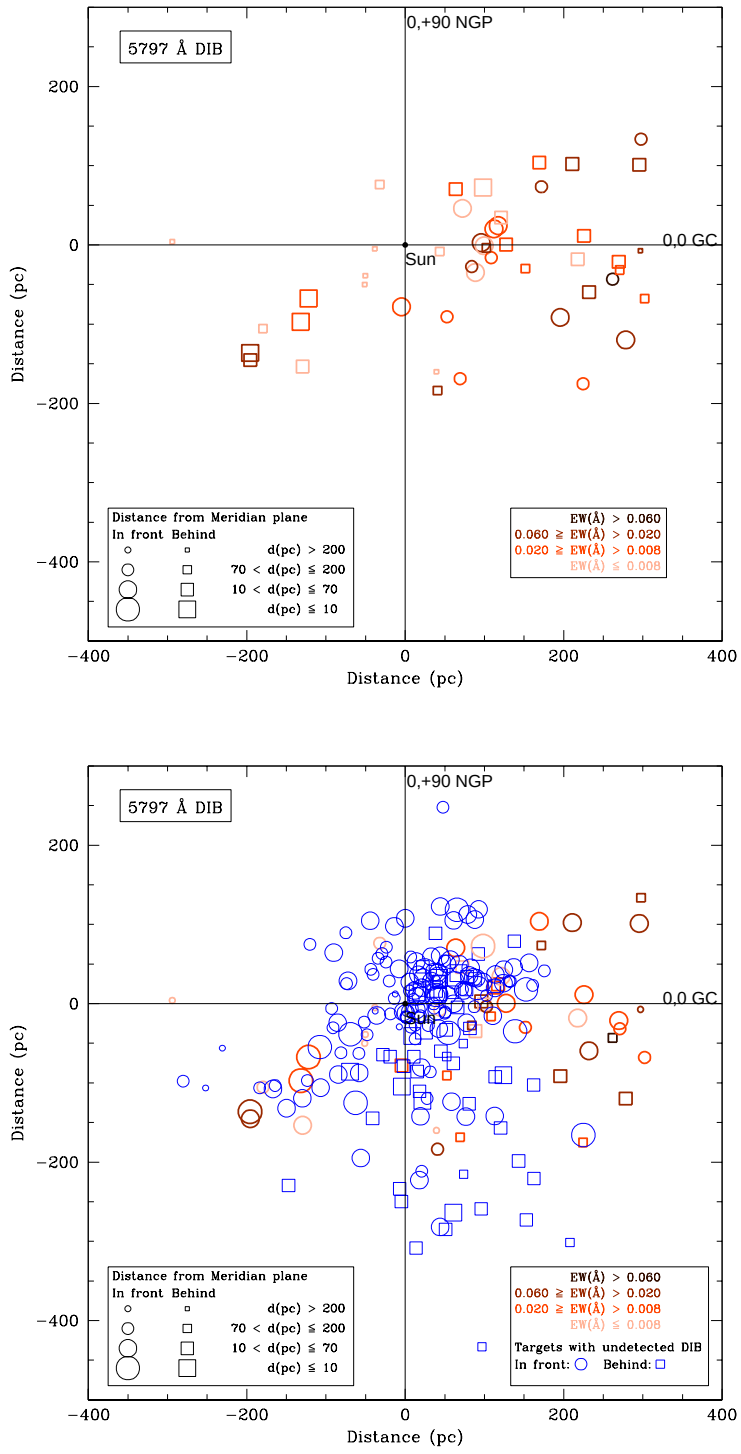

Figure 3.21: EW maps in the Meridian Plane projection of (Top:) the 5797 Å DIB absorption and (Bottom:) the same map including all the sight lines for which there was no the 5797 Å DIB absorption detected (marked in blue).

The Na I D_2 absorption maps

Like the Galactic Plane projection the maps in Figure 3.22 are 'busy'. The walls of the Bubble as revealed by the bottom panel in Figure 3.1 are also being traced in the Na I D_2 map in Figure 3.22. However yet again there are significant differences in the regions close to the Sun with some cases where there is strong Na I D_2 absorption but no trace of either of the DIBs in the same sight-line; see the target at coordinates of $\sim (-10°,40°)$ in Figure 3.22 and compare with the same coordinates in Figures 3.21 and 3.20.

The bottom map in Figure 3.19 shows the sight-lines where no DIB detection could be certain as in previous figures but, as in the Galactic Plane projection, there are few of these sight-lines.

The Na I D_2 maps do reveal structure in the ISM that is not shown by the Na I volume density maps of Welsh et al. (2010). Moreover, the EW strengths of the DIBs show more variation in some regions than the Na I D_2 does in the same region, thus revealing more structure in the environment. This is probably because the DIBs require more specific environmental conditions to survive than the less discriminate sodium which can trace a range of environmental conditions.

Maps of the equivalent width of the 5780/5797 Å DIB ratio

The maps in Figure 3.23 are different to the preceding maps in the Section. They show the ratio between the EW strengths of the 5780 and 5797 Å DIBs. The top map in Figure 3.23 shows the 5780/5797 Å DIB ratio in the Galactic Plane projection and the bottom map shows the 5780/5797 Å DIB ratio in the Meridian Plane projection. Both maps have the Sun located at the coordinates (0°,0°) and the size, shape and position of the symbols are the same as in previous maps. The biggest difference is that the colour of the symbols now represent the ratio, with the darkest colour representing those sight-lines where only the 5780 Å DIB was detected. The colours of the symbols then get progressively lighter as the value of the ratio decreases as the strength of the 5797 Å DIB increases with respect to the strength of the 5780 Å DIB.

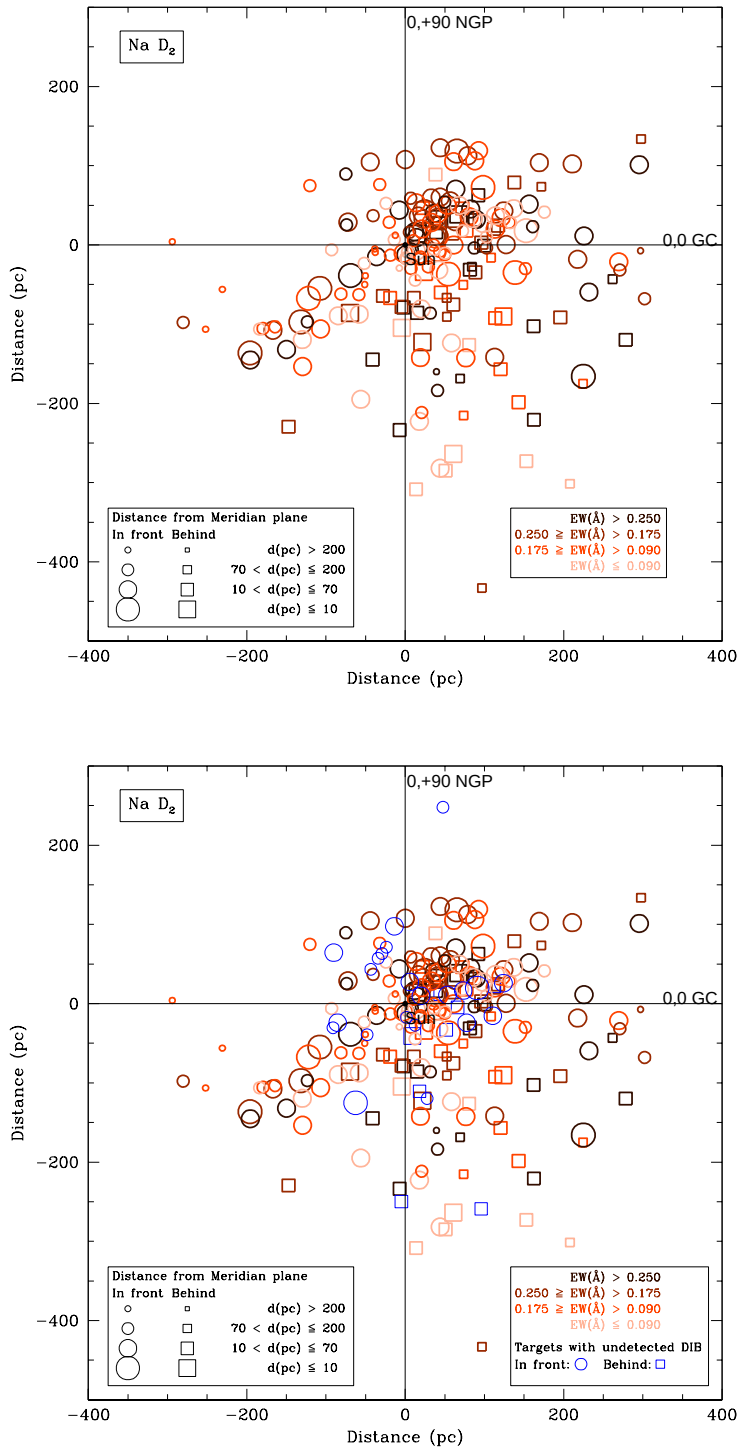

Figure 3.22: EW maps in the Meridian Plane projection of (Top:) the Na I D_2 absorption and (Bottom:) the same map including all the sight lines for which there was no Na I D_2 absorption detected (marked in blue).

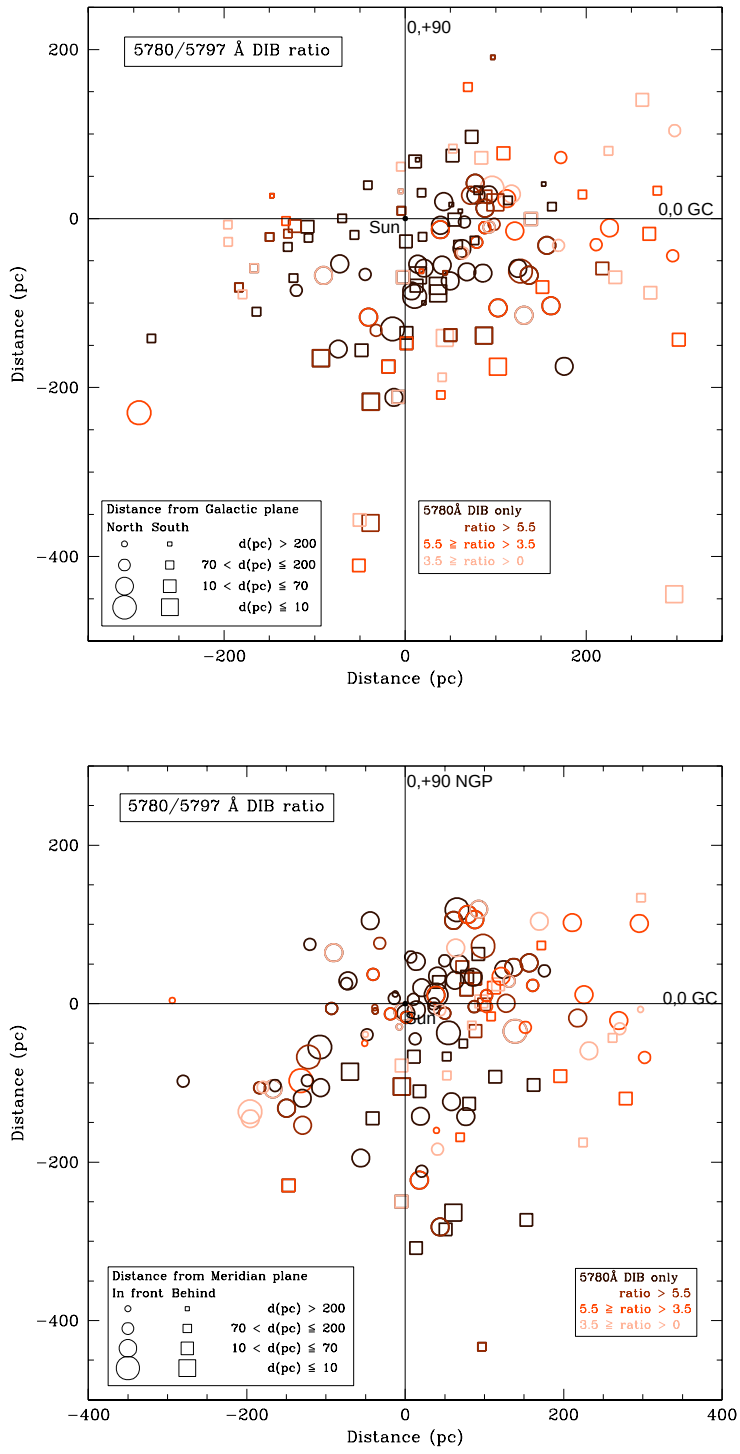

Figure 3.23: Maps of the 5780/5797 Å DIB ratio in (Top:) the Galactic Plane projection and (Bottom:) the Meridian Plane projection.

Therefore, in the maps in Figure 3.23 it is the paler colours that trace the neutral gas and so the walls of the LB and the cool cloudlets within it. In the top map of Figure 3.23 distances from the Sun of greater than $\sim$ 100 pc show that the paler symbols representing regions of significant 5797 Å DIB absorption, and thus the neutral gas this DIB favours for its existence, closely resemble the high values of the Na I volume density shown in the Welsh et al. (2010) maps in Figure 3.1. Within a distance of 100 pc in this map, many of the symbols show that only the 5780 Å DIB is present, indicating this is an ionized region of gas, thus tracing the cavity of the LB extremely well. The exciting thing about this map is that within this cavity the DIB ratio clearly shows some discrete regions of a low 5780/5797 Å DIB ratio; see the targets at coordinates: (0°,−75°), (70°,−40°) and (−10°,30°) for examples. These sight-lines must be tracing regions of cold neutral gas in order for them to have the significant levels of the 5797 Å DIB indicated by the ratio values of less than 3.5.

A similar story of the local bubble is told by the map in the bottom panel of Figure 3.23. The walls of the LB are clearly traced by the paler map symbols and they compare well the bottom panel of Figure 3.1. showing the Welsh et al. (2010) map. As for the Galactic Plane projection, this Meridian Plane projection picks out the cold neutral gas clouds; see the targets at coordinates: (0°,−10°), (−5°,−25°) and (45°,10°) for examples. In particular note the cluster of three targets around the coordinates (−50°,−50°); all three are in front of the Meridian Plane. One is between 70 and 200 pc from the Galactic Plane the other two are greater than 200 pc from the Galactic plane. There may be great distance between them all or they may be be fairy close in location. What they do show is that closer to the Meridian Plane, only the 5780 Å DIB is present indicating a hot ionized region. The other two targets show a difference in the ratio but it is not clear where these lie relative to each other and the third target. What is clear is that the environment traced by these targets is very different in that relatively small region.

Thus, the DIBs are an excellent diagnostic of environmental conditions in these extreme and harsh environments as noted by van Loon et al. (2009). The DIBs are, indeed, very picky about the environment in which they reside.

4 The Magellanic Clouds

"I saw in the heaven three Canopi, two certainly bright, and the other obscure"

– Amerigo Vespucci (1451-1512), "Letter on his Third Voyage; describing the Magellanic Clouds and the Coalsack nebula"

4.1 Introduction

Diffuse Interstellar bands have not only been observed in the Milky Way Galaxy; in 1966 Hutchings (1966) reported the detection of the DIB at 4430 Å in the Magellanic Clouds. It was found to be strong in both Clouds; however, Dachs (1970) found the dust content of neutral ISM in the SMC was too low for such strong bands so argued they were Galactic in origin. Later studies by Blades; Madore; Hutchings and Houziaux (as referenced in Westerlund (1997)) confirmed that weak 4430 Å bands were formed in the Clouds but that the original measurements by Hutchings had been affected by interfering stellar lines causing them to appear stronger than expected (Westerlund 1997). Since then and often using space observatories such as the International Ultraviolet Explorer (IUE) and the Hubble Space Telescope (HST) a large number of DIBs in the Magellanic Clouds have been detected, (Xiang, Liang & Li 2009) and references therein. If the carriers of the DIBs could be associated with some of the clouds defined by the radial velocities of the interstellar lines in this direction there is a possibility of obtaining some clues to the formation of these bands (Westerlund 1997).

There is great interest in using the Magellanic Clouds to investigate DIBs. This is due to the fact the Magellanic Clouds have a different composition to the Galaxy (i.e. lower metallicity and much larger gas-to-dust ratio), which may reveal the nature of the DIB carriers (Herbig 1995) and the fact the radial velocity of the LMC ensures that LMC interstellar lines and narrow DIBs are clearly separated from those with a Galactic origin (Cox et al. 2006). The work of Welty et al. (2006) is of particular importance. Their observations indicate the abundance of CH in the Magellanic Clouds appears

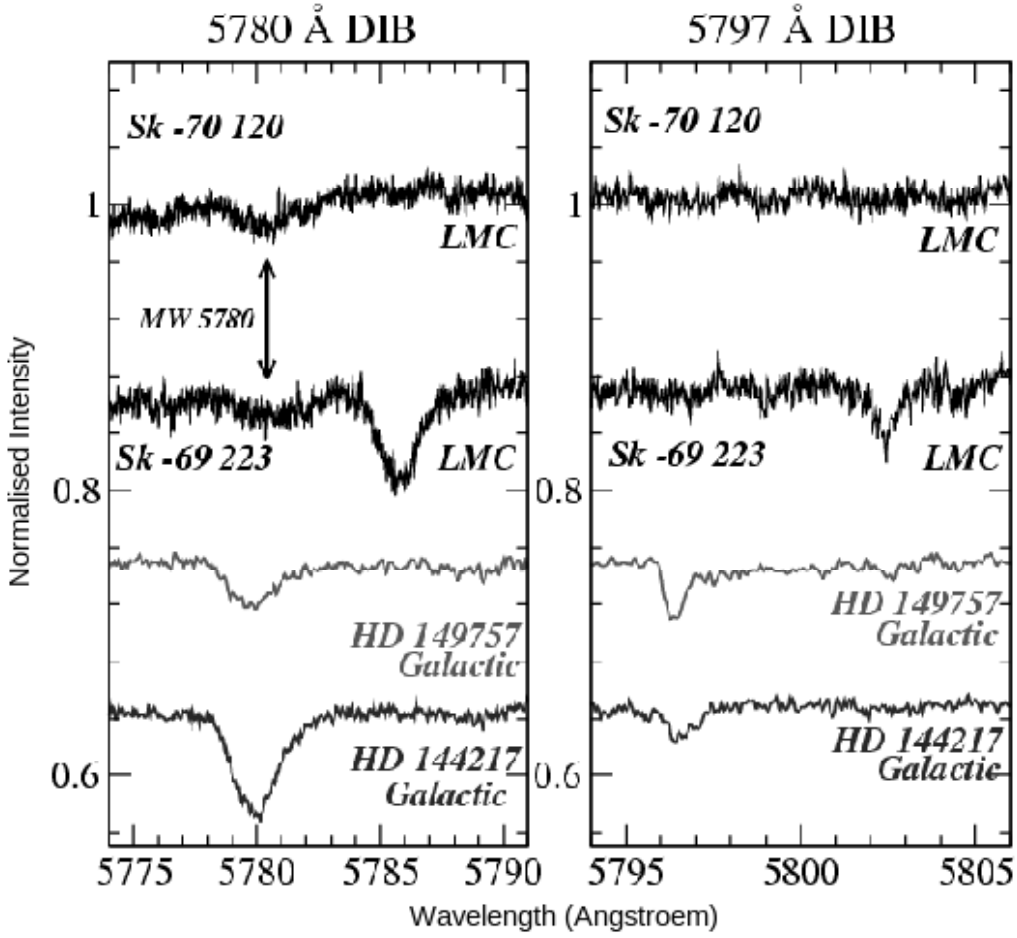

Figure 4.1: Comparison of DIBs observed in the lines-of-sight towards Sk-70 120 and Sk-69 223 in the LMC and DIBs in two Galactic lines of sight (Cox et al. 2006)
.

to depend on local physical conditions and not just on metallicity, and which appear to also play a major role in determining the relative strengths of DIBs in individual lines-of-sight.

As the Magellanic Clouds are our near neighbours, and so enable us to observe individual stars within them, they are a unique laboratory with which we can study DIBs under conditions that are profoundly different from those in the Galaxy. To

illustrate this point, Figure 4.1 shows the comparison of the 5780 and 5797 Å DIB profiles observed towards Sk-69 223 and the low reddening standard Sk-70 120 with DIB profiles in two typical Galactic lines-of-sight. This is taken from a study undertaken by Cox et al. (2006) of DIBs in the LMC including 30 Dor, in which the dense cluster of OB stars produce a strong UV field, to gain an insight to the chemical properties of the DIB carriers. They examined the relationship between the DIBs and atomic lines of several key interstellar species, which were observed simultaneously in several LMC sight-lines. The shift in wavelength is due to the receding velocity of the LMC ($\sim$ 250 - 300 $\mathrm{km\,s^{-1}}$).

The similarity of the 5780 and 5797 Å profiles between HD 144217 and Sk-69223 together with the other results Cox et al. (2006) produced from this survey (the similar UV impact and large grain distribution) imply that either the physical conditions of the lines-of-sight are comparable or the respective conditions in the different lines-of-sight result in a very similar local balance of DIB carrier formation and destruction processes (Cox et al. 2006).

Observations at the AAT

For this project I used the 2dF AAΩ instrument on the AAT as its 2° -diameter field and multiple fibres allowed me to observe $\sim$ 350 targets at a time. I observed early-type stars as these are bright at optical wavelengths and provide a relatively clean continuum against which interstellar features stand out. The aim was to measure the strongest DIBs (at 5780 and 5797 Å) in the spectra of these early-type stars in order to probe the molecular ISM within the SMC, LMC and the foreground Milky Way Disc and Halo. The fact that the Magellanic Clouds recede from us at velocities of $\sim 150 - 200\ \mathrm{km\,s^{-1}}$ (SMC) and $\sim$ 250-300 $\mathrm{km\,s^{-1}}$ (LMC) means there is sufficient separation between the contributions from the Magellanic Clouds and Milky Way Galaxy to enable a comparison to be made in a similar way to the method illustrated in Figure 4.1. As well as the 5780 and 5797 Å DIBs I obtained the strong interstellar lines of Ca II K and Na I D_2. This allowed me to link the molecular gas traced by the DIBs to the warm atomic gas.

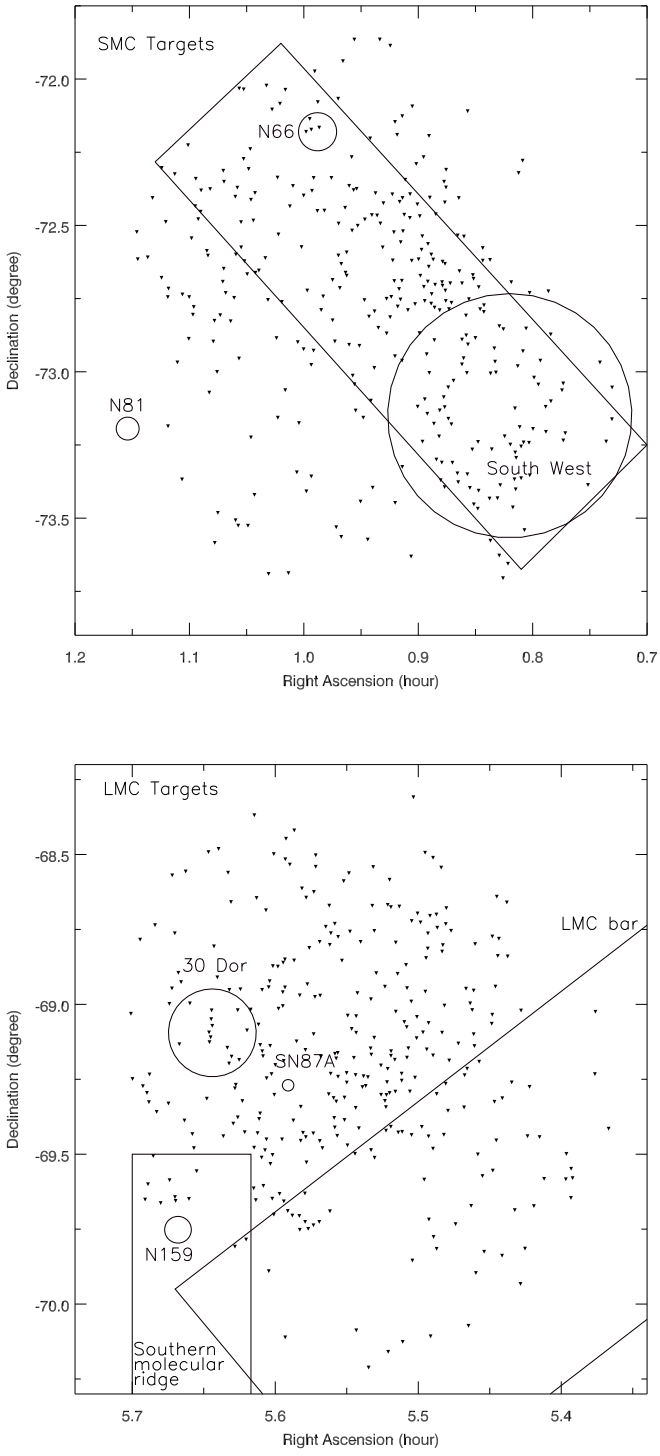

Figure 4.2: Distribution of targets in the SMC and LMC.

Figure 4.2 shows the locations of the chosen target stars in the SMC (top panel) and the LMC (bottom panel); compare with Figure 2.6 in Chapter 2 that shows all the possible targets identified with 'Configure'(see Section 2.1.2.2.

The 2° field of view of the AAΩ instrument almost covers the entire region of the SMC, even so I chose to cover the southern part of the SMC as best I could so that I sampled some regions not normally observed. I also ensured I covered some regions that have been well studied so that I could compare my results from the different regions of the SMC and give me some confidence in my interpretation of the results in the diffuse regions. The rectangle marked on the SMC target field in Figure 4.2 represents the location of the bar in the SMC. In the North the location of N66 is marked, this is the largest and brightest HII region in the SMC. The circular area marked South West is the approximate region which contains giant molecular clouds and is a region of star formation. Although the survey did not extend as far as the star forming nebula, N81, its location in the wing of the SMC is marked to give the reader a sense of the scale and layout of the area observed in this survey. The Magellanic Bridge, which connects the SMC and the LMC stretches out to the East.

The LMC is much larger than the SMC but again my aim was to observe some of the southern less well studied portion of the LMC as well as the extensively studied HII region, the Tarantula Nebula (30 Dor). The larger rectangle marked on the LMC target field in Figure 4.2, which runs from South East to North West represents the location of the bar in the LMC. The location and approximate size of 30 Dor, is shown in the East. The rectangle below 30 Dor marks the region of the southern molecular ridge, an elongated region containing a number of large molecular clouds of gas. Within the southern molecular ridge the well studied HII, star forming region, N159 is marked, although my survey only just reaches the area of N159 it is included to help the reader navigate the map. To the South West of 30 Dor lies the supernova remnant, SN1987A. The circle marking SN1987A is not to scale and, like N159, it is included to help illustrate the region of the LMC covered by this survey.

All the features marked on both these maps are repeated on the Na I, Ca II K and DIB maps created from the data and discussed later in this chapter.

4.2 Analysis

In this section correlation plots and maps are presented. The correlations in section 4.2.1 look at the 5780 and 5797 Å DIB strength ratios and some data points of interest are discussed. The correlations in Section 4.2.2 look at the relationships between the DIBs and the Na I D_2 and Ca II K lines, noting any differences in DIB behaviour. The maps in Sections 4.2.4 and 4.2.5 show the spatial distribution and relative abundances of the Ca II K, Na I D_2, 5780 Å and 5797 Å DIBs and the ratio of the EW strengths of the 5780 and 5797 Å DIBs. The maps are described and interesting features discussed. In Section 4.3 the plots and maps are further discussed to draw together any conclusions that can be made from these data.

Average profiles of spectral features

Throughout this section reference is made to some of the absorption profiles to illustrate features that, when considered in conjunction with the maps, help to interpret the data; for example, when the Galactic component of a feature is weaker than its counterpart in the SMC or LMC. When fitting the profile to the spectra the average profile of each absorption line was determined and plotted. This was to enhance any features that had been detected. As many of the individual absorption features were quite weak, especially when considering the 5780 Å and 5797 Å DIBs, the average profiles helped to give an overall picture showing the underlying trend of the behaviour for each feature. The average profile also shows what the DIB might look like in the integrated light of an unresolved distant star forming region or star forming galaxy. Figure 4.3 shows the average profiles for each of the Ca, Na, 5780 Å and 5797 Å DIBs in the SMC sight-lines and Figure 4.4 shows the average profiles in the LMC sight-lines.

For spectra in the SMC sight-line the average of the Ca II K line shows one Galactic and one SMC component yet in the individual spectra two components are often seen in the SMC component; as will be discussed later this shows there may be two distinct parts to one large cloud or two distinct clouds along the line-of-sight. The average profiles for the 5780 Å and 5797 Å DIBs show that the Galactic DIBs

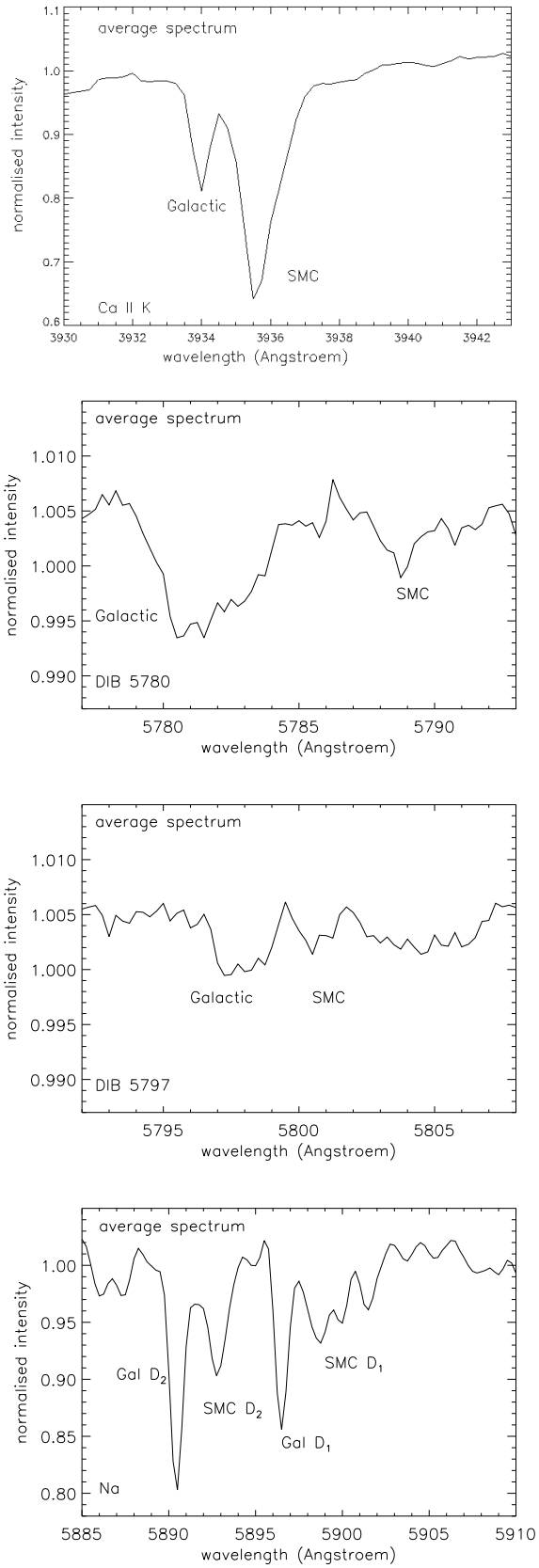

Figure 4.3: Average profiles of (Top:) the Ca II K line, (Second:) the 5780 Å DIB, (Third:) the 5797 Å DIB and (Bottom:) the Na I D lines in the SMC.

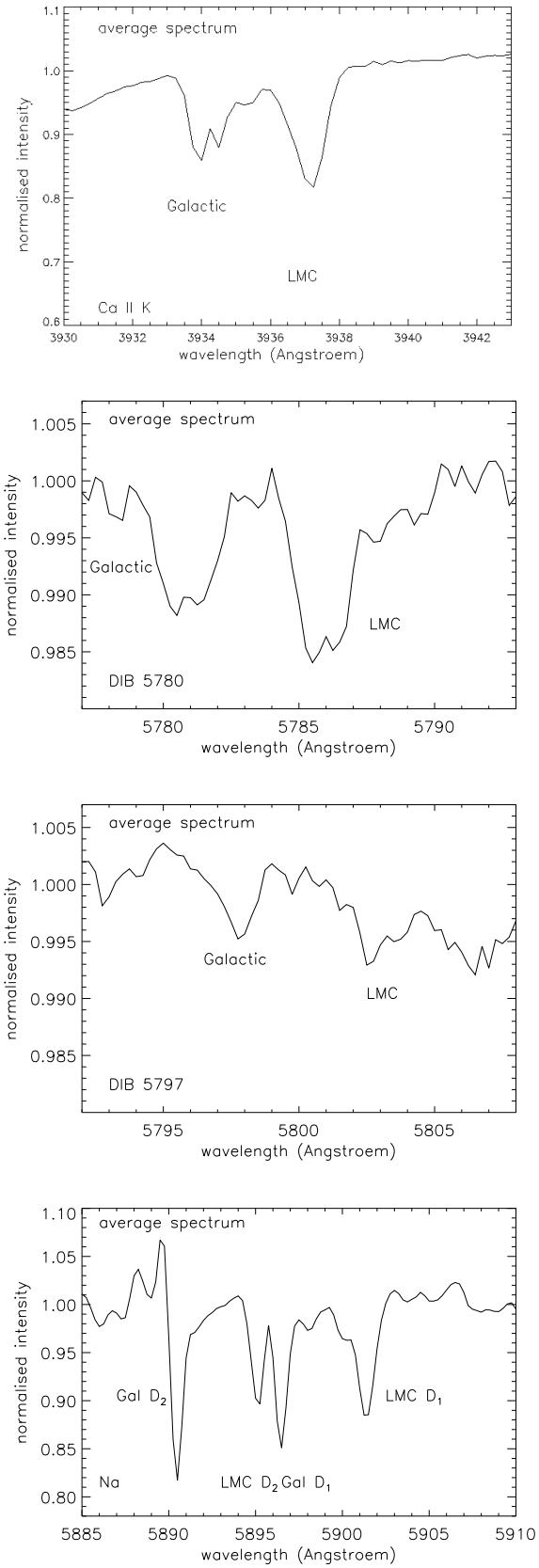

Figure 4.4: Average profiles of (Top:) the Ca II K line, (Second:) the 5780 Å DIB, (Third:) the 5797 Å DIB and (Bottom:) the Na I D lines in the LMC.

are stronger than their SMC counterparts and they are also broader. The average profiles for the Na lines show that the Galactic component is stronger than its SMC counterpart even though many individual sight-lines show the converse. This results from more sight-lines in the Galactic region than the SMC itself showing Na absorption.

For spectra in the LMC sight-line the average of the Ca II K line shows two Galactic and one LMC component. Again, in the individual spectra two components are often seen in the LMC component as well as in the Galactic region. This shows there may be two distinct clouds in the Galactic region and one large cloud in the LMC as in the case of the SMC. The average profiles for the 5780 Å and 5797 Å DIBs show that there is not as much difference in the strength of the Galactic and LMC components but with the 5780 Å DIB showing a slightly stronger average absorption in the LMC. The broadening of the DIBs is not so pronounced as it was for the SMC but there is still some evidence for DIBs being detected at distinct regions as shown by the double peaks in Figure 4.4. The average profiles for the Na lines show that the Galactic component is stronger than its LMC counterpart and again many individual sight-lines show the converse to be true. Another point to notice in the LMC average spectra for the Na absorption is that despite many of the Galactic D_1 and LMC D_2 components being blended the individual components were detected separately. Despite the blending of these two components the constraints chosen to fit the data for the Na absorption lines were rigorous enough to allow the individual components to be measured. The maps created from the data also reflect the two distinct regions and thus substantiate the method chosen to fit the profiles. The profiles of all the data are shown in Appendix C on the accompanying CD.

4.2.1 DIB strengths and band ratios (5780, 5797 Å)

The correlation plots shown in this section are all colour coded to give some indication of the data for which I can be confident in the values measured and to what extent I can be confident. With some sight-lines having very few positive detections for the DIBs, it was necessary to include all the data in order to get a reasonable overview of

the correlations. In all cases sight-lines where it was not certain absorption features actually represented DIB detections are indicated by small dots. The coloured points being described by the legend in each plot to show which DIB I was confident had been detected along the sight-line. Where there was obviously no absorption in one or other of the DIBs detected at all the points lie along the axes and are included for completeness.

The DIB strengths in the SMC

Figure 4.5 shows that there is a reasonable correlation between the equivalent widths of the 5780 Å and 5797 Å DIBs in the SMC. There is some scatter in the relation especially where the EW of the 5780 Å DIB is less than 0.04 Å. There are a large number of sight-lines for which the DIB detection was uncertain but these are, with only one exception, confined to EW values of the 5780 Å DIB that are less than 0.06 Å. Where both DIBs are weak there is generally some uncertainty in whether or not one or other of the DIBs is being detected at all. There appears to be a threshold above which there are certain detections in both the 5780 Å and 5797 Å DIBs, this occurs for EW values greater than 0.04 Å for the 5780 Å and greater than 0.015 Å for the 5797 Å DIB.

One noticeable exception to this has a 5780 Å EW of 0.111 Å and a 5797 Å EW of 0.020 Å. The profile of this target (number 479) is shown in the top panel of Figure 4.6 where uncertainty in the 5797 Å DIB measurement is clear to see. The Na detected in the SMC is quite strong and can be seen in Figure 4.6 so it is surprising the 5797 Å DIB is so weak. This target has RA 0.88 and Dec -73.3 which places it at the eastern side of the South West region which contains giant molecular clouds so I could be seeing a region where there is a lot of hot diffuse gas giving rise to the strong 5780 Å DIB in the transition region between the cooler molecular clouds and the very diffuse ISM. Another target of interest, highlighted by this correlation, is the solitary point on the plot at a 5780 Å EW of 0.280 Å and a 5797 Å EW of 0.079 Å. The profile of this target (number 135) is shown in the bottom panel of Figure 4.6. Here the Na absorption is very strong in the SMC. This target has RA 0.80 and Dec -73.25 which places it in the centre of the South West region which is most likely a molecular cloud region.

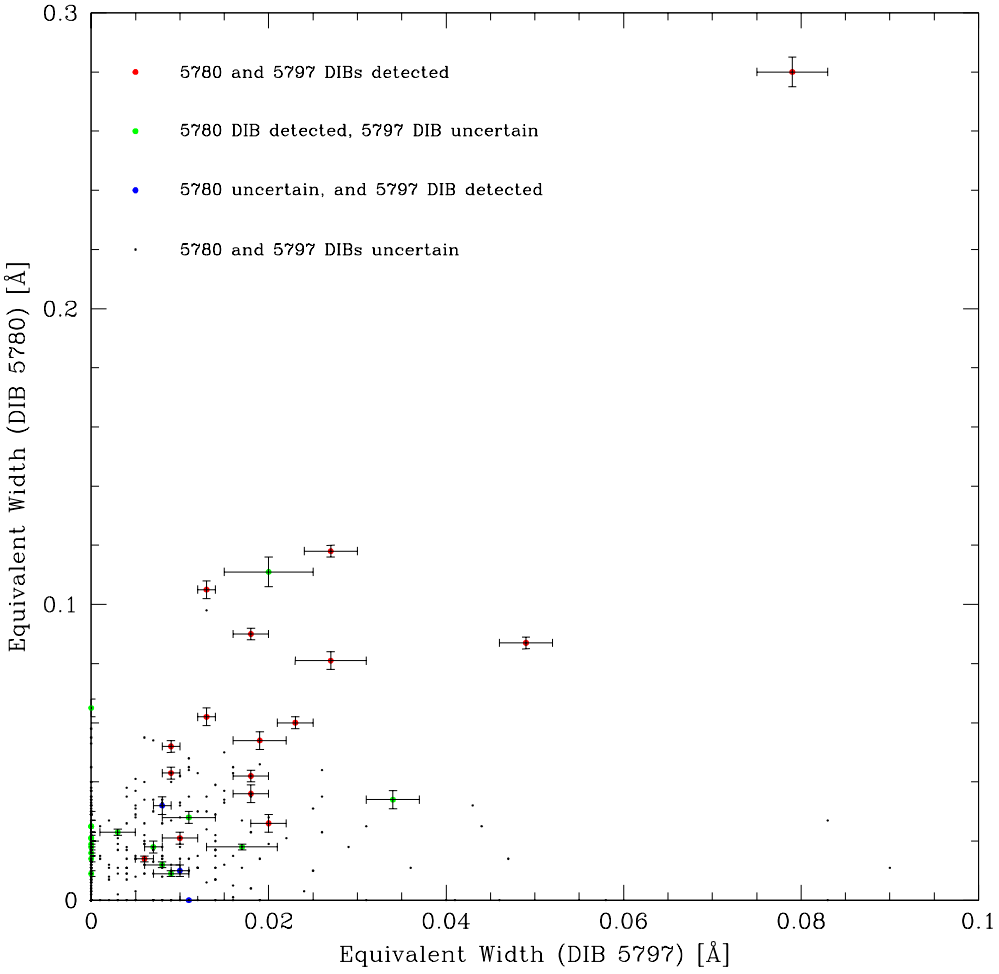

Figure 4.5: Correlation between the equivalent widths of the 5780 and 5797 Å DIBs for the SMC component in the SMC sight-line.

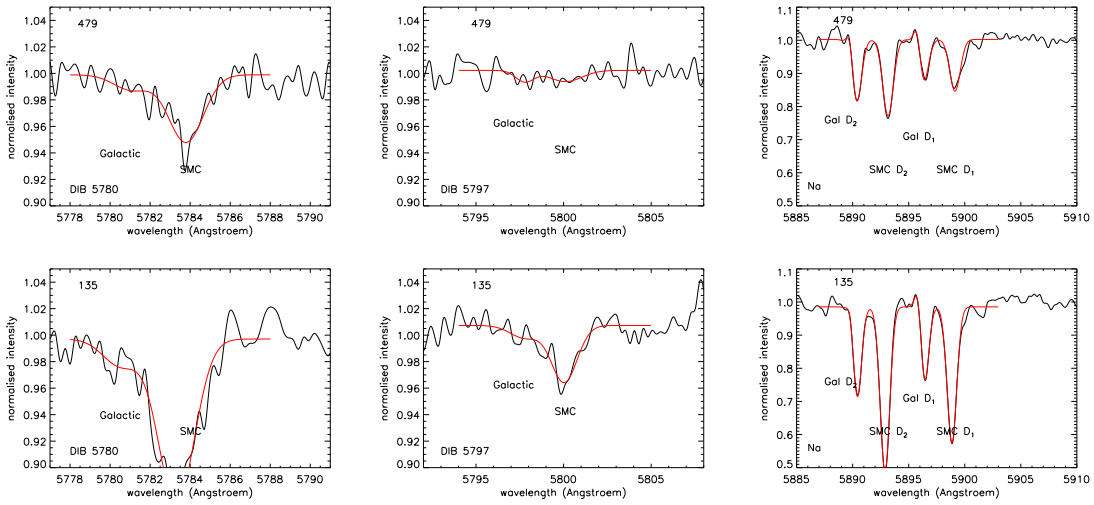

Figure 4.6: Profile of (Top:) target 479 which has a strong 5780 Å DIB absorption but little, if any, 5797 Å DIB and (Bottom:) target 135 which has very strong Na absorption and also shows strong 5780 and 5797 Å DIB absorption.

The DIB strengths in the Galactic region along the SMC sight-line

Figure 4.7 reveals three targets of high 5797 Å DIB absorption. These targets all show an anomaly in the region around the 5797 Å DIB which is caused by a region of bad pixels on the CCD camera. As an example, target 215 is shown in Figure 4.8.

For this reason the correlation plot was cropped to omit these targets (see the bottom panel in Figure 4.7. There is some correlation evident here but the scatter is more widespread than it was in the SMC itself and the sight-lines for which the DIB detection was uncertain is more randomly distributed. The threshold above which the majority of targets have a certain detection in both DIBs occurs for EW values greater than 0.0 Å for the 5780 Å and greater than 0.010 Å for the 5797 Å DIB. The scattering in the plot here could indicate that there are distinct regions of clouds here that vary between the hot diffuse clouds and cooler molecular clouds.

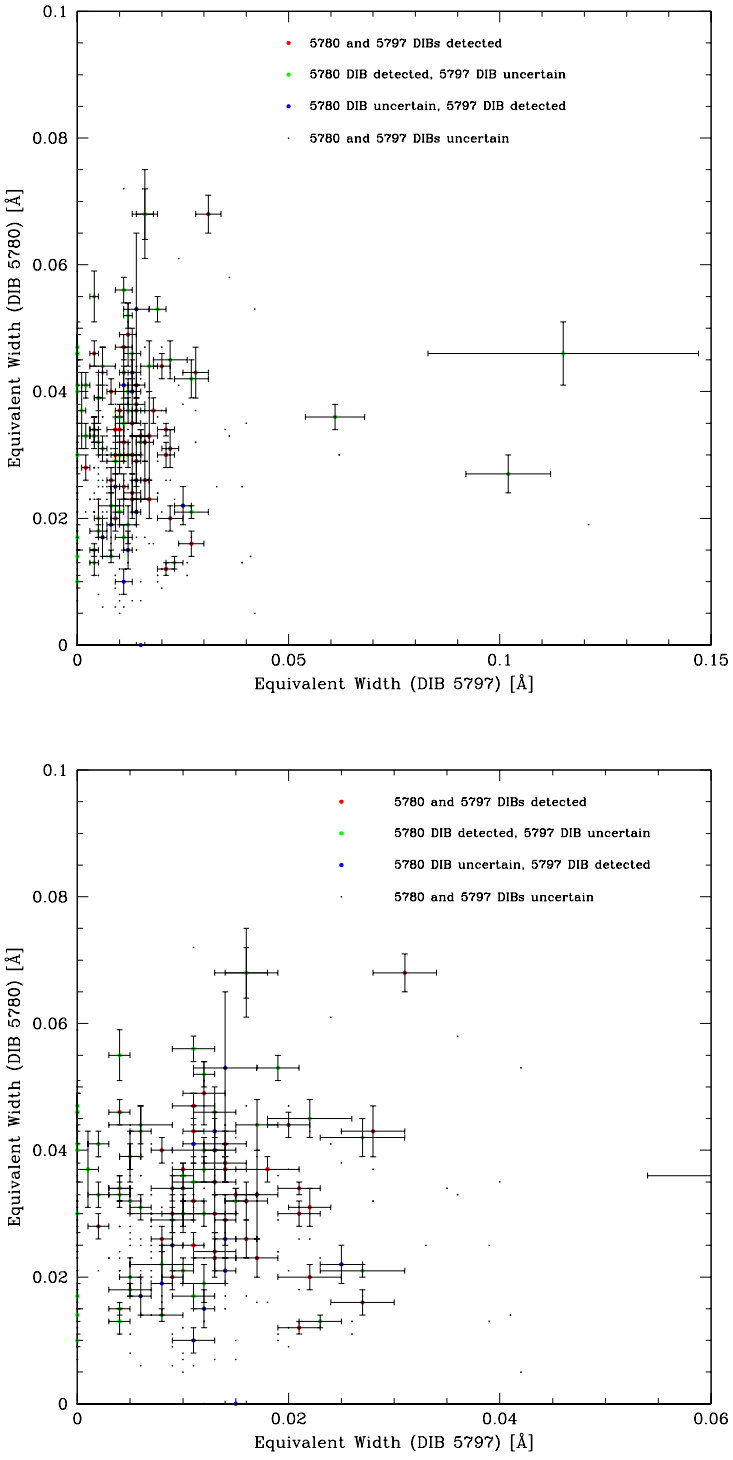

Figure 4.7: Correlation between the equivalent widths of the 5780 and 5797 Å DIBs for the Galactic component in the SMC sight-line, (Top:) all targets, (Bottom:) cropped version.

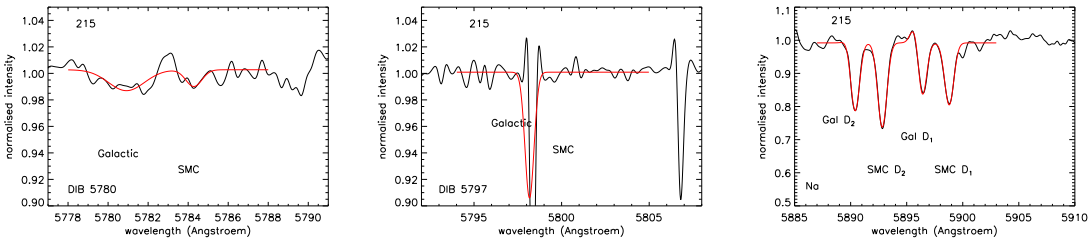

Figure 4.8: Profile of target 215 showing the anomaly around the 5797 Å DIB in the SMC.

The DIB strengths in the LMC

Figure 4.9 also shows that there is a reasonable correlation between the equivalent widths of the 5780 Å and 5797 Å DIBs in the LMC. With more sight-lines detected than for the SMC the relationship is easier to see. Some scatter is still evident but mainly in the weaker DIBs. The threshold above which when there are a certain detections in both the 5780 Å and 5797 Å DIBs here occurs for EW values greater than 0.1 Å for the 5780 Å and greater than 0.02 Å for the 5797 Å DIB. There also appears to be a point at which the 5780 Å DIB does not increase in strength in line with an increase in strength of the 5797 Å DIB. This occurs for EW values greater than 0.28 Å for the 5780 Å and greater than 0.05 Å for the 5797 Å DIB. The two targets which show the highest levels of absorption for the 5797 Å DIB are target number 1544 (RA 5.693, Dec -69.2) and number 1176 (RA 5.60, Dec -69.2) in the 30 Doradus region of the LMC, which will have more molecular material in the region as it is an area of star formation and so consistent with the stronger 5797 Å DIB.

The DIB strengths in the Galactic region along the LMC sight-line

The correlations for the EW in the Galactic region along the line of sight towards the LMC shows reasonable correlation (see Figure 4.10) but still has scattering that is more widespread than it is in the LMC itself. There is no clear threshold here so it is difficult

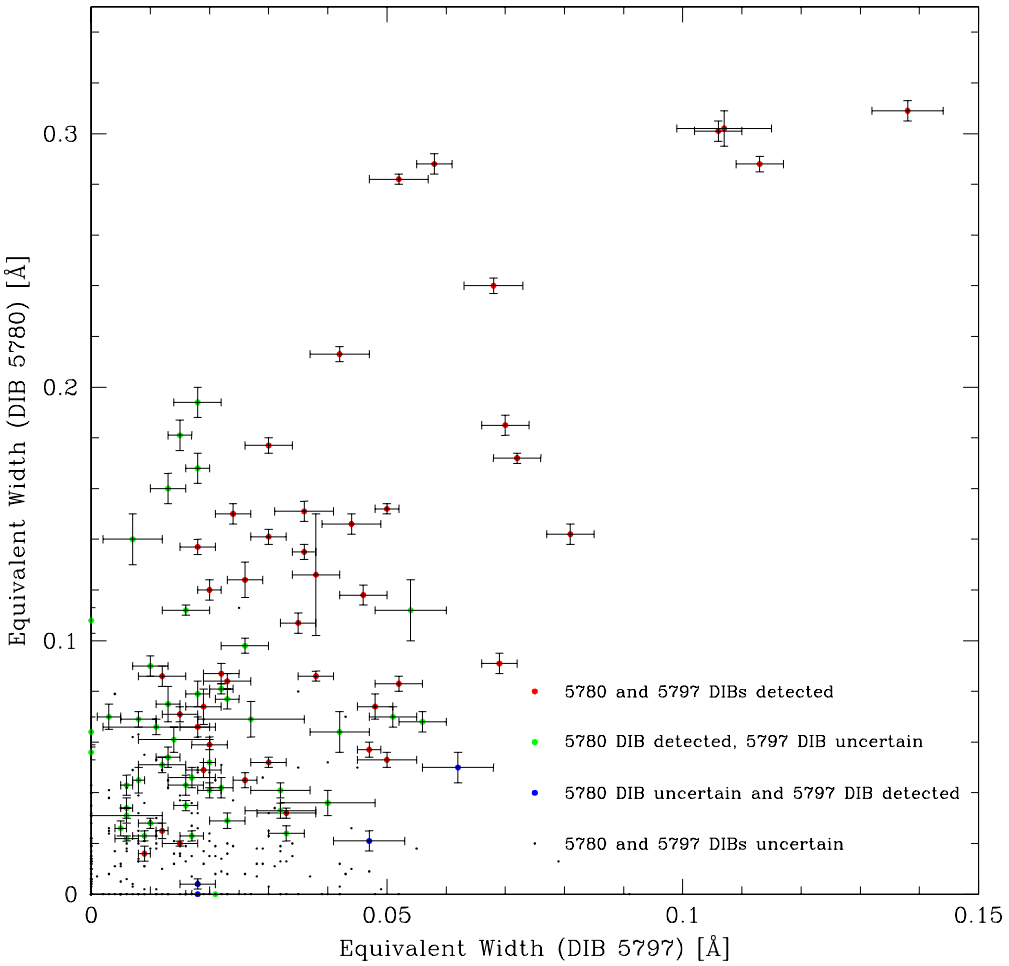

Figure 4.9: Correlation between the equivalent widths of the 5780 and 5797 Å DIBs for the LMC component in the LMC sight-line.

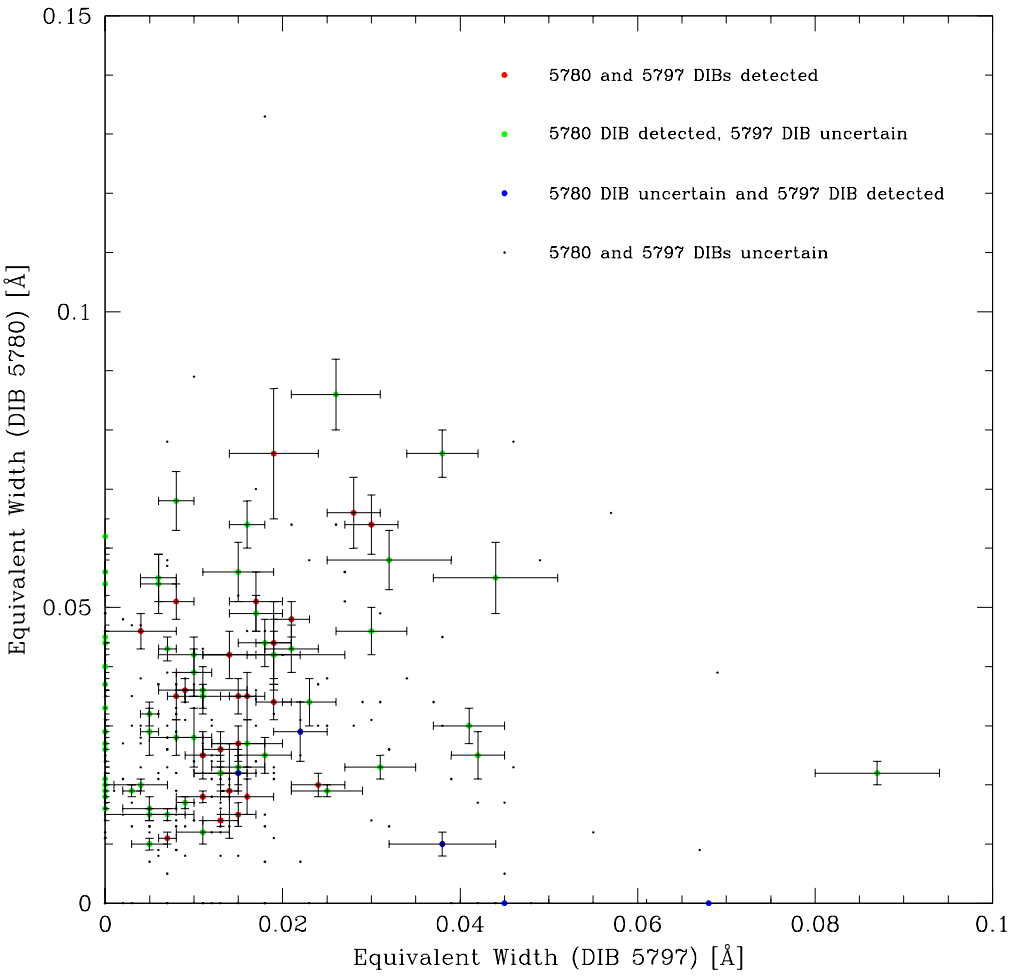

Figure 4.10: Correlation between the equivalent widths of the 5780 and 5797 Å DIBs for the Galactic component in the LMC sight-line.

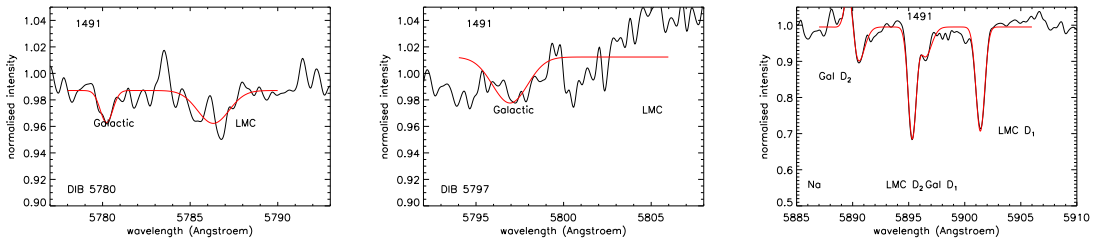

Figure 4.11: Profile of target 1491 showing the the unreliability of the 5797 Å DIB.

to draw any hard and fast conclusions from the plot. The one outlier here is target number 1491 (RA 5.63, Dec -69.0). Care must be taken with interpreting this point though as the legend shows that although the 5780 Å DIB has been detected there is some uncertainty about the 5797 Å DIB. The profile of this target (see Figure 4.11) confirms that I cannot have any confidence in the 5797 Å DIB and so this point should be discarded from any further analyses.

4.2.2 The neutral sodium D line and weakly ionized calcium K line

The correlation plots shown in this section are similar to those in the preceding section. However, in these plots it is only the detections where both the DIB and the Na I D_2 or Ca II K lines are certain that have been plotted in red points. The small dots represent the remaining sight-lines where it was not certain that absorption features were detected and are included to give an overview of any possible trend. Where there was obviously no absorption in one or other of the DIBs detected at all the points lie along the axes and are included for completeness.

The Na I D Doublet is well detected in the majority of the spectra for both the Galactic and Magellanic Clouds components and their detection does not appear to be affected by any other spectral feature. The D_2 absorption in the LMC is sometimes blended with the D_1 absorption in the Galactic component but as discussed in Chapter 2 and sections 4.2.5 and 4.2.5 of this chapter, the method of profile fitting successfully dealt with this. The Galactic component is often slightly affected by telluric emission as is the D_2 absorption in the LMC component, again the profile fitting accommodates this.

The 5780 Å DIB in the SMC and LMC

The correlation between the 5780 Å DIB and the Na I D_2 line in the SMC and LMC components are shown in Figure 4.12. There are more positive DIB detections in the LMC than in the SMC but in both cases some correlation can be seen.

In the SMC (top panel in Figure 4.12) there is a positive correlation between 5780 Å DIB EW up to ~ 0.065 Å and the Na I D_2 line EW up to ~ 0.3 Å. Within this range a large number of the uncertain absorption detections also appear to follow this correlation. This could mean that some of these absorptions are actually very weak detections and it does support the underlying trend of the correlation seen in the positive detections, as the majority of these dots will actually correspond to positive Na I D_2 detections where the 5780 Å DIB is uncertain and in a small number of cases the reverse relation is true. Outside of this range, 5780 Å DIB EW strengths greater than 0.08 Å only occur at Na I D_2 EW strengths of greater than 0.16 Å but weaker DIBs are also seen at those larger Na I D_2 EW strengths. This suggests that both weak and strong 5780 Å DIBs coexist where neutral gas abundance is relatively high. Below an Na I D_2 EW threshold of 0.08 Å it can not be certain that the 5780 Å DIB is present.

Similar relationships between the 5780 Å DIB and the Na I D_2 line can be seen in the LMC (bottom panel in Figure 4.12). Here the greater number of positive detections shows a stronger correlation with a significant number of the uncertain absorption detections also following the trend. As well as a greater number of detections the DIB and Na I D_2 EW absorption strengths are also stronger by a factor of ~ 2. There

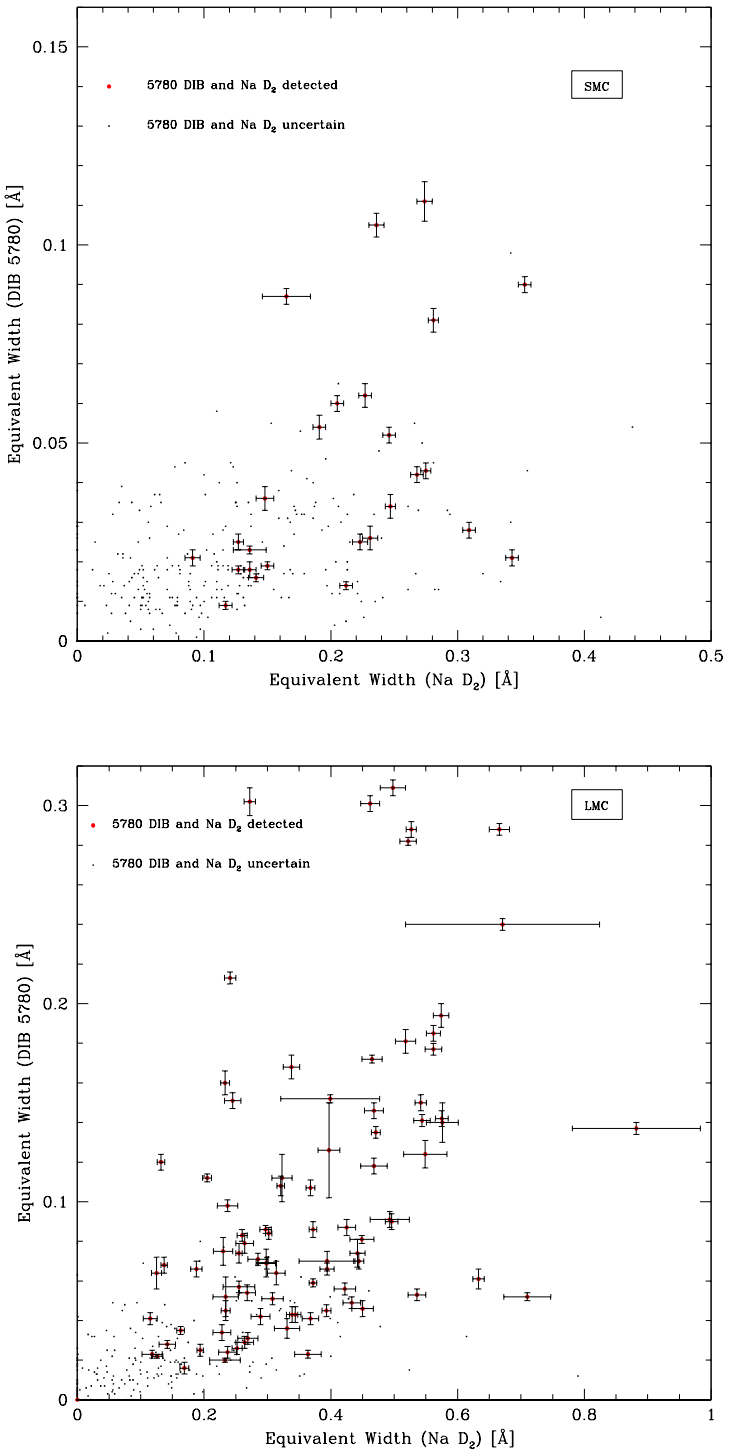

Figure 4.12: Correlation between the equivalent widths of the 5780 Å DIB and Na I D_2 line for (Top:) the SMC and (Bottom:) the LMC.

is a similar increase in the range within which a positive correlation is seen, that is, between 5780 Å DIB EW up to $\sim$ 0.2 Å and the Na I D_2 line EW up to $\sim$ 0.6 Å. Outside of this range, 5780 Å DIB EW strengths greater than 0.2 Å only occur at Na I D_2 EW strengths of greater than 0.25 Å, again weaker DIBs are also seen at those larger Na I D_2 EW strengths. For the LMC, the Na I D_2 threshold below which it can not be certain that the 5780 Å DIB is present, is an EW of 0.1 Å, very close to the SMC value and as the detections at such levels are very uncertain it seems there could be a common threshold below which the 5780 Å DIB is not present.

The 5780 Å DIB in the Galactic regions along the SMC and LMC sight-lines
The correlation between the 5780 Å DIB and the Na I D_2 line in the Galactic components along the SMC and LMC sight-lines are shown in Figure 4.13. There are about the same number of positive detections in both sight-lines although there are greater uncertainties in the Na I D_2 measurements than there were in the SMC and LMC. This is due to a combination of the shallower absorption lines in the Galactic components of both sight-lines and the presence of the telluric emission lines (see the profiles in Appendix C on the accompanying CD).

In the SMC sight-lines (top panel in Figure 4.13) a correlation can not be identified. There is a threshold of Na I D_2 EW strength below which it can not be certain that the 5780 Å DIB is present, this is an EW of 0.1 Å, similar to the threshold noted in the SMC and LMC. Above this level of Na I D_2 EW strength the 5780 Å DIB appears to be present with a wide range of strengths. However, it must be noted that the DIB strength in the Galactic component is about half that of the DIB strength in the SMC. Furthermore, if the SMC plot were capped at an 5780 Å DIB EW strength of 0.06 Å then the two plots would look very similar with a comparable amount of scatter and little evidence of a correlation.

This situation is mirrored along the line of sight to the LMC as can be seen in the bottom Figure 4.13. The threshold of Na I D_2 EW strength below which it can not be certain that the 5780 Å DIB is present, is again an EW of 0.1 Å. As for the SMC sight-line the plot shows scatter and when compared to the LMC plot the DIB

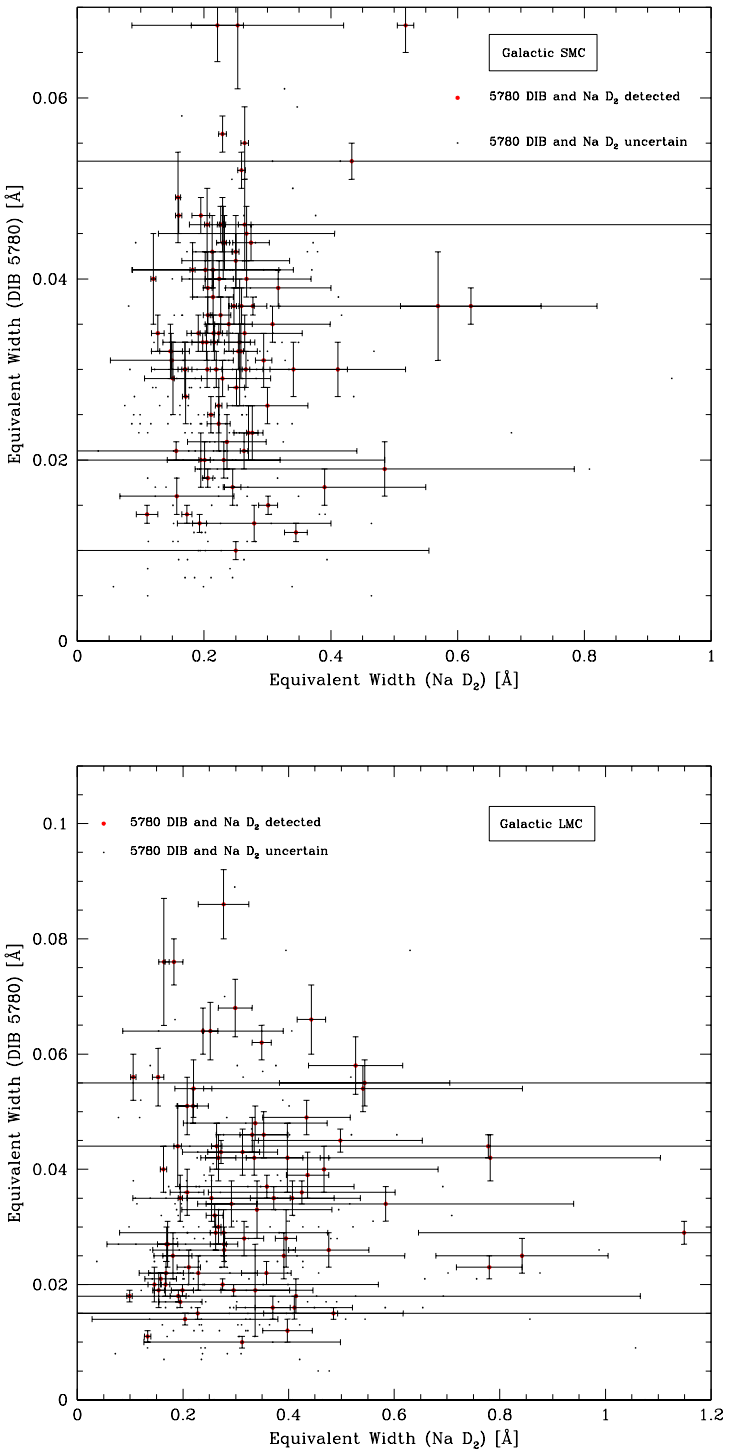

Figure 4.13: Correlation between the equivalent widths of the 5780 Å DIB and Na I D_2 line for the Galactic component in (Top:) the SMC sight-line and (Bottom:) the LMC sight-line.

strength in the Galactic component it is seen to be about a third of that in the LMC with a comparable amount of scatter when the two plots are compared up to a 5780 Å DIB EW strength of 0.1 Å.

The 5797 Å DIB in the SMC and LMC

The correlation between the 5797 Å DIB and the Na I D_2 line in the SMC and LMC components are shown in Figure 4.14. In common with the 5780 Å DIB there are more positive DIB detections in the LMC than in the SMC.

In the SMC (top panel in Figure 4.14) there are so few positive detections that no reasonable conclusions can be drawn from the data. Once again, below an Na I D_2 EW threshold of 0.08 Å it can not be certain that the 5797 Å DIB is present. The 5797 DIB is much weaker than the 5780 DIB (compare with Figure 4.12) but like the 5787 Å DIB it also seems to be stronger where there is a greater abundance of the Na I D_2.

There are a few more detections of the 5797 Å DIB in the LMC (bottom panel in Figure 4.14), though not enough to show there is a true correlation. The Na I D_2 threshold below which it can not be certain that the 5797 Å DIB is present is in agreement with all previous plots. The highest levels of EW strength for the 5797 Å DIB correspond to Na I D_2 EW strengths of greater than 0.25 Å but there are also weaker DIBs present at higher Na I D_2 abundances.

The 5797 Å DIB in the Galactic regions along the SMC and LMC sightliness

The correlations between the 5797 Å DIB and the Na I D_2 line in the Galactic components along the SMC and LMC sight-lines are shown in Figure 4.15.

These show a similar behaviour to the 5780 Å DIB. The threshold of Na I D_2 EW strength below which it can not be certain that the 5797 Å DIB is present, is the same at 0.1 Å, the strength of the DIB is weaker in the Galactic components than it is in the SMC and LMC components and greater scatter is shown in the Galactic components.

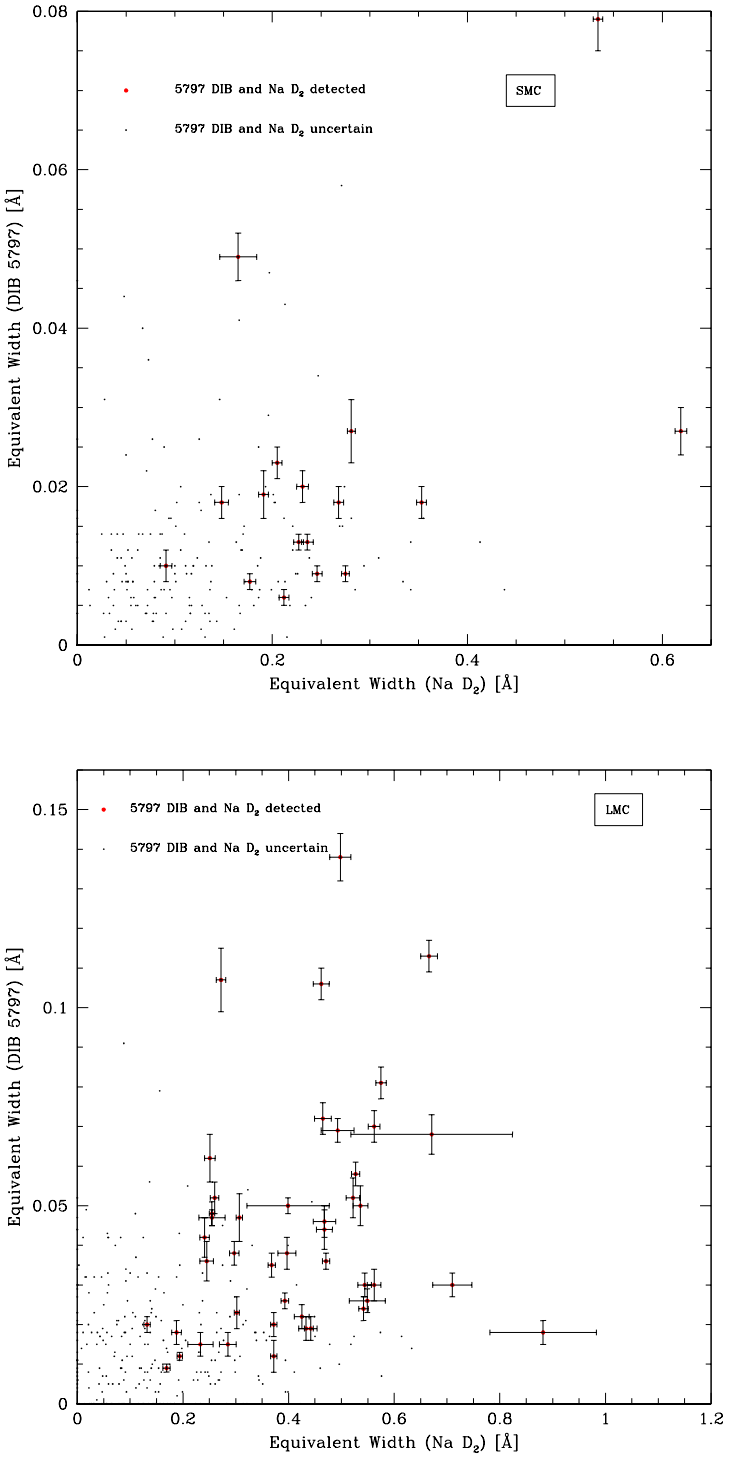

Figure 4.14: Correlation between the equivalent widths of the 5797 Å DIB and Na I D_2 line for (Top:) the SMC and (Bottom:) the LMC.

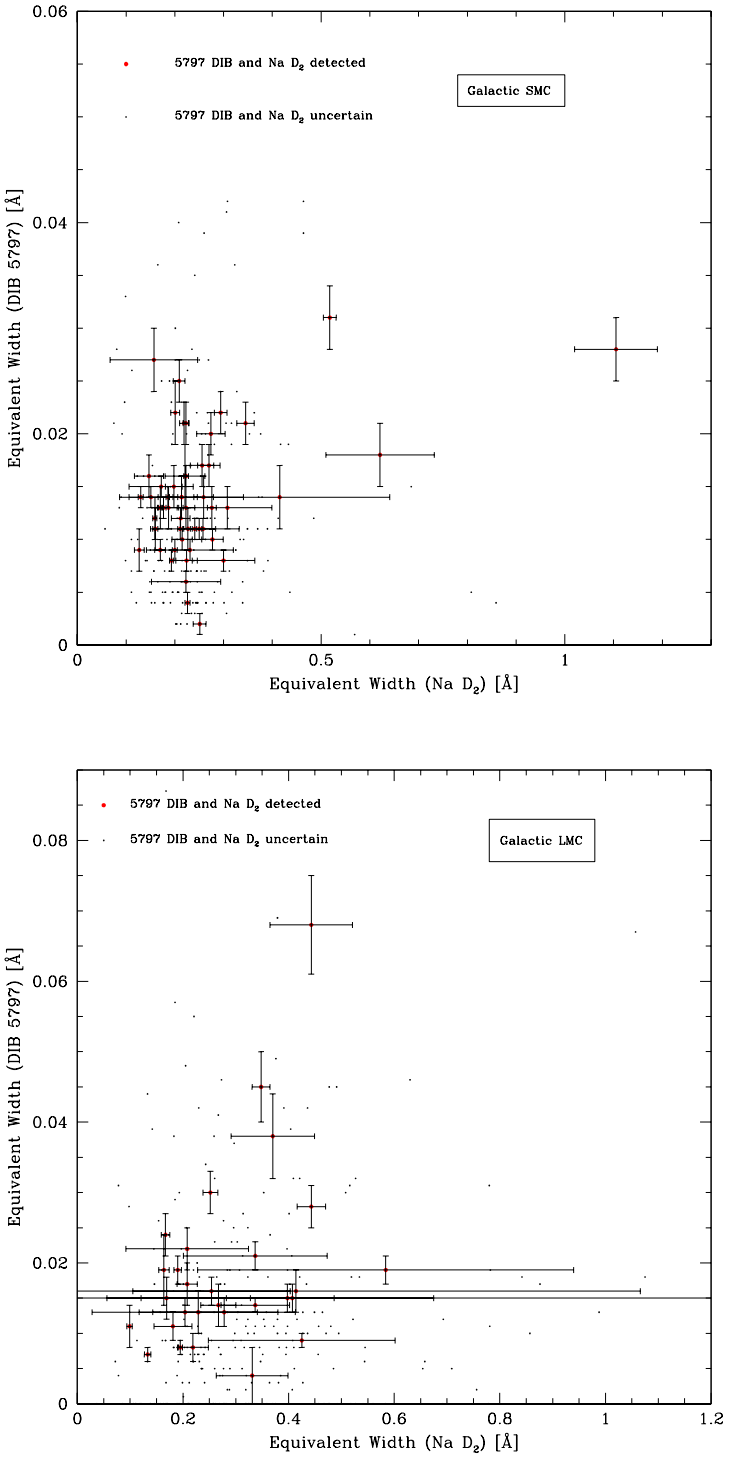

Figure 4.15: Correlation between the equivalent widths of the 5797 Å DIB and Na I D_2 line for the Galactic component in (Top:) the SMC sight-line and (Bottom:) the LMC sight-line.

Correlations between DIBs and the weakly ionized calcium K line

The weakly ionized calcium K line is well detected in the majority of the spectra for both the Galactic and Magellanic Clouds components. In all bar the Galactic component along the SMC sight-line two components of the Ca II K line were detected. As these two components could relate to different clouds or kinematically separated regions of one large cloud the correlations between the DIBs and the two features were plotted separately. To distinguish between the two detections in the same component they were labelled as blue (for the absorption feature towards the bluer end of the spectrum) and red (for the absorption feature towards the redder end of the spectrum). Some of the Ca II K lines appeared broadened indicating either the presence of a hot gas or that it originates from the photosphere of the target star. Profiles could not accurately be fitted for these lines and they are treated as null detections for the purpose of these correlations and the maps in sections 4.2.5 and 4.2.5 of this chapter.

The 5780 Å DIB in the SMC and LMC

The correlations between the 5780 Å DIB and the blue and red components of the Ca II K line in both the SMC and LMC are shown in Figures 4.16 and 4.17. As for the Na correlations there are more positive DIB detections in the LMC than in the SMC.

In the SMC plots, (Figure 4.16), no correlation between 5780 Å and the Ca II K line can be seen. There is scatter, not only in the positive detections but also in the uncertain detections. In the correlation plot for the blue Ca II K line the positive detections are scattered throughout the range of the EW strength for the Ca II K line, whereas for the red Ca II K line the certain detections are bunched up towards the weaker Ca II K detections. As will be seen in the following section 4.2.4 the two Ca II K components appear to probe different regions of the SMC. This observation (and others like it) is further explored in the discussion section.

There is also no correlation seen in the LMC plots, (Figure 4.17). In both cases there is scatter in the positive and uncertain detections. In both cases the majority of the scatter lies in the EW strength of the Ca II K line up to ~ 0.3 Å. The maps in section 4.2.4 relating to the LMC show a more uniform distribution of the Ca II K

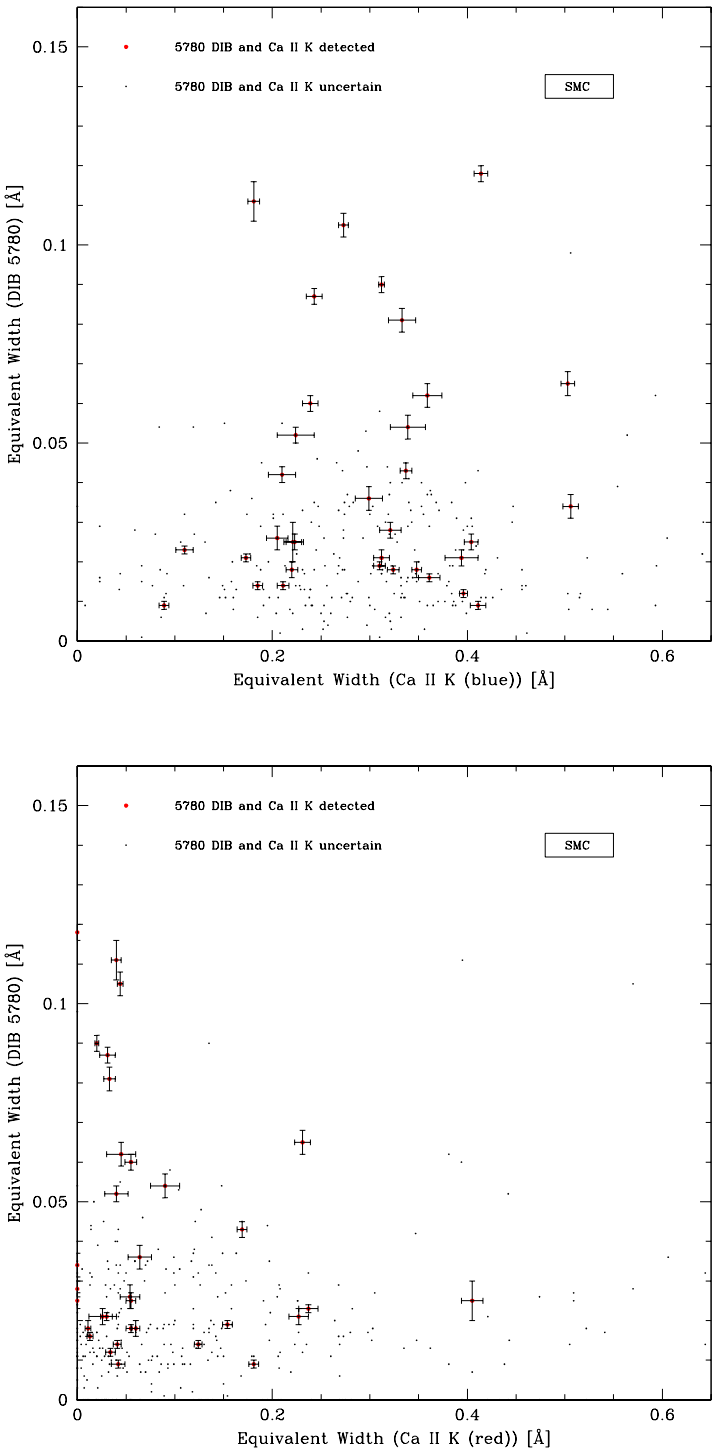

Figure 4.16: Correlation between the equivalent widths of the 5780 Å DIB and Ca II K line in the SMC for the (Top:) the blue component and (Bottom:) the red component.

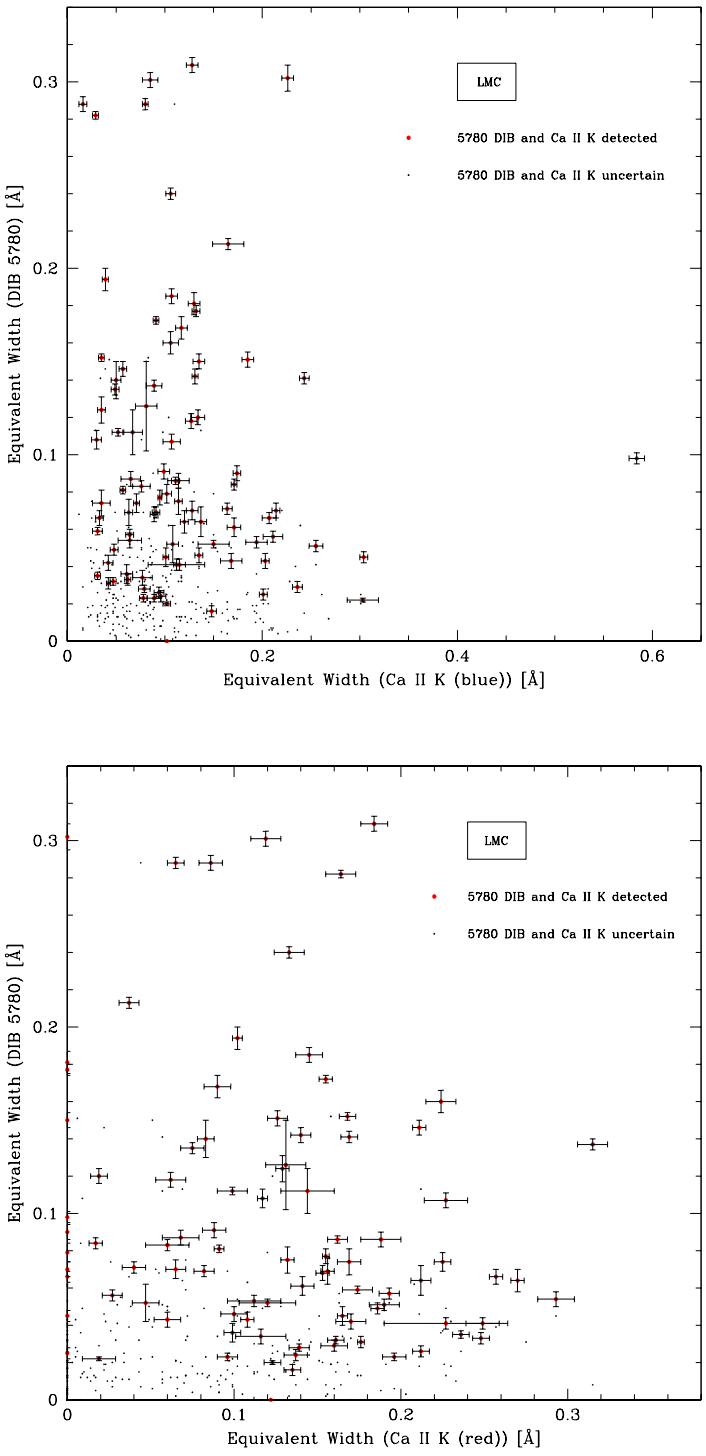

Figure 4.17: Correlation between the equivalent widths of the 5780 Å DIB and Ca II K line in the LMC for the (Top:) the blue component and (Bottom:) the red component.

absorption so although there does not appear to be any clear correlation between the 5780 Å and the Ca II K line there may be some link between them.

There is no clear threshold in Ca II EW below which the 5780 Å DIB is not detected.

The 5780 Å DIB in the Galactic regions along the SMC and LMC sight-lines

The correlations between the 5780 Å DIB and the Ca II K line in the Galactic component along the SMC sight-line and both the blue and red components of the Galactic component along the LMC sight-line are shown in Figures 4.18 and 4.19. There are more positive DIB detections along the SMC sight-line than in the SMC itself and a similar number along the LMC sight-line as there are in the LMC for both blue and red components.

In both the SMC and LMC sight-line plots for the Galactic component, no correlation between 5780 Å the Ca II K line can be seen. In the SMC sight-line the positive detections seem to be mainly within the EW strength for the Ca II K line range of 0.075 – 0.2 Å and the EW strength for the 5780 Å DIB range of 0.0 – 0.05 Å.

In both blue and red Galactic components along the LMC sight-line the scatter is evident in the positive and uncertain detections, there is not much difference in the pattern of the scatter with the exception that there does not appear to be any DIB detections below an EW strength for the Ca II K line of 0.04 Å. The strength of the DIB is weaker in the Galactic components than it is in the SMC and LMC components. Interestingly the maps of the blue and red components of the Ca II K line in the Galactic component towards the LMC sight-line do show a difference which does not seem to be reflected in the correlation plots. This observation is revisited in the discussion section.

The 5797 Å DIB in the SMC and LMC

The correlations between the 5797 Å DIB and the blue and red components of the Ca II K line in both the SMC and LMC are shown in Figures 4.20 and 4.21. As for the 5780 Å DIB there are more positive DIB detections in the LMC than in the SMC.

As for the 5780 Å DIB no clear correlations can be seen in these plots and there are fewer positive detections. However, there are similarities between the 5780 and 5797 Å DIB correlation behaviour. In the SMC, the blue Ca II K line positive detections are scattered throughout the range of the EW strength for the Ca II K line, whereas for the red Ca II K line the certain detections are again bunched up towards the weaker Ca II K detections. In the LMC the majority of the scatter lies in the EW strength of the Ca II K line up to ~ 0.3 Å. Therefore, it would seem both the 5780 and 5797 Å DIBs behave in a similar way in the presence of Ca II K.

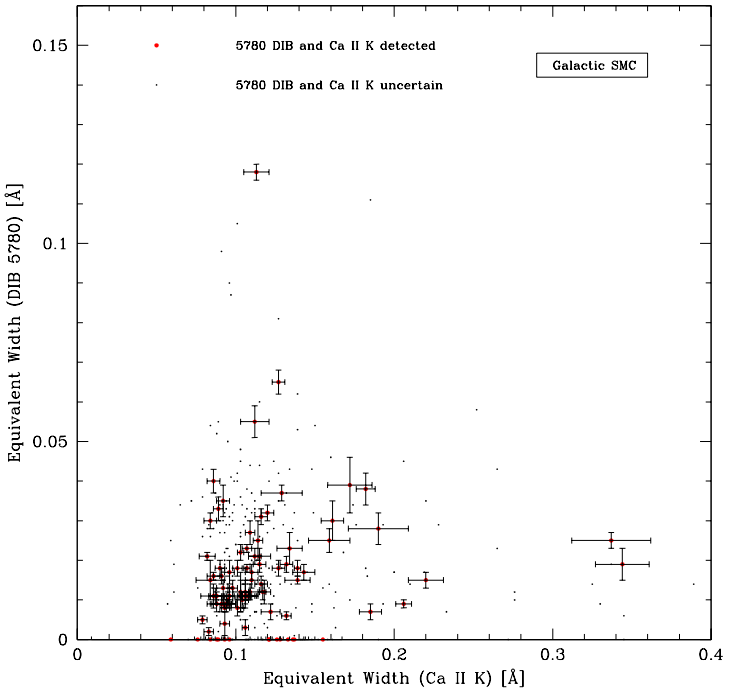

Figure 4.18: Correlation between the equivalent widths of the 5780 Å DIB and Ca II K line for the Galactic component along the SMC sight-line.

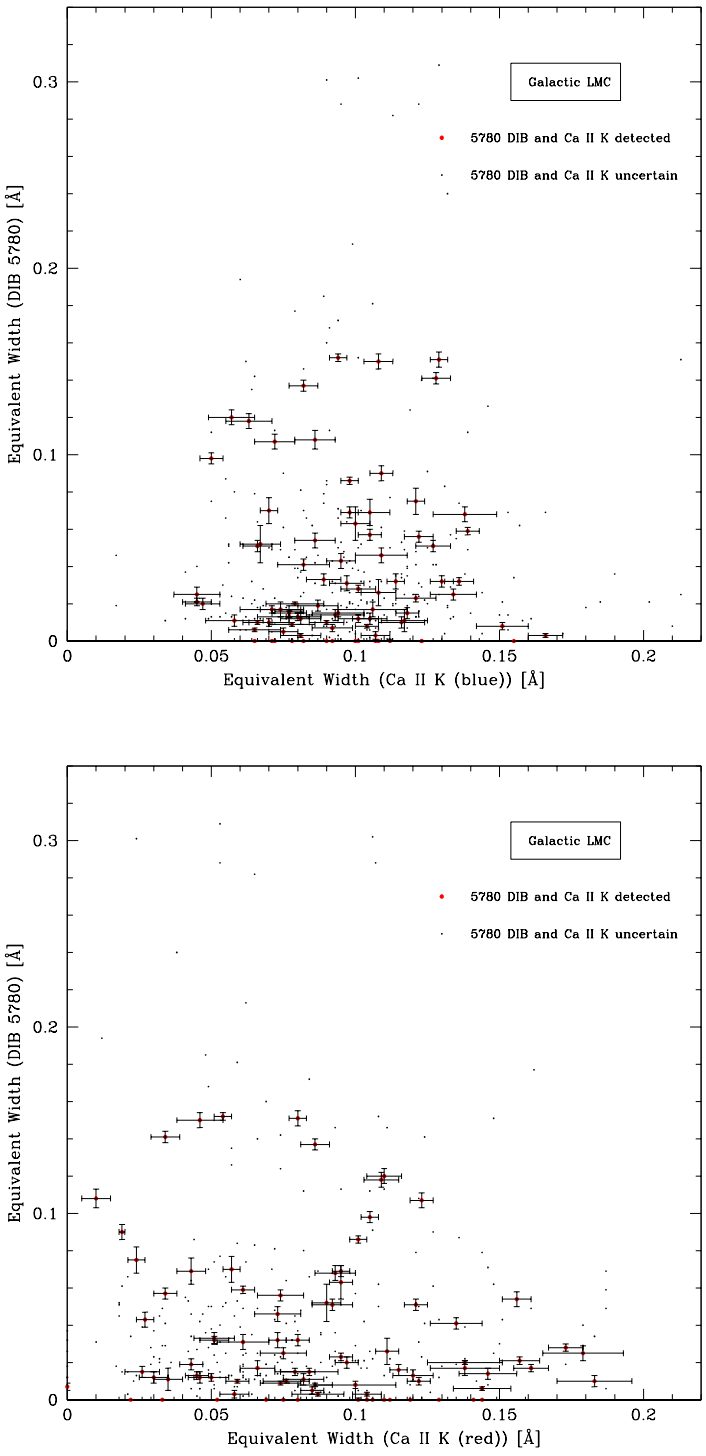

Figure 4.19: Correlation between the equivalent widths of the 5780 Å DIB and Ca II K line for the Galactic component for (Top:) the blue component and (Bottom:) the red component along the LMC sight-line.

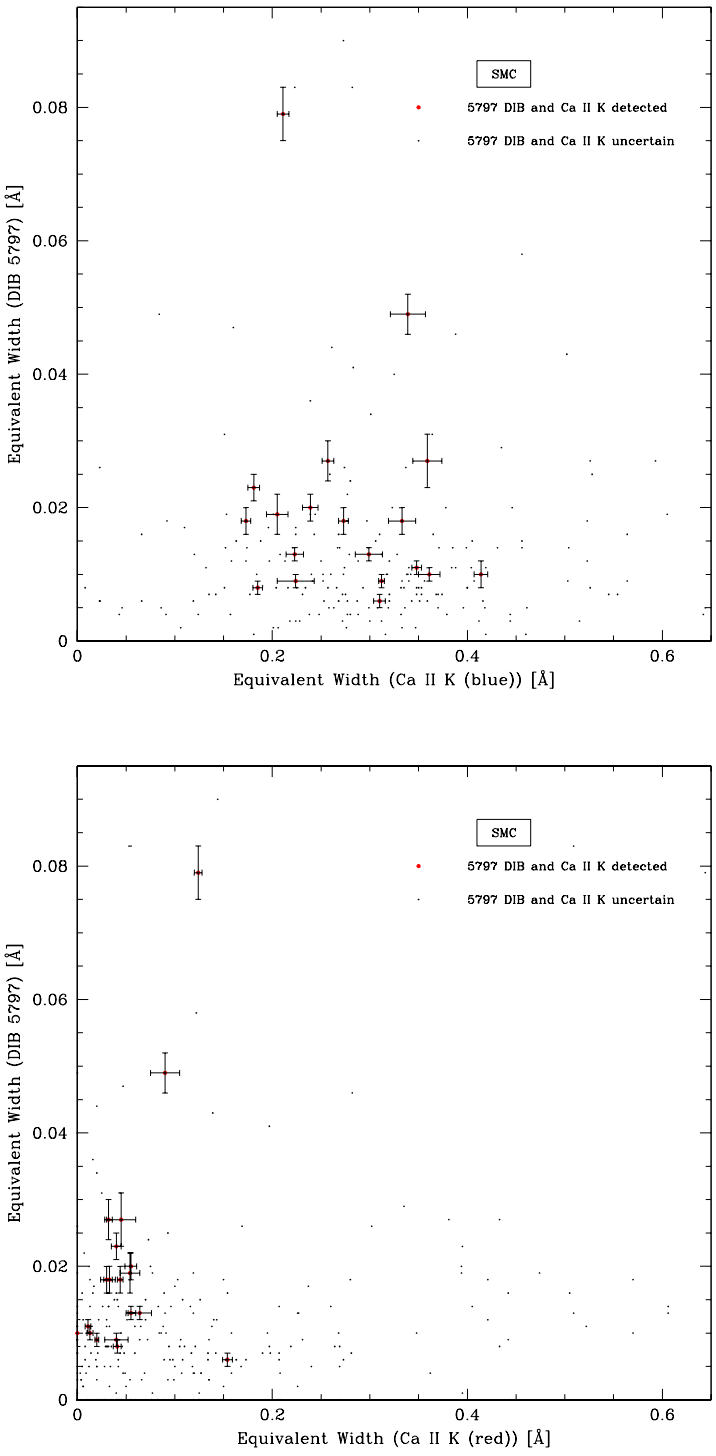

Figure 4.20: Correlation between the equivalent widths of the 5797 Å DIB and Ca II K line in the SMC for the (Top:) the blue component and (Bottom:) the red component.

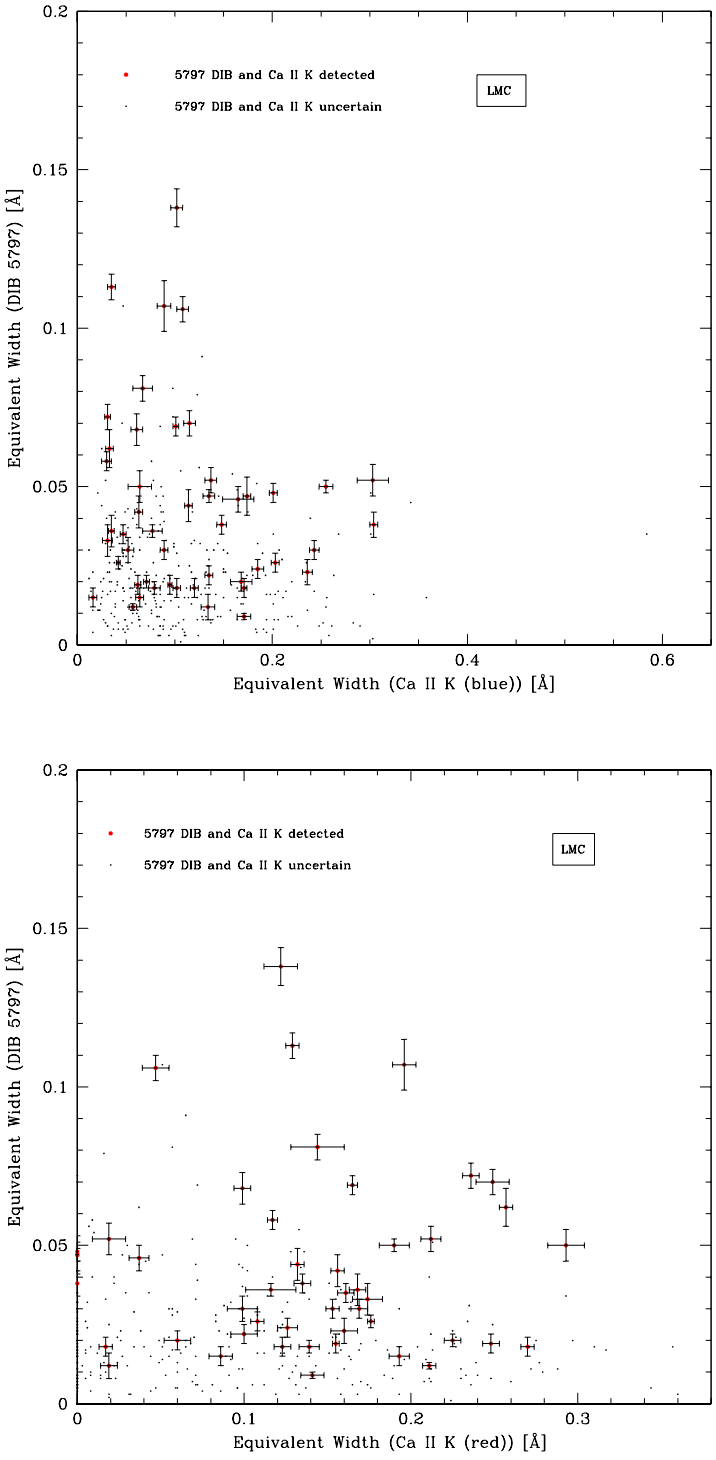

Figure 4.21: Correlation between the equivalent widths of the 5797 Å DIB and Ca II K line in the LMC for the (Top:) the blue component and (Bottom:) the red component.

The 5797 Å DIB in the Galactic regions along the SMC and LMC sight-lines
The correlations between the 5797 Å DIB and the Ca II K line in the Galactic component along the SMC sight-line and both the blue and red components of the Galactic component along the LMC sight-line are shown in Figures 4.22 and 4.23. There are more positive DIB detections along the SMC sight-line than in the SMC itself and but less along the LMC sight-line than there are in the LMC for both blue and red components.

These show a similar behaviour to the 5780 Å DIB. No correlation is obvious, again in the SMC sight-line the positive detections seem to be mainly within the EW strength for the Ca II K line range of 0.075 – 0.2 Å but for the 5797 Å DIB the EW strength is weaker at a range of 0.0 – 0.03 Å. In both blue and red Galactic components along the LMC sight-line the pattern of scatter is very similar to that seen in the 5780 Å DIB correlation plots.

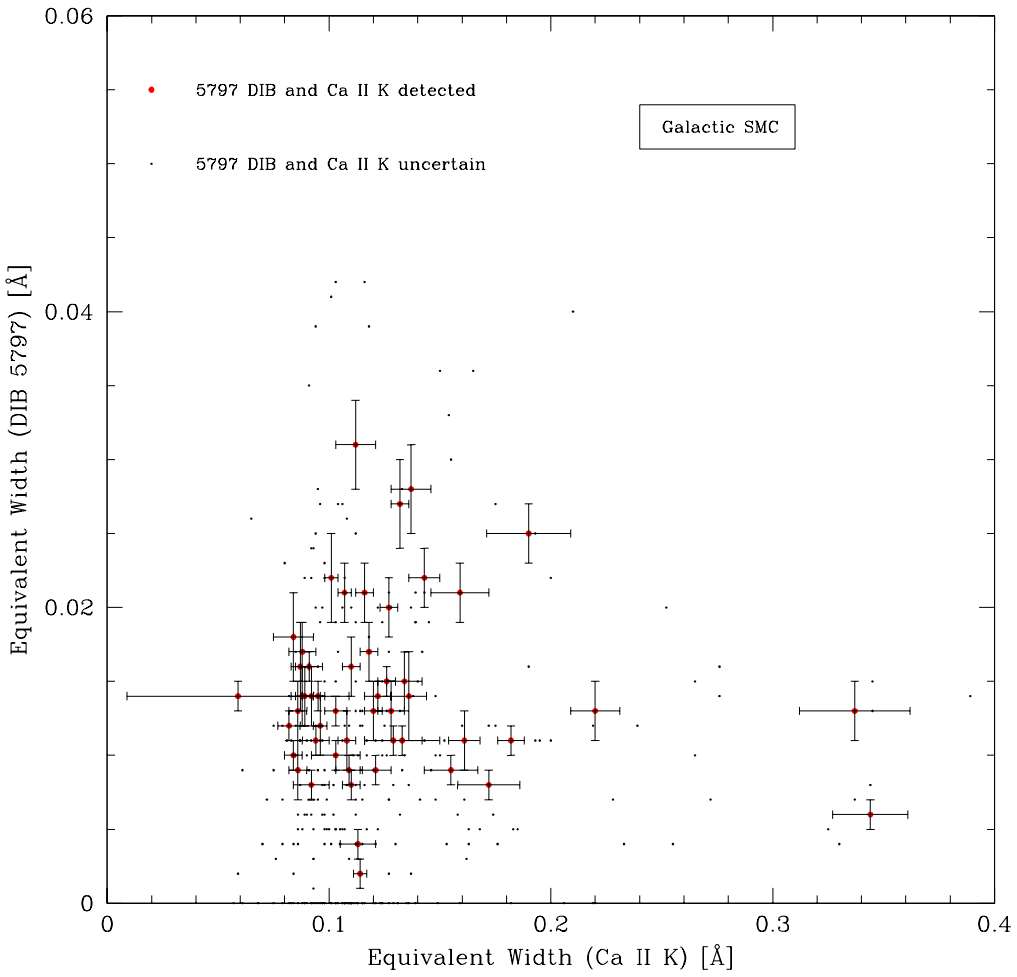

Figure 4.22: Correlation between the equivalent widths of the 5797 Å DIB and Ca II K line for the Galactic component in the SMC sight-line.

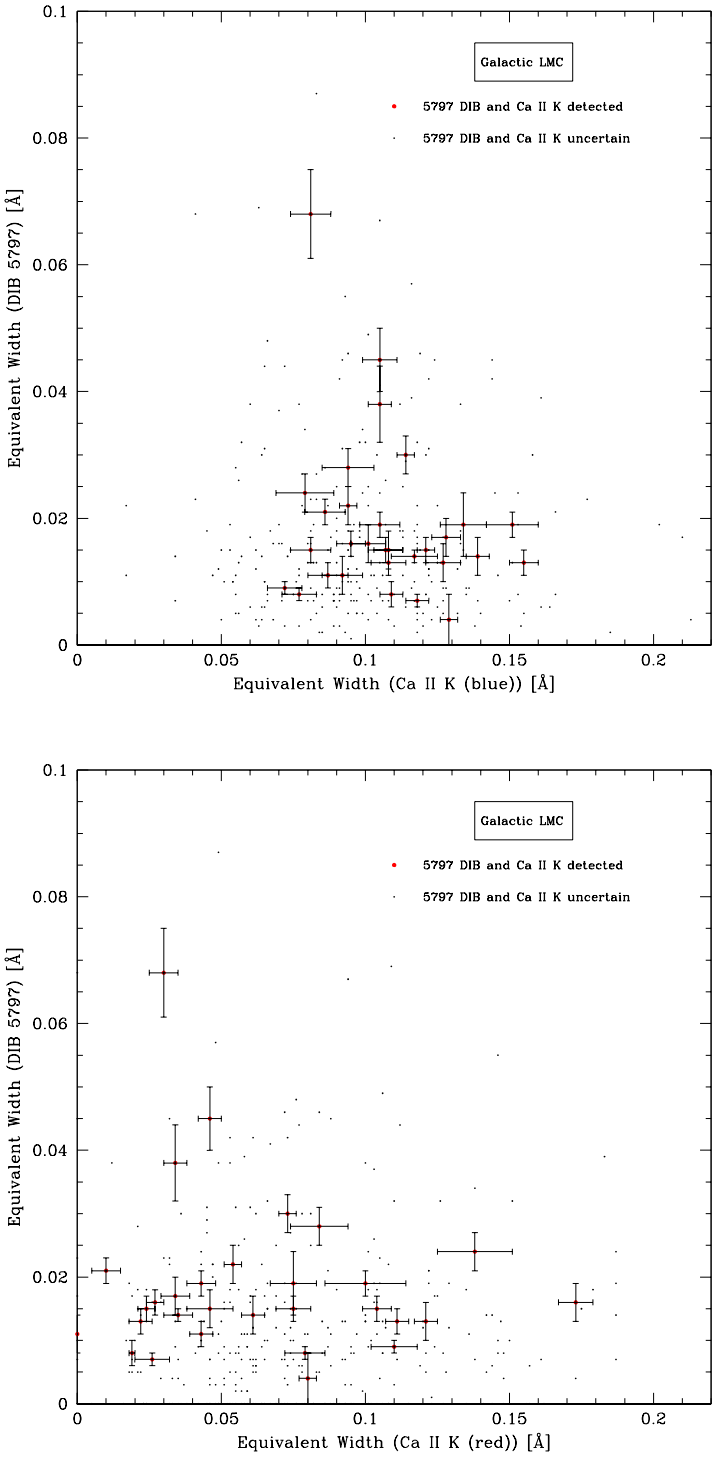

Figure 4.23: Correlation between the equivalent widths of the 5797 Å DIB and Ca II K line for the Galactic component for (Top:) the blue component and (Bottom:) the red component along the LMC sight-line.

4.2.3 Correlations; probing the ISM in the Magellanic Clouds and their Galactic foreground

Linear regression was used to calculate the correlation values between 5780 and 5797 Å DIBs and Student's *t*-test was used to determine the significance of these correlations figures in a similar manner to the approach used in Section 3.2.3. Tables 4.1 and 4.2 list the calculated correlation values between 5780 and 5797 Å DIBs together with their Student's *t*-test values and their corresponding critical values of *t*. As for the Local Bubble data the correlation coefficients were calculated for all data points for which I was certain I had a DIB detection. As noted from the plots in Section 4.2.1 I could be certain of DIB detections in relatively few spectra, particularly in the Galactic components of both the SMC and LMC data which showed a more widespread scatter of the data in the data for the SMC and LMC clouds themselves. This observation is substantiated by the correlation coefficients and *t* values shown in Tables 4.1 and 4.2.

For the SMC (Table 4.1) it is clear that there can be no confidence in the Galactic sight-line measurements. The error on the slope measurement is much greater than the measurement itself, the correlation coefficient is very small (0.085) and the *t* value (0.52) much less than its corresponding critical value of *t* (2.58). In the SMC itself, which had stronger DIB detections, the situation is different. Here the errors on the measurements are reasonable, the correlation coefficient is fairly strong (0.863) and at the *t* value (6.39) is larger than the critical value of *t* (2.98) which is quoted at the 99% confidence level as it was for the LB data, therefore I can have some confidence in the significance of these measurements. For the LMC (Table 4.2)the situation is similar; for the Galactic sight-line the errors are significant, the correlation coefficient is small (0.440) and the *t* value (2.35) is less than its corresponding critical value of *t* (2.81). Therefore, at the 99% confidence level I cannot say that these correlations are significant. However, it is interesting to note that the critical *t* value at a 95% confidence level for this relationship is 2.069 so at this level of confidence the measurements could be taken as significant. This could indicate that the trend is towards a significant

Table 4.1: Values of the correlation coefficients between the 5780 and 5797 Å DIBs for the SMC data; also showing the *t*-test values and the corresponding critical values of *t*.

5780/5797 Å	Galactic sight-line	SMC
Slope	0.160 ±0.311	2.972 ±0.465
Constant Å	0.032 ±0.005	0.007 ±0.005
Coefficient (r)	0.085	0.863
t-test	0.51	6.39
critical value of t	2.58	2.98

Table 4.2: Values of the correlation calculations between the 5780 and 5797 Å DIBs for the LMC data; also showing the *t*-test values and the corresponding critical values of *t*.

5780/5797 Å	Galactic sight-line	LMC
Slope	1.235 ±0.525	2.165 ±0.280
Constant Å	0.016 ±0.003	0.036 ±0.013
Coefficient (r)	0.440	0.766
t-test	2.35	4.13
critical value of t	2.81	3.06

correlation. As for the SMC the data for the LMC can be considered significan with a correlation coefficeint of 0.766, and the t value (4.13) being larger than the critical value of t (3.055), which is quoted at the 99% confidence level.

4.2.4 Global maps of the neutral ISM in the Magellanic Clouds

The maps presented in this and Section 4.2.5 were created with the IDL command CONTOUR with the keyword IRREGULAR applied so that IDL used a triangulation method to map the irregular points. This method produces a set of triangles from a set of points, such that a circle formed by connecting the vertices of any triangle does not contain any other data points. The maps give an impression of the density of the Ca II K, Na I D, 5780 Å DIB and 5797 Å DIB in the SMC, LMC and the foreground Milky Way along the sight-lines towards the SMC and LMC regions. In all maps, the sight-lines where I am confident I detected an absorption line are marked with little white squares, whereas the sight-lines where I did not or I was not certain I detected an absorption line are marked with little pink diamonds. Each plot shows the range of the absorption levels mapped in the bar above it. There are two main challenges to creating such maps, (i) the targets are non-uniformly distributed and quite sparse in some regions, (ii) it was often quite difficult to distinguish small scale structure (particularly for the DIBs) from the noise fluctuations. This means that in some cases the maps have been "filled up" between the sparsely distributed targets where detections were made and so do not show as much structure as areas where the majority of targets showed strong absorption lines. This is particularly noticeable for the DIB maps where not only relatively large areas for the equivalent width strengths are mapped but also the maps themselves are truncated because there is not enough information to extend the maps further. This does not mean that the DIB maps are unreliable, as it will be pointed out, even with this sparse sampling features in the DIB maps can be identified with features in the other maps. What it does mean, is that caution must be taken when interpreting these maps.

Most of the gas in the ISM is hydrogen, which has an ionisation potential of 13.6 eV. The ionisation potentials of CaII and Na I are 11.9 eV and 5.1 eV respectively, therefore both CaII and Na I will occur in regions of neutral hydrogen. The Na I/CaII ratio depends upon photo-ionisation, recombination and the differential depletion of

Na I and CaII onto grains. Recombination depends on electron density and Ca depletion is enhanced in regions that are sheltered from UV radiation. Therefore, the relative strengths of the Na I and CaII lines are generally sensitive to both the radiation field and to density. However, in the diffuse ISM it is probably the case that CaII predominantly traces weakly ionised gas and Na I traces neutral gas. This is the assumption upon which the discussion in this thesis is based.

Maps of the SMC

The weakly ionized calcium K line

Figure 4.24 clearly shows marked differences between the two components of the Ca II K line detected in the SMC. Many of the SMC components of the absorption profiles (see Appendix C on the accompanying CD for all plots) showed a double feature, some well separated as in target 317 and some with the redward feature blended and appearing as a "wing" on the blueward feature as in target 395 (see Figure 4.25).

From the profiles it appears that the blueward profile is the stronger of the two and with a significant portion of the targets showing the two features blended it was doubtful that any differences between the two maps would show up. The fact that the two maps are very different shows that the constraints chosen to fit the profiles managed to separate the two components, to a degree. The blueward map shows two areas of high Ca II K absorption. The corresponding regions on the redward map show a lesser amount of absorption but neighbouring regions show an increase in absorption where the blueward map has decreasing absorption. In addition the redward map shows a large relatively uniform region of absorption populated with clumps of high absorption in the South West region of the bar, whereas in the blueward map this region appears to be very empty. A clue as to how best to interpret these maps is given by the region around N66. The circle marking the location of N66 conveniently highlights a region which appears to be the "negative" of its counterpart in the other map. In the blueward map there seems to be a blue "wedge" surrounded by a green area yet in the redward map the same "wedge" shape is seen in green surrounded by blue. It is impossible to tell from these data if the Ca II K line is associated with N66.

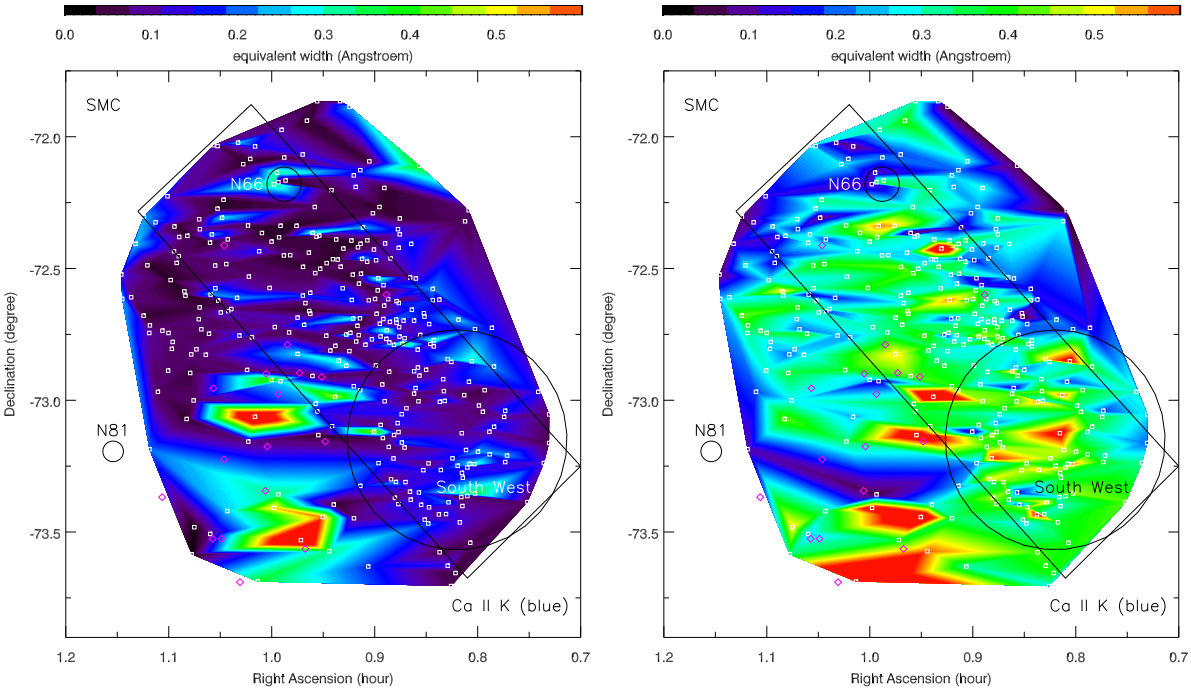

Figure 4.24: Equivalent width maps of (Left:) the Ca II K line for the blueward absorption line, and (Right:) the redward absorption line in the SMC. The rectangle represents the SMC bar and the circle represents an area containing giant molecular clouds and is a star forming region.

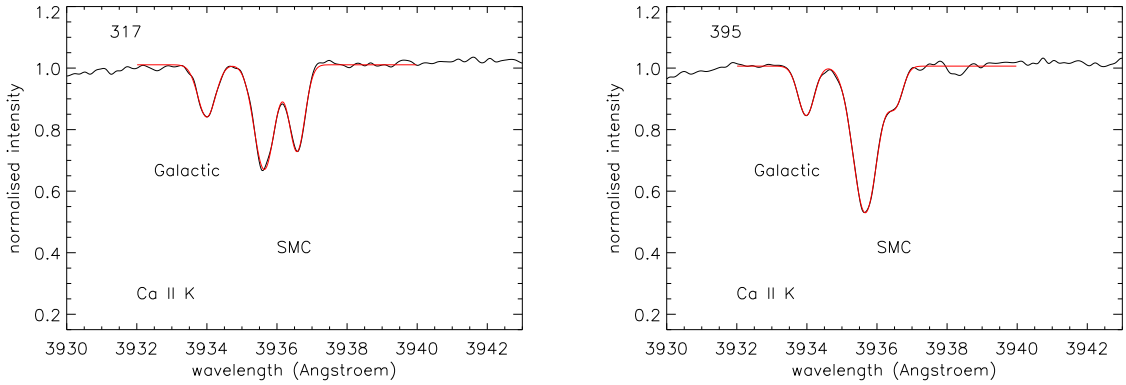

Figure 4.25: Profiles of the Ca II K line showing the double feature in the SMC component for (Left:) target 317 and (Right:) target 395.

Taking the profiles and the maps together the most likely interpretation is that the redward feature is highly contaminated by the blueward feature and the level of absorption is inflated to the detriment of the absorption values for the blueward component. On the other hand the differences between the two maps in the South East region which show distinct regions of high absorption in both maps that do not seem to link to one another would indicate that there are either two distinct clouds along this line of sight or one large patchy cloud. It could also be that the blue component is a Galactic Halo High Velocity Cloud. From these Ca II K maps I cannot say for certain which is the true scenario but conclude that the likely contamination of the redward feature coupled with the "negative" feature around N66 indicates this is one large cloud with different regions of the clouds being shown by the distinct features in the South East region.

The neutral sodium D line

The maps showing the Na I D absorption in Figure 4.26 show a strong correlation with each other. In the SMC the D_1 and D_2 components of both the SMC and the Galactic

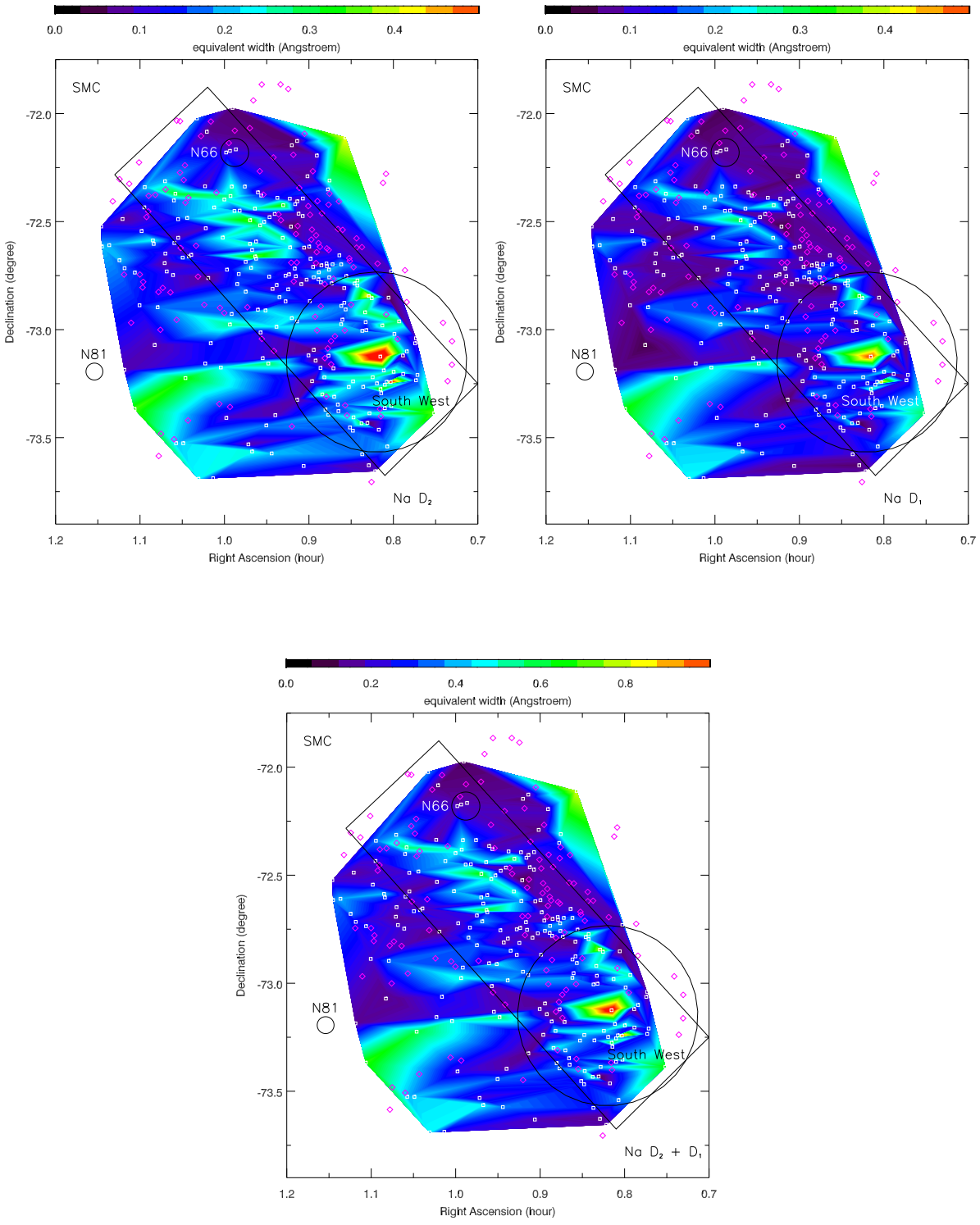

Figure 4.26: Equivalent width maps of (Top left:) the Na I D_2 absorption line, (Top right:) the Na I D_1 absorption line and (Bottom:) the sum of the absorption lines in the SMC. The rectangle represents the SMC bar and the circle represents an area containing giant molecular clouds and is a star forming region.

foreground are well separated allowing the profile of each feature to be accurately fitted. The top maps in Figure 4.26 show the equivalent widths of the individual Na Components, comparing the two I can see that where there is absorption in the Na I D_2 line there is a corresponding, albeit weaker, absorption in the Na I D_1 line. Comparison with the Ca II K maps shows that the Ca II K has a larger filling factor than Na I, as it corresponds to generally hot gas.

As the individual maps are so well correlated a map of the combined Na I D_1 and D_2 components was created to enhance the structural features shown. The Na absorption displays some structure in the bar of the SMC with a greater concentration in the star forming South West region yet being absent in the region around N66. The green area in the South East of the map stretching out towards N81 traces the wing of the SMC but it must be noted that there is a lack of sight-lines with good detections in this area and so there may not actually be the extensive band of uniform Na absorption that is indicated here. Similarly there are regions along the two long edges of the SMC bar that lack sight-lines with good detections. In these areas there may be more Na present than is indicated.

The 5780 and 5797 Å DIBs

The maps showing the equivalent widths of the 5780 Å and 5797 Å DIBs in Figure 4.27 cover only a small region of the whole target field. The data collected for the SMC were not as good quality as those collected for the LMC due to observing through cloud and dome closure as a result of bad weather. Therefore, it was particularly difficult to separate the signal from the noise in the majority of cases. This resulted in just 31 sight-lines for the 5780 Å DIB and 20 sight-lines for the 5797 Å DIB out of a total of 329 sight-lines which could be used to create the maps (see Figure 4.28 for examples of good and bad DIB detections in the SMC data).

Despite the poor number of targets available to create maps significant differences are seen between the 5780 Å DIB and the 5797 Å DIB. Generally speaking where the 5780 Å DIB is detected the 5797 Å DIB is absent. One exception to this is in the South West region where a high intensity of both DIBs is represented by red patches.

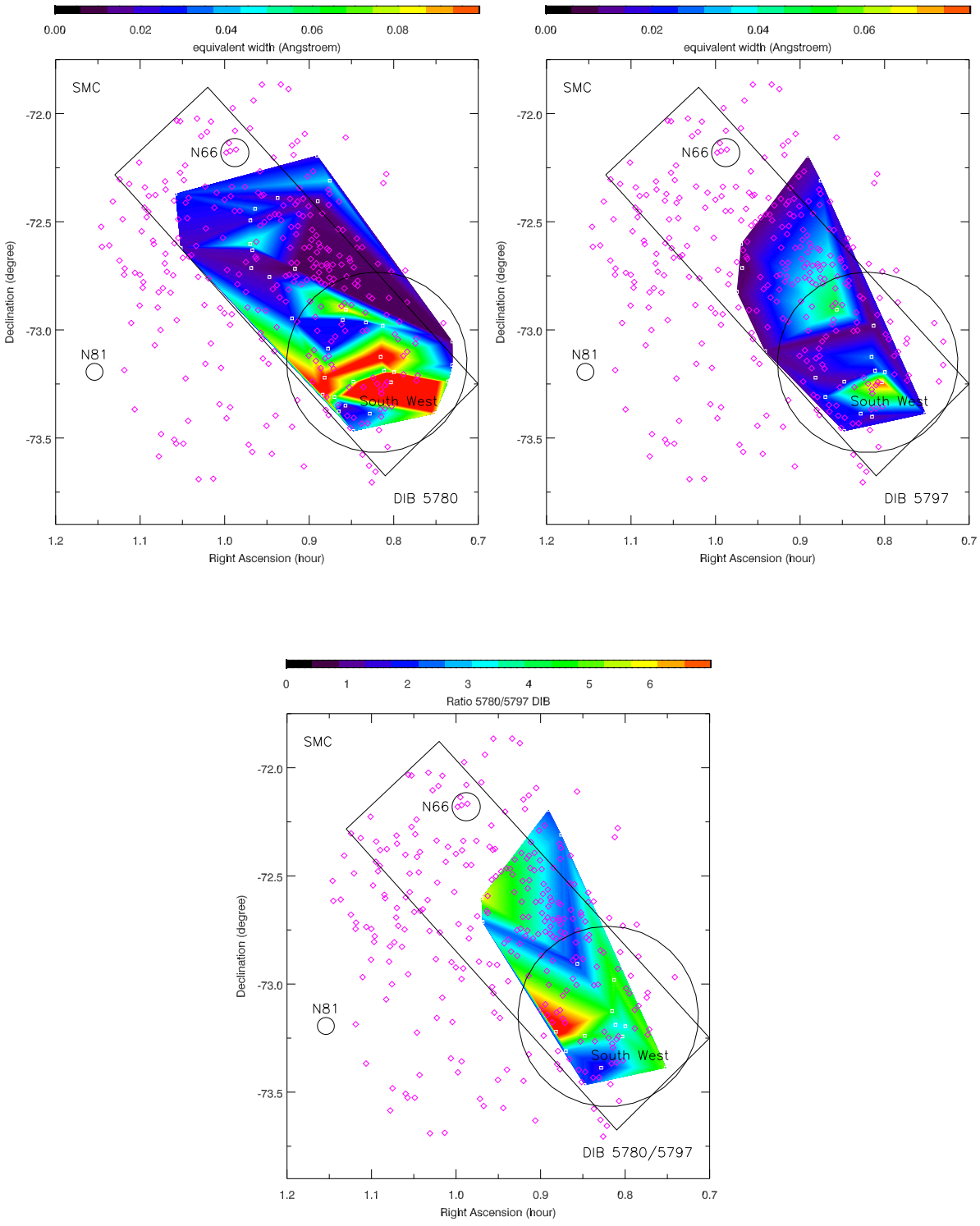

Figure 4.27: Equivalent width maps of (Top left:) the 5780 Å DIB absorption line, (Top right:) the 5797 Å DIB line and (Bottom:) the ratio of the 5780/5797 Å DIBs in the SMC. The rectangle represents the SMC bar and the circle represents an area containing giant molecular clouds and is a star forming region.

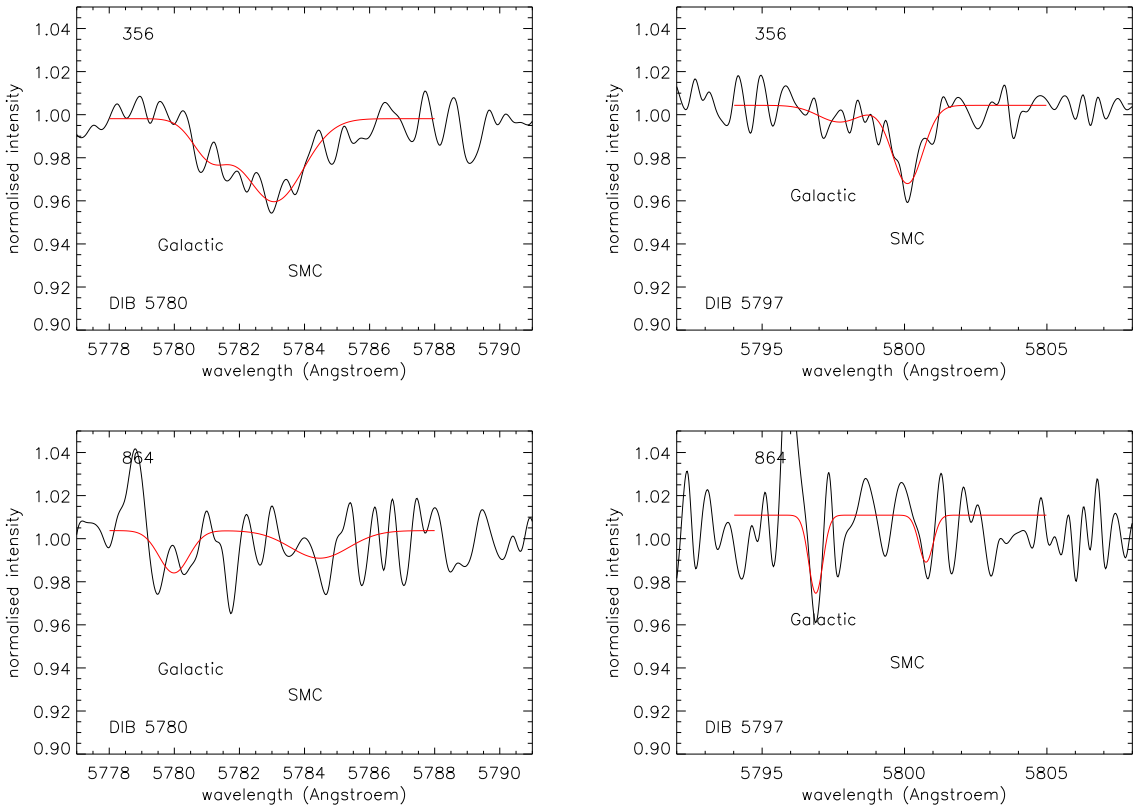

Figure 4.28: Profiles of the 5780 and 5797 Å DIBs showing (Top:) a good detection if target 356 and (Bottom:) a bad and unreliable detection in target 864.

As the 5780 Å DIB is generally observed in ionised regions, whereas, the 5797 Å DIB is observed in molecular regions, it is expected that these maps should show these differences. The region where both seem to be present can be reconciled with the idea of the 'skin-effect' in clouds, where the centre of the cloud is more dense and molecular in nature than its diffuse and ionised envelope or 'skin', which corresponds to a "σ-type cloud". This effect has been observed in the interstellar clouds in front of ω Centauri (van Loon et al. 2009). Krełowski & Sneden (1993) described σ-type clouds as regions in which only the 5780 Å DIB is present or where it is very much stronger than the 5797 Å DIB; the name arises from the similarity in the 5780/5797 Å DIB ratio observed in the spectrum of σ Sco (HD 147165) by Krełowski & Westerlund (1998) and Krełowski & Walker (1987). This type of cloud is not usually seen in the relatively warm and diffuse regions of the ISM but the region highlighted by the maps correspond to a star forming region there is a distinct possibility such a cloud has been detected in this case.

Maps of the LMC

The weakly ionized calcium K line

As in the case for the SMC, two components of the Ca II K line were detected in the LMC (see Figure 4.29) although they are not as well separated as they are in the SMC nor is one component consistently stronger than the other (see Figure 4.30).

Although it is practically impossible to differentiate between these two components when looking at the profiles the constraints chosen to fit the profiles has resulted in equivalent widths, which when plotted, show marked differences in the maps. The area around SN1987A both to the North and South East show a similar "negative" region in the redward map when compared to its blueward counterpart, with strong Ca II K absorption being shown around SN1987A in the blueward map and an absence of it in the redward map. Other than that there appears to be uniform distribution of the gas with some areas showing greater density of Ca in differing regions of both maps. Given the profile of these two components is heavily blended there is likely to

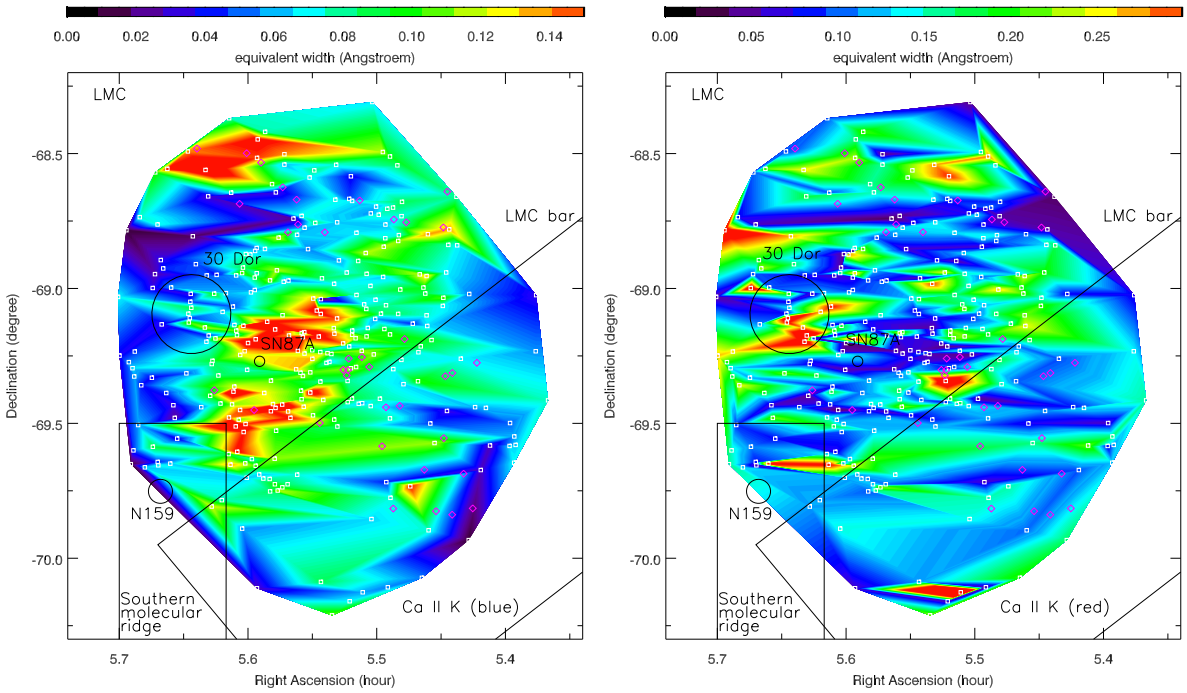

Figure 4.29: Equivalent width maps of (Left:) the Ca II K line absorption for the blueward absorption line, and (Right:) the redward absorption line in the LMC.

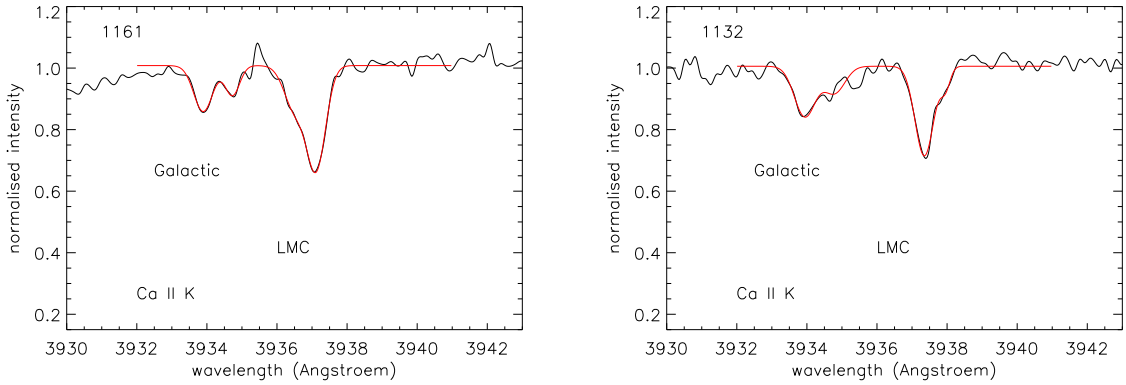

Figure 4.30: Profiles of the Ca II K line showing the double feature in the LMC component for (Left:) target 1161 showing a blueward wing and (Right:) target 1132 showing a redward wing.

be some cross contamination between the two levels of absorption measured. For the LMC the conclusion is that this represents a large cloud, possibly in the Halo of the Milky Way (inferred from the global distribution of the Ca II K shown in both maps) with some areas of denser material.

The neutral sodium D line

The velocity separation between the MW and the LMC is coincidentally similar to the separation between the Galactic D_1 and LMC D_2 components of the Na absorption lines. This results in these two features being blended in the line profiles, in some cases appearing as if it is a single absorption line. The majority of the targets show evidence of two components in the profile with a few showing a significant difference enabling profiles to be fitted to the individual components, see Figure 4.31 for examples of the profile fitting. As the D_1 and D_2 arise from the same electronic transition, and therefore have a fixed distance between them, it is relatively simple to fix the separation and match their widths for the two profiles in each of the Galactic and LMC absorption

features so it is with some confidence that the equivalent width values of the blended components can be separated and used to create representative maps as shown in Figure 4.32.

These maps show there is a strong correlation between the two Na components in the LMC and justify the method used to separate the blended Galactic/LMC profiles. Comparing the two maps in the top panel of Figure 4.32 I can see, as expected, that where there is absorption in the Na I D_2 line there is a corresponding, albeit weaker, absorption in the Na I D_2 line. This was also noted for the SMC where all four components of the Galactic and LMC Na I D lines were well separated, so again justifying my profile fitting methods. As the individual maps are so well correlated a map of the combined Na I D_1 and D_2 components was created to enhance the structural features shown.

Here, in the LMC, the concentration of the Na absorption lies around the 30 Dor and Southern molecular ridge regions. This is expected as these regions are areas of star formation and so contain molecular material. Therefore, it is likely that the Na I D absorption is connected to gas in these regions. The lack of Na absorption mapped in the LMC bar must be interpreted with caution. The pink diamonds on the map show sight-lines of no or of uncertain Na absorption and they dominate the sight-line symbols in the LMC bar region. Where the white squares are shown in the LMC bar (representing sight-lines where Na was detected) some structure is shown, indicating that if detection of Na along these sight lines had been more certain more structure would be shown. Contrast this to the area north of the LMC bar where many sight-lines do show some, if weak, absorption. The lack of absorption shown in this area would seem to be a true reflection of the environment there. Figure 4.33 shows profiles where in the top panel there is an uncertain detection in the LMC bar (target 344, at RA 5.46, Dec -69.5), in the middle panel, a positive but weak detection to the North of the LMC bar (target, 737, at RA 5.50, Dec -69.0) and in the bottom panel negative detection to the North of the LMC bar, (target, 242 at RA 5.45 and Dec -68.6), thus illustrating the reasoning behind the interpretation of the Na maps.

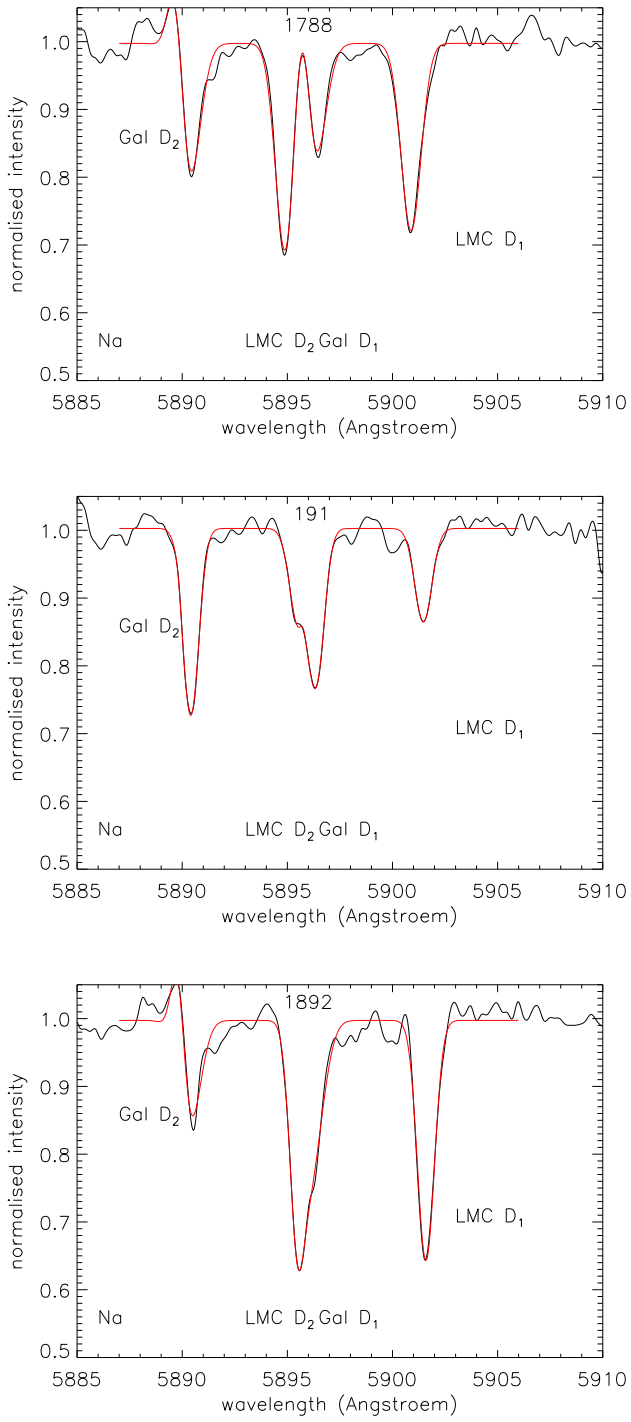

Figure 4.31: Profiles of the Na I D_1 and D_2 absorption lines. Showing (Top:) an example of good separation between the Galactic Na I D_1 and the LMC Na I D_2 lines, (Middle:) a typical blended profile showing evidence of the two components and (Bottom:) an example where the fact there are two components is barely noticeable.

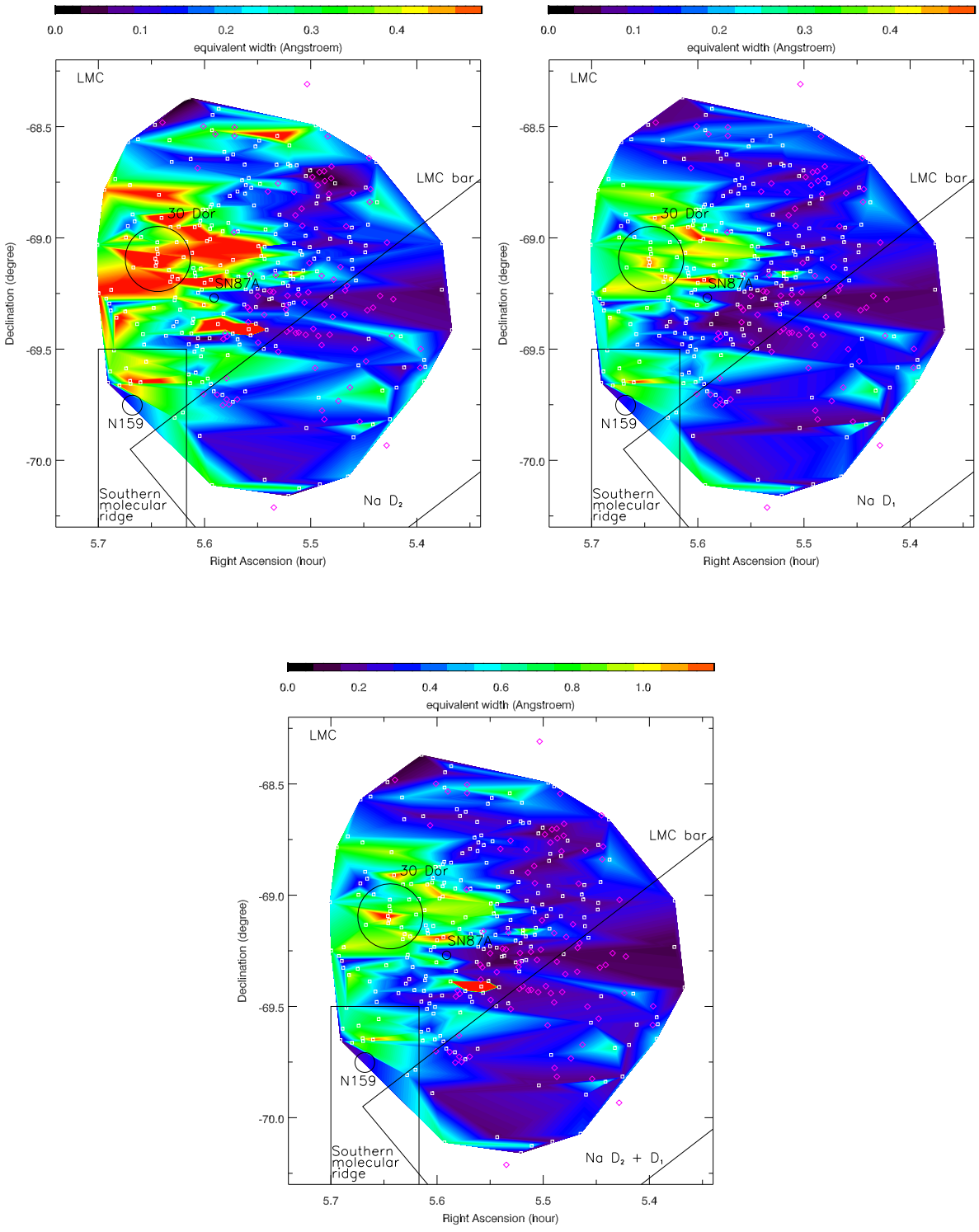

Figure 4.32: Equivalent width maps of (Top left:) the Na I D_2 absorption line, (Top right:) the Na I D_1 absorption line and (Bottom:) the sum of the absorption lines in the LMC.

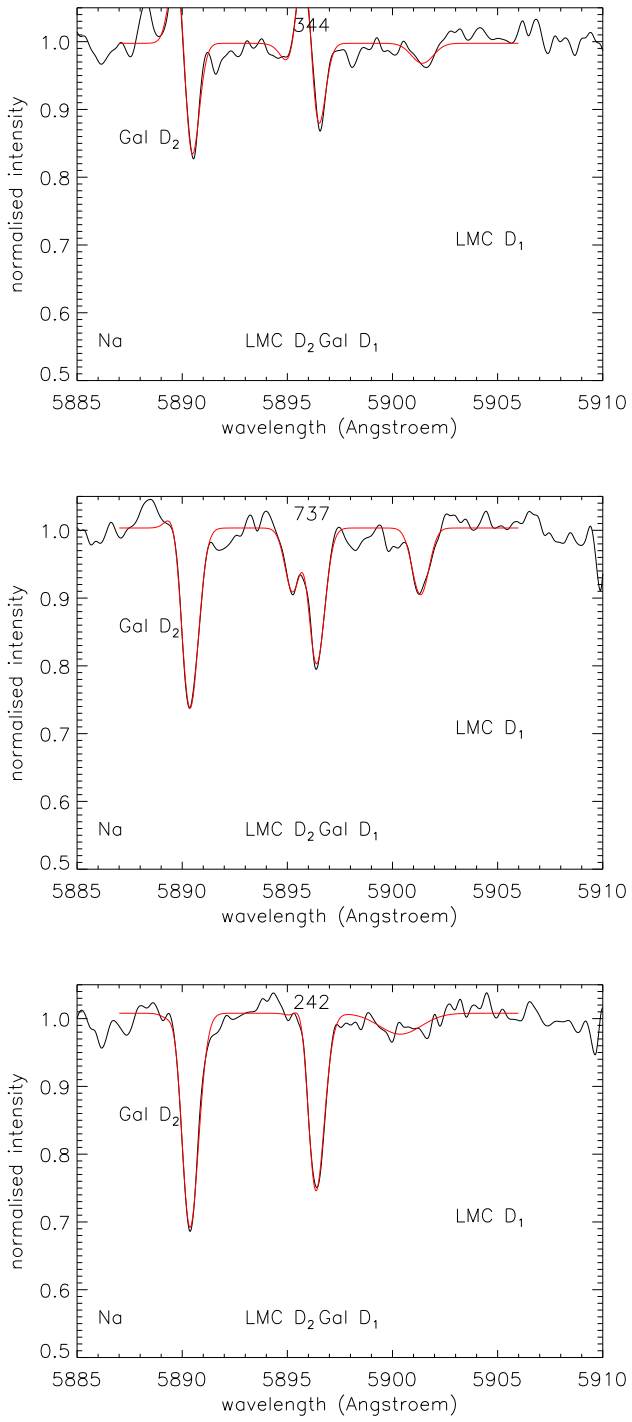

Figure 4.33: Profiles of the Na I D_1 and D_2 absorption lines. Showing (Top:) an uncertain detection the the LMC bar region, (Middle:) a positive but weak detection to the North of the LMC bar and (Bottom:) a negative detection to the North of the LMC bar.

The 5780 and 5797 Å DIBs

The maps showing the equivalent widths of the 5780 Å and 5797 Å DIBs in Figure 4.34 cover a larger region of the whole target area than their SMC counterparts. The data collected for the LMC was of a better quality than that collected for the SMC. This resulted in just 91 sight-lines for the 5780 Å DIB and 43 sight-lines for the 5797 Å DIB out of a total of 329 sight-lines which could be used to create the maps (see Figure 4.35 for examples of good and bad DIB detections in the LMC data).

Although there are far more sight-lines without reliable detections than with, significant differences are seen between the 5780 Å DIB and the 5797 Å DIB and each map shows some structure which was not possible to determine in the SMC maps. In both DIB maps the region to the South and West of 30 Dor and above SN1987A show that both DIBs are present. Like the south west region in the SMC, this is an area of star formation and it is likely I am seeing the 'skin-effect' for a cloud again. Further evidence for this lies in the relative absorption levels between the two DIBs. The 5780 Å DIB is the stronger of the two DIBs yet the maps show I am detecting far more of the 5797 Å DIB than I am of the 5780 Å DIB; note that the intensity levels of the two maps are on different scales with the range for the 5780 Å DIB being a third of the range for the 5797 Å DIB. This means I must be observing a molecular cloud and as this is a well known star forming region I can be confident in that conclusion. The fact I also detect a very small amount of the 5780 Å DIB in the same means I must be seeing a transitional region between the molecular cloud and its diffuse surroundings, the 'skin-effect'. This is also supported by the detection of some of the 5780 Å DIB stretching out to the east of 30 Dor and where there is no 5797 Å DIB counterpart, indicating that this is now an ionised region and the transition between the molecular cloud and its diffuse surroundings has been completed. Interpreting the rest of the map is quite difficult as the majority of the sight-lines are poor. However, it seems to hold true that where the 5797 Å DIB is detected the 5780 Å DIB is absent even though it is likely the detection of the 5797 Å DIB is not quite as extensive as the map indicates. With so few good detections the map has been "filled" to connect a few sight-lines of relatively strong absorption. What is clear though is that there is no 5780 Å DIB detection in that region.

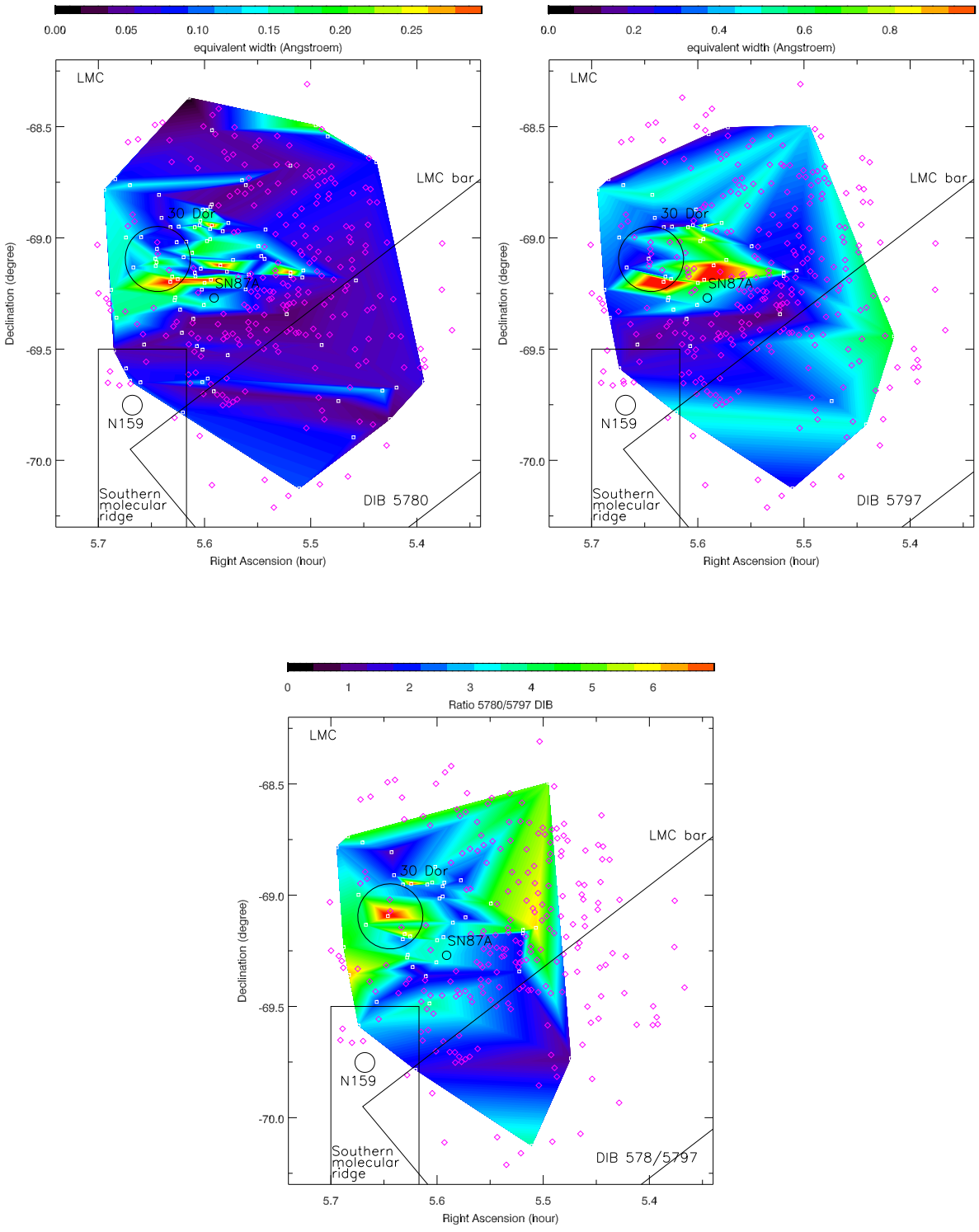

Figure 4.34: Equivalent width maps of (Top left:) the 5780 Å DIB absorption line, (Top right:) the 5797 Å DIB line and (Bottom:) the ratio of the 5780/5797 Å DIBs in the LMC

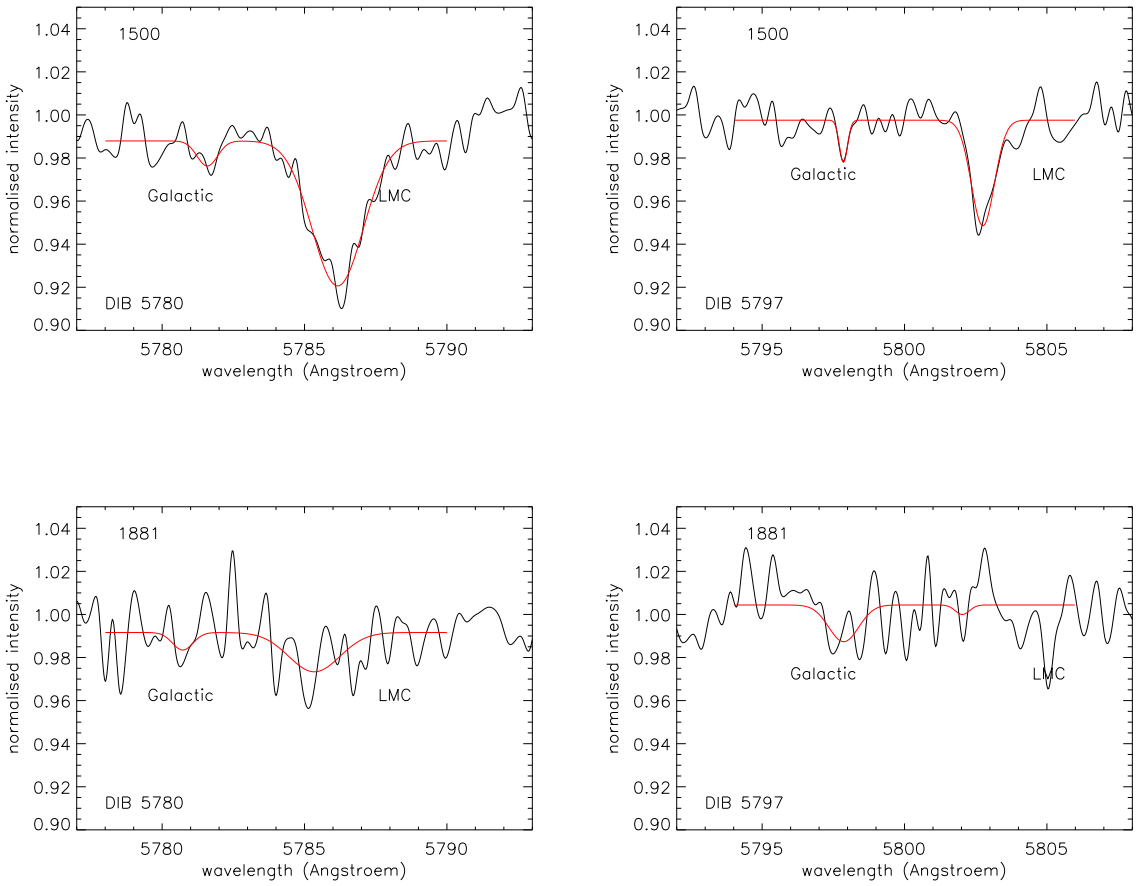

Figure 4.35: Profiles of the 5780 and 5797 Å DIBs showing (Top:) a good detection and (Bottom:) a bad and unreliable detection.

The map showing the 5780/5797 Å DIB ratio (bottom panel in Figure 4.34) is interesting in the 30 Dor region. Here there is a high 5780/5797 Å DIB ratio; comparing this to the individual maps indicates that this could mark a boundary of the cloud in that direction were the transition from molecular to diffuse environment is rapid.

4.2.5 Maps of the neutral ISM in the foreground Milky Way

Maps of the Galactic foreground in the SMC sight-line

The weakly ionized calcium K line

Unlike the detection of the Ca II K line in the SMC itself the Galactic component shown in my spectra only picked up one component of this line. Naturally this map (Figure 4.36) shares the same sight-lines as those in Figure 4.24 but the map produced is very different showing that I am, indeed, detecting a different cloud. As most of the sight-lines show good detections of the Ca II K line I can be confident in the structure that is revealed. The South East region of this map contains most of the sight-lines with unreliable detections and so the "filling" effect of the intensity gradient for the absorption levels is noticeable in this region. A point to note is that for the Galactic component the intensity level range is smaller than for the corresponding maps for the SMC as can be seen by comparing the colour bar above each map. The Ca II K line absorption is detected across the entire region, at no point does the equivalent width value drop to 0.05 and there are some discrete patches of greater intensity. Some of the profiles for which I could not reply upon the measurement taken do show a very broad Ca II K line, indicating the presence of a hot gas (see Figure 4.37). The interpretation of this map is that there is a large cloud of hot gas in the Milky Way in the direction of the SMC, within which are denser clumps of hot gas.

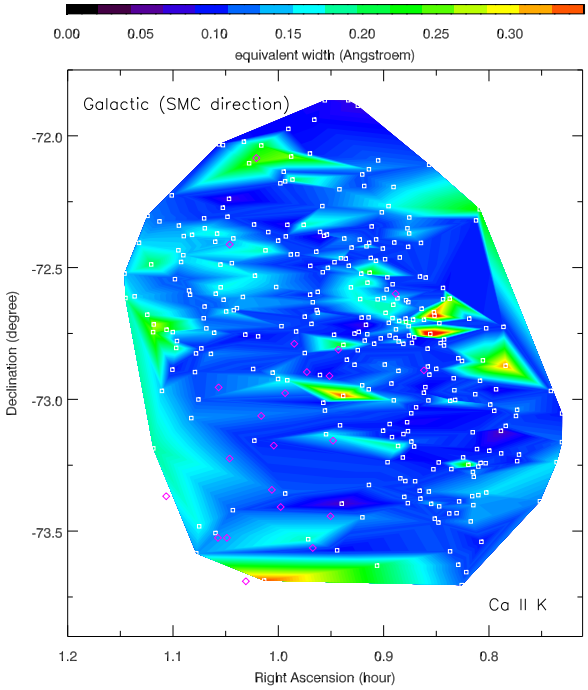

Figure 4.36: Equivalent width map of the Ca II K line in the Milky Way Galaxy in the direction of the SMC.

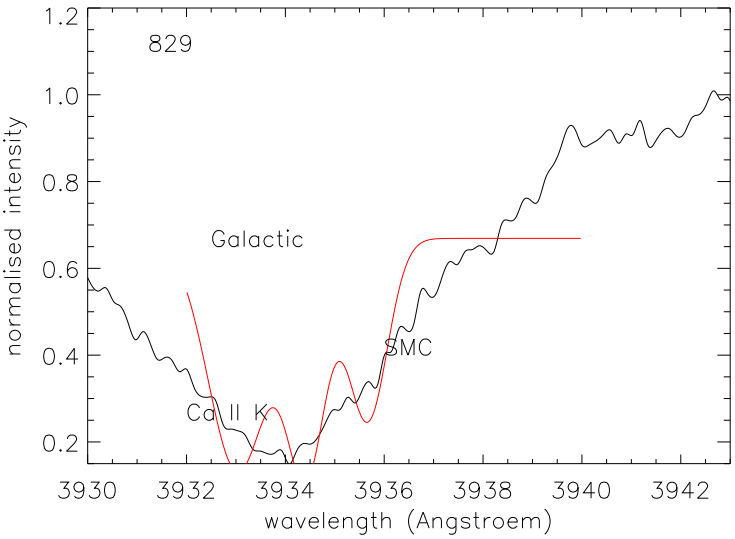

Figure 4.37: Profile of the Ca II K line showing a very broad feature in the Galactic component.

The neutral sodium D line

The maps showing the Na I D absorption for the Galactic component in Figure 4.38 show a strong correlation with each other just as they did for the SMC component yet they are very different to their SMC counterparts. In contrast to the situation with the Ca II K more Na I D is detected in the Galactic component than in the SMC as can be seen by comparing the colour bars. The top maps in Figure 4.38 show the equivalent widths of the individual Na components. Comparing the two I can see that where there is absorption in the Na I D_2 line there is a corresponding absorption in the Na I D_1 line. Although the Galactic maps show a stronger Na absorption than the SMC maps did, the profiles where both Galactic and SMC components are detected show that often the SMC component is stronger than the Galactic component as in the example shown in Figure 4.39. However, there are many cases where the Na absorption is detected in the Galactic region but not the SMC region as shown in the lower hand panel of

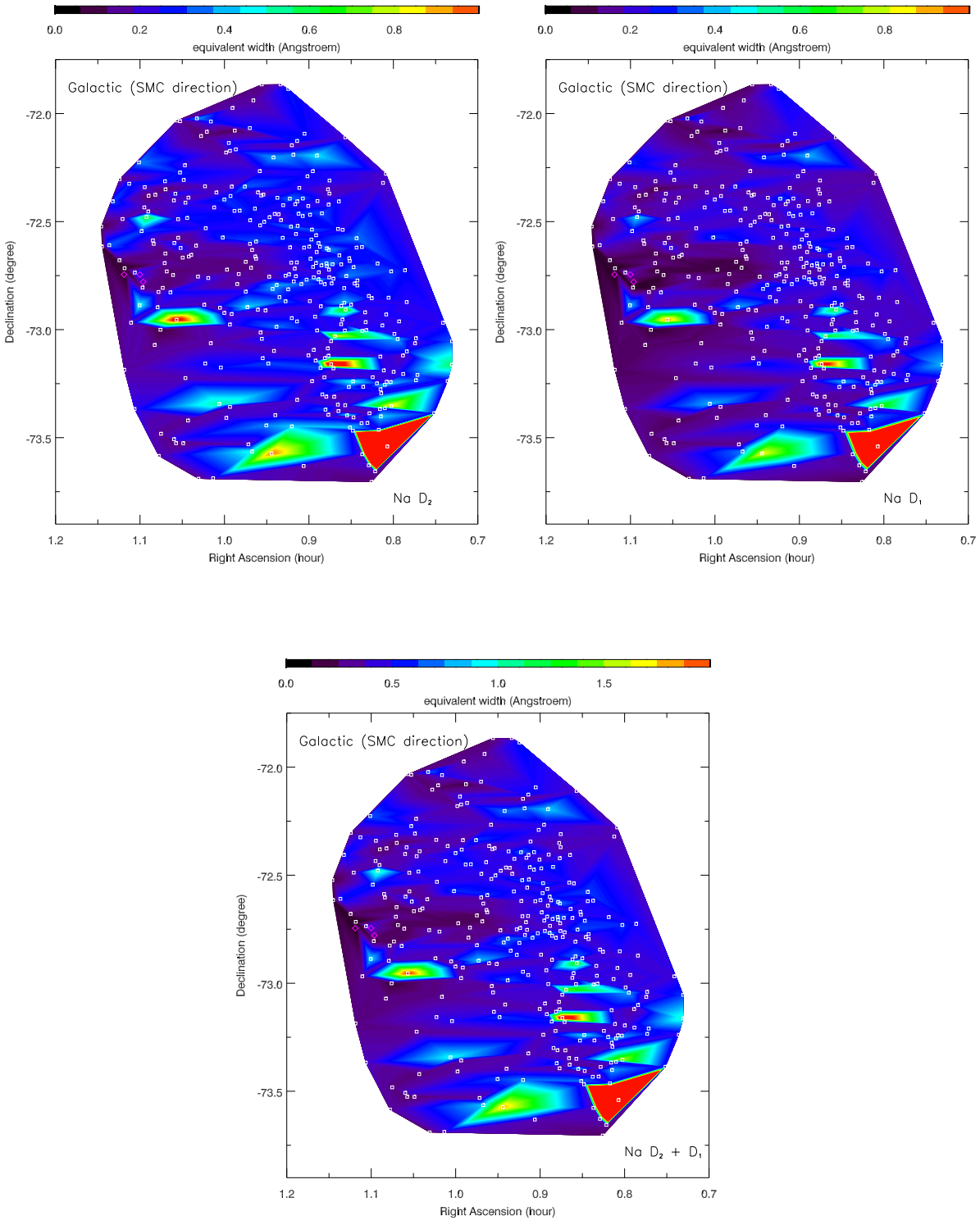

Figure 4.38: Equivalent width maps of (Top left:) the Na I D_2 absorption line, (Top right:) the Na I D_1 absorption line and (Bottom:) the sum of the absorption lines in the Milky Way Galaxy in the direction of the SMC.

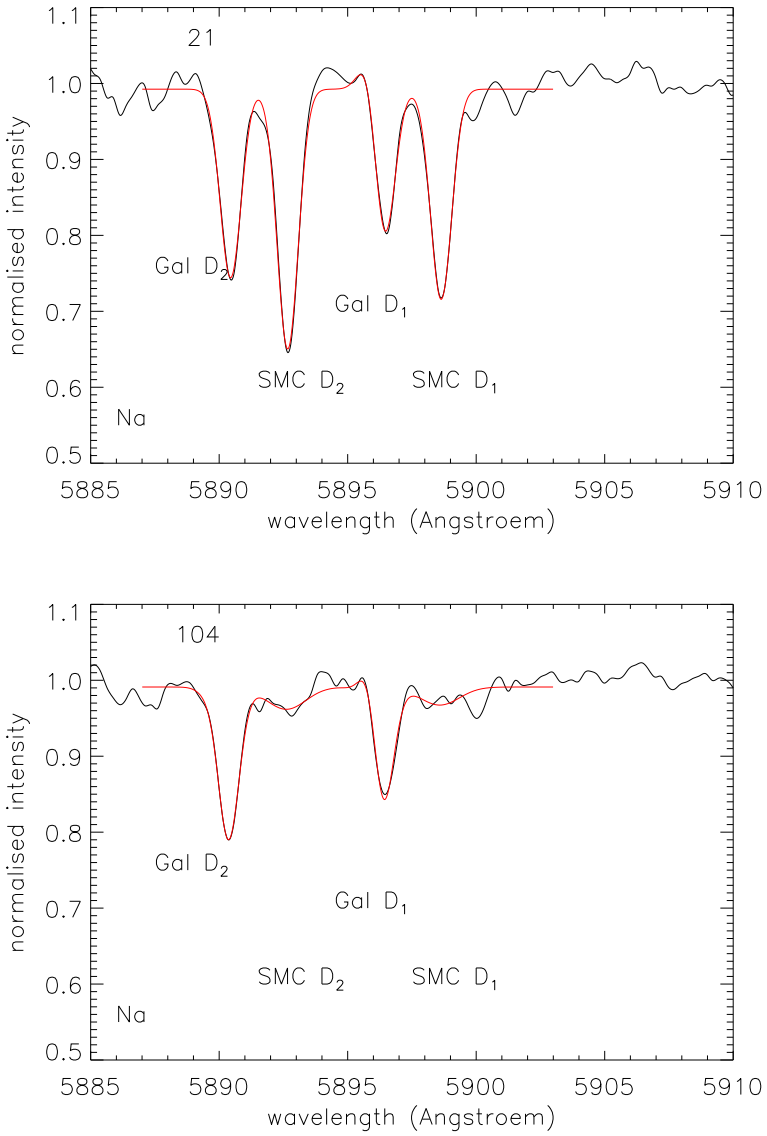

Figure 4.39: Profiles of the Na I D_1 and D_2 lines showing (Top:) the D_1 and D_2 components in both the Galactic component and the SMC component and (target 21) (Bottom:) an example where the Na is present in the Galactic observations but absent in the SMC observations (target 104).

Figure 4.39, thus accounting for the maps showing a stronger overall Na component in the Galactic foreground.

Again, as the individual maps are so well correlated a map of the combined Na I D_1 and D_2 components was created to enhance the structural features shown (see Figure 4.38). Unlike the Ca II K maps the Na absorption is shown to be in small distinct regions and it is noticeable that when the Na I D absorption is present the Ca II K absorption is absent. This is indicative of the environment on the region as the Ca II K favours an environment of high ionization, a hot gas, whereas the Na I D favours a cooler, molecular environment.

The 5780 and 5797 Å DIBs

For the sight-lines in the SMC direction more of the DIBs were detected in the Galactic component than for the SMC component with 91 sight-lines for the 5780 Å DIB and 52 sight-lines for the 5797 Å DIB showing DIB detections with which the maps in Figure 4.40 were created. As with other maps, the sparse sampling has resulted in a "filling" effect but still significant differences are seen between the 5780 Å DIB and the 5797 Å DIB seen in the top two panels of Figure 4.40. The expected general pattern of the 5780 Å DIB being detected where the 5797 Å DIB is absent and vice versa is evident. In the South East region the map shows that the 5780 Å DIB and the 5797 Å DIB are both present in the same region. Here, note must be taken of the colour bar to guide interpretation as, despite a first glance indicating otherwise, the 5780 Å DIB is the stronger of the two as is normally the case when the two DIBs are observed in the same spectra (see Figure 4.41).

The 5797 Å DIB is very weak though and so this must be mostly a diffuse cloud with a small area or areas of slightly denser material. Comparing the DIB maps to the Ca and Na maps for the same region it appears that the behaviour of the DIBs in the South East region more closely resembles the Na maps once the "filling" effect is taken into account. In the bottom panel of Figure 4.38 three distinct areas of Na absorption can be seen in the South, South West and East. The 5797 Å DIB (Figure 4.40) shows stronger absorption between RA 0.9 and RA 1.0 hr at Dec-73.5 degree, in the Na map

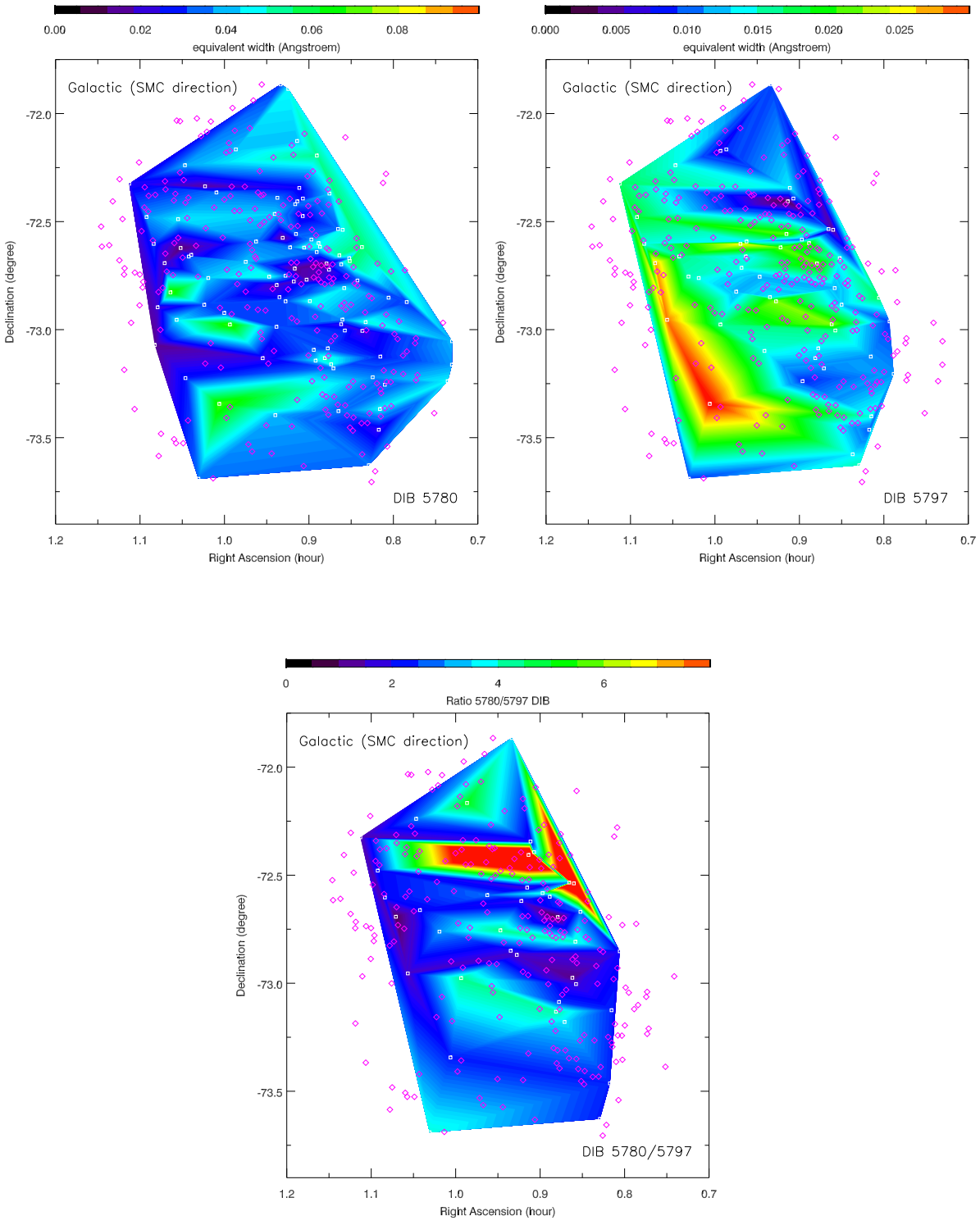

Figure 4.40: Equivalent width maps of (Top left:) the 5780 Å DIB absorption line, (Top right:) the 5797 Å DIB line and (Bottom:) the ratio of the 5780/5797 Å DIBs in the Milky Way Galaxy in the direction of the SMC.

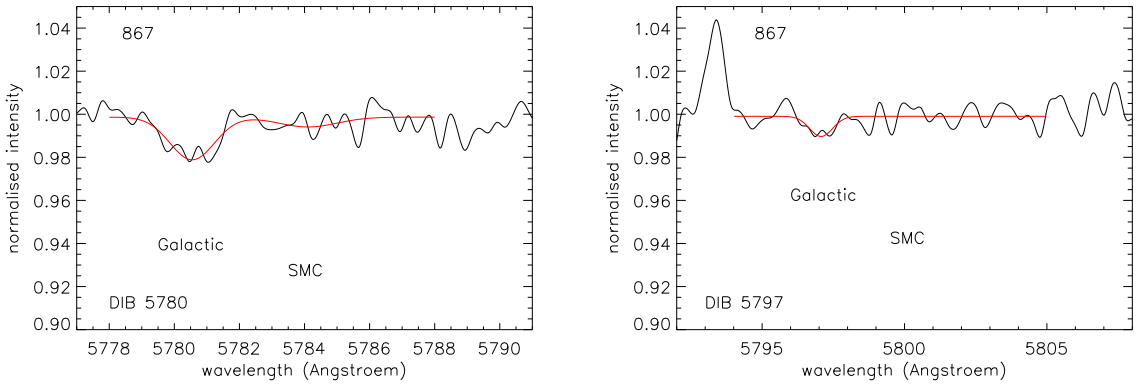

Figure 4.41: Profiles of the 5780 Å and 5797 Å DIBs showing that the 5780 Å DIB is the stronger of the two in the Galactic region (target number 867).

(Figure 4.38) the absorption in the South is also around the RA 0.9 to 1.0 hr region but slightly further South than Dec -73.5 degree. At $\sim$ RA 1.05 hr, Dec -73.0 degree the 5797 Å DIB (Figure 4.40) shows a strong absorption and this corresponds with the Na absorption in the East. The Na absorption in the South East corresponds to the area in the 5797 Å DIB which has the appearance of being "filled" between the other two regions. The 5780 Å DIB also shows some absorption along that South to East path. Comparing the Ca region, on the other hand, shows that very little Ca is detected in the same region. Therefore, it would seem the behaviour of the 5780 Å and 5797 Å DIBs more closely follows the behaviour of the Na I rather than the Ca II.

Another point of interest regarding DIB strength is that both DIBs are weaker in the Galactic component than they are in the SMC component; this is also seen in the DIB profiles (See Figure 4.42).

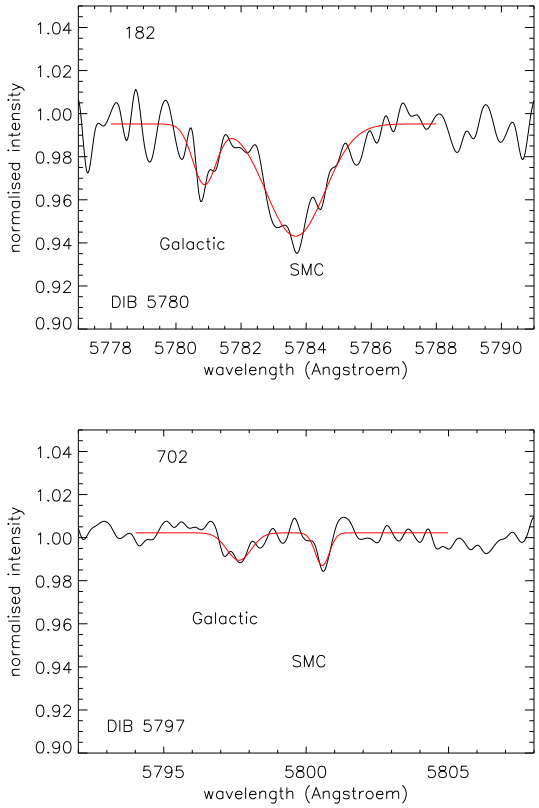

Figure 4.42: Profiles of (Left:) the 5780 Å DIB (target number 182) and (Right:) the 5797 Å DIB (target number 702) showing that these DIBs are weaker in the Galactic region than they are in the SMC.

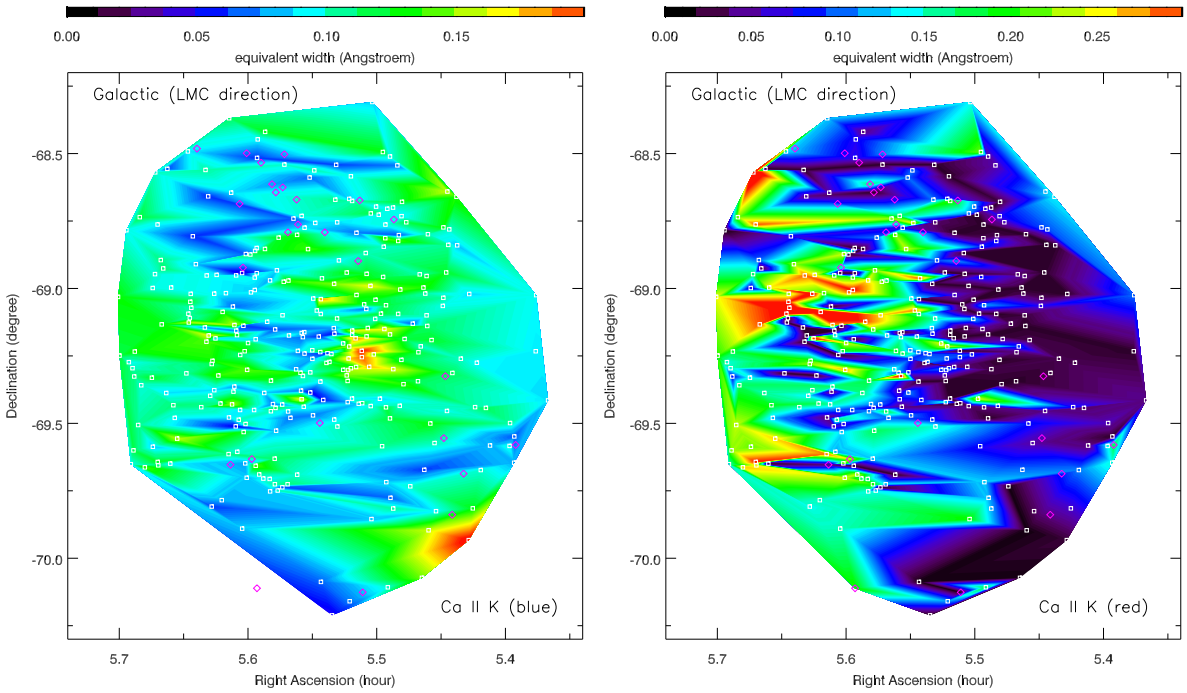

Figure 4.43: Equivalent width maps of (Left:) the Ca II K line absorption for the blueward absorption line, and (Right:) the redward absorption line in the Milky Way Galaxy in the direction of the LMC.

Maps of the Galactic foreground in the LMC sight-line

The weakly ionized calcium K line

For the Galactic component in the LMC direction two components of the Ca II K line are detected with notable differences between the two (see Figure 4.43). Here, the maps indicate that the redward component of the Ca II K line is the stronger of the two yet many of the profiles show that the strength of the two components are very similar to each other where both are detected or that the blueward component is slightly stronger (see the top and middle panels in Figure 4.44). This is probably a cumulative effect with more redward components being detected than blueward components.

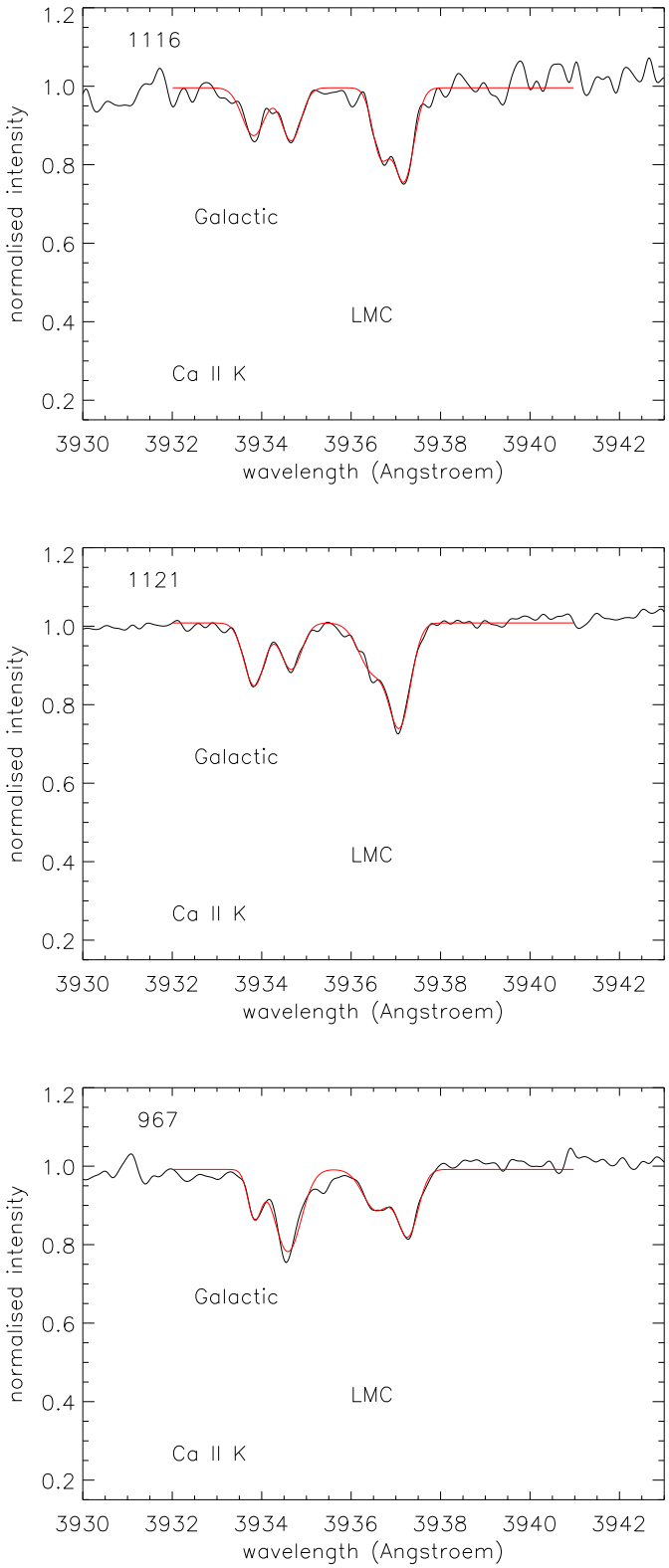

Figure 4.44: Profiles of (Top:) similar strength blueward and redward components (target number 1116), (Middle:) a stronger blueward component (target number 1121) and (Bottom:) a stronger redward component (target number 967) of the Ca II K line
.

The average profile of the Ca II K line (see Figure 4.4) shows that the blueward component is, on average the stronger of the two. There are a few occasions where the redward component is much stronger than the blueward component (see the bottom panel in Figure 4.44). This explains the apparent strength of the redward components as shown by the right hand panel in Figure 4.43 and is consistent with the more structured map produced by the redward component. The two components of the Ca II K line are well separated in the majority of the spectra. This is reflected in the average spectrum (See Figure 4.4). The Galactic component of the Ca II K line in the direction of the LMC is the only one of the average Ca profiles to show the two components clearly. Here, the implication is that I am are seeing two clouds in the Milky Way along the line of sight towards the LMC. The blueward map shows a large relatively uniform region of absorption with two small areas of high absorption. Conversely the corresponding areas in the redward map show very little if any absorption. In addition the areas of high absorption in the redward map correspond to regions of intermediate or low absorption in the blueward maps. Crucially, unlike the Ca maps of the SMC and the Galactic component in the SMC direction there are no areas where regions of intensity seem to disappear in one map to appear in the other at neighbouring points or where one map appears to be the inverse of the other. As the two components are well separated and there are no noticeable links between the two maps the conclusion is that there is little, if any, cross contamination in the absorption line measurements and I am detecting two separate clouds. The redward map appears to show the edge of the cloud it represents as there is a clear intensity gradient from high in the East to low in the West. With the majority of the sight-lines showing good detections of the Ca II K line I can have confidence in the structure revealed and the conclusions drawn.

The neutral sodium D line

The maps for the Galactic Na absorption in the direction of the LMC show a strong correlation between the two Na components (see Figure 4.45). This confirms the method used to separate the blended Galactic/LMC profile for this sight-line was justified. Comparing the two maps in the top panel of Figure 4.45 I can see that where there

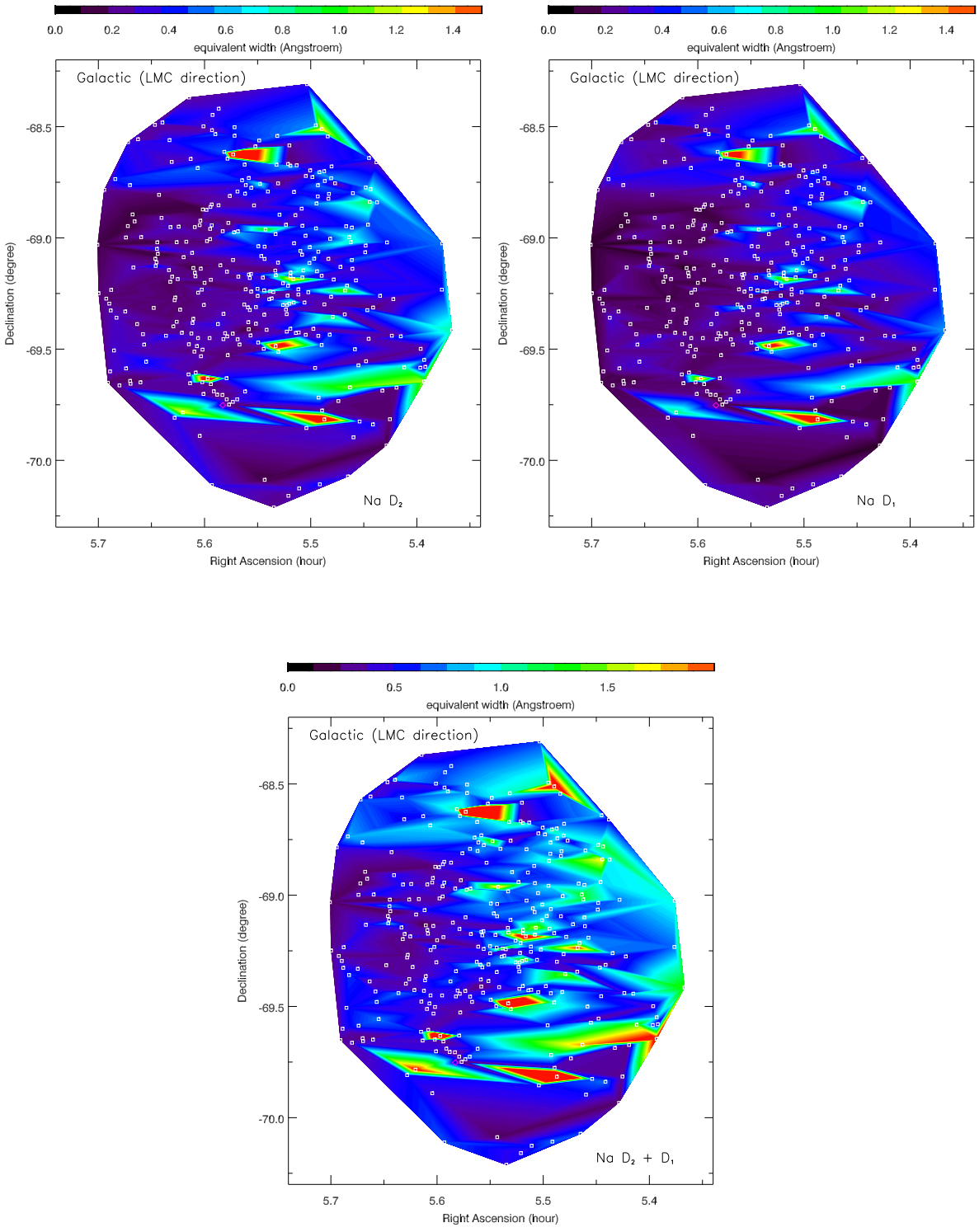

Figure 4.45: Equivalent width maps of (Top left:) the Na I D_2 absorption line, (Top right:) the Na I D_1 absorption line and (Bottom:) the sum of the absorption lines in the Milky Way Galaxy in the direction of the LMC.

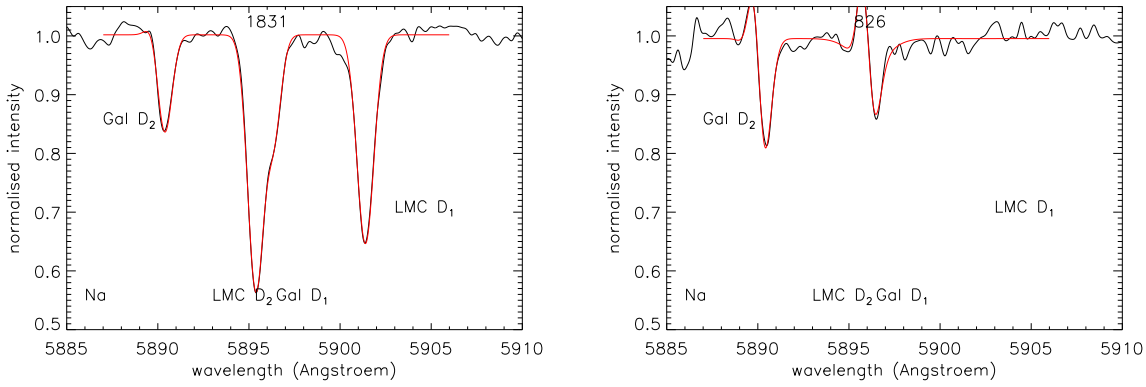

Figure 4.46: Profiles of (Left:) stronger Na absorption in the LMC component (target number 1831) and (Right:) no Na absorption in the LMC component (target number 826).

is absorption in the Na I D_2 line there is a corresponding absorption in the Na I D_2 line. As the individual maps are so well correlated a map of the combined Na I D_1 and D_2 components was created to enhance the structural features shown (see the bottom panel in Figure 4.45). Comparing the colour bars of Figure 4.45 and Figure 4.32 it is evident that where the Na is detected in the Galactic component it is much stronger than any Na absorption seen in the LMC itself. This is again in contrast to the picture presented by the profiles of the Na absorption.

Often the LMC component is stronger than the Galactic component as in the example shown in the left panel of Figure 4.46 but there are also many cases where the Na absorption is detected in the Galactic region but not the LMC region as shown in the right panel of Figure 4.46, thus accounting for the maps showing a stronger overall Na component in the Galactic foreground as was the case for the sight-lines in the SMC direction. The Na detected in the Galactic region along the LMC sight-line shows few areas of intense Na absorption unlike the Na map of the LMC itself. However, all bar one of the sight-lines does show some, albeit very weak in many cases, Na absorption so

again I can have some confidence in the structure revealed by the map. Comparing the Na I D maps with the Ca II K maps it is noticeable that, for the redward component of the Ca II K line, that when the Na I D absorption is present the Ca II K absorption is absent. For the blueward component of the Ca II K line when the Na I D absorption is strong there is little or very weak Ca II K absorption which is consistent with the different environment favoured by both elements.

The 5780 and 5797 Å DIBs

For the sight-lines in the LMC direction slightly fewer DIBs were detected in the Galactic component than for the SMC component with 88 sight-lines for the 5780 Å DIB and 31 sight-lines for the 5797 Å DIB showing DIB detections with which the maps in Figure 4.47 were created. Despite the "filling" effect due to the sparse sampling significant differences between the 5780 Å and the 5797 Å DIBs are seen in the the top two panels of Figure 4.47. In common with the other DIB maps where the 5780 Å DIB is detected the 5797 Å DIB is absent and vice versa. In this case there is very little overlap with the two DIBs being observed in the same area indicating there must be distinct regions of diffuse gas (favoured by the 5780 Å DIB) and molecular gas (favoured by the 5797 Å DIB). In this region the 5780 Å DIB is the stronger of the two as for the Galactic region in the SMC sight-line but in contrast to the situation in the LMC itself where the 5797 Å DIB is the stronger. Comparing the DIB maps to the Ca and Na maps for the Galactic region in the LMC direction it appears that the behaviour of the DIBs in the South East region more closely resembles the Na maps although this is not as clear as it was for the maps in the SMC direction. The main resemblance is in the region around and to the south of RA 5.5 hr and Dec -69.5 degree, here both the 5780 Å DIB and the Na absorption have peaks where the corresponding region in the Ca maps show little absorption. The peak shown in the 5797 Å DIB does not appear to correspond to any absorption in the Na or Ca but as the "filling" effect is very noticeable for the 5797 Å DIB no conclusion can be reasonably drawn from this. As was the case for the SMC sight-line it is interesting to note that both DIBs are weaker in the Galactic component than they are in the LMC component as comparison of the colour bars above the maps show, this is again seen in the DIB profiles (see Figure 4.48.)

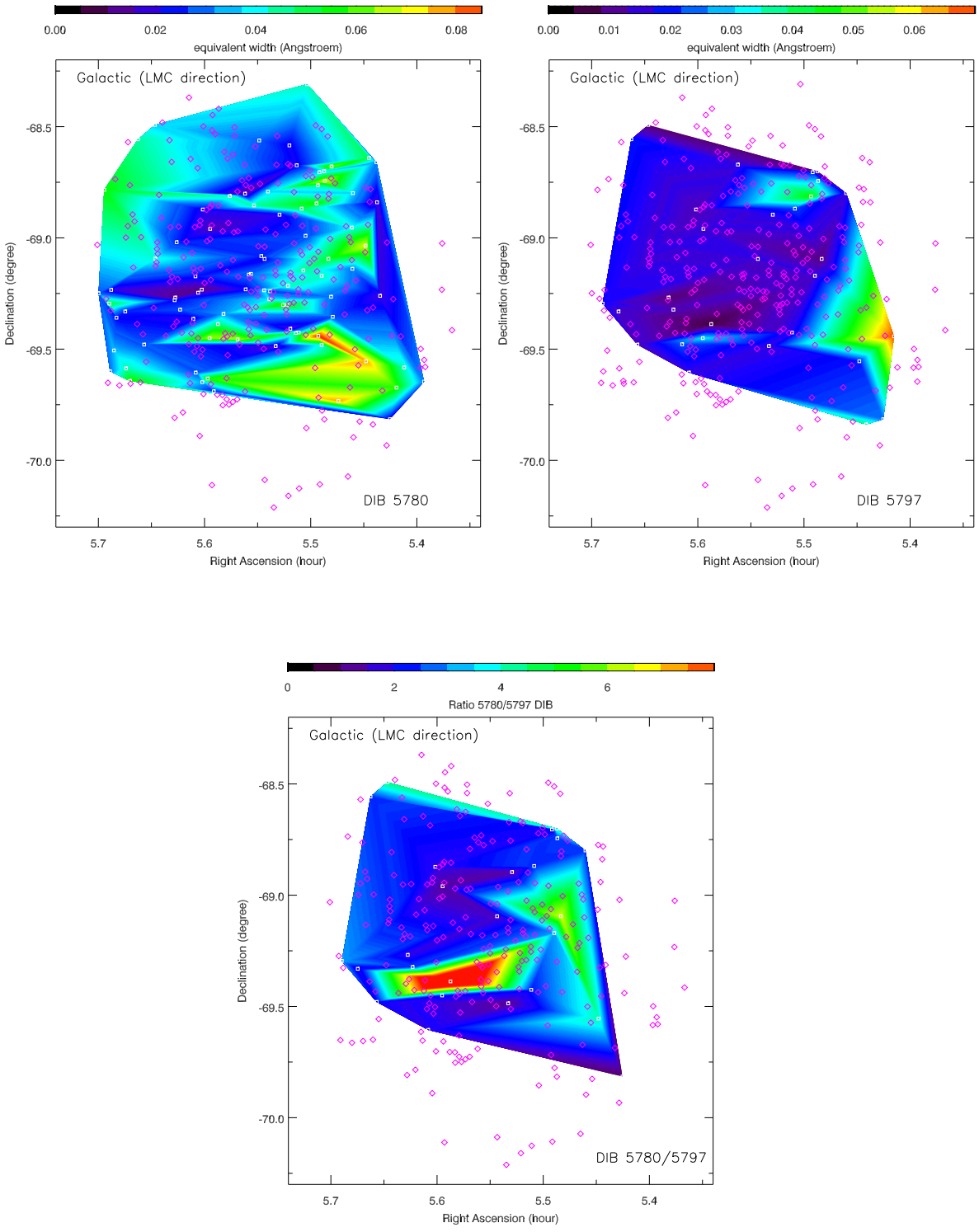

Figure 4.47: Equivalent width maps of (Top left:) the 5780 Å DIB absorption line, (Top right:) the 5797 Å DIB line and (Bottom:) the ratio of the 5780/5797 Å DIBs in the Milky Way Galaxy in the direction of the LMC.

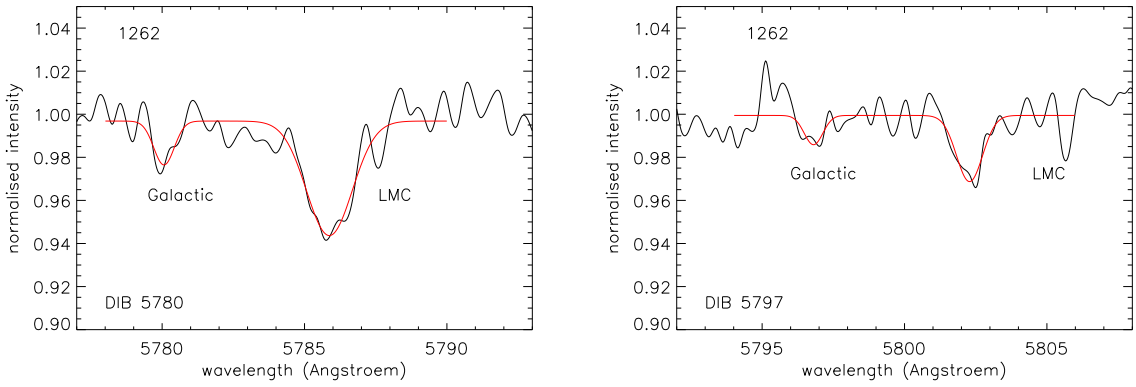

Figure 4.48: Profiles of (Left:) weaker 5780 Å DIB in Galactic component and (Right:) weaker 5797 Å DIB in Galactic component (target number 1262 for both).

4.3 Discussion

DIB correlations in the Galactic, SMC and LMC regions

From the plots in section 4.2.1 a correlation can be seen between the 5780 and 5797 Å DIBs in the SMC and LMC, especially at the lower EW strengths. The EW strength of the 5780 Å DIB increases more rapidly than EW strength of the 5797 Å DIB but there does come a turn off point where the increase in the 5797 Å DIB EW strength is not accompanied by a noticeable increase in the EW strength of the 5780 Å DIB; this is particularly noticeable in the LMC plot 4.9. The highest values of the 5797 Å DIB were identified as belonging to targets in the 30 Dor region, a molecular region in which the 5797 Å DIBs are expected to dominate. The environment in the Galactic region along the lines of sight towards the SMC and the LMC is much different to that in the SMC or LMC. There is much more scatter in the plots so the question is 'are there small discrete structures that vary between hot diffuse clouds and cooler molecular clouds located randomly but ubiquitously throughout this field of view?'

DIB correlations with weakly ionized calcium in the Galactic, SMC and LMC regions

The DIB correlations with the Ca II K line in the SMC and LMC show an anticorrelation (see Figures 4.16,4.17, 4.20, 4.21. Both the 5780 and 5797 Å DIB plots show similar trends. In both DIB cases the blue and red components of the Ca II K line in the SMC show a difference, where the scatter of DIB detections lies between Ca II K line EW strengths of 0.2–0.4 Å. A difference in these two Ca components is also noticeable in the maps of EW strength of the Ca II K line and supports the case for multiple clouds. There does not appear to be a lower threshold of Ca II K line EW strengths below which DIBS are not detected.

The behaviour of both the 5780 and 5797 Å DIBS in the Galactic components of the SMC and LMC sight-lines for the Ca II K line show similar trends. Unlike the correlations with the Na I D_2 line, the DIB strengths in Galactic, SMC and LMC are all very similar, there is no reduction in strength in the Galactic component as seen for the correlations with the Na I D_2 line.

From these plots it seems as though the 5780 and 5797 Å DIBs have a similar relationship to the the abundance of Na I D_2 line in both the Galactic components and the SMC and LMC components along these sight lines and also to the abundance of the Ca II K line albeit the relationship with sodium is different to that with the calcium.

The greater scatter and lower DIB EW strengths in the Galactic component coupled with the greater DIB EW strengths only being present in the SMC and LMC (when considering the Na I D_2 line) suggest that, along these sight-lines, the conditions in the SMC and LMC are more hospitable to the the carrier of the 5780 Å DIB than they are in the Milky Way.

DIB correlations with neutral sodium in the Galactic, SMC and LMC regions

The DIB correlations with the Na I D_2 line show that both the 5780 and 5797 Å DIBs have a good correlation with the Na I D_2 line in the SMC and LMC and show a similar increase of strength with increasing strength of the Na I D_2 line while lower EW strengths of the DIBS are also present at higher EW strengths for the Na I D_2 line. Although the 5780 and 5797 DIBs favour different environments this is not a surprising result. The strength of the Na I D_2 line is indicative of the column density and the greater the amount of gas the more likely it is that DIBS will be detected with increasing strength regardless of the nature of the gas. The EW strengths in the LMC are stronger than the strengths in the SMC by a factor of 2 but in both cases there is a similar threshold of Na I D_2 line EW strength below which the detection of DIBs is not certain, that is 0.8 Å for the SMC and 1.0 Å for the LMC

The DIB correlations with the Na I D_2 line in section 4.2.2 for the Galactic component along the SMC and LMC sight-lines show an anticorrelation. The EW strengths of the DIBs are about half that seen in the SMC and LMC but show the same threshold of Na I D_2 line EW strength below which the detection of DIBs is not certain and seen in the LMC, that is 1.0 Å.

Equivalent width maps of the DIBs, neutral sodium and weakly ionized calcium in the Galactic, SMC and LMC regions

Maps of SMC and LMC

The maps of the equivalent widths give a spatial representation of the EW strengths. The maps of the Ca II K line in the SMC clearly show the differences that were evident in the correlation plots. The map of the red component of the Ca II K line shows the gas is spread across the entire field of view and therefore this could represent hot gas in the Halo of the Milky Way. The maps of the Na I D_2 line does not show such extensive gas coverage of the area and thus is more likely to represent the cooler neutral gas regions within the SMC. There is just one small area in the South West region where

there is evidence of both the Ca II K and Na I D_2 lines being present. This is an area of star formation. The 5780 Å DIB map shows a high concentration in the same area as the Ca II K and Na I D_2 lines and also to the south which corresponds to the red Ca II K map but not the blue map. Presence of the 5780 Å DIB in this region could correspond to the hotter gas shown by the red Ca II K, the 5780 Å DIB is generally seen where the Na I D_2 line is sparse. The 5797 Å DIB map also shows a high concentration in the molecular south west region, in agreement with the Na I D_2 line. With so few sight-lines showing a DIB detection it is difficult to infer much from the DIB maps but it appears that in all but the denser regions, where I may be seeing the 'skin-effect' in clouds, the 5797 Å DIB is present where the 5780 Å DIB is weak or non-existent.

The maps of the Ca II K line in the LMC show more of a similarity to each other than the corresponding Ca II K line maps in the SMC, there was difficulty in separating the two components here and the two maps possibly show material from the same large cloud. However, there are three distinct areas in the blue map, one of which is close to the supernova remnant, SN87A. Therefore, these areas of Ca II K concentration could relate to shells of hot expanding gas with the weaker concentration perhaps relating to hot Halo gas. The maps of the Na I D_2 line, show that the Na I D_2 is concentrated in the star forming regions in and around 30 Dor, generally being stronger where the Ca II K line is weak or absent. Both DIB maps show a concentration in areas where the Na I D_2 concentration is higher than the Ca II K and are in areas surrounding the central cluster of the Tarantula Nebular R136. The DIB ratio map shows that the 5780 Å DIB is more prevalent than the 5797 Å DIB at the location of R136, so indicative of a strong radiation field as a result of the prolific star formation in that region. An interesting point to note about these DIBs maps is that in both cases there is no detection of either DIB in the region surrounding the nebula N159, a starburst region, yet the Na I D_2 line was detected just to the North of N159. This could indicate that the carrier of both DIBs is not present in dense molecular regions where there is an absence of a strong radiation field.

Maps of The Galactic region in the SMC and LMC sight-lines

The Galactic Ca II K EW map in the SMC sight-line one has one component of the calcium and presents a very different view to the Ca II K maps in the SMC. The calcium appears to be present across the whole field of view with four very small areas of high concentration which could relate to small shells of hot expanding gas. As noted in section 4.24 a number of the profiles showed a very broad Ca II K line. The example shown in Figure 4.37 is for target 829. Using Wien's Law to estimate the temperature of this target from its peak wavelength I estimate a temperature of ~ 5000 K making this a spectral type G star. In this case the calcium is likely to be photospheric and not interstellar. All target stars that displayed a similar feature were not included when creating the maps or the correlation plots so I can be confident there are no stellar features contaminating the maps. Comparing the sodium maps with the calcium map it is clear that areas of high Na I D_2 concentration coincide with areas of very low Ca II K concentration, The DIB maps have been created from few sight-lines so the 'filling factor' that occurs in construction of the DIB maps make it difficult to convincingly connect regions of high DIBs concentration to either the sodium or calcium maps. However, it is just possible that the 5797 Å DIB map does show that the 5797 Å DIB correlates with the Na I D_2 as the two small areas of high Na I D_2 concentration shown on Figure 4.38 seem to be the extreme ends of the area of high 5797 Å DIB concentration shown on Figure 4.40 which has undoubtedly been 'filled' by the map creation trying to link the few DIB detections together.

In the Galactic region in the LMC sight-line the Ca II K maps clearly indicate the presence of two clouds and reveal distinct areas of high Ca II K which, again, probably relate to shells of hot expanding gas. The Na I D_2 maps show that the cooler molecular gas traced by the Na I D_2 is concentrated in a different region to the hotter gas traced by the Ca II K. The DIB maps here are a little more detailed and it is easier to see that the 5780 and 5797 Å DIBs favour different regions. In particular the 5797 Å DIB map (Figure 4.47) shows high DIB concentration where the Na I D_2 is stronger and no DIB absorption where the Ca II K is generally stronger. The 5780 Å DIB shows some concentration in regions of strong Ca II K absorption but also in some areas of Na I D_2. These regions being, as previously stated, candidates for the presence of 'skin-effect' clouds, the so called σ clouds.

5 Synthesis

"The most exciting phrase to hear in science, the one that heralds new discoveries, is not 'Eureka!' but That's funny..."'

– Isaac Asimov

To summarise and link together the two projects contained in the preceding chapters, let us return to the question raised in the introduction Section 1.6.1. They are big questions and it is beyond the scope of my work, a single PhD thesis, to be able to do more than make a contribution. Therefore, I do not discuss these questions in great detail but I do make some interesting observations and conclusions.

5.1 Results

Two types of maps are constructed in this work. The maps of the LB give a four dimensional view of our local neighbourhood; three spatial dimensions and one dimension of EW strength showing the density of the different DIBs in all the sight-lines observed. We are uniquely placed in the LB, we are at the centre of our own 'experiment', we are looking out from the inside and trying to understand the nature of our local surroundings and of the nature of the environment further afield. In this work I have also mapped regions of the Magellanic Clouds, dwarf galaxies that are our near neighbours and the closest laboratories to hand outside of our own 'local laboratory'. These are three dimensional maps; two spatial dimensions and one dimension of EW strength.

Although the two types of map are very different, similar trends in both can be looked for to see if the different environments between the LB and the LMC and SMC can shed any light on the long standing question of the nature of the carrier or carriers of the DIBs. Certainly both types of map do reveal the small scale structure we set out to find.

5.1.1 What happens in the Local Bubble

The maps of the LB traced the cavity and the wall of the LB well. The sight-lines where there were non detections shown are of equal importance as the sight-lines where the DIBs or sodium is detected. These 'empty' sight-lines showed the cavities in the LISM tracing the shape of the Bubble. This was most noticeable in the DIB maps as most of the sodium maps showed that Na I D_2 was detected in nearly all sight-lines. Taking the global view of these maps and considering the three different absorption maps together, the small scale structure of our LISM begins to appear. The sodium maps show that throughout most of the LB there is some trace of sodium. Only in a very few places is there no sodium at all and when that occurs there are also no DIBs to be found, so here we can see the porous nature of the LISM. However, many of these 'empty' sight-lines are surrounded by sight-lines where DIBs have been detected. With the size of the symbol revealing the relative distances of the targets, careful inspection of the maps reveals cloudlets, sometimes close to the Galactic or Meridian Planes, sometimes quite distant - the LISM is clumpy. The DIB maps reveal more variation in absorption strengths than the sodium maps, both in this work and when compared to the work of Welsh et al. (2010). A point to highlight from the discussion on the sodium maps in the Galactic Plane projection is the case where strong Na I D_2 has been traced in a sight-line where the target is in close proximity to the Sun and less than 70 pc from the Galactic Plane and yet no DIBs are detected in that sight-line. The sodium absorption does trace weakly ionised gas as well as neutral gas but is the nature of the environment traced by that target unsuitable for DIBs to survive despite the presence of sodium? It seems so.

5.1.2 Comparing in-plane with out-of-plane sight-lines: did the Bubble burst?

The Galactic Plane maps all show that the Sun is surrounded by denser material in all directions, the further away from the Sun the targets are, the more likely they are to

show stronger absorption in an extended region, thereby tracing out the walls of the LB. The sight-lines where no DIB or Na I D $_2$ was detected are concentrated towards the centre of the maps, tracing out the cavity of the LB.

The Meridian Plane maps on the other hand tell a different story. The sight-lines without DIB or sodium detections on all maps extend to the North and the South; this is particularly noticeable in the DIB maps but it is also seen in the sodium maps. The sight-lines with no detections break through the walls of the LB and extend out to the Halo in both northerly and southerly directions. The 5780/5797 ratio maps highlight the difference in the two planes. I have shown the DIBs are more discerning about their environment than the sodium is. The 5780 Å DIB favours ionised gas whilst the 5797 Å DIB favours neutral gas. Therefore, a high ratio reveals the presence of highly irradiated material, a harsh environment and a diffuse environment. On the ratio maps, the darker the symbol, the harsher the environment and here it is easy to see the central concentration of diffuse gas surrounded by the cooler, denser material traced by lighter the symbols in the Galactic Plane projection but in the Meridian Plane projection it is different, the darker symbols, tracing the region where the 5797 Å DIB is not detected at all and the 5780 Å DIBs are weak, are in a central column extending north and south. This is consistent with other observations of the local interstellar medium showing a 'chimney'. Did the Bubble burst? Indeed it did! See Lallement et al. (2003), Welsh et al. (1999), Welsh, Sallmen & Lallement (2004), Welsh & Shelton (2009), Welsh et al. (2010), Welsh & Lallement (2012).

5.1.3 What happens in the Magellanic Clouds

The maps of the SMC and LMC also reveal the small scale structure of the ISM and include maps of the Ca II K line. The calcium maps are a better indicator of the presence of weakly ionised gas than the sodium maps are as they trace a stronger level of ionization and therefore are a good indicator of the presence of a hot gas. The on-line Handbook of Basic Atomic Spectroscopic Data (http://www.nist.gov/pml/data/handbook/index.cfm) gives the following information: Ca^0 ionization energy is 6.1 eV, Ca^+ ion-

ization energy is 11.9 eV, Na^0 ionization energy is 5.1 eV and Na^+ ionization energy is 47.3 eV. The high ionization energy level for Na^+ means that Na I traces ionised gas as well as neutral gas, whereas calcium only traces ionised gas. The calcium maps showing a weaker concentration across the whole field of view appear to trace the hot Halo gas and the stronger concentration of calcium occurs around regions of star formation where there is a strong radiation field. The sodium maps also show a concentration around the star forming regions but generally the sodium is stronger where the calcium is weak. The DIB maps for the Magellanic Clouds are quite sparsely populated but they show that generally the 5797 Å DIB is present in regions of high sodium concentration and the 5780 Å DIB is generally present where the sodium is weak. Even though the DIB maps are sparse they do tell a slightly different story to the sodium maps. In all but the densest regions, the 5797 Å DIB is only present where the 5780 DIB is weak or non existent and so the DIBs show more of the small scale structure of the ISM than the sodium or calcium maps do. The 5780/5797 Å ratio maps indicate that regions where this ratio is high, the environment is highly irradiated.

5.1.4 How different is the diffuse ISM in the SMC, LMC and Milky Way?

The Magellanic Cloud project also mapped the Galactic region along the sight-lines to the SMC and LMC. Two distinct clouds along the sight-line to the LMC are picked up via the calcium maps, revealing areas of high Ca II K, probably we are looking mainly through the hot gas of the Disc-Halo interface. It is clear that areas of high Na I D_2 concentration coincide with areas of very low Ca II K concentration and that applies in the SMC, LMC and the Milky Way.

The DIB maps of the SMC and LMC and the LB show that the 5780 and 5797 Å DIBs favour different regions. In particular the 5797 Å DIB maps show high DIB concentration where the Na I D is stronger. In the LB this traces the wall of the bubble, and in the Magellanic Clouds it traces the cooler neutral gas of star forming regions. Also in the SMC and LMC it is evident that there is no DIB absorption where the Ca II K is generally stronger.

The 5780 Å DIBs favour weakly ionised regions; this is clearly shown in the LB maps - particularly the 5780/5797 Å DIB ratio maps which show the higher concentration of the 5780 Å DIB in the LB cavity. In the SMC and LMC the 5780 Å DIB maps show some concentration in regions of strong Ca II K absorption but they are also in some areas of Na I D. These regions being, as previously stated, candidates for the presence of 'skin-effect' σ-type clouds that characterise the Halo/Disc interface (van Loon et al. 2009). Although I have no calcium maps for the LB data, some of the DIB maps when compared to the sodium maps also indicated a transition region between the wall of the bubble and the warmer ionised gas of the bubble interior similar to the 'skin-effect'. Figure 5.1 summarises the situation observed in the SMC and LMC and illustrates the 'skin-effect'. This shows that the denser interior of the cloud is home to the neutral sodium gas and the 5797 Å DIB, as the cloud becomes less dense toward the outer regions of the cloud where it is being irradiated, the sodium is still observed but it is weaker. Here the 5780 Å DIB appears and the 5797 Å DIB disappears. Further away from the centre of the cloud where it is less dense and subject to greater irradiation the sodium and the 5780 Å DIB disappear leaving the weakly ionised calcium tracing a harsh environment in which the DIBs can no longer survive; the environment traced by the Ca II is too hostile. The walls of the LB show a similar phenomenon certainly mimicking the behaviours of the inner two regions of the skin-effect cloud as illustrated in figure 5.1.

The plots in figure 3.15 in Chapter 3 are interesting and show the progression in Galactic Plane concentration; increasing from the scattered Na I to 5797 Å DIB and then to the more concentrated 5780 Å DIB showing that high concentrations of the 5780 Å DIB only occur within a few tens of parsecs from the Galactic Plane. This appears to be the first noticeable difference between the diffuse ISM in the SMC, LMC and Milky Way, as one would think that as the 5780 Å DIB traces warmer gas that this should be the other way around. However, with the LB project the nearest stars were selected and neutral cloudlets are seen even at high Galactic latitudes but still within the Galactic Disc, so this is most likely a selection effect and not an overturning of what we know. Also Na I starts to saturate in low-latitude sight-lines and this could add to the poor correlation between DIBs and Na I at larger EW values.

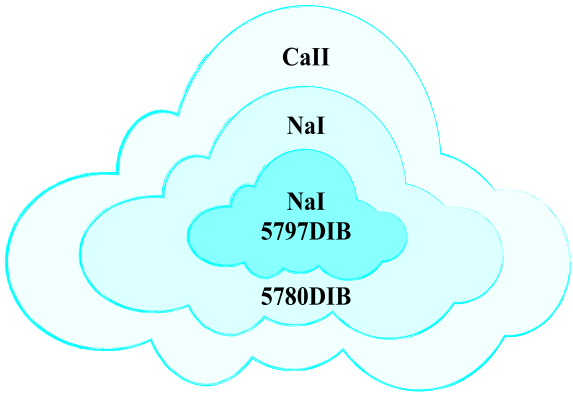

Figure 5.1: A schematic diagram of a σ type or 'skin-effect cloud. With thanks to Ben Gilliland for creating the illustration from the author's sketch.

5.1.5 Environmental behaviour of the DIBs: clues as to the nature of their carriers

To date the assumption is that the DIBs do have molecular carriers. Under this assumption the DIBs must represent vibronic transitions from a large number of different molecules (McCall et al. 2010). The further assumption that all molecules in a given sight-line that give rise to a particular DIB are in their ground state implies that two or more DIBs arising from that molecule should be part of a vibronic progression in the molecule and the relative strengths of the vibronic bands should be exactly the same from one sight-line to another (McCall et al. 2010). Therefore, a tight correlation between two DIBs is a promising, although insufficient, condition to identify DIBs with a common carrier. The problem with this assumption is, of course, that the molecules of DIB carriers may not be in the ground vibration state. My observations of the well known 'near-perfect' correlation for the 6196 vs 6614 Å DIBs is not so 'near-perfect'. The coefficient value for the 6196/6614 Å DIB calculated for observations in this work is 0.886 which is just over a 10% difference from the generally accepted value calculated by McCall et al. (2010) of 0.986. Figure 3.7 in Chapter 3 shows a break in the EW

values for the 6614 Å DIB with no detection of that DIB with EW between 0.02 and 0.04 Å. Closer inspection of the two areas and comparing the slopes in these data with those seen in the McCall et al. (2010) paper show that my data are not so inconsistent, either the 6196 Å DIB is a little weaker or the 6614 Å DIB is a little stronger in my data.

I also find that the 5797 Å DIB appears to correlate well with the 6196 and 6614 Å DIBs. This has not been remarked upon in the literature before and given the unusual behaviour I see with the 6196/6614 Å DIB correlation in my data the question arises about the nature of the environment in the LB walls and wall/bubble interface and does that environment have an effect on the carrier of the 6196/6614 Å DIB ratio, and if there is actually a common carrier for both of these DIBs.

The observations and investigations in this work indicate that there is very little difference between the diffuse ISM in the SMC, LMC and Milky Way, and what differences there are, are subtle. This is seen from the analysis of the DIB behaviour in Sections 3.2.3 and 4.2.3. To compare the SMC, LMC and Milky Way we can only look at the DIB correlations that are common to both, namely the correlation values between 5780 and 5797 Å DIBs and then only for the measurements for which there is some confidence in their significance. From Tables 3.1, 4.1 and 4.2 it is seen that for the LB the correlation coefficient is 0.884, the *t*-test value is 12.54 and the corresponding critical value of t is 1.96, for the SMC the correlation coefficient is 0.864, the *t*-test value is 6.39 and the corresponding critical value of t is 2.98 and for the LMC the correlation coefficient is 0.766, the *t*-test value is 4.13 and the corresponding critical value of t is 3.06. Although the level of significance is lower in the SMC and LMC than in the LB they are still significant and show that there is a similarity in DIB behaviour in the three environments. In order to further investigate this possibility that this situation does hold true more observations of the three regions should be taken and similar comparisons made.

There is one very big difference between the Magellanic clouds and the Milky Way and that is metallicity. The LMC has a metallicity of about 40% of the Milky Way Galaxy and the SMC has a metallicity of about 20% of the Milky Way Galaxy.

It is known that Na I D scales to metallicity and this has been noted in the work here. More of the sight-lines towards the Magellanic Clouds detected the Na I D_2 line in the Galactic component than they did the SMC or LMC component and the Na I was well detected in all sight-lines of the LB. Other points to note about the Magellanic Clouds is that the radiation is higher than in the Milky Way. This is because less dust has been created in the Magellanic Clouds to provide a shield against radiation and hot stars are hotter as a result of the stellar evolution of stars in a lower metallicity environment. This will produce harsher radiation, a harsher environment and so the abundance of molecules will be reduced. Yet the pattern of the DIB behaviour does not change between the SMC, LMC or the LB!

There are different regions probed in the SMC and LMC: star forming regions; neutral gas regions and hot highly irradiated regions. The DIB maps do show difference in behaviour across these different regions and it seems some DIB behaviour seen in the Magellanic Clouds is also seen in the LB. The general behaviour of the DIBs is the same: the 5780 Å DIB favouring weakly ionised environments and the 5797 Å DIB favouring neutral environments. Interestingly there is a similarity seen between the 'skin-effect' in clouds in the SMC and LMC and what we observe near the walls of the Local Bubble.

5.2 Answers to the scientific questions

Returning to the specific questions posed at the start of this thesis.

What is the structure of the Interstellar Medium, particularly the Local interstellar Medium? The short answer is: the LISM is clumpy! The detection in the LB of strong Na I D in close proximity to the Sun but no DIBs being detected in the same sight-line show that the DIBs are more discerning tracers of their environment than the sodium is. The DIBs, being very particular about where they hang out, have revealed the cavity of the local Bubble to be both porous and clumpy. The Bubble has burst, being open to the Halo in both the North and the South and within the

cavity cloudlets have been identified. Some of these are traced by DIBs some only by the sodium. Similar patterns of DIB concentration around star forming regions are seen in the SMC and LMC, so one could conclude the ISM structure there is clumpy too. However, in the Magellanic cloud data, both in the Galactic component and the Magellanic Cloud components it appears to be true that Na I and Ca II are largely non-coexistent.

What is the Earth going to run into next? We have identified cloudlets of Local Fluff and they are spread about in the local cavity. The Sun is moving at about 20 km per second (Frisch 1981), with respect to the Local Standard of Rest (LSR), in the direction of Vega in Lyra with Galactic coordinate of (67°4, 19°2). Unfortunately that is an area of the Galactic Map that is uncharted by this LB survey. With the edge of the bubble at approximately 100 pc away it will take about 5 million years for us to reach the wall of the bubble, chances are we will run into a cloudlet some day and that could be within short cosmological timescales. However, as it seems the LISM is clumpy, having small discrete clouds rather than very large clouds, then we may just miss the next one we come close to. If we did run into a cloudlet it may not actually affect us; we are close to the Sun. On the other hand the Heliosphere could be affected; if the clouds had strong magnetic fields the Heliosphere could be compressed further than it is now (Opher et al. 2009). This could have consequences for life on Earth; more cosmic rays could reach us, altering our terrestrial climate (Frisch 1981; Opher et al. 2009). Although this survey has not mapped the direction in which we are travelling yet, some relatively dense clouds do appear to be in the vicinity behind us (Frisch 1981), so we may have passed through one already.

What is or are the carriers of the Diffuse Interstellar Bands? The has been a long standing question since their discovery in 1922 and the question still stands. What this work has done is shown that the DIB behaviour appears to be independent of metallicity. The DIBs also seem to need some radiation in order to exist as dense neutral clouds do not appear to show evidence of the 5780 Å DIB. However, if that irradiation is too strong, as in the Ca II environments, the DIBs cannot survive. This work has shown the DIBs are particular about the environment they reside in; it

has to be just right; not too hot and not too cold. The investigations regarding the 6196/6614 Å DIB correlation are interesting. It is assumed that a good correlation is the result of a common origin, which can be either a particular type of molecular or grain species or a reaction to particular physical environmental conditions (Josafatsson & Snow 1987). There is an assumption that all the molecules of a particular DIB carrier are in the ground vibrational state (see McCall et al. (2010)). If this is the case and if the 6196 and 6614 Å DIBs did have a common carrier then it is expected that the ratio between the two DIBs would always be the same. However, this work shows that in environments such as the Local Bubble the DIBs behave differently as they do not exhibit such a near-perfect correlation. It may be that the 6196 and 6614 Å DIBs do arise from the same carrier, the observed difference being due to the conditions in the LB, which may result in low lying excited vibrational levels becoming populated. Then the relative populations of the states would influence the intensities of the individual transitions, resulting in the relative intensities not being constant across all sight-lines (McCall et al. 2010). If they do have the same carrier as implied by their near-perfect correlation, then this work shows that in harsh environments such as the Local Bubble the DIBs behave differently as they do not exhibit such a near-perfect correlation. This leads me to wonder whether the harsh environment of the Local Bubble is an environment in which the carriers of the DIBs are being created, or maybe, destroyed and we are seeing that process reflected in the different correlation coefficient values. The fact that the Na I and Ca II seem to be largely non-coexistent is also an indicator for the carrier of the DIBs. Na I seems to be needed for DIBs to exist yet the appearance of Ca II could signal the start of their destruction.

5.3 Conclusions

The LB survey probed the structure of the LB on scales of degrees, which, for structure at a distance of 100 pc would correspond to scales of a few pc. This is similar to the scales of small molecular cloudlets, and would correspond to scales of a dozen arcseconds

at the distance of the Magellanic Clouds. The latter were probed in the VLT Flames Tarantula Survey (Evans et al. 2011) in the 4428 Å and 6614 Å DIBs but smaller scales, down to arcsecond-scale were probed in the Na I D and 5780 Å and 5797 Å DIBs (van Loon et al. 2013). The AAOmega Magellanic Clouds survey presented here probes scales of several arcminutes, which corresponds to dozens of pc at the distance of the Magellanic Clouds but only a tenth of a pc in the Galactic foreground. The Magellanic Clouds surveys thus provide an interesting complement to the LB survey to probe small-scale structure in and around the LB. In addition, the sight-line towards the massive nearby globular cluster ω Centauri was probed also in Na I D (and Ca II K) and the 5780 Å and 5797 Å DIBs (van Loon et al. 2009).

The ω Cen sight-line (Galactic coordinates 309°, +15°) is characterized by 5780 Å DIB absorption with an average EW of 0.1 Å (up to 0.25 Å), and 5797 Å DIB absorption with an average EW of 0.033 Å (up to 0.13 Å). Comparing with our LB maps (figure 3.16 on p.108) we see that the EWs of these DIBs surrounding the position of ω Cen in the LB data are all well below these values. This confirms that the ω Cen observations mostly probed the Disc-Halo interface beyond the LB and nearby spiral arm. The small-scale structure (on scales below a pc) described in their work thus mostly reflects structure outside the LB, though some contributions would be expected. Their 5780 DIB/ 5797 DIB EW ratio was typical of highly irradiated σ environments and this is also the case in most of the LB.

The Tarantula Nebula sight-line probes higher Galactic latitude (see figure 3.16). The foreground 5780 DIB EW was typically < 0.07 Å; that of the 5797 DIB < 0.02 Å (van Loon et al. 2013). That is not out of line with our LB survey data: while most of the neighbouring sight-lines show weaker DIBs the Tarantula data are also generally weaker than the above limits and one of our sight-lines near to the Magellanic Clouds, at Galactic coordinates (280°, −44°) is comparable to the above high values. The Tarantula Nebula Galactic foreground map does reveal small-scale structure that helps understand why we see such large variations between adjacent sight-lines in our own LB maps. It confirms the idea of a porous, and highly structured LISM. Again, the Galactic foreground probed by the Tarantula Nebula survey is characterized by a σ-

type environment, as is typical in the direction leading out of the LB into the Galactic Halo.

In the direction towards the SMC (figure 4.7 the 5780 DIB has an EW of typically 0.03 Å, up to $\sim$ 0.06 Å; the 5797 DIB has an EW typically 0.01 Å, up to $\sim$ 0.03 Å. Again this is consistent with our LB maps (figure 3.16), and also their ratio indicates a σ-type environment. In conclusion, the Magellanic Clouds and ω Cen sight-lines provide additional evidence for a highly irradiated and/or hot-gas environment in the LB and the external hot environments (Halo, Disc-Halo interface), and for small-scale structure traced by DIBs on scales of parsecs or perhaps less.

5.4 Future directions

There is much more work to be done on both projects. Both surveys had their technical challenges but both produced good data and interesting results. The strength of the Magellanic Cloud survey was being able to target about 350 stars at a time for the observations allowing many sight-lines to be sampled. With the Local Bubble survey the main weakness was in the narrowness of the slit used to take the spectra. With the bright target stars excellent seeing conditions were a problem as it was very difficult to manually place the slit in exactly the right place to ensure a decent spectrum was obtained. Both surveys could be repeated or expanded on; the problems encountered did not end up being insurmountable.

Future observations - the Local Bubble

A number of interesting sight-lines were revealed in this survey and plans to observe areas of interest are underway.

1. Some of the 'clumpy' regions should be observed further in order to try and reveal even more structure in the LISM.

2. The area around the Local Leo Cold Cloud should be probed to try to reveal structure and evidence of the 'skin-effect' to link that with observations in the SMC, LMC and walls of the LB.

3. Further observations for the 6619/6614 Å DIB correlation - is there really a difference in this harsh environment?

4. Observe fainter targets to increase the number of sight-lines observed.

5. Observe later type stars, removing a stellar standard synthetic spectra to help identify DIB (possible for use with the 6619/6614 Å DIB correlation and broad sodium dip investigations).

6. Observe the Ca II line to compare with what was seen in the SMC and LMC survey.

7. A second all sky survey of the same target stars so that, because of the high proper motions of these targets, we probe a slightly different sight-line to reveal the LISM structure in tiny scales.

Future observations - the Magellanic Clouds

Having proved the usefulness of the maps created in this work further areas of the Magellanic Clouds should be investigated.

1. Extend the mapping of the LMC to cover all regions in a similar manner to this survey so one large map can be produced.

2. Extend the mapping of the SMC to get the wing and part of the bridge.

3. Longer integration times to improve the S/N, especially in the SMC.

4. Observe the same field but omitting these stars and choosing different targets to improve the sampling and reveal more structure.

5. Extend the range of wavelength observations to observe the 6196 and 6614 Å DIBs in the SMC and LMC to see if a similar 'less-that-perfect' correlation is seen in similar harsh areas as this was observed in the LB.

A Abbreviations and Glossary

The conventional abbreviations for SI units and astronomical quantities are used.

2dF	–	Two-degree Field: a multiple object spectrograph at the AAT
2dFdr	–	A reduction package developed for use with 2dF
AAO	–	Australian Astronomical Observatory
AAT	–	Anglo-Australian Telescope at the AAO Siding Spring, Australia
ADC	–	Analogue-to-digital conversion
ADU	–	Analogue data units
B-type star	–	2 to 16 times the mass of the sun, young, hot (T 10,000−33,000 K) and very luminous main sequence star
CCD	–	Charge-coupled device
CHIPS Satellite	–	Cosmic Hot Interstellar Plasma Spectrometer satellite
collimator	–	Device for limiting the size and angle of spread of a beam of radiation or particles
Dec	–	Declination
DIB	–	Diffuse Interstellar Band
dichroic beam-splitter	–	splits a bean of light into spectrally distinct output beams
$E(B-V)$	–	Color excess which describes the amount of interstellar reddening
EFOSC2	–	Faint Object Spectrograph and Camera (mark 2)
ESO	–	European Southern Observatory
ew	–	Equivalent width
EUV	–	Extreme UltraViolet
FWHM	–	Full width half maximum
gb	–	Galactic latitude
bl	–	Galactic longitude
grism	–	Combination of a grating and a prism
GUI	–	Graphical User interface
He	–	Helium
HII region	–	Hydrogen II: a low-density cloud of partially ionized gas
HD	–	Prefix used to identify stars in the Henry Draper catalogue
HeAr	–	Helium Argon: quartz-halogen lamps used for wavelength calibration
Hipparcos	–	Catalogue of very high quality astrometric and photometric data
HST	–	Hubble Space Telescope
INT	–	Isaac Newton Telescope
IRAF	–	Image Reduction and Analysis Facility

ISM	–	Interstellar Medium
IUE	–	International Ultraviolet Explorer: space observatory
LB	–	local bubble
LISM	–	Local Interstellar Medium
LLCC	–	Local Leo Cold Cloud
LMC	–	Large Magellanic Cloud
MIDAS	–	Munich Image Data Analysis System
MCL	–	MIDAS Control Language
Na	–	Sodium
NIST	–	National Institute of Standards and Technology
NTT	–	New Technology Telescope at ESO, La Silla, Chile
O-type star	–	Very massive, young, hot ($T\,33,000\,\mathrm{K}$) and very luminous main sequence star
P2PP	–	Phase 2 Preparation Tool used to prepare observing blocks at the NTT
PAH	–	Polycyclic aromatic hydrocarbon
RON	–	Readout effect of the noise
SMC	–	Small Magellanic Cloud
S/N	–	Signal-to-noise ratio
VPH grisms	–	Volume-Phased Holographic prisms

B Appendix B

Note All supplementary data described by appendices B, C, D, E and F are found on the accompanying CD.

Tables of target stars and sample table of the calculations to scale the bias frames obtained at the New Technology Telescope (NTT) at La Silla, Chile

The following PDF files give the details of the target stars used for the observing runs at the New Technology Telescope (NTT) at La Silla, Chile and the Anglo Australian Telescope (AAT) in Australia as well a sample of the calculations needed to scale the bias frames obtained at the NTT in order to be able to reduce the data. These are all discussed in Chapter 2.

B.1 Local Bubble

This table lists the target stars for the Local Bubble project, see Section 2.1.1.2. Each row in the table gives the information relating to one star. From left to right the information in the columns of the table are 1) name of target star, 2) the right ascension coordinate of the star in hours, minutes and arcseconds, 3) the declination coordinate of the star in hours, minutes and arcseconds, 4) the two values describing the stars propper motion, 5) the distance in parsecs to the target star, 6) the V magnitude of the target star and 7) the spectral type of the target star.

B.2 SMC TARGETS

This table lists the target stars for the SMC in the Magellanic Cloud project, see Section 2.1.2.2. Each row in the table gives the information relating to one star. From left to right the information in the columns of the table are 1) name of target star (which for these stars are just numbers), 2) the right ascension coordinate of the star in hours, minutes and arcseconds, 3) the declination coordinate of the star in hours, minutes and arcseconds, 4) the V magnitude of the target star and 5) the spectral type of the target star.

B.3 LMC TARGETS

This table lists the target stars for the LMC in the Magellanic Cloud project, see Section 2.1.2.2. Each row in the table gives the information relating to one star. From left to right the information in the columns of the table are 1) name of target star (which for these stars are just numbers), 2) the right ascension coordinate of the star in hours, minutes and arcseconds, 3) the declination coordinate of the star in hours, minutes and arcseconds, 4) the V magnitude of the target star and 5) the spectral type of the target star.

B.4 Scaling Bias frames

This table is an example of the calculations for the 20th August 2012 needed to scale the bias frames from the NTT data to a common intensity level. This procedure is described in Section 2.1.1.3.

Each line of the table relates to one bias frame. The figures are ADU values The bias frames were split in two by a difference in intensity values, the left hand side of the bias frame having a higher average intensity than the right hand side. As described in Section 2.1.1.3 the bias frames had various intensity values throughout the night and it was not possible to combine them into a useful master bias frame. Statistical analysis of the frames gave a median value for the intensity of both halves. The average value of the intensity of each frame was calculated (see the last line of the table) and the difference in intensity between each bias frame and this average value was calculated. From left to right each column of this table is 1) the median value of intensity for the left hand side of each bias frame, 2) the addition factor needed to adjust the value in column 1 to the mean value of all bias frames, 3) the mean value of the intensity of the left hand side of all bias frames, 4) the median value of intensity for the right hand side of each bias frame, 5) the addition factor needed to adjust the value in column 4 to the mean value of all bias frames and 6) the mean value of the intensity of the right hand side of all bias frames.

C Appendix C

Spectral Atlas

The following PDF files show the spectra and profiles of the fitted spectral features for the data obtained from the New Technology Telescope (NTT) at La Silla, Chile and the Anglo Australian Telescope (AAT) in Australia. The spectra obtained from the NTT are discussed in Chapter 3; the spectra obtained from the AAT are discussed in Chapter 4

C.1 Local Bubble

These are the spectra obtained from the NTT. Each row of the PDF corresponds to the spectrum of one star, the name of which appears at the bottom right hand corner of the plot in the first column. Each plot corresponds to a wavelength range that spans the spectral feature of interest. The columns from left to right are: 1) the 5780 and 5797 Å DIBs, 2) the 5850 Å DIB, 3) the He line of the target star, 4) the Na lines of the ISM, 5), the 6196 and 6203 Å DIBs, 6) the 6270 Å DIB, 7) the 6283 Å DIB and 8) the 6614 Å DIB.

The fit of all bar the 5797 Å DIB is shown by a red line, the fit of the 5797 Å DIB is shown by a green line to distinguish it from the 5780 DIB. As discussed in Section 2.2.1 the overlying spectral feature around the 5780 line resulted in the best method of normalising that part of the spectrum involving a 2nd order polynomial. The 5780 and 5797 Å DIBs were fitted separately but displayed in the same plot, as a result the 5797 Å DIB sometimes looks to have a normalisation level higher than 1.0. If the two DIBs had not been plotted on the same graph they would have been normalised independently and the fits of both DIBs would have had continua closer to 1.0 as is normally the case. The reason for plotting both DIBs at the same time was because of the importance of these two DIBs, plotting them together gave a better overview of the relationship between them. Although not ideal, fitting theses two DIBs in this way gave the most accurate fits and therefore the most accurate measurements for both.

Many of the fits appear to be fitting noise, all of these plots were inspected by eye and only those data for which I could be certain there was a spectral feature fitted were used for the analysis and creation of the maps.

C.2 Small Magellanic Cloud (blue)

These are the spectra obtained from the ATT. Each row of the PDF corresponds to spectra of four stars (two plots for each star). The name of the star (in this case just a number) is given at the top left hand corner in the first plot for each star. The first plot in each pair shows the Ca II K line detected in both the Galactic sight-line and in the SMC itself, the second plot in each pair shows the Ca II H line again detected in both the Galactic sight-line and in the SMC itself. Only the Ca II K line was fitted with a profile (red line) as there was too much spectral contamination to accurately fit the Ca II H line. However, from the known wavelength separation of these two spectral lines it was possible to mark the expected peak postion for the on the plot for the Ca II H line for both the Galactic sight-line and in the SMC.

All of these plots were inspected by eye and only those data for which I could be certain there was a spectral feature fitted were used for the analysis and creation of the maps.

C.3 Small Magellanic Cloud (red)

These are the spectra obtained from the ATT. Each row of the PDF corresponds to spectra of two stars (three plots for each star). The name of the star (in this case just a number) is given at the top left hand corner in the first plot for each star. The first plot in each pair shows the 5780 Å DIB detected in both the Galactic sight-line and in the SMC itself, the second plot in each pair shows the 5797 Å DIB detected in both the Galactic sight-line and in the SMC itself and the third plot in each pair shows the Na I D lines again detected in both the Galactic sight-line and in the SMC itself, both the D_2 and D_1 components of the Na I line in both Galactic sight-line and in SMC were sufficiently separated to be detected. There was also often a detection of the telluric Na I line which showed as an emission line connected to the Galactic component of the Galactic D lines, this was fitted in order to provide a more accurate fit for the Na I absorption lines. Both DIBs and Na lines were fitted (red lines).

Many of the fits appear to be fitting noise or the DIBs are so weak it is uncertain whether or not the fitting profile is actually detecting a DIB. All of these plots were inspected by eye and only those data for which I could be certain there was a spectral feature fitted were used for the analysis and creation of the maps.

C.4 Large Magellanic Cloud (blue)

These are the spectra obtained from the ATT. Each row of the PDF corresponds to spectra of four stars (two plots for each star). The name of the star (in this case just a number) is given at the top left hand corner in the first plot for each star. The first plot in each pair shows the Ca II K line detected in both the Galactic sight-line and in the LMC itself, the second plot in each pair shows the Ca II H line again detected in both the Galactic sight-line and in the LMC itself. Only the Ca II K line was fitted with a profile (red line) as there was too much spectral contamination to accurately fit the Ca II H line. However, from the known wavelength separation of these two spectral lines it was possible to mark the expected peak postion for the on the plot for the Ca II H line for both the Galactic sight-line and in the LMC.

All of these plots were inspected by eye and only those data for which I could be certain there was a spectral feature fitted were used for the analysis and creation of the maps.

C.5 Large Magellanic Cloud (red)

These are the spectra obtained from the ATT. Each row of the PDF corresponds to spectra of two stars (three plots for each star). The name of the star (in this case just a number) is given at the top left hand corner in the first plot for each star. The first plot in each pair shows the 5780 Å DIB detected in both the Galactic sight-line and in the LMC itself, the second plot in each pair shows the 5797 Å DIB detected in both the Galactic sight-line and in the LMC itself and the third plot in each pair shows the Na I D lines again detected in both the Galactic sight-line and in the LMC itself. In the case of the LMC the Galactic D_1 line is often blended with the LMC D_2 line and D_1 components of the Na I, where they are sufficiently separated this is shown by the fitting profile. There was also often a detection of the telluric Na I line which showed as an emission line connected to the Galactic component of the Galactic D lines, this was fitted in order to provide a more accurate fit for the Na I absorption lines. Both DIBs and Na lines were fitted (red lines).

Many of the fits appear to be fitting noise or the DIBs are so weak it is uncertain whether or not the fitting profile is actually detecting a DIB. All of these plots were inspected by eye and only those data for which I could be certain there was a spectral feature fitted were used for the analysis and creation of the maps.

D Appendix D

MIDAS programmes The following MIDAS programmes were written to aid the reduction of the spectral images obtained from the New Technology Telescope (NTT) at La Silla, Chile. The procedure is fully described in Section 2.1.1.3.

1. bias_ext.prg
2. bias_ins.prg
3. bias_insL.prg
4. bias_insR.prg
5. flat_prep.prg
6. flat3.prg

E Appendix E

IDL programmes and measurements

The following IDL codes were written to plot the spectra obtained from the New Technology Telescope (NTT) at La Silla, Chile and the Anglo Australian Telescope (AAT) in Australia. The NTT code is fully described in Section 2.2.1 and the ATT code is fully described in Section 2.2.2.

1. lb_dibs_2012.pro: Code to plot all spectra obtained at the NTT
2. lmcb.pro: Code to plot the LMC blue spectra obtained at the AAT
3. lmcr.pro: Code to plot the LMC red spectra obtained at the AAT
4. smcb.pro: Code to plot the SMC blue spectra obtained at the AAT
5. smcr.pro: Code to plot the SMC red spectra obtained at the AAT

The following data files contain all the measurements made by the above IDL codes. Each line corresponds to the measurements made by the IDL code for on target star. Some of these data files are large and the page will need exanding a lot to see the data displayed on a single line.

1. measures_LB.dat: Measurement taken by running IDL code lb_dibs_2012.pro
2. measures_lmcb.dat: Measurement taken by running IDL code lmcb.pro
3. measures_lmcr.dat: Measurement taken by running IDL code lmcr.pro
4. measures_smcb.dat: Measurement taken by running IDL code smcb.pro
5. measures_smcr.dat: Measurement taken by running IDL code smcr.pro

On the following page there is a table for Local Bubble project which displays the column number and description of the entry in that column. This is a subset of the measurements made from that data

The four data files for the Magellanic Cloud data are included on the CD in full and are exactly as desribed in the discussion of the code in Chapter 2.

E.1 measures_LB.dat

NOTE

Column 8: 'Selection value'is a value calcualted to aid a decision on whether or not a spectral feature detection was considered to be valid. A value greater than 20 was considered a significant detection.

a Flag value of 1 denotes a true detection of spectral feature.

a Flag value of 0 denotes a false detection of spectral feature.

Table E.1: measurements made by the IDL code lb_dibs_2012.pro.

Column	Description	Column	Description
1	target name	2	RA
3	DEC	4	gl
5	gb	6	Distance
7	EW 5780 Å DIB	8	error in EW 5780 Å DIB
9	selection value 5780 Å	10	Chi squared 5780 Å
11	EW 5797 Å DIB	12	error in EW 5797 Å DIB
13	selection value 5797 Å	14	Chi squared 5797 Å
15	EW 5850 Å DIB	16	error in EW 5850 Å DIB
17	selection value 5850 Å	18	Chi squared 5850 Å
19	EW He	20	error in He
21	selection value He	22	Chi squared He
23	EW Na 1st	24	error in Na 1st
25	EW Na 2nd	26	error in Na 2nd
27	selection value Na 1st	28	selection value Na 2nd
29	Chi squared Na	30	EW 6196 Å DIB
31	error in EW 6196 Å DIB	32	EW 6203 Å DIB
33	error in EW 6203 Å DIB	34	selection value 6196 Å
35	selection value 6203 Å	36	Chi squared
37	EW 6270 Å DIB	38	error in EW 6270 Å DIB
39	selection value 6270 Å	40	Chi squared 6270 Å
41	EW 6283 Å DIB	42	error in EW 6283 Å DIB
43	selection value 6283 Å	44	Chi squared 6283 Å
45	EW 6614 Å DIB	44	error in EW 66614 Å DIB
47	selection value 66614 Å	48	Chi squared 6614 Å
49	flag 5780 Å DIB	50	flag 5797 Å DIB
51	flag 5850 Å DIB	52	flag He
53	flag Na 1st	54	flag Na 2nd
55	flag Na dip	56	flag 5196 Å DIB
57	flag 6203 Å DIB	58	flag 6270 Å DIB
59	flag 6283 Å DIB	60	flag 6614 Å DIB

F Appendix F

Data reduction method

A step by list of instructions on how to reduce the data obtained from the EFOSC2 spectrograph on the New Technology Telescope at La Silla, Chile.

Bibliography

Avila-Reese V., 2007, in Carramiñana A., Guzman F., Matos T., eds, Solar, stellar and galactic connections between particle physics and astrophysics, Springer, p. 115

Baker E., 1949, Publications of the Royal Observatory of Edinburgh, 1, 15

Barlow R. J., 1989, Statistics: a Guide to the Use of Statistical Methods in the Physical Sciences, John Wiley Sons, 1.0 edition

Barstow M. A., Boyce D. D., Welsh B. Y., Lallement R., Barstow J. K., Forbes A. E., Preval S., 2010, ApJ, 723, 1762

Beals C. S., Blanchet G. H., 1938, MNRAS, 98, 398

Bland-Hawthorn D. P., Sutherland R., Agertz O., Moore B., 2007, ApJ, 670, 109

Breitschwerdt D., de Avillez M. A., 2006, A&A, 452, 1

Breitschwerdt D., de Avillez M. A., Baumgartner V., 2009, in Smith R. K., Snowden S. L., Kuntz K. D., eds, Modeling the Local Warm/Hot Bubble, American Institute of Physics Conference Series, p. 271

Cami J., Sonnentrucker P., Ehrenfreund P., Foing B. H., 1997, A&A, 326, 822

Cioni M. R. L., K. Bekki K., Clementini G., de Blok W. J. G., Emerson J. P., Evans C. J., de Grijs R., Gibson B. K., Girardi L., Groenewegen M. A. T., Ivanov V. D., Leisy P., Marconi M., Mastropietro C., Moore B., Naylor T., Oliveira J. M., V. Ripepi V., van Loon J. T., Wilkinson M. I., Wood P. R., 2008, publications of the Astronomical Society of Australia, 25, 121

Cordiner M. A., Fossey S. J., Smith A. M., Sarre P. J., 2006, Faraday Discussions, 133, 403

Cox D. P., Anderson P. R., 1982, ApJ, 253, 268

Cox D. P., 2005, Annu. Rev. Astron. Astrophys., 43, 337

Cox N. L. J., Cordiner M. A., Cami J., Foing B. H., Sarre P. J., Kaper L., Ehrenfreund P., 2006, A&A, 447, 991

Crawford I. A., 2003, Astrophysics and Space Science, 285, 661

Dachs J., 1970, A&A, 9, 95

Duke D., 1951, ApJ, 113, 100

ESO., 2011, EFOSC2 Pipeline User Manual, European Southern Observatory, 1.0 edition

Evans C. J., Taylor W. D., Henault-Brunet V., Sana H., de Koter A., Simon-Diaz S., Carraro G., Bagnoli T., Bastian N., Bestenlehner J. M., Bonanos A. Z., Bressert E., Brott I., Campbell M. A., Cantiello M., Clark J. S., Costa E., Crowther P. A., de Mink S. E., Doran E., Dufton P. L., Dunstall P. R., Friedrich K., Garcia M., Gieles M., Graefener G., Herrero A., Howarth I. D., Izzard R. G., Langer N., Lennon D. J., Maiz Apellaniz J., Markova N., Najarro F., Puls J., Ramirez O. H., Sabin-Sanjulian C., Smartt S. J., Stroud V. E., van Loon J. T., Vink J. S., Walborn N. R., 2011, A&A, 530, 108

Fitzgerald M. P., 1968, AJ, 73, 983

Frisch P. C., 1981, Nature, 293, 377

Frisch P. C., 1998, in Breitschwerdt D., Freyberg M. J., Truemper J., eds, IAU Colloq. 166: The Local Bubble and Beyond, Lecture Notes in Physics, Berlin Springer Verlag, p. 269

Fuchs B., Breitschwerdt D., de Avillez M., Dettbarn C., Flynn C., 2006, MNRAS, 373, 993

Grosbøl P., 1989, in Klare G., ed., Reviews in Modern Astronomy, Springer-Verlag, p. 242

Hartmann J., 1904, ApJ, 19, 268

Heger M. L., 1922, Lick Observatory Bulletin, 10, 141

Herbig G. H., 1975, ApJ, 196, 129

Herbig G. H., 1993, ApJ, 407, 142

Herbig G. H., 1995, Annu. Rev. Astron. Astrophys., 33, 19

Hill G. J., Wolf M. J., Tufts J. R., Smith E. C., 2003, in Atad-Ettedgui E., D'Odorico S., eds, Society of Photo-Optical Instrumentation Engineers (SPIE) Conference Series, Society of Photo-Optical Instrumentation Engineers (SPIE) Conference Series, p. 1

Hobbs L. M., York D. G., Snow T. P., Oka T., Thorburn J. A., Bishof M., Friedman S. D., McCall B. J., Rachford B., Sonnentrucker P., Welty D., 2008, ApJ, 680, 1256

Horne K., 1986, PASP, 98, 609

Hutchings J. B., 1966, MNRAS, 131, 299

Izzo C., 1998, ESO_MIDAS User guide, European Southern Observatory

Jenniskens P., Desert F. X., 1994, A&AS, 106, 39

Jenniskens P., Porceddu I., Benvenuti P., Desert F. X., 1996, A&A, 313, 649

Josafatsson K., Snow T., 1987, ApJ, 319, 436

Kaler J. B., 1989, Stars and their spectra. an introduction to spectral sequence, Cambridge University Press, 1.0 edition

Krełowski J., Sneden C., 1993, PASP, 105, 1141

Krełowski J., Walker G. A. H., 1987, ApJ, 312, 860

Krełowski J., Westerlund B. E., 1998, A&A, 190, 339

Krełowski J., 1988, PASP, 100, 896

Krełowski J., Ehrenfreund P., Foing B. H., Snow T. P., Weselak T., Tuairisg S. Ó., Galazutdinov G. A., Musaev F. A., 1999, A&A, 347, 235

Krełowski J., Sneden C., Hiltgen D., 1995, Planetary and Space Science, 43, 1195

Lallement R., 2004, A&A, 418, 143

Lallement R., Welsh B. Y., Vergely J. L., Crifo F., Sfeir D., 2003, A&A, 411, 447

Lewis I. J., Cannon R. D., Taylor K., Glazebrook K., Bailey J. A., Baldry I. K., Barton J. R., Bridges T. J., Dalton G. B., Farrell T. J., Gray P. M., Lankshear A., McCowage C., Parry I. R., Sharples R. M., Shortridge K., Smith G. A., Stevenson J., Straede J. O., Waller L. G., Whittard J. D., Wilcox J. K., Willis K. C., 2002, MNRAS, 333, 279

Lucke P. B., 1978, A&A, 64, 367

McCall B. J., Drosback M. M., Thorburn J. A., York D. G., Friedman S. D., Hobbs L., Rachford B., Snow T., Sonnentrucker P., Welty D., 2010, ApJ, 708, 1628

Merrill P. W., Humason M., 1938, PASP, 50, 212

Merrill P., Wilson O., 1938, ApJ, 87, 9

Merrill P. W., 1934, PASP, 46, 206

Merrill P. W., 1936, ApJ, 83, 126

Meyer D. M., Lauroesch J. T., Peek J. E., Heiles C., 2012, ApJ, 752, 119

Monaco L., Snodgrass C., 2008, EFOSC2 User Manual, European Southern Observatory, 3.1 edition

Opher M., Bibi F. A., Toth G., Richardson J. D., Izmodenov V. V., Gombosi T., 2009, Nature, 462, 1036

Peek J. E. G., Heiles C., Peek K. M. G., Meyer D. M., Lauroesch J. T., 2011, ApJ, 735, 129

Sarre P. J., 2006, Journal of Molecular Spectroscopy, 233, 1

Sasseen T. P., Hurwitz M., Team C., 2004, Two Years of EUV Observations with the Cosmic Hot Interstellar Plasma Spectrometer (CHIPS), Bulletin of the American Astronomical Society, p. 1408

Sharp R., Saunders W., Smith G., Churilov V., Correll D., Dawson J., Farrel T., Frost G., Haynes R., Heald R., Lankshear A., Mayfiel D., Waller L., Whittard, 2006, in McLean, I. S.and Iye M., ed., Performance of AAOmega: the AAT multi-purpose fiber-fed spectrograph, Society of Photo-Optical Instrumentation Engineers (SPIE) Conference Series, p. 62690

Smith G. A., Saunders W., Bridges T., Churilov V., Lankshear A., Dawson J., Correll D., Waller L., Haynes R., Frost G., 2004, in Moorwood A., Iye M., eds, Society of Photo-Optical Instrumentation Engineers (SPIE) Conference Series, Society of Photo-Optical Instrumentation Engineers (SPIE) Conference Series, p. 410

Snow T. P., Destree J. D., 2011, in Joblin C., Tielens A. G. G. M., eds, The Diffuse Interstellar Bands in History and in the UV, EASPublications Series, p. 341

Snowden S. L., Egger R., Finkbeiner D. P., Freyberg M. J., Plucinsky P. P., 1998, ApJ, 493, 715

van Loon J. T., Smith K. T., McDonald I., Sarre P. J., Fossey S. J., Sharp R. G., 2009, MNRAS, 399, 195

van Loon J. T., Bailey M., Tatton B. L., Maíz Apellániz J., Crowther P. A., de Koter A., Evans C. J., Hénault-Brunet V., Howarth I. D., Richter P., Sana H., Simón-Díaz S., Taylor W., Walborn N. R., 2013, A&A, 550, 108

Welsh B. Y., Lallement R., 2012, PASP, 124, 566

Welsh B. Y., Shelton R. L., 2009, Astrophysics and Space Science, 323, 1

Welsh B. Y., Sfeir D. M., Sirk M. M., Lallement R., 1999, A&A, 352, 308

Welsh B. Y., Lallement R., Vergely J. L., Raimond S., 2010, A&A, 510, 54

Welsh B. Y., Sallmen S., Lallement R., 2004, A&A, 414, 261

Welty D. E., Federman S. R., Gredel R., Thorburn J. A., Lambert D. L., 2006, ApJS, 165, 138

Westerlund B. E., Krełowski J., 1998, A&A, 189, 221

Westerlund B. E., 1997, The Magellanic Clouds, Cambridge University Press

Wszołek B., 2007, in Ivashchenko G., Golovin A., eds, Puzzling Phenomenon of Diffuse Interstellar Bands, 14th Young Scientists Conference on Astronomy and Space Physics, p. 87

Xiang F., Liang S., Li A., 2009, Science in China G: Physics and Astronomy, 52, 489

Zaritsky D., Harris J., Thompson I. B., Grebel E. K., Massey P., 2002, AJ, 123, 855